Applications of freeze casting in biomaterials fabrication and cell cryopreservation

Kankan Qin

To cite this version:

Kankan Qin. Applications of freeze casting in biomaterials fabrication and cell cryopreservation. Biological Physics [physics.bio-ph]. Sorbonne Université, 2020. English. NNT : 2020SORUS352 . tel-03774276

HAL Id: tel-03774276
https://theses.hal.science/tel-03774276v1

Submitted on 10 Sep 2022

Sorbonne Université

Ecole doctorale 397 - Physique et Chimie des Matériaux

Laboratoire de Chimie de la Matière Condensée de Paris

Applications of freeze casting in biomaterials fabrication and cell cryopreservation

Par **Kankan Qin**

Thèse de doctorat Physique et Chimie des Biomatériaux

Présentée et soutenue publiquement le 09 Septembre 2020

Devant un jury composé de :

Nicolas TSAPIS	Directeur de Recherche CNRS (IGPS - Université Paris-Saclay, Paris)	Rapporteur
Maria Luisa FERRER	Directeur de Recherche CSIC (ICMM - CSIC, Madrid)	Rapportrice
Dominique HOURDET	Professeur Sorbonne Université (SIMM - ESPCI, Paris)	Examinateur
Marjo YLIPERTULLA	Professeur des Universités (University of Helsinki, Helsinki)	Examinatrice
Sylvain DEVILLE	Directeur de Recherche CNRS (ILM - Université Claude Bernard Lyon1, Lyon)	Examinateur
Thibaud CORADIN	Directeur de Recherche CNRS (LCMCP - Sorbonne Université, Paris)	Directeur de thèse
Francisco M. FERNANDES	Maître de conférences (LCMCP - Sorbonne Université, Paris)	Encadrant de thèse

Acknowledgements

First of all, I want to express the depth of my gratitude to my supervisors, Thibaud Coradin and Francisco M. Fernandes, for welcoming me as one of the members of the MatBio team in LCMCP. During those four years, Thibaud gave me help and suggestions for my life and progression of projects with fruitful discussions. I really appreciate his expertise and wisdom in directing projects and solving problem. I want to thank Francisco as well. It was him who interviewed me and finally gave me opportunity to join this team. He is a good researcher full of novel ideas. I could always get some impressive points after discussing with him. He is also a good friend. From the start to the end, he helped me adjust myself, always considered my personal life and helped me out when I was in trouble.

I would like to show my appreciations to all the members of the jury: Dominique Hourdet, Marjo Yliperttula, Sylvain Deville, Maria Luisa Ferrer, Nicolas Tsapis, Thibaud Coradin and Francisco M. Fernandes for their acceptance and presence to the thesis presentation and for their time to review my manuscript. With their constructive suggestions, the whole thesis will surely much more solid.

I want to thank: a) our lab directors – Christian Bonhomme (present) and Florence Babonneau (previous) – for their dedication to the normal lab running and the safe and comfortable working environment, especially during the quarantine period; b) administrative stuff in LCMCP: Corinne Pozzo Di Borgo, Hélène Gervais, Diana Lesueur, Nora Abdoul-Aribi for their help that makes my life and research easy to go. c) Alban Politi and Simon Dadoun for their help to solve the computer-related problem.

I would like to thank Verónica Cortés de Zea Bermudez and Rui FP Pereira for their help in advancing the silk fibroin projects and in writing the article. I also want to thank Sylvain Deville, Felix Ginot and Dmytro Dedovets for the observation of yeast cells under confocal microscope and for their constructive suggestions.

I would like to thank Christophe Helary and Ahmed Hamraoui for the training about bacteria and animal cell culture and for their good suggestions about the thesis projects. I want to thank the people who helped me for the characterization: Bernard Haye (sample preparation for Synchrotron), Isabelle Genois (Scanning electronic microscope), Nora Abdoul-Aribi (thermogravimetric analysis), Carole Aimé (Circular dichroism), Julien Dumont (confocal microscope, College de France), Muriel Andrieu and Clément Vaz (flow cytometry, Plateforme Cytometrie et immunologie, Institut cochin centre de recherche), Bénédicte Hoareau-Coudert (flow cytometry, Plateforme de Cytométrie, Faculté de Médecine Sorbonne Université).

It was my pleasure to work with all the LCMCP members. Present and previous MatBio team members: Thibaud, Francisco, Lea, Gervaise, Christophe, Ahmed, Cecile, Sylvie, Bernard, Corinne, Carole, Antoine, Nicolas, Camille, Océane, Marie, Pierre, Isabelle, Klio, Sarah, the two Clements, Dounia, Lise, Julien, Kevin, Estelle, Xiaolin, Yupeng, etc. Especially thank to Corentin, he helped me a lot not only in research, but also in providing energy (cookies and cakes). I would also like to thank all the other lab members including permanent and non-permanent stuff: Christian, Francois, Laurence, Nadine, Thierry, Marie, Natacha, Cédric, Silvia, Alexis, Xavier, Laetitia, Thibaut, Madeleine, Viviane, Elora, Caroline, Ghazi, etc.

I want to thank office members (402): Milena, Julie, Tristan, Chloé, Clio, Widad and Chrystelle. Thank you all for your help and concerning about my research and life. With you in the office, daily life looks much more interesting.

I would like to thank Binghua, Yang and Runhe for accompanying me in eating and playing during leisure time. Especially to Binghua, thanks for her help in writing and for providing delicious dishes. It made the life full of joy and happiness. And my gratitude to all my friends: Yao Zheng, Lin Zhang, Wenyi Wu, Jia Yi, Yuan Zhang, Hongyi Shi, Can Zhao, Wei Wang, Teng Zhang, Wei Zhang, *etc*, for your company and food.

Finally, I really want to show my gratitude to my family members: mom, dad, brother and sister. It is with their dedications to the family that I could plunge into research without burden. My success is your success. I wish you happiness and health all the life.

Thanks again to all of you.

Kankan

Table of contents

General introduction

In order to achieve successful tissue engineering, biomaterials need to possess some essential properties such as porosity, mechanical strength, biocompatibility and immune acceptance, all impacting on their interaction with cells.[1] In order to get an ideal scaffold from a structural point of view, many techniques have been explored, such as 3D printing (for example, stereolithography), porogen-based techniques (like solvent casting/particle leaching, freeze casting, *etc*) and electrospinning. Among them, freeze casting (also called ice templating) has been proved as a good approach for making porous scaffolds due to its high processing biocompatibility and the resultant high porosity.

Since the publication of Deville's paper in 2006[2], the exploration of this technique has flourished from biomimetic (nacre and bone, for instance) to multi-functional materials. Various building blocks (like nanosheets[3,4], nanofibers[5,6], macromolecules[7–9], *etc*) have been studied for fabricating materials with different structures and/or different functions for multiple applications ranging from energy storage device[10–12] to tissue engineering[13–16].

Freeze casting also enable cell encapsulation during material processing. Our group successfully encapsulated yeast cells in the presence of alginate via freeze casting and demonstrated that a fraction of the cells kept their metabolic activity even in dry alginate foams.[17] Without the ultimate drying process, this technique may also be applied to cryopreservation and could avoid the presence of common cryoprotectants with potential harmful effects on cells on the long-term[18,19]. In particular, directional freezing, one type of freeze casting with an horizontal thermal gradient, has been found useful for cell[20] and even tissue (like ovary[21–23] and liver[24]) cryoprotection.

In this context (presented in more detail in Chapter 1), this PhD work aimed at exploring novel applications of the freeze-casting techniques to health-related issues, with a specific emphasis on the relationship between the processing parameters and the bio-physical and bio-chemical properties of the resulting systems.

In a first approach, described in Chapter 2, we have designed antibacterial dermal patches based on reconstituted silk foams. Freeze-casting was used to prepare porous silk fibroin matrices that were loaded with an antibiotic molecule and coated with sericin and exhibited antibacterial properties over more than one week. This work highlighted the impact of the freezing rate on the porous structure of the matrix, which in turn influenced sericin coating and antibiotic release kinetics.

In the context of cryopreservation, Chapter 3 is dedicated to the understanding of the physico-chemical evolution of a biopolymer solution during freeze-casting and how it impacts on the viability of cells present in this solution. Using an alginate/yeast cells system, we coupled *in situ* microscopic observation of cells and their surroundings during freezing under confocal microscope with the freezing medium phase diagram analyzed by differential scanning calorimetry (DSC). We also used our home-made directional freezing apparatus to study the influence of ice front velocity on yeast viability. We could establish some relationships between cell viability and freezing events but highlighted that these can be both cell- and biopolymer-dependent.

Based on these promising results, we have tried to address the major challenge of long-term cryo-preservation of red blood cell.[25] We used Albumin as a cryoprotectant during directional freezing. By this method, we could prolong the storage time of frozen red blood cells to 106 days in -80 °C freezer. Relationships between cell viability and freezing environments were established on the basis of the thermal behavior of Albumin (Chapter 4).

Overall, this work opens new perspectives for the application of freeze-casting to the (bio)-medical field but also illustrates that establishing relationships between physico-chemical conditions and biological responses is a highly challenging task, especially in unusual conditions such as a low temperature gradient.

Chapter 1

Context and state of the art

Sections 3 and 4 of Chapter 1 are to be submitted as *Kankan Qin, Cleo Parisi and Francisco M. Fernandes* "Recent advances in ice templating: from biomimetic composites to cell culture scaffolds and tissue engineering" to Journal of Materials Chemistry B.

1.1 Tissue engineering

Tissue damage and degeneration have always been a major societal and medical concern, especially for the wellbeing of older people who account for gradually increasing ratio of the population thanks to the increase of human's life expectancy. The two most traditional approaches, tissue grafting and alloplastic repair, have their own limitations such as additional surgery, limited donor, poor integration into host tissues and immune issues.[26] Tissue engineering, firstly coined in 1993, is based on colonizing cells expanded *in vitro* onto a matrix able to support cell growth into culture medium.[27] In USA, 21 commercialized tissue engineering companies earned approximately 9 billion dollars by selling tissue engineering related products in 2017, while only 66 clinical tests were ongoing or completed from 2011 to 2018.[28] In other words, an increasing demand of tissue engineering products exist and further endeavors are worth being donated into this field.

As pointed out above, a tissue engineering system includes one (or several) cell types and a matrix within which these cells can survive and exert their full biological activity towards the formation of a new tissue. Considering cells, the paradigm has evolved from primary cell lines to stem cells, and, more recently, organoids. In terms of matrix, the currently most favored approach relies on porous materials, or scaffolds, whose cavities are large enough that allow cell penetration and proliferation (*i.e.* colonization). However, besides porosity, many other parameters have to be considered when designing such scaffolds in order to orient and optimize cellular behavior towards neo-tissue formation. Thus, before presenting the different strategies available to control the porous structure of biomedically-relevant materials (section 1.2), it is important to recapitulate our current knowledge on cell-materials interactions.

1.1.1 Cell-materials interactions

1.1.1.1 Introduction of cell-material interactions

Cell behaviors are controlled by soluble factors, cell-cell interactions and by cell adhesion to the extracellular matrix (ECM). Among those, the interaction between cells and ECM plays a key role in the regulation of the multiple biological responses of cells onto support matrix.

1.1.1.2 Cell-matrix adhesion

In natural tissues and organs, cells are interacting with the ECM which contains glycoproteins (such as fibronectin and laminin), collagens, proteoglycans and non-matrix proteins including growth factors. In order to induce this interaction, the first necessary step lies in a well-known event – cell adhesion – between cells and matrix.[29] Cell-matrix adhesion plays a crucial role in regulating important cell events, like cell survival, migration, differentiation, *etc*.[30] Therefore, a good understanding of cell-matrix adhesion can direct matrix design for tissue engineering. Cell adhesion can also be affected by pathological disorders. For instance, local ECM degradation, which affects cell adhesion to some extent, is regarded as one of the causes for the invasiveness of cancer cells[31].

Adhesion involves cell adhesion molecules (CAMs) which are receptors located on the cell surface. Although various CAMs (such as integrins, immunoglobulin superfamily, cadherins, and lectin-like domains)[32] have been identified, the integrin family is one of the most impactful factor in tuning cell-matrix adhesion.[30]

1.1.1.3 Integrin

Adhesion mechanisms of integrin family have been well explored, especially by Abercrombie[33,34] and Curtis[35] groups, by observing adhered fibroblast under electron microscope or interference reflection contrast microscope. Integrins as transmembrane heterodimeric receptors are located on cell surface and 24 integrins (Figure 1.1) have been identified with different integrations of 18 α and 8 β subunits.[36] Based on their structure, ligand and location specificity, nine groups are classified. For example, α5β1 expressed by fibroblasts, endothelial cells and myoblasts can interact with fibronectin to induce the adhesion process. Several of the subunits could be expressed in specific time and space, for example, β6 subunit can only be detected during wound healing for adult people.[37] Among all integrin family members, α and β subunits bond with each other via their ‘head’ in the endoplasmic reticulum and are then secreted and subsequently anchored on the cell surface.[38] α and β subunit share a similar structure and are mainly composed of three parts: an extracellular domain, a transmembrane domain and an intracellular tail.[39] The extracellular domain can interact with other molecules (like growth factor receptors, matricellular proteins) which are located on the cell surface.

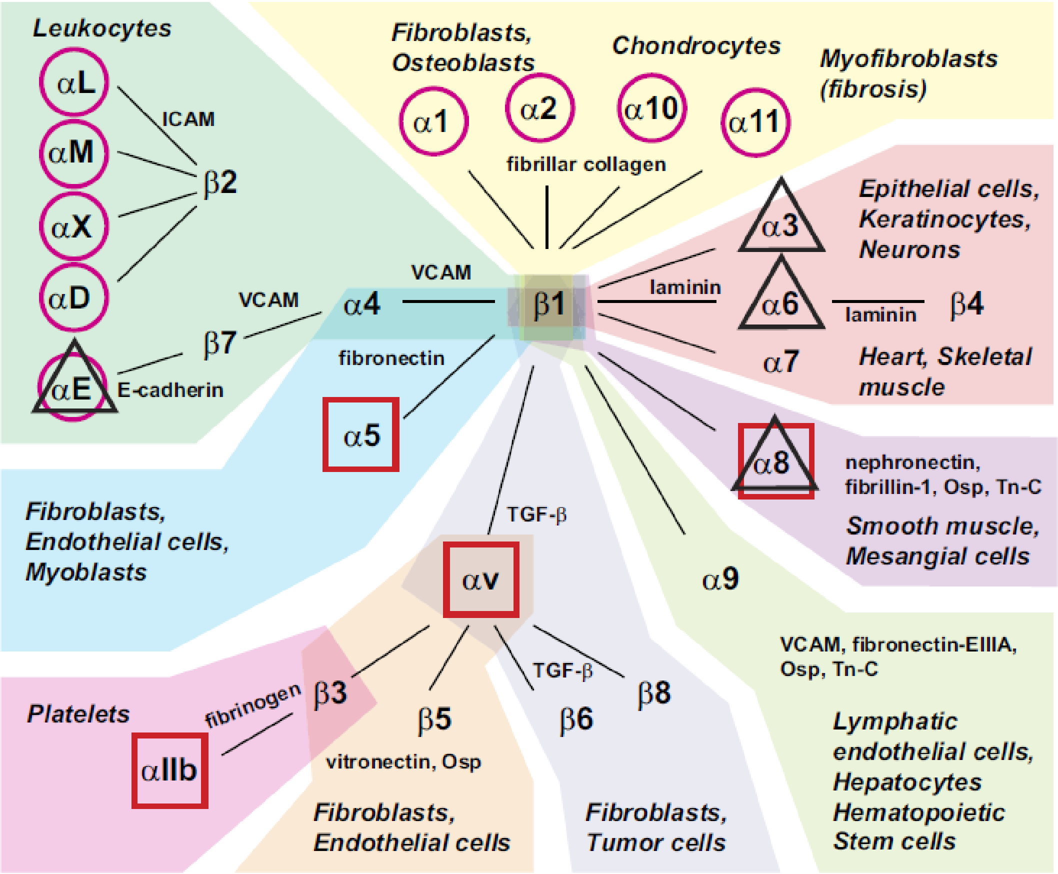

Figure 1.1 Integrins, their ligands, and cellular distributions. Nine groups of integrins with different background color were classified based on their structure, ligands and expression places. α-I domain (I; purple circle), integrins binding to RGD ligands (RGD; red square), integrins with sequence deviating from CGFFKR (black triangle). Adapted from Bachmann[40].

Integrin activation is related to the conformational change of subunits. To date, the most well-known integrin activation models, “deadbolt” and “switchblade”, both involve structure change of α and β subunit.[36,41] In the “deadblot” model, the activation is initiated by ligand binding while it is also accepted that before ligand binding the integrin have already experienced a bent, an extended-closed and finally an extended-open state in the "switchblade" model.[42,43] Integrin clustering, as one of the downstream intracellular event triggered by integrin activation, has been found in osteoblasts, fibroblasts and melanocytes.[44] This event is induced by the initial attachment between integrin and ECMs, which leads to the recruitment of integrins to the adhesion site. Adaptor proteins are subsequently recruited and establish connections with cell cytoskeleton, which results in large adhesomes, such as focal complexes, focal adhesions and fibrillar adhesions.[45] The adaptor proteins can be categorized into three groups: a) catalytic adaptors responsible for correct signal transductions, such as integrin-linked kinase and focal adhesion kinase; b) structural adaptors (including filamin, talin) regarded as mediators between integrin and actin cytoskeleton; and c) scaffold adaptors (like parillin and kindlin) forming binding sites for other adhesion proteins.[39] In some cases, adaptor proteins could be regarded to some extent as signals for regulating protein binding to integrins.[46] Besides, they could also act as regulators of cytoskeleton construction due to their linkage with the actin and cytoskeleton components.[39]

Inhibitors also exist for preventing interactions between integrin intracellular tails and adaptor proteins, which could be negative regulations for the downstream signaling transduction.[47] For example, filamin could competitively bind to intracellular tails of subunit against talin.

1.1.1.4 Integrin-mediated mechanotransduction

ECM or ECM-derived protein binding onto cells initiating cell adhesion is the basis of force transmission (also called mechanotransduction) across cell membrane.[48,49] The force is transmitted from actin filaments through myosin head to integrins and then to cell membrane and/or bound proteins surrounding cells. During the force transmission, cell nucleus could probably receive the signal from the mechanical tension and correspondingly regulate its behavior (such as gene expression, cell survival, migration, proliferation and differentiation).[50,51]

The mechanotransduction could be related to three main adhesomes that are involved in cell migration. As shown in Figure 1.2, nascent adhesions (NAs) composed of three to six integrins tend to form at the forward edge of cell protrusions.[52,53] Mechanosensitive adapters such as talin and vinculin in NAs act as mediators to transmit the retrograde pushing forces from actin network to ECMs.[54] In turn, the tunable retrograde flow rate due to transient coupling of integrins and F-actin could be related to the assembly of NAs between lamellipodium and lamellum.[55] Although NAs are short-lived, a few of them further cluster and form into bigger focal adhesions (FAs) along actomyosin bundles in the lamellum. The stronger binding results in the formation of catch bond through which high traction force are transmitted. [54] Then the decreased force transmission induces the formation of the slip bond between integrins and ECMs into fibrillar adhesions (FBs).[56,57] At the rear of migrating cells, the high traction force probably helps to detach cell and propel cells body forward.[54]

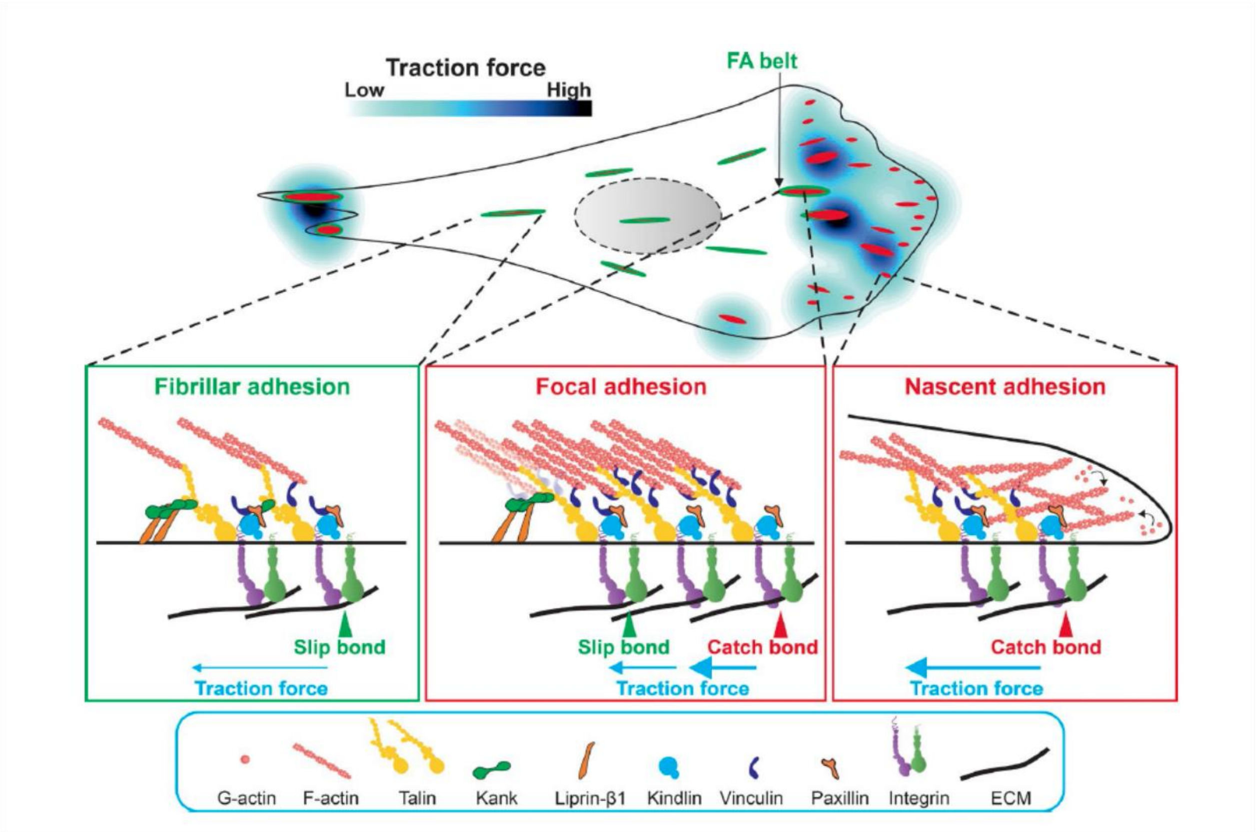

Figure 1.2 Model of a migrating cell containing diverse integrin-based adhesion structures that transmit different levels of traction forces.[58]

1.1.2 Tunable parameters for cell-material interactions

Although plenty of artificial scaffolds have been successfully fabricated and applied to tissue engineering, mimicking the cell-ECM interactions found in nature is still challenging. Mechanical, topological and chemical properties (Figure 1.3) have been found essential in order to regulate cell behaviors like adhesion, proliferation, differentiation, *etc*. The individual or synergistic effects of those parameters on cell behaviors could further provide fruitful knowledge in designing biomedical related scaffold.

1.1.2.1 Mechanics

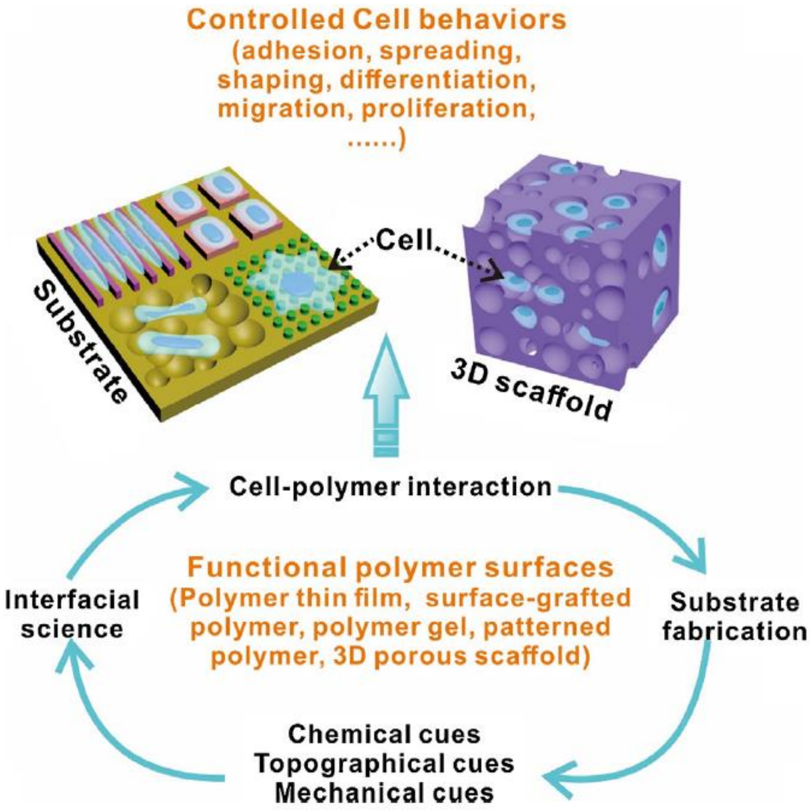

Figure 1.3 Influence of three main parameters on cell-polymer interaction contributing to controlled cell behaviors (such as adhesion, migration and differentiation). Reproduced from ref[59].

As described above, substrate mechanics influence cell adhesion[60] and migration[61–63], and it also affect other cell behaviors, such as proliferation[64] and differentiation[65,66]. For example, Fusco et al.[60] used two common synthetic polymers – polyacrylamide (PAA) and polydimethylsiloxane (PDMS) – to fabricate substrates with different stiffness ranging from 1 to 1000 kPa. FA number and size increased with stiffness, revealing a cell response against substrate stiffness at the beginning of the adhesion event. FA size and cell mobility were inversely associated, probably due to the difference of time intervals needed in the assembly and disassembly of FA structures. Thus, substrate stiffness tunes FA size and the following cell migration. Saha et al.[65] created a PAA-based hydrogel system to study the effects of substrate modulus (10-10000 Pa) on differentiation of adult neural stem cells (aNSCs). When cultured in differentiation medium in presence of serum, stem cells differentiated to neurons onto softer gels ranging from around 100 to 500 Pa, while glial cells were present on harder gels (1000 to 10000 Pa).

In nature, cells are surrounded by ECMs exhibiting dramatically different mechanics depending on tissue types, from around 0.1 kPa (brain tissues) to 100 GPa (bone tissues).[67] Since mesenchymal stem cells (MSCs, derived from bone marrow) need to migrate to other tissues for achieving its functionalities, mechanical gradient could be encountered during its passage.[10] In literature, mechanical gradient have been proved beneficial for cell migration[61,62] and differentiation[10]. Chao et al.[62] assembled PDMS base and collagen top layers to create linear stiffness gradient without changing chemical and transport properties. Both ligament fibroblasts (LFs) and MSCs responded to the stiffness gradient and showed directed migration. Tse et al.[68] created a stiffness gradient (around 1 kPa/mm) on a synthetic hydrogel system. Results indicated that MSCs migrated to stiffer matrix and even differentiated into myogenic phenotype.

Although stiffness (or elastic modulus)[66,69,70] has been well explored, loss modulus (also called viscous modulus)[64] as one of the main properties of viscoelastic behaviors of polymer materials also plays a role in modulating cell behaviors. Cameron et al.[64] achieved constant elastic modulus (around 4.7 kPa), while varying loss modulus (1 to 130 Pa) on PAA gel system. After seeding hMSCs onto the gels, cell spread area increased by approximately 4000 μm^2 when increasing the loss modulus from 1 to 130 Pa (Figure 1.4A-B). Higher cell proliferation ratio (60.3%) was obtained for 130 Pa gels compared to 54.9% (10 Pa) and

52.5% (1 Pa). Furthermore, hMSCs on 130 Pa gels showed improved differentiation to smooth muscle cell lineage than 10 Pa and 1 Pa after culture for 7 days. The reason underlying the effect of loss modulus on stem cell behaviors may lie in the reduction of isometric cytoskeleton tension caused by creep and high loss modulus of the gel.

Outside-in and inside-out pathway have been studied as two common features for the mutual interaction between cells and their microenvironment.[39] In other words, the substrate mechanics influence cell mechanics, and simultaneously cell mechanics can in turn remodel the substrate and tune its mechanics. Substrate mechanical properties have been proved essential for cell mechanics.[69,71] For example, cell intracellular elastic modulus was found to increase in the same ascending manner as stiffness of both PAA and PDMS substrates, which could be confirmed by the higher stress fiber diameters in higher stiffness.[60] Zhang et al.[69] also mentioned that stiffer matrix could improve elastic modulus, instantaneous modulus, relaxed modulus and apparent viscosity of chondrocytes when seeded on PDMS-based substrates. Cell seeding could in turn change mechanical properties of substrate during culture.[72–74] With a culture of hMSCs, cell-matrix composites experienced high contraction exerted by cell growth, which could be alleviated by increasing polymer concentration.[74] Arahira et al.[73] also found that osteoblast cells seeded β-tricalcium phosphate (β-TCP)/gelatin composites exhibited gradually increasing elastic modulus with continuous culture for 8 weeks. This is likely due to the sufficient penetration and proliferation of cells into the scaffold.

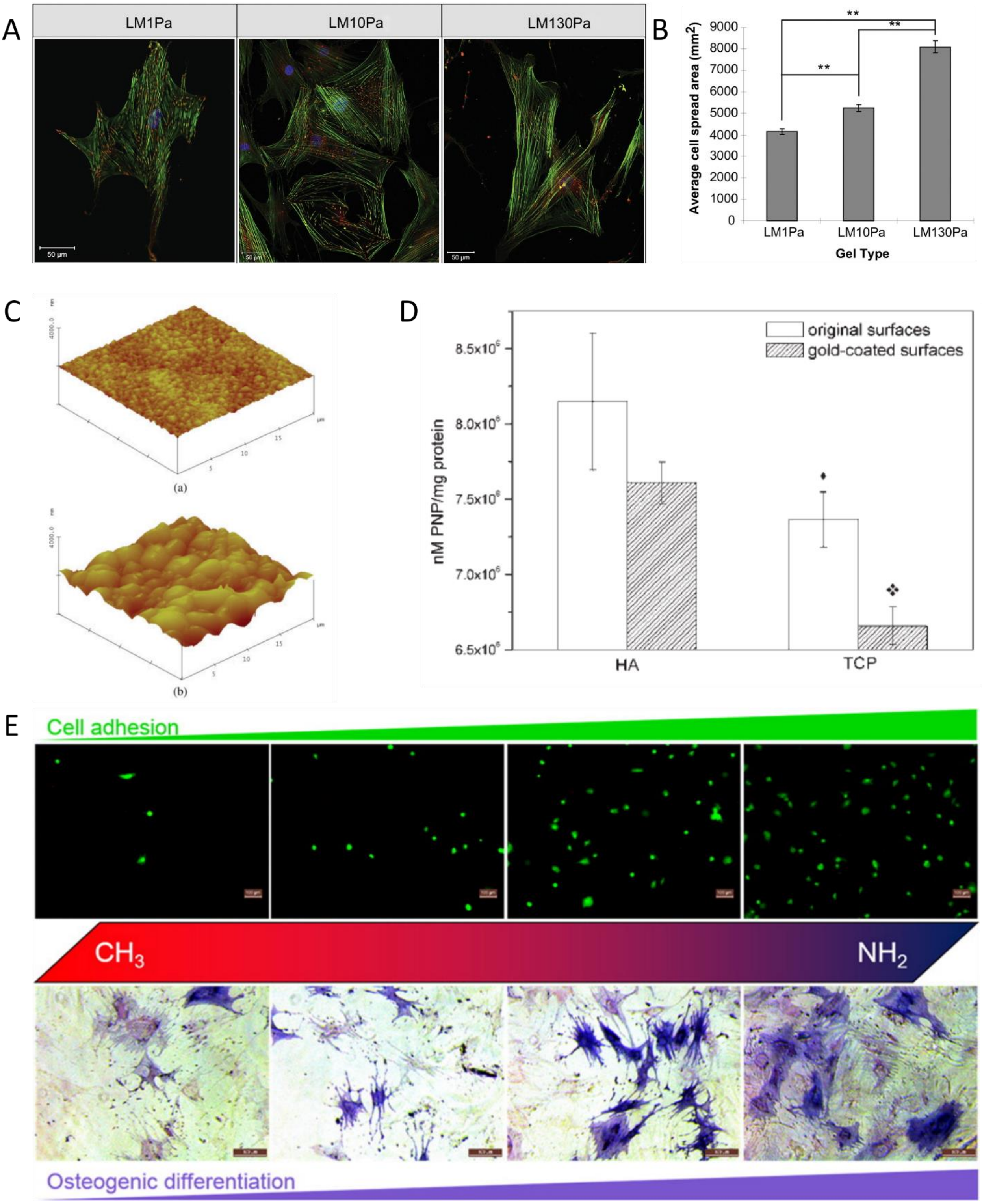

Figure 1.4 Effects of mechanics, topology and chemistry on cell behaviors. (A) hMSCs spreading on polyacrylamide gels of different loss moduli (LM) showing actin (green), nucleus (blue) and vinculin (red). Scale bar, 50 µm. (B) Average spreading area (at 48 h)

based on median cell sizes for gel substrates with different loss moduli. (C) 3D profiles of HA (above) and TCP (below) surface roughness via Atomic Force Microscope. (X×Y×Z, 20×20×4 μm^3) (D) Human osteoblastic cell (SaOs2) differentiation after 7 days' culture on the non-coated and gold-coated Hap and TCP surfaces. (E) Human adipose-derived stem cells (hASCs) adhesion and osteogenic differentiation along surface gradient of CH_3 and NH_2 (produced from) controlled plasma deposition of 1,7-octadiene and allylamine, respectively). Scale bar, 100 µm. (A and B) Reproduced from ref[64]. (C and D) Reproduced from ref[75]. (E) Reproduced from ref[76].

1.1.2.2 Topography

Topological features also play an important role in regulating interactions between cells and matrix.[77] To date, various surface features, such as roughened[75,78], grooved[79], spike-like[80], curved[81] and point-like[82] structures have been studied in view of their effects on cell behaviors. Zhang et al.[79] applied UV-nanoimprinting method to fabricate nanogrooved poly (ε-caprolactone) (PCL) surface with chemical modifications of carboxyl or benzyl group. Results indicated that the nanogrooved patterning promoted adhesion, proliferation, orientation and alignment of human foreskin fibroblast. Furthermore, cells exhibited elongated fibroblast-like shape and enhanced collagen secretion on the nanogrooved surfaces.

Specific topologies can induce cell differentiations.[75,83] Santos et al.[75] prepared surfaces of hydroxyapatite (Hap, average surface roughness Ra, 33 nm) and tricalcium phosphate (TCP, Ra equals 144 nm) (Figure 1.4C), coated by gold particles in order to mask the surface chemical effects. Human osteoblastic cells (SaOs-2) exhibited favorable differentiation with high alkaline phosphatase (ALP) activity on less rough Hap surface than TCP surface (Figure 1.4D), while no significant difference was shown for cell spreading and proliferation among those two surfaces. Topology gradient was thought useful not only for reducing cell numbers and decreasing the experimental variability, but also for observing cell preference.[84] Liu et al.[84] fabricated gold particle gradient on an amine-modified coverslip by tuning immersion time. From short time (2 mm) to long time immersion (11 mm), gold particle density was gradually increased. SaOs-2 cells showed less initially adhered cell number at low density sites than the following part of the surface, which indicated that surface roughness did play a role in regulating cell adhesion. Besides, an optimal intermediate immersion condition was found to favor initial cell adhesion revealing the cell preference on specific surface topology.

So far, we mentioned the surface topology effects on cell behaviors, but most situations in tissue engineering involve 3D environments. The topology effect in 3D is also worth being studied. In 3D scaffolds, topology features such as pore size[85], porosity[86], gradient pore structure[87] and ridges[16] have been proved to regulate cell behaviors like penetration, cell self-seeding, directed cell growth, differentiation, *etc*. More details will be discussed in the second section of this chapter.

1.1.2.3 Chemistry

Similarly to mechanical features and topology, chemistry have been regarded as an important parameter for modulating cell behaviors. Researchers have explored surfaces presenting diverse chemical groups, such as -OH, -COOH, $-NH_2$ or $-CH_3$, to characterize their cell-regulating roles.[88–91] Zhang et al.[79] showed that human foreskin fibroblast adhesion was slightly enhanced on benzyl-modified PCL surface compared to bare and carboxyl-modified PCL. The increased density of carboxyl groups resulted in reduced cell adhesion but improved proliferation. Carboxyl- and benzyl-modified surfaces exhibited higher cell alignment along the nanogrooved pattern compared to non-modified PCL surface.

Surface chemistry-dependent properties have been shown for cell adhesion, migration and differentiation.[76,89,92] Shen et al.[89] revealed an ascending migration rate of vascular endothelial cells in the order $CH_3 > NH_2 > OH > COOH$, which was ascribed to the integrin-related signal cascades. On the hydrophobic CH_3-modified surfaces, cells showed high levels of induced Rho GTPase proteins, Paxillin, total FAK and phosphorylation of FAK, leading to the fastest cell migration dependent on β1 clustering. On the contrary, on the hydrophilic COOH surface, the depressed expression of Rho GTPases and higher amount of talin, zyxin and α-actinin led to the lowest migration rate. In another example, Liu et al.[76] created a chemical gradient from the highest CH_3 density side (hydrophobic) to the highest NH_2 (hydrophilic) density side by fine regulation of gas composition during plasma deposition, while keeping its surface topography. Serum-free group showed no significant difference for cell behaviors, while improved adhesion (Figure 1.4E upper panel) and spreading area were observed toward the NH_2 side for human adipose-derived stem cells when serum was added to the culture medium. Surface chemistry variation here regulated the adsorption of serum that mediated cell adhesion on substrate. Therefore, surface protein adsorption (such as serum and fibronectin), that is beneficial for integrin-mediated intracellular signaling cascades[93,94] is likely to be responsible for the diverse cell behaviors on different surface chemistries. In view of differentiation, human adipose-derived stem cells showed increased osteogenic (Figure 1.4E lower panel) but decreased adipogenic differentiation with the increase of NH_2 density, indicating that the differentiation is also surface chemistry-dependent.[76]

Proteins related to cell adhesion[60,95] and growth factors[66] can improve cell behaviors on substrates. Arg-Gly-Asp (RGD) sequence existing within ECM proteins has been regarded as one essential mediator for cell membrane receptors and substrate.[59] Fusco et al.[60] applied a bifunctional photolinker (N-sulfosuccinimidyl-6-(40-azido-20-nitrophenylamino) hexanoate, sulfo-SANPAH) to mobilize RGD sequence on PDMS substrate. Sulfo-SANPAH was firstly coupled on PDMS surface under UV light and then reacted with RGD sequence in pH 8.5 bicarbonate buffer solution. After seeding mouse embryo fibroblasts NIH/3T3 cells, RGD-functionalized substrates showed more elongated cells compared to untreated material surfaces. In another example, recombinant transforming growth factor β (TGF-β) was introduced to culture medium, resulting in enhanced adhesion of hMSCs on silk fibroin hydrogels irrespective of their stiffness.[66]

Based on the discussion above, mechanical properties, topology and chemistry can regulate cell behaviors on substrates. In that case, synergistic effects among those parameters are worth being explored.[84,96–100] For instance, Liu et al.[84] integrated topology via immobilization of gold nanoparticles and chemistry via modification using allylamine or acrylic acid of substrate surface. They found that in spite of the dominant role of topology compared to chemistry on cell adhesion and spreading, those two factors synergistically influenced osteogenic differentiation of SaOS-2 cells. However, it is very challenging to tune those three parameters independently. Another noticeably issue in this field is that most published researches focus on 2D substrates that are dramatically different from most tissue environments. Therefore the transition from 2D to 3D environments for exploring effects of mechanical, topological and chemical properties on cell behaviors will be much more impactful for guiding practical cases.

1.2 Overview of porous scaffold fabrication techniques

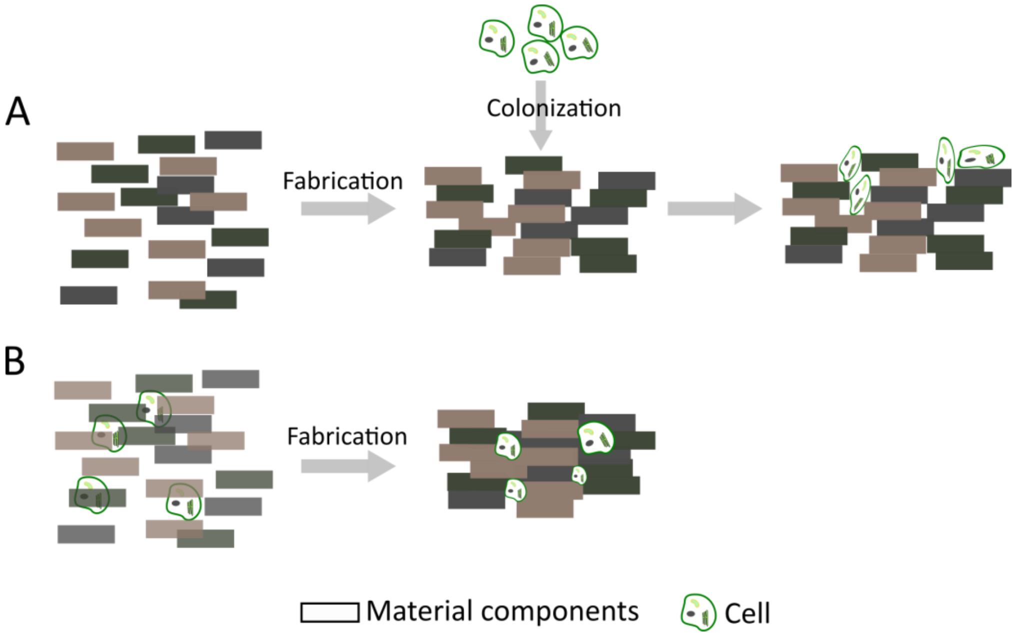

Figure 1.5 Cell colonization (A) vs cell encapsulation (B). In cell colonization, cells are seeded onto pre-fabricated materials. In cell encapsulation, cells and water-soluble materials are mixed and processed to obtain cell-laden composites. Adapted from Sarah Christoph's PhD thesis[101].

One key point for tissue engineering lies in the utilization of 3D scaffold to support and guide cell growth and tissue regeneration. In this regard, two main strategies are introduced: cell colonization and cell encapsulation. Cell colonization (Figure 1.5A) involves a porous matrix that can support growth, proliferation and even differentiation of seeded cells. It is the most common method for selecting ideal scaffolds for tissue engineering. As described above, the mechanical, topological and chemical properties of matrix play important roles in regulating cell behavior. That will give hints for practical cases. However, one aspect that needs to be kept in mind is that, during colonization, cells are still attached to a 2D surface instead of a 3D environment existing in ECM of normal tissues. Thus, in parallel to the development of scaffold fabrication methods, the search for 3D matrices allowing to encapsulate cells within the matrix during processing has emerged. Cell encapsulation (Figure 1.5B) processes mixtures of cells and polymers simultaneously into cell-laden matrix. In this case, nature-mimicking 3D cell culture environments could be obtained, providing more impactful insight for future tissue engineering. In this section, several techniques for material fabrication will be described and their suitability for cell colonization and cell encapsulation will be discussed.

1.2.1 3D printing

1.2.1.1 Selective Laser Sintering

Solid freeform fabrication (SFF) techniques have long been used for manufacturing porous materials for tissue engineering applications.[102] SFF is a method using computer-aided design (CAD) to fabricate well-controlled 3D scaffolds. Among SFF technologies, an important one is selective laser sintering (SLS) which was developed in the 1980s[103]. With the help of computer software, a 3D material can be split into data of two-dimensional layers. According to those data, a thin layer of powder particles is heated to a temperature above their melting point by a CO_2 laser beam in an exact trace of geometry. In that case, particles scanned by the laser melt and solidify with their "neighbors", which contribute to the first layer of the final material.[104,105] Powder platform is then lowered down with a thickness of one layer while a roller is used to spread a layer of new powder and smooth the surface. The process is repeated until the last layer and the final 3D construct can be obtained after brushing away excess powder.

Parameters of SLS such as laser pulse frequency, scan speed, scan space and layer thickness influence the properties of final materials[106,107,108]. Besides, characteristics of the powder material including flowability, laser absorption, thermal properties, sintering behavior, aging stability and recyclability are to be considered for the application of SLS, which significantly influence material properties such as internal stresses and distortion.[103] In the biomedical field, several biocompatible polymers like PCL[109–112], poly (L-lactide) (PLLA)[113], PEEK[114–116], PVDF[117–119] and poly (3-hydroxybutyrate-co-3-hydroxyvalerate) (PHBV)[120] are used either as single ingredients or as composites.

Bioceramics are often incorporated to improve bioactivity[86,91,117],[96] and/or mechanical properties[110,112,121]of composite materials. Bioactivity of composites also could be promoted by other ingredients such as collagen[111], MgO [118] and even MSCs[114], while the incorporation of molecules like graphene nanoplatelets[122] and nanodiamonds[119] significantly improved the mechanical properties. Another two significant aspects of final scaffolds (surface property[123] and degradation rate[124]) should also be considered in view of cell colonization. However, SLS also have some limitations such as the shrinkage of scaffolds[103] and the high melting temperatures[125] which hinders its application to cell encapsulation.

1.2.1.2 Fused Deposition Modeling

Fused deposition modeling (FDM) is another SFF technology, economical and simple, that was invented by Scott Crump in 1989 and has been widely used to fabricate 3D constructs.[103] In this technique, thermoplastic filaments are heated above their melting temperature to keep a semi-molten state and then pass through an extrusion nozzle to form one layer of materials on a support with the help of CAD. Then, platform below the support is moved down vertically and the printing process is repeated layer by layer until a 3D scaffold is obtained.[106,126] Similar with SLS, the heating process of FDM makes it a more suitable technique to fabricate scaffolds for cell colonization than cell encapsulation.

In view of biomedical applications, PCL[127–129], PLA[130–132] and poly(lactic-co-glycolic acid) (PLGA)[129,133,134] are commonly used materials. Barbara et al.[135] applied FDM to fabricate PCL scaffolds with different interconnected pores ranging from 380 to 400 μm by changing layer deposition angle. Increased deposition angle enhanced elastic modulus of the final products, which influenced the growth and proliferation of hMSCs. The incorporation of bioactive components such as Hap[136], TCP[137], and de-cellularized bone matrix (DCB)[138] has been explored to improve cell behaviors within the scaffolds. Ben et al.[138] incorporated DCB into PCL scaffold by FDM. The obtained hybrid materials showed an increased surface roughness compared to pure PCL ones. Human adipose-derived stem cells (hASCs) exhibited a better attachment and a promoted upregulation of expression of osteogenic genes in PCL/DCB scaffolds. Other research suggested that PCL/DCB and PCL/Bio-Oss scaffolds exhibited better osteo-induction properties than PCL/Hap and PCL/TCP composites.[128] Considering that surface properties also play an important role for cell behaviors on materials,[139] Wasana et al.[127] applied low pressure oxygen plasma (an effective surface modification technique) as a post-treatment process of PCL/PHBV scaffolds fabricated by FDM. Results showed that surface properties of final 3D structures such as roughness, wettability, and hydrophilicity were enhanced and a better proliferation and differentiation of porcine chondrocytes could be achieved. FDM also can be used to fabricate 3D printed biomimetic nanocomposite scaffolds for specific applications like bone tissue engineering. Margaret et al.[140] manufactured high impact polystyrene scaffolds with graded pore distributions over the thickness of scaffolds and infiltrated those constructs with UV-crosslinked PEG/PEG–diacrylate (40/60 wt%) hydrogel incorporating with nano-Hap particles. Enhanced cell attachment, proliferation and differentiation of hMSC in graded scaffolds compared to non-porous or homogeneous porous scaffolds indicated the importance of graded pore structures. This result is consistent with other researches on gradient materials.[141,142]

Although FDM could well control microstructures of fabricated 3D scaffolds, it still have some limitations such as preparation of composites in a filament state and removal of support parts for obtaining final materials.[143]

1.2.1.3 Stereolithography

Compared with other SFF technologies, stereolithography (SLA) technique commonly based on an ultraviolet laser, possesses the best resolution in fabricating 3D scaffolds.[106] This method requires a light source, a reservoir containing a photocurable polymer solution and a movable platform.[144] According to the direction of laser beam, bottom-up or top-down process can be employed in SLA.[106,145,146] For example, the top-down process involves the exposition of the polymer solution to the laser beam in an exact trace according to predesigned CAD model. Owing to the photopolymerization, the first layer is obtained by solidification of exposed sites. The platform is then lowered by one-layer thickness and the second layer is fabricated on the previous one following the same procedure. The process is repeated layer by layer until the last one and the fabricated construct is then taken out and drained off. Excess of resin is removed to get the final scaffold. As one of the main advantages of SLA, the high resolution could be improved down to the nanoscale with microstereolithography (MSTL)[147], digital mask projection device[148] or two-photon polymerization process[149]. This makes it one of the most popular technologies for fabricating highly controlled 3D porous materials. Another advantage is that, by using a visible-light source, SLA is able to incorporate living cells into fabrication process avoiding cell-seeding parts in cell colonization.[150,151]

For polymers to be used for SLA, there are some requirements such as low viscosity, fast cure times, photopolymerizability.[152] Several synthetic polymers including polypropylene fumarate/diethyl fumarate (PPF/DEF)[148], PCL[153], polyurethane (PU)[154] and poly (ethylene glycol) diacrylate (PEG-DA)[155] have been used to fabricate porous materials. Laura et al.[156] applied SLA to methacrylic anhydride functionalized PCL and obtained a highly interconnected scaffold displaying high Young's modulus (15.4 ± 0.7 MPa) allowing for good preservation of seeded fibroblasts. Although they are more difficult to process, natural polymers have been used for the design of SLA-based materials.[152] Shie et al.[154] revealed that the incorporation of hyaluronic acid (HA) to PU not only increased Young's modulus (up to 50 MPa) but also improved cell viability after 3 days' culture. High mechanical property and biocompatibility of scaffolds fabricated by SLA could also be achieved with bioceramics[147,157], graphene oxide[158] or growth factors[155,159]. An ink containing 60% wt/wt PEG-DA and 40% PEG was processed by table-top stereolithography printer with the incorporation of nano-hydroxyapatite (nHap) and chondrogenic transforming growth factor β1 (TGF-β1) (either bare TGF-β1 or TGF-β1 encapsulated into PLGA nanospheres) to fabricate biomimetic graded osteochondral scaffolds. Different concentrations of nHap (10 % and 20%) were employed to form middle and bottom layer respectively, which showed a 29% increase of compressive strength compared to un-mineralized control. A continuous release of TGF-β1could be observed over 14 days for graded materials integrating with TGF-β1-loaded PLGA nanosphere. A significant increase (> 100 %) of GAG production from week 1 to week 2 and a 22% increase of extracellular calcium deposition were achieved after seeding with hMSCs.[159] For SLA technique, selection of photoinitiators is of great importance because of their toxicity towards different cell types of cells.[160] One study explored the toxicity of three commonly used photoinitiator (2-hydroxy-1-[4-(hydro- xyethoxy) phenyl]-2-methyl-1-propanone (Irgacure 2959), 1-hydroxycyclohexyl phenyl ketone (Irgacure 184), and 2,2-dimethoxy-2-phenylacetophenone (Irgacure 651)) towards six kinds of cells. Irgacure 2959 displayed less toxicity than the others, especially on bovine chondrocytes (BC), hMSC, goat mesenchymal stem cells (gMSC) compared to human embryonic germ cells (LVEC), human fetal osteoblasts (hFOB), corneal epithelial cells (SIRC).[160] A photoinitiator-free curing process of SLA was also developed to improve the cytocompatibility of the materials.[161] Instead of traditional SLA, indirect-write SLA process could fabricate temporary mold or support with following infiltration of other biocompatible ingredients, which promote cell behaviors on scaffolds.[147,162] Overall, the main limitation of SLA is the scarcity of biocompatible materials that are compatible with this technique but it can be alleviated either by the incorporation of other bioactive molecules or by optimization of fabrication process such as selection of most suited photoinitiator and indirect-write SLA.

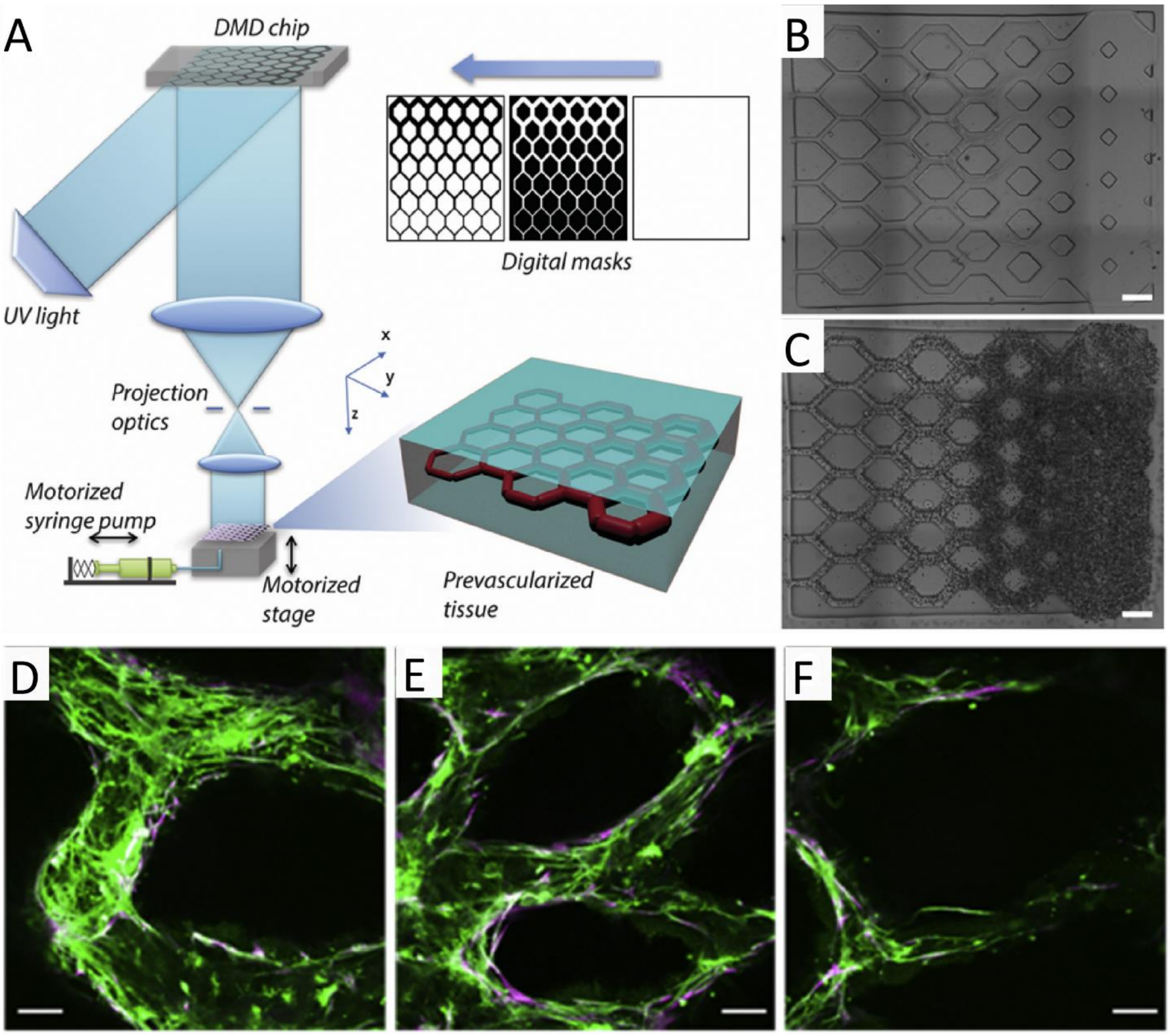

Figure 1.6 Stereolithography of pre-vascularized tissue constructs. (A) Schematic illustration of the printing setup. Printed constructs in absence (B) and presence (C) of cells. (D-F) *In vitro* endothelial network formation after culturing pre-vascularized tissue construct for 1 week. Green, CD31-stained HUVECs; Purple, alpha-smooth muscle actin-stained mesenchymal cells (C3H/10T1/2). Scale bars, 250 µm (B-C); 100 µm (D-F). Reproduced from ref[163].

Although SLA technique is mostly used with UV-light sources, some attempts have been made to encapsulate living cells inside of scaffolds during fabrication process.[163–165] Zhu et al.[163] utilized a mask-based SLA to encapsulate human umbilical vein endothelial cells (HUVECs) and C3H/10T1/2 cells into Gelatin methacrylate (GelMa)/ hyaluronic acid (HA)-based scaffold (Figure 1.6A-C). This scaffold was composed of three layers fabricated with different masks and the middle layer was fabricated in presence of HUVECs and 10T1/2s in a vascular-like geometry. *In vitro* experiments indicated that GelMa/HA scaffold allows good cell viabilities (>80%) and an induction of 10T1/2s into a pericyte phenotype essential for vessel formation after a one-week culture (Figure 1.6D-F). After two-week subcutaneous implantation *in vivo*, an endothelial network could be observed. In order to further improve the cell-material interactions, functional molecules such as RGD peptide, heparin and growth factors have been used during encapsulation process.[166,167] Laura et al.[167] synthesized a new water-soluble poly(ethylene glycol-co-depsipeptide) (PEG-co-PDP) macromere covalently cross-linked with RGD which was fabricated into cell-laden scaffolds with HUVECs by visible-light based SLA. PEG-co-PDP/RGD showed a good degradability with 13–21% mass loss after 7 days in PBS and a significantly enhanced cell viability compared to scaffolds without RGD peptide. For cell encapsulation by SLA, photoinitiators of lithium phenyl-2,4,6-trimethylbenzoylphosphinate (LAP)[150,163,167,168] and eosin Y disodium salt[151] are more widely used than others like Irgacure 2959, because of their lower cytotoxicity and applicability in visible light source. However, the very limited number of visible-light photopolymerizable polymers and photoinitiators with low cytotoxicity still restrain applications of SLA for the fabrication of cell-laden materials.

1.2.2 Porogen-based scaffold fabrication techniques

The most popular method used to create pores within polymer materials is based on phase separation.[169] However, there is a high risk of traces of toxic ingredients, and particularly organic solvents, remaining in the final materials. Thus alternative approaches using water[170], particles[171–173]or gas were developed to obtain biomedical scaffold. In the following paragraphs, thermally induced phase separation method (TIPS), solvent-casting/particle-leaching (SC/PL) and gas foaming technologies will be presented while the freeze-casting method, which is the core technology used during this PhD work, will be described in detail in the next sections (1.3 and 1.4).

1.2.3.1 Thermally-Induced Phase Separation (TIPS)

Thermally induced phase separation mostly use solvents as porogens. It is based on quenching the polymer solution below the solvent's freezing point.[174] A liquid-liquid or solid-liquid phase separation system can be induced because of the existence of a polymer-rich phase and a polymer-poor phase.[175176] After the extraction of porogens, a highly porous materials with well-interconnected structures can be obtained, which is very important for the cell colonization.

Parameters of TIPS (eg., type of polymers, polymer concentration, quenching rate and quenching temperature) have to be optimized to tune material structures.[177] Several synthetic (such as PLA, PLLA and PU) and natural (such as chitosan, collagen and gelatin) biocompatible polymers were recently processed by TIPS. Gioacchino et al.[170] used an homogeneous solution containing 4 wt% PLLA polymer solution and dioxane (as porogen) and varied quenching temperature and quenching time (25 °C for 45 min and 32°C for 75 min) which led to highly porous scaffold materials with different pore size (100 μm and 200 μm, respectively). After seeding human chondrocytes, PLLA scaffold with pore size of 100 μm shown a better cell viability and significant promotion of the expression of cartilaginous genes compared to the 200 μm scaffold.

To further tune cell-materials interactions[178], particles or biomolecules (such as growth factors[179]) can be added to the polymer solution. Maria et al.[180] fabricated mineral-doped PLA scaffolds with dicalcium phosphate dihydrate (DCPD) and/or hydraulic calcium silicate (CaSi) by TIPS and then dispersed DCPD and/or CaSi into interstitial spaces of the composite. The result indicated the range of the pore size increased from 10-20 μm (pure PLA) to 10-100 μm (PLA-10CaSi). Those composite scaffolds possessed a high surface area and internal open porosity. Moreover, they could release Ca^{2+} and OH^{-} ions, leading to the deposition of apatite. They were demonstrated to be suitable hosts for mouse embryo fibroblast cells.

Although TIPS is suitable for the fabrication of high porous materials, pore sizes above 200 μm are hard to achieve[181], which limits its use in biomedical fields. Therefore, advanced technologies combining TIPS with other methods, such as particle-leaching or supercritical CO_2 ($scCO_2$) drying have emerged[182–184], which open new possibilities for TIPS to fabricate scaffold materials for biomedical applications.

1.2.3.2 Solvent Casting/Particle Leaching (SC/PL)

The SC/PL technology is based on the incorporation of particles within the initial polymer solution, that can be leached out after material formation. This technology was firstly applied to scaffold fabrication in 1994 by Mikos et al.[185]. The authors firstly dissolved PLLA in chloroform and then added NaCl particles as porogens into the polymer solution. The evaporation of the solvent and the following leaching procedure in water led to porous materials, with pore size *ca*. 150 μm, with high interconnectivity. Besides inorganic salts, gelatin, sugar, sucrose and starch particles were also used as solid porogens.[186,187]

SC/PL method is a facile operation without need of a specific apparatus.[175] But several key parameters, such as particle features (size and initial density of particle) and polymer concentrations should be considered to control pore size, porous structure and even mechanical properties of final materials[188–190]. Elzbieta et al.[191] introduced sodium citrate particles of three different sizes (40, 200 and 600 μm) as porogens to fabricate PLG (a copolymer of L-lactide and glycolide) scaffolds. Scaffolds with pore size of 200 μm and 600 μm allowed human osteoblast-like MG cells to grow not only on the surface but also inside of the materials, whereas pore size of 40 μm just shown the cell growth on the surface. However, the largest pore size had the highest cell numbers and highest DNA synthesis among those three samples. Other kinds of cells also revealed to have their own optimal pore size, such as 325 μm for osteoblast cells[192] and 215 μm for mesenchymal stem cells (MSCs)[188].

SC/PL technique can be applied to many polymers, including synthetic ones (PCL[173], PLG[191], PU[193] and PLGA[171]) and natural ones (gelatin[179], fibroin[194], HA[172]). Besides, composite scaffolds containing multiple polymers or incorporating biomolecules can be fabricated in order to meet some special needs for the cell colonization. For successful tissue engineering, functional vascularization of scaffold materials after cell colonization is imperative.[195,196] Matteo et al.[194] integrated silk fibroin fibers into poly-(D, L-lactic acid) (PDLLA) scaffold materials by SC/PL with NaCl particles as porogens. The addition of silk fibroin fibers promoted the formation of anisotropic pores and improved the elastic modulus of the final composite materials. Besides, the proliferation of HUVECS was favored and cell numbers at 21 days were higher for the scaffold with silk fibroin fibers than without. Interestingly, *in vivo* experiment showed more blood vessels with preferred direction in coincidence with scaffold anisotropy.

However, SC/PL technique also have some disadvantages. The first one is that the thickness of most scaffold materials made by SC/PL is less than 4 mm because of the difficulty of complete salt-leaching.[197] In addition, due to the difference of the density between polymer solutions and salt particles, the pore interconnectivity of the final materials is not well-controlled.[198] In that case, some other techniques, such as centrifugation[193] or solvent self-proliferating process[199] are used to improve the SC/PL method, allowing to significantly promote cell colonization inside the scaffold materials.

1.2.3.3 Gas foaming

Gas foaming is a method using gases as porogens to generate porous scaffold materials.[200] The principle of this technology is to use gas bubbles generated by internal reactions or by external introduction, to induce the formation of gas bubbles within polymer solutions. Scaffolds fabricated by the gas foaming technique are preferably used for cell colonization rather than cell encapsulation due to the potential deleterious effect of pressure variation on cells.

For internal reactions, gas-forming agents, like sodium bicarbonate, are used to react with one of the component inside the polymer solution system and then release gases such as N_2[201,202] or CO_2[203] which are then removed in order to obtain porous materials.[204] Andrea et al.[202] applied the *in situ* N_2 release, gelation upon cooling and crosslinking with EDC to fabricate gelatin scaffolds. Voids and interconnections with average diameters of 230 and 90 μm led to a steady increase of hepatocytes population in culture conditions. However, the kinetics of the internal reactions are difficult to control, which restricts their application in scaffold fabrication.[35]

External introduction is performed by applying gases at high pressure from outside to polymer solutions. [206–209] One of the most common gases is CO_2 which benefits from the supercritical CO_2 ($scCO_2$) technology.[208,210] Compared with other conventional techniques (like SC/PL), $scCO_2$ technology does not involve organic solvents, making it a good method to generate porous materials for tissue engineering. Xin et al.[211] evaluated the possibility to guide the growth of liver cells (human hepatoma cell line Hep3B) within PLGA scaffolds generated by $scCO_2$ technology. The fabricated porous materials possess uniform pore size (30-60 μm) and relatively high porosity (76–84%). *In vitro* cell experiments showed improved cell growth and infiltration but limited proliferation activity of cells inside of the materials, calling for further optimization.

During the $scCO_2$ foaming process, the formation of a “skin” layer and the poor interconnectivity between pores are of particular concern.[210,212] Generally, $scCO_2$ technique involves three main steps: plasticization of polymers, nucleation and growth of gas bubbles.[213] Parameters driving these three steps, (such as saturation pressure[214] or depressurizing rate[215]) can be used to control morphologies and properties of the final materials. White et al.[215] studied the effect of PLA polymers molecular weight (57, 25 and 15 kDa) and depressurizing rate on the properties of scCO2-generated porous materials. A typical stress-strain curve for soft elastic materials was obtained for scaffolds generated from 57 kDa sample while those obtained from the other two led to brittle systems. Wider range of pore size and highly interconnected structures could be obtained with decreased depressurization rate. The integration of other methods to $scCO_2$ technology could also be implemented to manipulate material properties. Tairong et al.[214] integrated a pressure-induced flow (PIF) method with solid-state $scCO_2$ technology to fabricate PLLA scaffold materials. They found that the PIF method increased the extent of PLLA crystallinity from 15.3% to 42.1% and conferred some orientation to the structure along the pressure direction. Besides, open-cellular structures and high strength of the PLLA scaffold supported cell growth (cell viability above 90% after culturing 10 days) and proliferation.

Thus the gas foaming technology appears well-adapted to prepare scaffolds for cell colonization. In contrast, due to the chemical reaction (internal) or the high pressure of gases (external), [216,217] it is poorly adapted to cell encapsulation.

1.2.3 Electrospinning

Electrospinning is an electrohydrodynamic atomization technique which was initially used around eighty years ago for producing nanofibers from polymer solutions,[218] and has been widely applied to imitate natural ECMs for tissue engineering.[219] This technology requires an injection system (including a syringe and a needle), a metal collector and a generator allowing to apply an electric field between the needle and the collector. During the fabrication process, a drop of liquid polymer solution experiences a morphology change from hemisphere to “Taylor cone” because of surface tension and exerted electric field.[220] The continuing increase of electric field and the following evaporation of solvent leads to a solid fiber.[218,221] Due to the relative simplicity and possibility of scalable fabrication process[218], electrospinning is widely applied to produce porous materials and many parameters can be tuned to adapt these to fit needs of cell colonization.

Regarding to the experimental conditions, parameters such as the extrusion speed of polymer solution, the exerted voltage or the distance between needle and collector impact the properties of final materials.[222,223] Besides, improvements of the electrospinning apparatus related to the needles[224,225], collectors[226,227] and electric fields[228] can also be used to regulate material properties.[223] Recently, Song et al.[229] mounted multiple movable needles on the collector to electrospun PCL fibrous materials (Figure 1.7A-C). Eleven rounds of electrospinning produced highly porous and interconnected 3D scaffolds which were seeded with murine pre-osteoblastic MC3T3 cells afterwards. Enhanced cell growth and proliferation was achieved. In addition, a deeper cell infiltration (~ 450 μm) in the Z-direction was observed (Figure 1.7D) compared to a 2D nanofiber surface (~100 μm). Such an improvement of the electrospinning setup overcomes the previous limits (small pore size and poor interconnectivity)[230,231] of the electrospun materials in cell colonization.

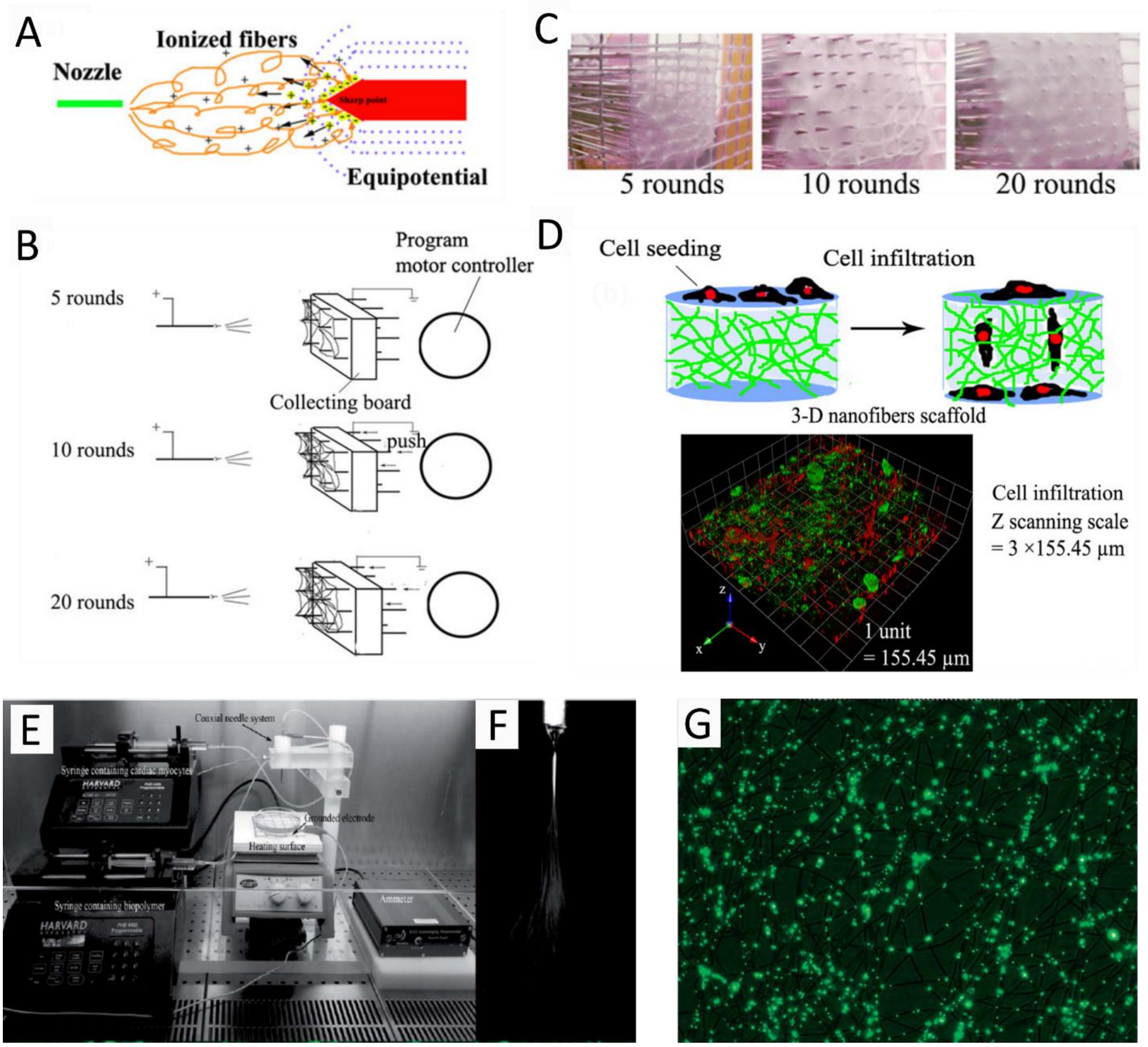

Figure 1.7 Electrospinning for cell colonization (A-D) and encapsulation (E-G). (A) Scheme of electrospinning setup with needle-pierced collector. (B) Illustration of a cross-section view of fiber formation between the spinneret and needle-collector. (C) Image of collected fibrous PCL scaffolds based on multiple rounds (5, 10 and 20). (D) Illustration and confocal image of adhesion and infiltration of MC3T3 fibroblasts into fibrous PCL scaffolds. (E) Micrograph of electrospinning set up. (F) Ongoing cell electrospinning in the stable spinning mode. (F) Merge of bright field and fluorescent image of electrospun collagen fibers with encapsulated

cardiac cells. Cells are labelled with GFP adenovirus. (A-D) reproduced from ref[229]; (E-F) reproduced from ref[232].

Until now, around 200 biodegradable polymers including synthetic and natural polymers have been successfully processed by electrospinning.[233] Mixtures of polymers, such as synthetic ones to reach suitable mechanical properties and natural ones to confer biological properties, have been well-described. For example, Ren et al.[234] blended 10% (w/v) PCL and 10% (w/v) gelatin solution in different ratios to produce composite materials that were then cross-linked by genipin. The PCL/gelatin composite were smoother and more hydrophilic that PCL scaffold. The incorporation of gelatin improved MC3T3-e1 cell viability (> 80%) and their osteogenesis capabilities. As for other techniques, successful incorporation of growth factors[235,236,237] and bioactive ceramics[238,235,239,240] was also reported.

Because of the existence of several electroactive cell types (e.g. neurons, cardiomyocytes and skeletal muscle cells)[241–243], it is of great importance to design electroconductive materials. To date, electroconductive materials could be obtained by incorporating conducting polymers[244–246], conductive particles[247,248] or electrically active bioceramics[249] into synthetic or natural polymers. As a promising technique, electrospinning could blend those ingredients together to obtain homogeneous fibrous materials.[241] For example, PLA solution containing polyaniline (PANI, a biodegradable and conductive polymer) was electrospun into nanofibrous materials. Those PLA/PANI conductive composite showed an enhanced differentiation of H9c2 cardiomyoblasts in terms of maturation (> 70%) and fusion (> 70%). Besides, the cell-seeded materials could form 3D bioactuators which exhibited more frequent spontaneous beats and displacements compared to non-conductive materials.[245]

Cell encapsulation could also be achieved via the so-called cell electrospinning process which was firstly reported in 2006.[250] Cell electrospinning overcomes the issues of small pore size and the poor cell infiltrations[251] after seeding cells inside of scaffold materials fabricated by traditional electrospinning technique. Jayasinghe group[232,250] showed that cardiac myocytes can be successfully co-electrospun with cell viability above 80% (Figure 1.7E-G). Surprisingly those cells were not influenced by the voltage and could keep their integrity.

Electrospinning also enabled bacteria encapsulation for applications such as water depollution[252] and biotherapeutics delivery[253]. However, owing to difficulties of selecting cell-friendly polymers and solidifying polymers[254], the development of encapsulating mammalian cells by electrospinning remains challenging.

1.2.4 3D bioprinting

Bioprinting is a 3D printing technology specifically implemented for cell-based biomedical applications, allowing to control the spatial positions of bioactive molecules and cells in a predefined pattern.[255,256] Here, two main types of bioprinting technologies, inkjet-based and microextrusion-based, will be more particularly discussed.

1.2.4.1 Inkjet-based bioprinting

As a non-contact technology, inkjet-based bioprinting deposits small droplets (1–100 picolitres) on the surface of a platform in a predefined pattern by using thermal or piezoelectric stimulation.[257,258] Thermal inkjet is based on a sudden increase of temperature in the print head which exerts a pressure to eject bioink droplets while piezoelectric inkjet causes mechanical stress by applying voltage to promote the generation and ejection of bioink droplets. As a main advantage, the speed of inkjet-based bioprinting could be achieved from 1 to 10,000 droplets per second.[258]

Inkjet-based bioprinting can utilize natural polymers (like alginate[259–261], collagen[262,263], gelatin[264] and silk fibroin[265]) and/or synthetic polymers (like poly(ethylene glycol) dimethacrylate (PEGDMA)[266–270]) that can be mixed with different types of cells to form bioinks. Christensen et al.[259] fabricated alginate-based cell-laden vascular-like scaffolds by applying calcium chloride as a cross-linking agent. The final constructs displayed both horizontal and vertical bifurcations. Besides, the viability of encapsulated fibroblasts cells was above 90% even after 24-h incubation. Cui's group widely explored the fabrication of cell-laden scaffolds with PEGDMA by thermal inkjet bioprinting.[266–270] They co-printed human mesenchymal stem cells with PEGDMA and gelatin methacrylate to get PEG-GelMA scaffolds that supported more than 80% cell viability. The significant role of GelMA on hMSCs differentiation and ECM production was confirmed since the modulus of cell-laden

PEG-GelMA scaffolds were higher than PEG scaffolds under osteogenic and chondrogenic differentiation after 21 days.[270] This group also employed peptide-modified PEGDMA[268] or incorporated Hap nanoparticles with PEGDMA[267] to improve mechanical properties and bioactivities of final scaffolds, which enhanced cell viabilities and differentiations.

Inkjet-based bioprinting have several drawbacks such as sudden exposure to high temperature or applied voltage which may result in cell death.[271] However, several researches showed that thermal or piezoelectric inkjet only induce minimal deleterious effects on cell viability.[272,273] Another potential drawback of this technique lies in the nozzle clogging that restricts the maximum viscosity of the solution, and therefore both the polymer concentration and cell density.[274,275] One option is to use inks composed of a crosslinker and cells that can react with the biomaterial substrate in order to obtain final 3D scaffolds.[276,277]

1.2.4.2 Microextrusion-based bioprinting

Microextrusion-based bioprinting have been used in many kinds of tissue engineering applications such as skin[278], nerve[279], muscle[280], heart[281,282], cartilage[283] engineering. This technology is based on extruding bioinks incorporating biomaterials and/or cells together onto a movable substrate by pressure caused by air or mechanical force.[284] During this process, several parameters such as bioink viscosity, processing temperature, needle shape, needle diameter and extrusion speed should be taken into account since they impact the final cell viability inside of 3D constructs.[251, 285,286] Thomas et al.[285] revealed that higher cell viability could be obtained at lower pressure for conically shaped needles while a significantly drop of viability was shown at higher pressure compared to cylindrical needles. Further optimization of processing parameters enabled higher cell viability (approximately 98%).

Noticeably, this technology has been more evaluated to prepare biomaterials composed of natural polymers (like chitosan[287], cellulose[256,288], alginate[282,283] and gelatin[281,289]) than with synthetic polymers (like PCL[280,290]). Alginate is one of the most commonly used polymers because of its gentler crosslinking strategy with calcium chloride compared to other crosslinking approaches (like UV light[291,292]). You et al.[283] successfully co-printed alginate (2 % wt) and primary chondrocytes into a 3D hydrogel construct with a submerged crosslinking method (calcium chloride solution). The cell-laden construct showed an increased cell viability from 76% (day 1) to 84% (day 14). The newly-formed ECM gradually secreted by cells from 7 days to 28 days of culture indicated a good chondrogenic differentiation.

Microextrusion-based bioprinting constructs are relatively soft, limiting this technology to soft tissue engineering.[275] Some researches tried to incorporate other technologies such as melting spinning into bioprinting process in order to improve mechanical properties of the final constructs.[280,290,293] Schuurman et al.[290] obtained 3D constructs by alternately depositing PCL fibers and cell-laden alginate hydrogels. This fiber-reinforced construct showed a significantly increased Young's modulus while preserving a comparable cell viability.

Microextrusion-based bioprinting have also been used to fabricate 3D constructs with vascular networks necessary for delivering nutrients such as oxygen to encapsulated cells.[294] Cell-laden microchannels can be introduced using coaxial nozzles,[295,296] or by incorporating sacrificial materials such as alginate[291,297], gelatin[289] and pluronic-F127[292,293] into bioprinting processes. Kang et al.[293] applied multi-nozzle system to fabricate a cell-laden 3D constructs incorporating synthetic polymer (PCL), sacrificial material (pluronic-F127) and cell-dispensing hydrogels (Figure 1.8A-C). In that case, microchannels could be obtained by washing out pluronic-F127 with cold PBS solution. Around 91%, 91% and 97% of cell viability could be obtained for 3D tissue constructs of bone, cartilage and skeleton muscle respectively after 1 day's culture. Thus, the microchannels have partly overcome the cell diffusion limit (100 to 200 µm) into tissue constructs.

Altogether, microextrusion-based bioprinting has many advantages as it can use concentrated polymer solutions with high cell density, resulting in robust highy-cellularized 3D constructs. However a compromise has to be found between cell viability and printing resolution.[271,298]

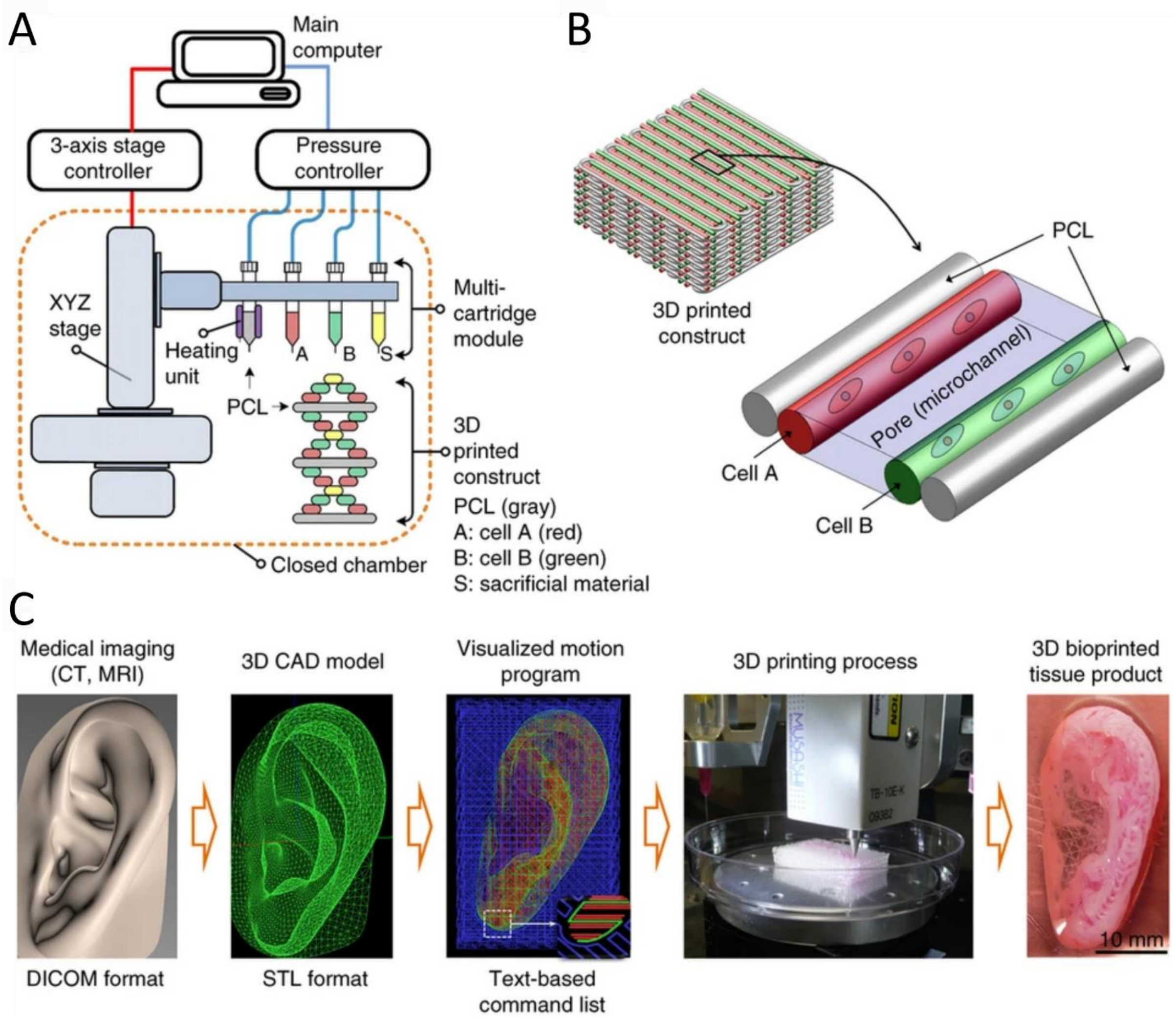

Figure 1.8 Microextrusion based on an integrated tissue-organ printer (ITOP). (A) Scheme of the ITOP system composed of three main units: 3-axis stage controller, pressure controller and multi-cartridge module. (B) Illustration of 3D printed constructs composed of cell-laden hydrogels and supporting PCL polymer. (C) CAD/CAM process for automated printing of 3D shape imitating target tissue or organ. Reproduced from ref[293].

1.3 Scaffold fabrication by freeze casting

1.3.1 From porous ceramics to biomaterials fabrication

Freeze casting, also called ice templating or ice segregation induced self-assembly, is a straightforward processing technique for the elaboration of macroporous materials.[299,300] Beyond porosity, materials elaborated via freeze casting display a diversity of other properties such as high specific elastic modulus[301], increased toughness[302,303] or efficient insulating properties[304] that can be easily tailored by adjusting the process parameters. Freeze casted materials have thus attracted significant attention in the last decades as they are expected to find application in a wide variety of domains such as structural ceramics[305], energy storage devices[10–12], sensors[306,307] and, more recently, 3D cell culture[13], tissue engineering[14–16] or cell-encapsulation systems[17,308]. The technique's underlying principle is remarkably simple (Figure 1.9). Starting with a suspension or a solution, and upon application of a temperature gradient that reaches values below the solvent freezing temperature, the sample freezes progressively and suspended particles and/or solutes are segregated into the interstitial zones defined by the solidified solvent. Removing the solvent without disturbing the interstitial zones reveals the materials' macroporosity, one of the central attributes of the materials obtained by freeze casting. If the thermal gradient applied during freezing is well defined, then the solvent solidification will – under most circumstances – generate a freezing front that follows locally the thermal field. While many solvents such as camphene[309], *tert*-butyl alcohol[310] or liquid CO_2[311] may be used to produce materials by freeze casting, water is by far the most commonly used, and the most relevant in the context of biomaterials fabrication.[312] Here we will limit the discussion to the latter and we will refer, from this point onwards, to the technique as freeze casting.

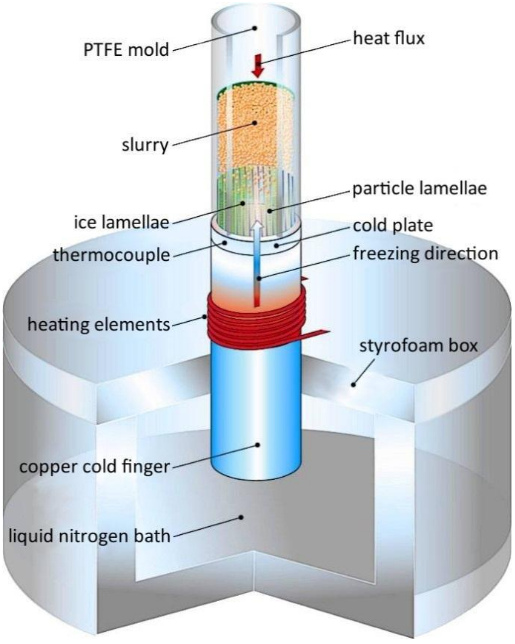

Figure 1.9 Simplified scheme of a freeze casting setup. Adapted from Wegst et al.[313]

As mentioned above, freeze casting can shape materials for a vast array of applications, which translates to a wide variety of compounds that can be shaped into macroporous foams. We will here retrace the evolution of freeze casting, from an industry-oriented materials processing technique – devoted mostly to the fabrication of macroporous ceramic green bodies[299,305,314] – to the fabrication of materials of increasing relevance in biological context such as macroporous gels for cell culture[13,315] or cryoprotection matrices for cellular cryopreservation[17,316–318]. Figure 1.10 retraces how the composition of suspensions and/or solutions treated by freeze casting has evolved from ceramics to living cells. More than a simple chronologic recital of the application or the chemical nature of the processed materials, we focus on how the control over the processing technique has led to the fabrication of materials whose composition is increasingly labile.

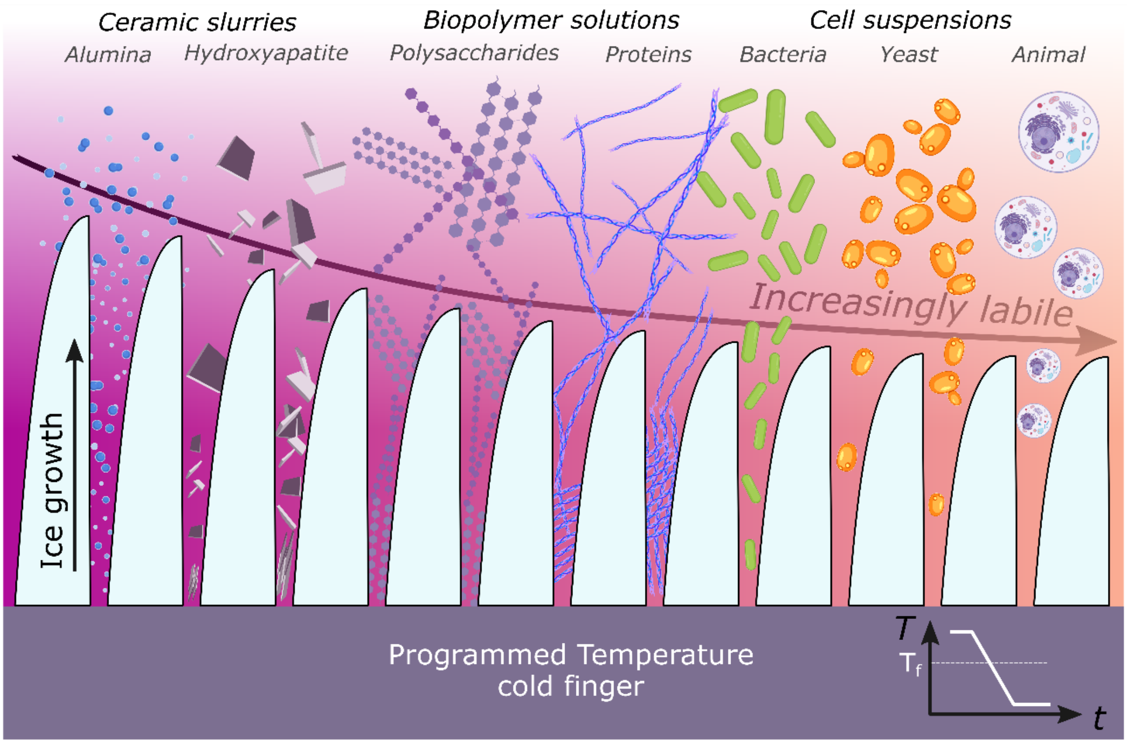

Figure 1.10 Freeze casting has evolved from a materials processing strategy designed to shape ceramic green bodies to a technique that enables the encapsulation of increasingly labile matter. From the left to the right: ceramic slurries such as alumina or hydroxyapatite, biopolymer solutions such as polysaccharides and proteins, and cell suspensions such as bacteria, yeast cells, and animal cells are trapped in the interstitial space defined by ice crystals. The height of the ice crystals is an approximation to the time line: bigger crystals correspond to initial ceramics-centered research and smaller crystals to more recent materials where freeze casting is used to shape materials containing biological entities.

Processing biomolecules using techniques that were not initially designed to do so requires a detailed analysis of the potential risks associated with denaturation and subsequent loss of functionality. In many processing strategies – such as those developed for the shaping of polymers in molten state – temperature poses the highest concern since most biomolecules degrade below the typical temperature range for thermoplastics extrusion. Such risks can, in many cases, be minimized by adjusting the processing window to meet the conditions tolerated by biomolecules, as reported for the extrusion of plant biopolymers.[319] An especially difficult scenario emerges when transposing techniques that rely on the evaporation of a solvent such as spray drying. Recent results have shown that even in case where the solvent is water (T_{vap} = 100 °C) and the biopolymer being processed into microparticles is type I acid soluble collagen ($T_{denat} \backcong$ 37 °C) the processing window can be adjusted to hinder collagen denaturation.[320] Similarly, techniques that rely on high pressure, high shear or the use of some organic solvents during the processing risk to denature the biological moieties and require thus an important work to shift their operational window as to preserve the identity – an thus the functionality – of biomolecules.

Shaping materials in presence of living cells is far more delicate and, as a consequence, less common. Here the notion of processing window narrows down to a large set of narrow conditions that are considered vital to maintain the integrity and activity of living cells. Controlling parameters such as the pH of the suspension medium, electrical field, O_2 partial pressure, presence of cytotoxic compounds, osmotic pressure, temperature, mechanical stress or the ability to create a sterile environment impose heavy constraints to most materials processing techniques. In this context, the number of successful examples drops dramatically, as seen in the previous sections.

1.3.2 Bioinspired composite materials obtained by freeze casting

The morphological resemblance between materials obtained by freeze casting and some of the most elusive structures in biological materials has triggered a major turn in the history of freezing as a path to fabricate materials. From the distance now, and apart from the inherent thrill in reproducing the morphologies of natural materials, two main aspects seem central in captivating materials scientists into designing bioinspired materials. *i*) As a ceramic processing technique, freeze casting enabled the effective assembly of organic binders and inorganic particles locally into highly concentrated composite systems, reminiscent of natural materials such as nacre and bone. *ii*) The mechanical attributes of those natural materials, in particular the combination of high toughness, high strength and controlled crack propagation, corresponded to desirable properties in ceramic materials.

Bone and nacre are the paradigmatic examples of natural materials in which the precise hierarchical architecture and composition result in structures that are particularly efficient in terms of their mechanical behavior. In some cases these materials are more efficient that the sum of their parts, challenging the upper bound set by the rule of mixtures.[321]

1.3.2.1 Nacre-inspired materials

Nacre is composed of an ordered assembly of *circa* 95% (v/v) aragonite platelets separated by an organic phase composed of chitin and proteins such as fibroin and lustrin. Despite its brick and mortar architectural simplicity, nacre's superior fracture toughness and flexural strength has been essential to unravel highly efficient mechanical reinforcement principles.[322–324] A variety of materials processing techniques aimed at reproducing nacre's native structures has been proposed, ranging from layer-by-layer techniques[325,326] to electrophoretic deposition of clay tactoids intercalated with polymers[327]. Opposite from the previous techniques, which are more appropriate for the fabrication of 2D materials, freeze casting allows to fabricate materials in 3D. Upon the formation of ice crystals, particles are segregated from the ice front, resulting in a local increase in concentration of particles and solutes initially in suspension or solution. In the case of highly anisotropic lamellar particles suspended in the initial slurry, the concentration increase due to exclusion from the ice fraction may lead to an effective alignment between particles. Many of the examples of nacre-mimicking materials produced by freeze casting – such as Al_2O_3[302,328–332] or graphene oxide[333–335] – take advantage of such phenomenon to define a structured lamellar morphology. Subsequent infiltration with another phase contributes to the final nacre-like brick-and-mortar architecture. Another advantage inherent to the technique lies in the ability to obtain extremely high particle volume fractions even from relatively diluted initial slurries. Deville et al.[2] have reported nacre-like morphologies produced both from alumina or hydroxyapatite (Hap) that reached mineral volume fractions comparable to some hard biological tissues: up to 45% (v/v) Al_2O_3 or 60% (v/v) Hap. The obtained alumina scaffolds were reminiscent of nacre, in particular due to their high inorganic volume fraction and periodical layered structures obtained. Adjusting the ice front velocity resulted in controlled change in wall thickness between $\sim$1 and $\sim$100 μm, evidencing the role of this simple parameter in tailoring the final architecture of the obtained materials. Upon infiltration with an epoxy resin to reproduce the binding role of the organic phase, both alumina and Hap composites revealed interesting crack deflection properties.[2]

One of the lessons that have emerged from the mechanics of nacre is that the interfacial properties play a major role for improved toughness. Features such as roughness, bridges and nano-asperities are critical in improving the mechanical response of final freeze casted nacre-like materials. Ice dendrites formed during freeze casting were found to promote surface roughening similar to the bridges found in nacre.[2] Favoring the formation of surface roughness would dramatically increase the strength and fracture toughness of final composites from 400 to 600 MPa and 5.5 to 10 MPa.m^{½} respectively. In other examples the bridges between alumina and PMMA [poly (methyl methacrylate)] phase were, along with the interfacial roughness considered helpful for efficient energy dissipation and high friction sliding between ceramic and polymer phase, contributing to the final toughening mechanism of nacre like composites.[302] Garnier et al.[329] fabricated alumina-based brick-and-mortar composites by freeze casting Ni-coated alumina platelets and NiO nano-particles (Figure 1.11A). Sintering process under reductive atmosphere transformed NiO to metallic Ni particles that served as bridges and asperities (Figure 1.11B), which were thought to be responsible for the lower crack driving force and high crack face friction. This approach was furthered by Bouville et al.[331] who, using only brittle components, achieved nacre-like materials from alumina platelets (500 nm thickness, 7 µm diameter, equivalent to aragonite platelets in nacre) associated with alumina nanoparticles (100 nm) and silica–calcia colloidal suspension (20 nm) between platelets. After pressing and sintering, the resultant nacre-like alumina materials exhibited high flexural strength (470 MPa) and fracture toughness (21 MPa.m$^{1/2}$), corresponding to a 600% increase compared to the reference alumina. The co-alignment of alumina platelets obtained during freeze casting, together with the bridges, nano-asperities and pores located in the interfaces between platelets, resulted in crack deflection behavior characteristic of nacreous materials.

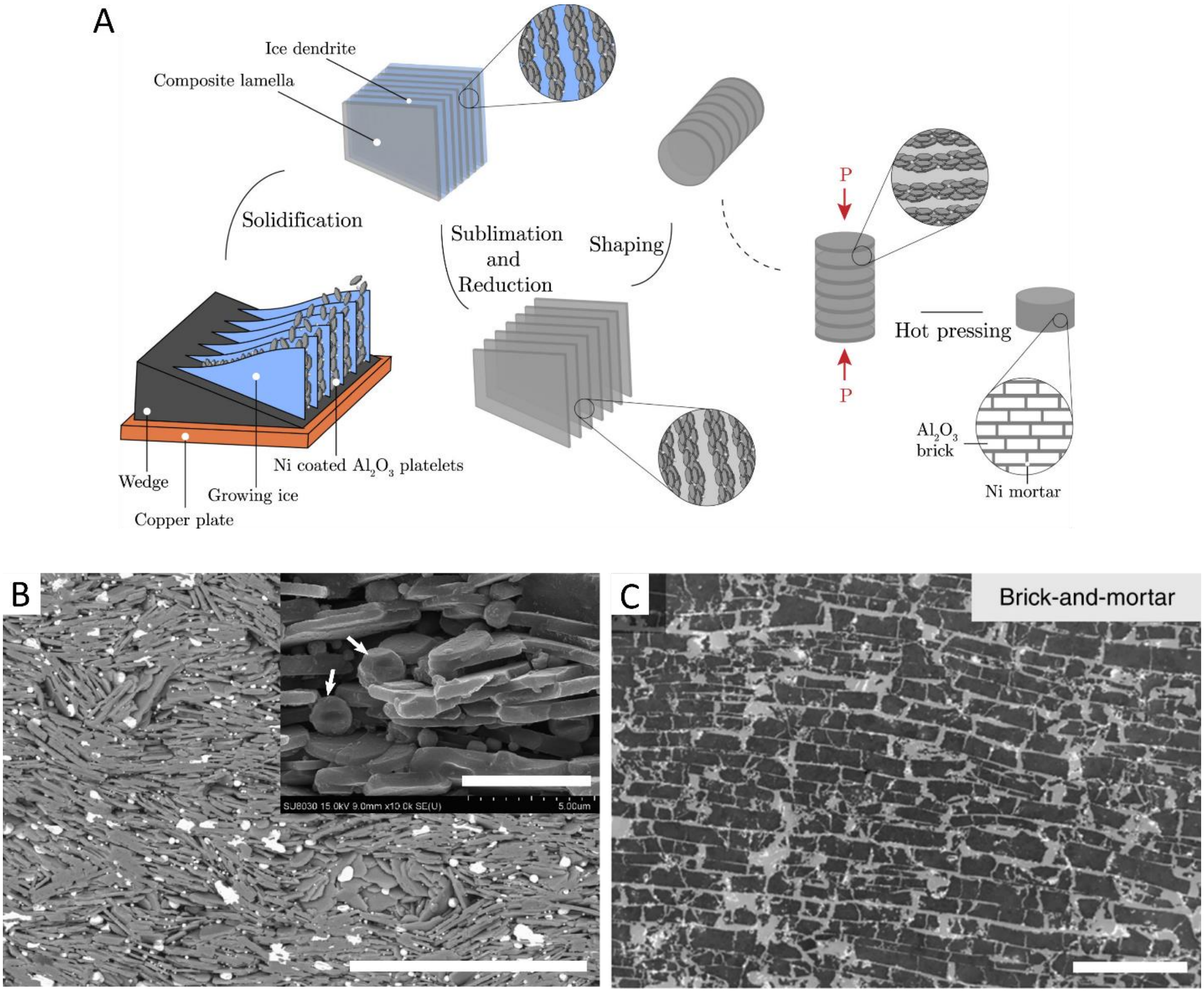

Figure 1.11 Structure and properties of nacre-inspired scaffolds via freeze casting. (A) Processing scheme for brick-and-mortar alumina composites. (B) SEM images of alumina composites (grey) with 10 vol.% Ni particles (white) located between platelets. White arrows in inset, indicating Ni particles in high magnification. Scale bar is 50 μm for main image and 5 μm for inset. (C) SEM picture of brick-and-mortar-like alumina/BMG (bulk metallic glass) alloy fabricated by four main steps: 1) freeze casting of alumina particles; 2) sintering and infiltration with paraffin wax; 3) high-pressure pressing and sintering; 4) infiltration of BMG phase into alumina scaffold. Scale bar is 100 μm. Images A and B were reprinted from ref[329], Copyright (2018), with permission from Elsevier. Image C was adapted from ref[328].

Beyond the morphological features of platelets and their interfaces also the chemical composition at those interfaces plays an important role in the toughness of nacre-like composites. Grafting of methacrylate group on the alumina surface before infiltration of PMMA was suggested as a strategy to maximize the interaction between the inorganic and the organic phases.[302] This approach resulted in covalent bonding between ceramic and polymer phases and, as a consequence, in a more cohesive brick-and-mortar system. Non-grafted composites showed delamination, while flatter and denser surfaces were observed for grafted composites. The interfacial covalent bonding increased strength and crack initiation toughness, especially for brick-and-mortar composites due to toughening mechanisms of the "pull-out" between bricks and friction sliding. Wat et al.[328] applied a pressureless, fast melt-infiltration with Zr-based bulk metallic glass (BMG) to alumina matrix fabricated by bidirectional freezing with a 20° wedge. The resultant alumina/BMG composites exhibited nacre-like brick-and-mortar structures with high alumina fraction of ∼80 vol.% (Figure 1.11C). In their report infiltration temperature was explored as a strategy to modulate the interfacial reaction between alumina and BMG phases, which could further tune its mechanical properties. Mao et al.[336] applied a consecutive assembly-and-mineralization process to fabricate nacre-inspired aragonite/chitin/silk fibroin (SF) composites, drawing the final materials one step closer to nacre's native composition. Laminated chitosan scaffold was transformed into β-chitin via unidirectional freezing followed by acetylation. The mineralization process was subsequently achieved by continuous flow of aqueous $Ca(HCO_3)_2$ solution in the presence of polyacrylic acid and Mg^{2+} using a circulating system. The following infiltration of SF and hot pressing yielded a final composite containing approximately 91 % (v/v) aragonite, comparable to mineral volume fraction found in natural nacre. The synthetic composite also shared other morphological features with the natural counterpart such as laminated structure and surface roughness. Nacre-like tile aragonite platelet layers with 2 to 4 μm thickness was alternated by 100 to 150 nm thick organic layers, leading to similar crack extension resistance curves compared to natural nacre.

Nacre-inspired materials have been prepared via freeze casting using different types of molecular, macromolecular and particle building blocks, resulting in materials with mechanical properties comparable to those of the biological tissues. Beyond the composition of the different composite materials – that ranges from metal matrices to highly sensitive biopolymers – the remarkable mechanics, in particular fracture toughness, rely on reproducing the architectural principles found in nacre. Freeze casting alone or coupled to other processing routes has enabled to produce materials where an effective 2D arrangement of particles was compatible with the fabrication of bulk, 3D objects. In this sense, freeze casting represents a quite unique combination of the *top-down* and *bottom-up* fabrication strategies. It allows to precisely control the macroscopic dimensions of the produced materials by a top-down approach while promoting a bottom-up assembly of the particles in suspension. The resulting materials show thus order at multiple scales, ranging from the co-alignment of anisotropic nanoparticles to the controlled macroporosity determined by ice growth.

1.3.2.2 Bone-inspired materials

Similarly to nacre, the unique mechanical properties of bone have long puzzled materials scientists. Both natural materials share a common aspect. They are hybrid materials composed of high volume fraction of high aspect ratio inorganic particles assembled together by a biopolymer-rich phase. In bone, these components, non-stoichiometric apatite and collagen, make up *circa* 95% (w/w) of its dry weight.[337] As with materials mimicking nacre, the pursuit to reproduce bone's mechanical performance has been mostly focused in reproducing the materials' architecture rather than its composition. There are some general similarities between both natural materials but the hierarchical complexity of bone remains unique. Recent reports define nine hierarchical levels between whole bone as an organ and its individual components.[338] If in nacre-inspired materials the "brick and mortar" structure seemed accessible by freeze casting followed by compression, the same cannot be said for bone. However, materials prepared by freeze casting do present a macroporous morphology that seems to recapitulate the architecture of cancellous – or trabecular – bone. Figure 1.12A depicts the cross-section of a human proximal femur obtained by Computed Tomography (CT) scanning and Figure 1.12B shows the macroporous structure of a pectin foam obtained by freeze casting. Beyond the pores' characteristic dimensions which are notably different, a first comparison between these 2D representations seems to indicate some degree of similarity in the architecture of both materials. However, a deeper look into the macroscopic morphology of cancellous bone reveals that the roughly analogous structures are, indeed, less similar than expected. Trabecular bone morphology has been shown to evolve with age, gender and site in the body[339], indicating a degree of specificity of the tissue that is not intuitive for the non-specialist. As an indication to its complexity we can take the diversity of histomorphometric indicators for trabecular bone. Indeed, a standard description of this tissue takes into account, among others, parameters such as the trabecular bone volume fraction, trabecular number, trabecular separation and trabecular thickness.[340] These descriptors are often accompanied by empirical observation parameters that describe the prevalence of plate-like or rod-like structures.[339] While some degree of control over the pores' architecture is possible in freeze casting – by using different additives during freezing, different ice front velocities, different suspended solid fraction or by the available knowledge in ice physics[341] – the differences in pore morphology that can be obtained in freeze casting are still dramatically far from reproducing bone's sophisticated trabecular structure.

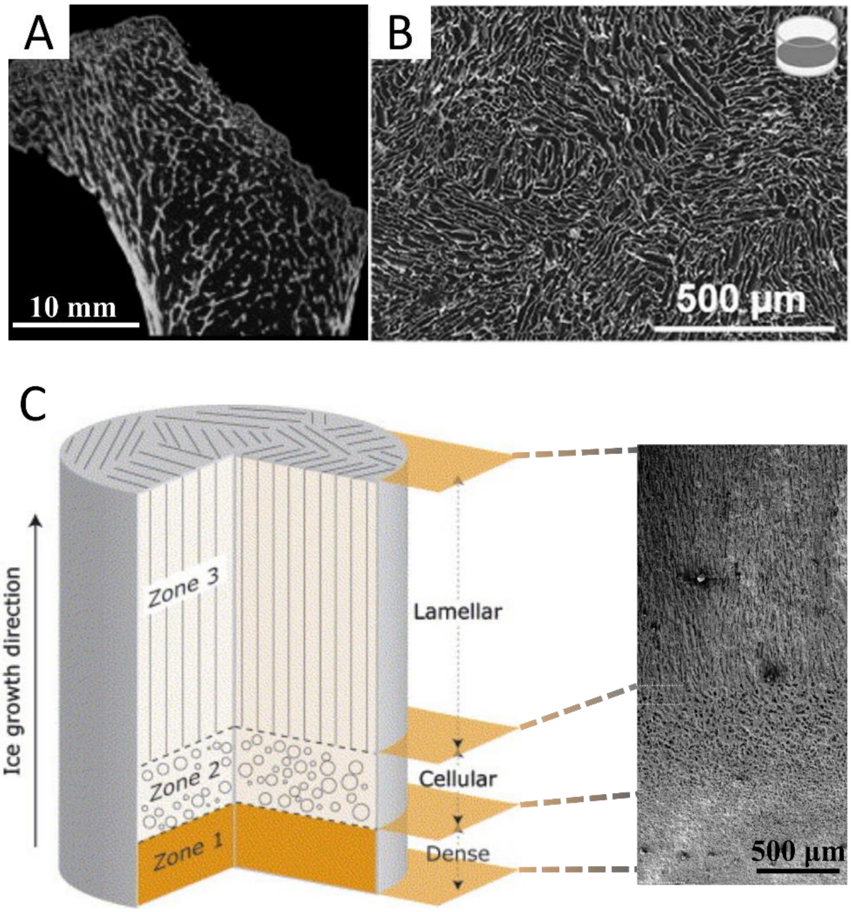

Figure 1.12 Morphology of bone-inspired materials obtained by freeze casting. (A) High-resolution CT cross-section image of human (2 to 3 years old) proximal femur. (B) SEM

cross-section image of porous pectin foam (20 g.L^{-1}). (C) Hierarchical structures of freeze-casted Hap scaffold along ice growth direction. (A) Reprinted from ref[342], Copyright (2006), with permission from Elsevier. (B) Reprinted from ref[301], Copyright (2018), with permission from Elsevier. (C) Reprinted from ref[343], Copyright (2006), with permission from Elsevier.

In the literature, multiple attempts at reproducing bone-like materials by freeze casting or by associating freeze casting with 3D printing are reported.[343–347] The structures obtained via freeze casting are often presented as parallel pores formed by ice growth. These parallel structures are, however, a partial view of the morphology of the materials obtained during freeze casting. The initial freezing zone, in contact with the cold interface, is normally characterized by a dense phase that freezes suddenly due to water supercooling. Above this dense zone a cellular pore zone is formed and further away from the cold interface the lamellar co-aligned pore zone is found. Figure 1.12C illustrates the different morphologies arising from the different freezing regimes that occur during freeze casting. Some of the most interesting materials obtained by freeze casting devoted to mimicking bone or bone-related tissues have explored such gradient structure rather than reproducing the “foam-like” architecture of cancellous bone – whose structure could be most likely obtained with “standard” freezing techniques.[348] Hap-based materials exhibiting gradient porosity that were fabricated by freeze casting featured a sequence of different pore structures along the thermal gradient axis (Figure 1.12C). From the bottom to the top the materials displayed a dense zone close to the cold finger, a middle zone with interconnected cellular structures and an upper zone with lamellar channels.[343,344] These structures could provide interesting experimental models to describe cortical-to-cancellous transition zones in bone or the materials and property gradients found in cartilage-related materials.[347,349]

Despite its name, compact bone tissue is a porous material. Similarly to trabecular bone, also the porosity plays a major role in the tissue functionality. Compact bone is characterized by two families of pores within the osteon or haversian system. One corresponds to the lacunar-canicular system, that features lacunae that host osteocyte bodies, with diameter of around 10 µm, connected by a network of canaliculi with diameters of around 500 nm responsible for the connection between adjacent lacunae.[350] The second family of pores corresponds to the interconnected haversian and Volkmann's canals with diameters of around 50 µm that host the vascular system of compact bone.[351] Both families of pores are critical for the cortical bone function and any attempt at reproducing this tissue should take into account the reproduction of these structures. In order to achieve the specific pore structure of cortical bone, freeze casting has been coupled with additive manufacturing processes to produce scaffolds with dual porosity.[344–346] For instance, a negative mold composed of acrylonitrile butadiene styrene (ABS) was designed with orthogonally distributed rods via 3D printing.[344] Subsequently, the 3D printed mold filled with chitosan-alginate solution was directionally freeze casted, freeze-dried, cross-linked with $CaCl_2$ and immersed in chloroform enabling mold removal to obtain the final dual pore structures. While the pore dimensions obtained were significantly larger that the characteristic porosity in compact bone (ϕ_{small} = 300 µm and ϕ_{large} = 3 mm) the obtained materials did show dramatically higher wicking rate in both 0.1% Safranin O aqueous solution and mice blood. The excellent fluid uptake properties of this hierarchically porous scaffold was thought to be more likely to promote the cell penetration and cell seeding in both 3D cell culture and *in vivo* implant.

To the ability of ice-templating to shape complex porous systems that may be relevant as bone substitutes, adds the fact that the technique is particularly suitable to shape the individual components found in bone since type I collagen is water soluble – provided the pH is low enough – and stable Hap slurries can be easily prepared. The possibility to reproduce some of bone's morphological aspects using apatite and collagen could respond to an increasing demand of materials that may act as efficient scaffolds in bone tissue engineering. It could also cope with the everlasting bottleneck of reaching concentrations (both mineral fraction and absolute collagen concentration) that are physiologically relevant.

1.3.3 Freeze casted scaffolds for bioengineering applications

As seen above, freeze casting has opened a new pathway to assemble in an effective manner inorganic particles and organic binders in order to mimic natural materials, based on previous experience in shaping ceramic green bodies. The materials discussed previously, nacre and bone, are heavily mineralized. Regardless of the mineralization degree, achieving a cohesive material from fully formed inorganic particles using freeze casting usually requires an organic binding phase (there are exceptions to this rule based on all-inorganic materials but they are beyond the scope of this work). This phase should be soluble in the chosen solvent – water in the cases discussed in this chapter – and provide a cohesive interface to hold the inorganic particles together. Among the molecules used as binders, water-soluble biopolymers such alginate, cellulose, chitin, chitosan, collagen, gelatin or pectin, among others, have been extensively used.[312] These water-soluble macromolecules are particularly interesting candidates for the development of freeze-casted biomaterials since they are abundant and present low immunogenicity.

As discussed above, there is a growing body of evidence suggesting that, beyond the specific cell interactions with a given biomaterial, the response of adherent cells to materials depends strongly on local environment cues such as pore geometry[352,353] or local substrate elastic moduli[354,355]. In this sense, shaping techniques such as freeze casting that enable to control the porosity and the local rigidity of biomaterials may provide excellent candidates as platforms for *in vitro* 3D cell culture[356] as well as future *in vivo* tissue engineering applications. In addition, the inherent porosity of freeze casted materials simplifies one of the key bottlenecks in designing biomaterials, the diffusion limit for oxygen and nutrients that hinders the full colonization of bulk hydrogels.[357,358] The following subsections address the different levers available to design freeze casted materials that are suited for 3D cell culture and tissue engineering.

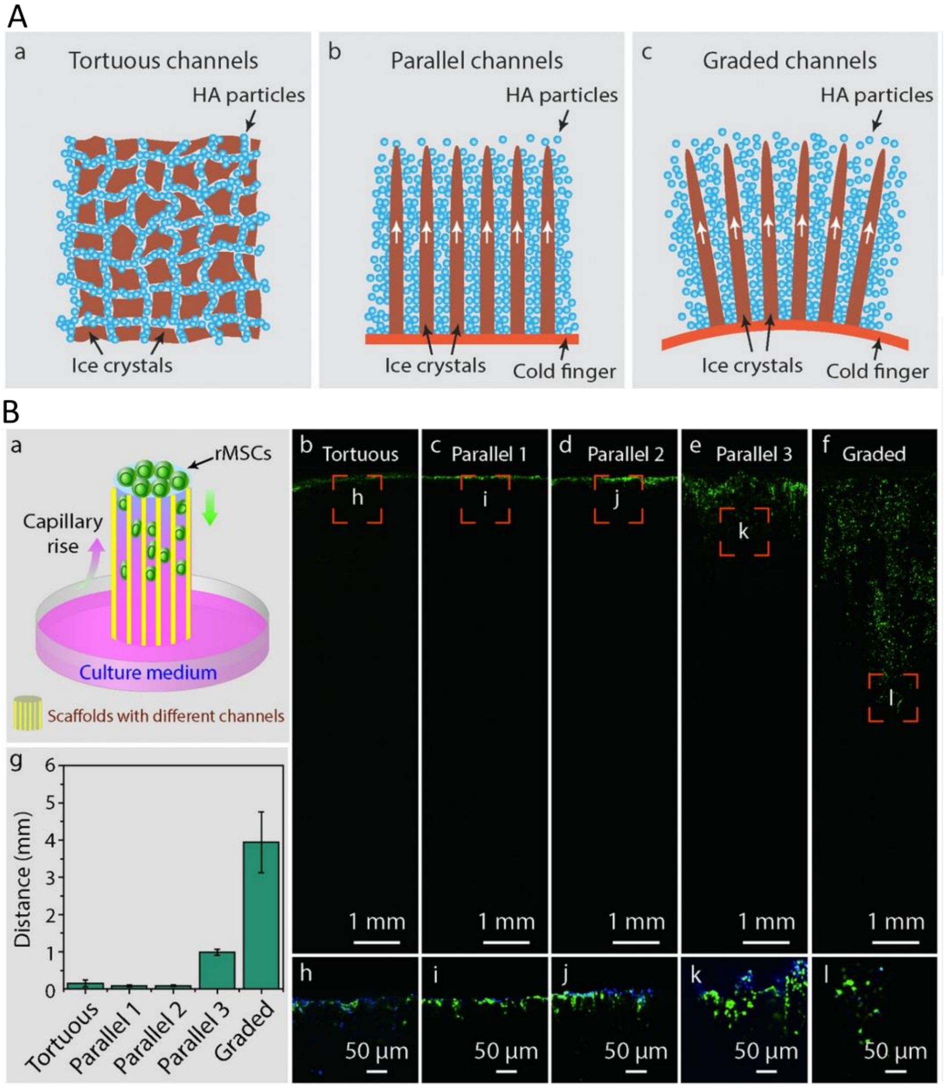

Figure 1.13 (A) Illustration of different microstructures of freeze casted Hap scaffolds with a. tortuous, b. parallel, and c. graded channels. (B) rMSCs (rat mesenchymal stem cells) penetration behavior in different scaffolds after 5 hours' culture. a. schematic illustration of cells penetration, b-i. fluorescence images of 4'-6-diamidino-2'-phenylindole (DAPI) stained rMSCs via confocal microscopy, b and f. indicating cell penetration in tortuous and graded scaffolds, respectively, c-e. indicating cell penetration in parallel scaffolds made at -170, -100, and -50 °C, respectively, h-l. high-magnification images from the parts indicated by the squares in b-f, respectively, g. statistical summary of cell penetration distance for different scaffolds shown in b-f. (A-B) Adapted from ref[359].

1.3.3.1 3D cell culture

The promise of physiological relevance inherent to 3D cell culture systems is strongly linked to the control over the architecture of biomaterials.[360] In this context, freeze casting presents an advantage among other biofabrication techniques, since it enables to create oriented pores of controllable dimensions from biopolymer solutions. Moreover, freeze casting achieves this at low temperatures which limits thermal denaturation as compared to most processing techniques. This aspect is particularly relevant to shape heat-labile proteins prone to denaturation such as collagen whose importance in cell culture is paramount.[13,361,362] Another interesting aspect that is inherent to freeze casting is the ability to reveal the porosity of the material without the use of leaching agents such as a second solvent. Different levers can be used to tune the suitability of a macroporous material to 3D cell culture, as discussed elsewhere.[356] These levers can be split into those that relate to the composition of the materials and those that relate to the process. The growth of ice causes the solutes to progressively segregate into the interstitial space defined by the newly formed crystals, because the solubility of most molecular or ionic species in ice is negligible.[363,364] As a consequence, the composition of the initial solution before freezing defines the composition of the obtained macroporous material. Moreover, the composition of the solutions also modifies the viscosity of the liquid medium which modulates ice growth.

Here we will discuss mainly two groups of levers readily available for the new freeze casting user: *i*) *the thermal gradient*, such as the target temperature, the freezing rate or ice front velocity, and *ii*) *solute effects*, including the nature and concentration of the solutes. Such factors are essential to fine tune the microstructure of final matrices and thus to approach as much as possible the architecture of the target tissue. In this section, the impact of these parameters on freeze casted scaffolds in terms of cell colonization will be discussed.

Target temperature - It is now well established that the shape and size of pores of freeze casted scaffolds can be modulated by the freezing gradient. Various authors have explored the impact of materials for 3D cell culture obtained by freeze casting using different thermal gradients. For the majority of such examples the thermal gradient is defined by the gap between the sample initial temperature (often room temperature) and the target temperature of the system (freezer, cold bath, *etc*…). The thermal gradient will be defined by the sample volume and geometry coupled with the absolute difference between the sample temperature and the target temperature. While this approach is particularly easy to implement it provides little control over the actual gradient endured by the samples since a simple variation in sample volume or sample geometry will dramatically affect the local thermal gradients. In spite of the poor control, many works have proceeded this way to template 3D cell culture scaffolds. Amyloid-based scaffolds obtained by freeze casting suspensions of amyloid fibrils (cross-linked with butanetetracarboxylic acid) at -20 and -196 °C (noted amyloid-20 and amyloid-196, respectively) exhibited different microstructure. The cellular-like morphology of amyloid-20 provided higher elastic moduli than the sheet-like morphology of amyloid-196. However, the two scaffolds provided comparable viability of Caco-2 (human epithelial colorectal adenocarcinoma) cells.[14] If little effect was observed on the cell culture in the case of Caco-2 cells on amyloid based-scaffolds, the topography has proven critical to determine the cell culture suitability of other freeze casted 3D cell culture systems. In a study aiming to design cardiac patches based on freeze casted SF/gelatin scaffolds, the freezing temperature was indeed a key factor.[365] The scaffolds obtained at -20°C exhibited isotropic morphology, whereas aligned pores were observed for scaffolds made at -30 and -80°C. These temperatures also resulted in smaller pores. After 2 weeks of porcine MSCs culture, the cells in the unidirectional scaffolds were aligned, guided by the scaffolds' pores. In contrast, the cells cultured in the isotropic scaffolds presented random adhesion without covering the whole sample volume. Also, in bone-mimicking materials temperature played an important role in cell colonization. Using Hap slurry suspended in a mixture of different water-soluble polymers (sodium polyacrylate, polyethylene glycol, and polyethyloxazoline), Yang et al.[359] fabricated freeze casted scaffolds at different freezing temperatures (-50, -100, and -170 °C) (Figure 1.13Ab), followed by lyophilization and sintering. When decreasing the freezing temperature from -50 to -170 °C, the characteristic pore sizes also decreased from ∼8 to ∼2 μm. Scaffolds fabricated at -50 °C (Figure 1.13Be,k) led to a faster migration of rat mesenchymal stem cells (rMSCs) than in those made at -100 °C (Figure 1.13Bd,j) and -170 °C (Figure 1.13Bc,i). Apart from pore size, also the pore volume fraction and the pores' interconnectivity define the cellular behavior within porous scaffolds. Mandal et al.[86] obtained scaffolds with different pore sizes and porosity by freezing SF solutions (ranging from 2 to 6 wt.%) at -20, -80, and -196 °C. The decreased freezing temperature resulted in increased pore volume fraction and decreased pore size, irrespective of the SF concentration. Upon seeding normal human dermal fibroblasts (NHDFs) at the center of the scaffolds extensive migration occurred in the scaffold fabricated at -196 °C (pore size of 80 – 100 μm and porosity of 96 ± 4.1%) compared to the one fabricated at -20 °C (pore size of 200 – 250 μm and porosity of 86 ± 5.8%). These results highlight the role of the thermal boundaries in controlling cell migration and colonization of macroporous scaffolds.

Freezing rate and ice front velocity – The growth rate of ice crystals determines many of the pores' attributes in freeze casting. The two most direct ways to control the porosity are thus to adjust the cold element cooling rate or the ice front velocity. From an experimental standpoint these are very different parameters to control. They demand radically different setups but their final purpose is similar, to provide some degree of kinetic control over the structuration induced by ice formation. Increased freezing rate generally results in lower pore section area which could impede cell migration. The threshold between facilitated and hindered cell migration in the macroporous scaffolds depends however on the pores' characteristic size and on cell type size.[356] Meurice et al.[366] obtained β-TCP (tricalcium phosphate) scaffolds with tubular interconnected elliptical pores, whose average large and small axis decreased from 209 to 13 μm and from 41 to 6 μm when the freezing rate increased from 1 to 20 $°C.min^{-1}$, respectively. MG-63 osteoblastic cells were only able to migrate into the scaffolds having pores larger than 100 μm. Cells penetrated ~250 μm into the tubular structure obtained at 1 $°C.min^{-1}$, whereas no invasion took place up to 7 days' culture in scaffolds prepared at 20 $°C.min^{-1}$. Besides defining the pore geometry and thus the conditions for cell migration, freezing rate also plays a role in swelling and degradation properties of the constructs that are central to cell colonization and survival. Recently, olibanum-collagen-gelatin scaffolds (OCG) cross-linked with glutaraldehyde were reported as suitable macroporous materials for neural tissue regeneration.[367] A small increase in freezing rate from 1 to 3 $°C.min^{-1}$, imposed a decrease in pore size from ~126 to ~93 μm while compressive strength increased from ~3.5 to ~9.0 kPa, probably ascribed to the increased wall thickness and density. Moreover, results showed a higher water uptake ratio (1131 ± 35% vs 1057 ± 31%) after incubating for 24 h and a higher degradation rate (~57% vs ~45%) for OCG1 vs OCG3. Regarding their biocompatibility, although both scaffolds supported rat bone marrow stromal cells (rBMSCs) proliferation, OCG1 performed better than OCG3 in terms of cells migration and proliferation rate, due to its larger pores.

Scaffold composition – How to define the composition of freeze casted scaffolds for 3D cell culture? Two criteria seem inevitable. The first relies on a formulation that is suitable for the process of freeze casting, i.e. that segregates into a part of solidified solvent and a part of enriched solute and that retains such segregation upon solvent removal. The second criteria relates to the suitability of the solute-rich phase as a scaffold to host cells. Here, criteria such as the solute's toxicity but also the local mechanical properties are central. 3D cell cultures developed using freeze casting have explored the intersection between these two criteria to develop macroporous scaffolds. As mentioned earlier, achieving biomaterials whose morphology is inspired by bone's ultrastructure can be attempted using freeze casting. Hap,[87,345,346,359,368–370] one of the main components of bone, is consequently holding a dominant place in the fabrication of scaffolds for bone tissue engineering applications. Hap scaffolds were obtained through the use of electric field assisted freeze casting.[369] Using H_2O_2 as pore-forming agent resulted in both lamellar and spherical pores in the scaffold. When the electric field intensity increased from 0 to 90 $kV.m^{-1}$, the average diameters of the lamellar and spherical pores increased from 460 to 810 μm and from 320 to 420 μm, respectively, due to the limited growth rate of ice crystals as the H_2O molecules had a more stable distribution along the direction of the electric field. Osteosarcoma cells cultured in these scaffolds, presented at first a filamentous and then an elongated morphology, which suggested, according to the authors, the scaffolds' suitability as a 3D culture platform. Cell adhesion was observed in a greater extent for the scaffold prepared with high electric field intensity, pointing out the crucial role of pore size for efficient cell colonization. Apart from the microstructure, the mechanical, and biological properties of bone biomimetic scaffolds, the liquid transport property is also an important factor as it enables nutrients exchange. This effect was studied by Bai et al.[87] in freeze casted Hap scaffold with graded lamellar pores, obtained by radial freezing using a copper rod in the center of a plastic mold. The width between lamellae changed gradually from ∼4.5 at the "tip" to 11.8 μm at the "base", where the tip is the center of the scaffold (where the copper rod was placed) and the base is the edge (where the border of the plastic mold is found), respectively. Interestingly, a piece of a dry Hap scaffold, when its base was in contact with a rMSCs suspension, presented the most efficient cell self-seeding effect. Because of the capillary effect, this orientation allowed for the cells' penetration all along the sample, with the cells aligned within the graded lamellar channels. The same group further confirmed these results by comparing freeze casted Hap scaffolds with a) tortuous, b) parallel, and c) graded channels in terms of cell migration[359] (Figure 1.13A). The previously reported graded scaffolds promoted a better migration of rMSCs in their channels, when cells were seeded on top (Figure 1.13B). Therefore, the capillary effect in the graded scaffolds plays an important role to the faster exchange of metabolic products of cells and their surrounding nutrients but also as a tool to promote faster colonization of the cells in the initial seeding moments. These results reinforce the significance of the scaffolds structural characteristics for their efficient use in 3D tissue engineering applications.

Collagens, are the most abundant component of the ECM (extracellular matrix) in connective tissues of mammals ranging from bone (as previously mentioned) to softer tissues such as tendon, skin or cornea. Such widespread distribution makes of collagen the protein of choice for the development of 3D biomaterials as *in vitro* models. The main difficulty in handling collagen based materials structured by freeze casting relies on their stability. In fact collagen (and in particular type I collagen) require stabilization to retain the shape and structural integrity imposed by freezing. Two main strategies have been proposed to ensure the stability of freeze-casted collagen materials: chemical crosslinking and fibrillogenesis. Most examples available in the literature rely on crosslinking, which produces collagen foams[371]. Freeze casted, freeze-dried, cross-linked collagen-hyaluronic acid (HA) composite constructs were reported as scaffolds for adipose tissue engineering towards a 3D *in vitro* model of the mammary gland.[372] Two different concentrations of HA were used, 7.5 and 15 wt%. With the addition of 15 wt% HA, Young's modulus and collapse plateau modulus of the final composite in the hydrated state were increased from ∼ 4.26 to ∼ 6.73 kPa and from ∼ 495 to ∼ 625 Pa, compared with pure collagen matrix, respectively. This scaffold was also found to better support 3T3-L1 murine pre-adipocytes proliferation and differentiation after culturing for 8 days. The other strategy available to stabilize collagen matrices requires fibrillogenesis, an important factor for the successful establishment of collagen-based biomimetic models that ensure their unique mechanical properties, essential for cell adhesion and proliferation. Although collagen is widely used as the starting material in biofabrication approaches, the induction of collagen fibrillogenesis, without disturbing the given structure of a scaffold, remains an important challenge that has only recently been tackled.[13] The ability to stabilize collagen matrices without imposing a chemical crosslinking step was achieved by topotactic fibrillogenesis that allows for ice thawing and simultaneous pH variation to induce fibrillogenesis. The topotactic process in freeze casted collagen scaffolds took place with the help of ammonia vapors. In contact with ice, ammonia vapors gradually lowered the melting point of ice crystals and simultaneously induced collagen pre-fibrillogenesis, without damaging the anisotropic structure obtained by freeze casting (Figure 1.14A). The obtained self-standing fibrillar collagen matrices exhibited two levels of structural organization, an increasing macroporosity along the freezing direction, and the presence of regular parallel micro-ridges on the walls of the lamellar pores. The obtained scaffolds in wet state showed unprecedented Young's modulus (33 ± 12 kPa) for pure collagen hydrated macroporous scaffolds. The *in vitro* 3D culture of NHDFs revealed cells migration into the scaffolds along their lamellar pores (Figure 1.14B) and better cell adherence when compared with the colonization of cross-linked scaffolds. Similar results were obtained when C2C12 cells (murine myoblasts) were cultured, while a limited differentiation to myotubes was also observed.

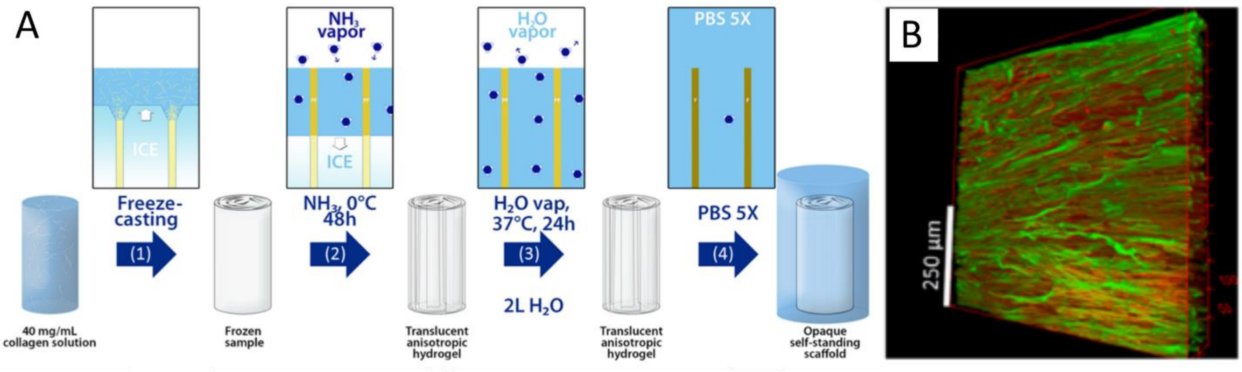

Figure 1.14 (A) Collagen topotactic fibrillogenesis approach for freeze casted scaffolds using ammonia vapors. (B) SHG (Second Harmonic Generation) of 3D reconstruction of NHDFs on fibrillar collagen scaffold after culturing for 3 weeks. (Red, collagen SHG signal; green, actin). (A-B) Adapted with permission from ref[13]. Copyright (2019) American Chemical Society.

The development of *in vitro* 3D tumour models towards the understanding of interactions between cancer cells and their surrounding microenvironment, is also a biomedical issue that could benefit from the ability to structure the ECM through freeze casting. Biomimetic materials are currently used in an effort to engineer the 3D cell microenvironment.[373] Regarding the ECM composition, collagen is a protein strongly influencing cancer cell behaviour through a variety of signalling pathways.[374] Towards this direction, Campbell et al.[375] fabricated radially anisotropic cross-linked collagen scaffolds for invasion studies of breast cancer cell lines. An enhanced migration was observed for the invasive cancer cell line MDA-MB-231 into anisotropic constructs compared with isotropic collagen scaffolds. Moreover, a 1/10% serum gradient could further improve cells migration into anisotropic collagen constructs. When invasive MDA-MB-468 cells were treated with epidermal growth factor, thus acquiring a mesenchymal phenotype, they migrated for a longer distance into anisotropic scaffolds, confirming the scaffolds ability to distinguish invasive phenotypes.

Apart from Hap and collagen, other natural materials such as gelatin,[376,377]SF,[365,378] and chitosan[16,315] have been turned into scaffolds suitable for *in vitro* tissue engineering purposes by freeze casting. Gelatin, derived from the partial hydrolysis of native collagen is a low cost product. It has been widely used in tissue engineering due to its hydrophilicity, low antigenicity, and potential collagen-related functions, like the RGD sequence, enabling better cell adhesion, differentiation, and proliferation. [376,379,380] Freeze casted, freeze-dried, cross-linked gelatin-based scaffolds were analyzed by microCT, in order to investigate the structural features of this type of scaffolds.[376] Also here, the dependence of structural properties with freeze casting parameters has been evidenced; highly directional structure was achieved at -30 °C, while the addition of hydrochloric acid in the initial gelatin solution doubled the pore diameter compared to pure gelatin matrices. In terms of cell culture, the larger pores resulted in significantly higher cell seeding efficiency of porcine chondrocytes. Gelatin was also used as an additive to improve the hydrophilicity of unidirectional PLGA freeze casted constructs, for artificial peripheral nerve regeneration.[379] Compared to pure PLGA scaffolds, composite PLGA-gelatin ones, showed increased pore size, slightly decreased compressive strength, and enhanced swelling ratio, biodegradation rate, and drug release levels. Although both PLGA and PLGA-gelatin constructs could support growth of L929 fibroblast cells, cells showed a better spreading into PLGA-gelatin matrices. Improved differentiation of P19 embryonic carcinoma cells with the addition of retinoic acid as a neural growth factor in PLGA-gelatin scaffolds further proved its potential for peripheral nerve regeneration. The same group further investigated gelatin-based freeze-casted scaffolds for bone tissue engineering.[377]

Silk fibroin, a natural polymer extracted from *Bombyx mori* cocoons, has also been selected as a starting material for freeze casted scaffolds because of its versatility, biocompatibility, tunable mechanical properties and biodegradability.[381–383] As we described earlier, SF combined with gelatin was used for the elaboration of anisotropic constructs.[365] The addition of gelatin resulted in smaller pore size, higher water retention, and lower scaffold shrinkage after methanol treatment. In addition, gelatin promoted better porcine MSCs proliferation and viability. Silk fibroin hydrated flat films were converted to 3D-like scaffolds thanks to the topography induced by freeze casting followed by freeze-drying.[378] Well distributed nanoridges were observed on the films with mean length and mean spacing between them of ~932 nm and ~640 nm, respectively. hMSCs could be successfully cultured on both flat and nanoridged films, but on the latter, they adopted an elongated morphology. Gene expression analysis for osteogenic specific markers showed significantly higher levels on nanoridged films, indicating that the sole nanotopography of SF films could induce the differentiation of hMSCs into osteoblasts without adding any supplements.

Chitosan, a linear polysaccharide, has also been used as a base material for the elaboration of biomaterials towards tissue engineering applications. Francis et al.[315] fabricated macroporous, highly aligned chitosan-alginate scaffolds by freeze casting at 1 $°C.min^{-1}$, for neural tissue engineering. Freeze-dried, cross-linked samples were then submitted to surface modification with a polycation (poly-L-ornithine or poly-L-lysine) and/or laminin. Modified scaffolds promoted a significantly longer neurite growth of embryonic chick dorsal root ganglia (DRGs) compared to non-coated scaffolds. In addition, the coated scaffolds could direct the alignment of neurite growth along the freeze casting direction. Further studies of the same group resulted in chitosan constructs combining aligned lamellae with a distance of 71 ± 22.1 μm between them and uniform ridges located on the lamellae.[16] Confocal microscopy showed an excellent neurite alignment after seeding of DRGs on laminin-coated chitosan scaffolds. Further 2D culture of DRGs on single laminin-coated lamellae extracted from the 3D constructs, revealed that ridges linearly aligned 62.4% of growing neurites presenting orientation with angle variations smaller than ± 10° compared to these of ridges (defined as 0°).

Solute concentration - The solute concentration for the fabrication of freeze casted scaffolds suitable for 3D cell culture has also a key role in their structural properties and mechanical behavior. More specifically, an increased solute concentration (both for ceramics[366,384] and macromolecules[14,86,385]) results in the reduction of pore size and porosity, the increase of density and the improvement of mechanical properties. An indicative example can be found at a previously mentioned study, concerning SF freeze casted scaffolds, where solutions of 2, 4, and 6 wt% concentration were used.[86] The comparison between pore size at the same freezing temperature, showed indeed that increasing SF concentration from 2 to 4, and 6 wt%, led to decreased pore size, from 200 – 250 to 100 – 150, and to 75 – 100 μm, and porosity, from 86 ± 5.8 to 79 ± 4.6, and 74 ± 2.3% respectively. Therefore, the cell culture experiments were restricted to the 2 wt% products. The amyloid-20 4 wt% discussed before, favored a better HT29 (human colorectal adenocarcinoma monolayer) cell growth than the 1 wt% amyloid-20 and -196 scaffolds.[14] Moreover, increasing the concentration, an increasing cell survival was observed only in amyloid-20, indicating that appropriate scaffold pore sizes for HT29 cells were maintained at every concentration in these samples. The impact of solute concentration was also studied by Rowland et al.[74] who fabricated freeze casted scaffolds in shapes of disks and hemispheres, with uniform or aligned pores, starting from porcine de-cellularized cartilage-derived matrix (CDM). As CDM concentration was increasing from 7 to 11 wt% pore size and porosity decreased, while compressive modulus dramatically increased. The pores of the uniform constructs were visibly smaller, in contrast to the large grooves present in those with aligned pores, thus promoting MSCs infiltration. In addition, after chondrogenic culture, higher cell infiltration was found in the 11 wt% CDM scaffolds compared to that of 7 wt%. Furthermore, although the compressive modulus of the uniform scaffold was higher than that of the aligned one, both 11 wt% CDM scaffolds, resisted cell-mediated contraction and their compressive moduli were decreased after chondrogenic culturing for 28 days. On the contrary, 7 wt% CDM scaffolds suffered from highest contraction and their compressive moduli were increased. Further analysis revealed that the 11 wt% CDM hemisphere scaffold could not only prevent cell-mediated contraction, but also facilitated cells infiltration, which in turn promoted cartilaginous matrix deposition.

All the aforementioned studies clearly demonstrate the flexibility provided by the freeze casting technique, leading to a large spectrum of biomaterials suitable for 3D cell culture applications; on one hand, by tuning freezing parameters and, on the other hand, by choosing the appropriate solute (and solute concentration), structural features and mechanical properties of freeze casted scaffolds can be further improved and optimized. The cell colonization of optimized scaffolds offers multiple possibilities in the field of biomedical applications, so that freeze casted scaffolds could serve as biomimetic models to elucidate cell behavior and their interactions with the surrounding environment in both physiological and pathologic conditions. Moreover, interaction of cells with the biomaterials themselves, should be evaluated prior to *in vivo* implantation studies.

1.3.3.2 *In vivo* implantation of freeze casted materials

Regardless of the merits of any cell culture system, the transposition between *in vitro* culture to *in vivo* integration is not trivial. The inherent difficulties are linked to the performance of each system but also depend on the ability to access to *in vivo* testing facilities, on ethical committees' approval and on effective collaborative links with surgeons. The history of ice-templating, as a materials processing technique solidly anchored in the ceramics community, has seldom produced the conditions for those interactions to be widespread. As a consequence, the research output drops dramatically when looking for the results of freeze casted 3D scaffolds tested *in vivo* as compared to 3D cell culture *in vitro*. Tissue engineering materials devoted to to bone[368,378,385–388], nerve[389], skin[390] and vascular grafts[391,392] have been attempted via freeze casting with composition ranging from ceramics, to natural and synthetic polymers, as well as hybrids. Appropriate microstructures, mechanical properties, and bioactivity are necessary for *in vivo* implantations but are not sufficient. Practical criteria such as ease of handling in the surgical block, ability to sterilize using standard medical equipment or the shelf-like of the 3D scaffolds prior to implantation pose major hurdles for the effective transposition of 3D cell cultures to *in vivo* setting.

The scaffolds' microstructure and mechanical properties are important parameters not only for *in vitro* applications but for *in vivo* implantation as well, as shown in the literature through various examples. A freeze casted chitosan conduit was successfully tested for peripheral nerve repair.[389] The application of two opposite thermal gradients during the freezing process resulted in scaffolds consisting of a double-layered highly-aligned porous structure, with suitable mechanical properties for *in vivo* testing. The conduit was able to bridge 10 mm sciatic nerve defects in rat models at 12 weeks post-implantation, while it favored the vascularization of its lumen. The structure of recently reported SF/collagen composite scaffolds for osteochondral tissue remodeling, had an important role on cell behavior *in vivo*.[387] Three different scaffolds were elaborated with random, axially aligned, and radially aligned pores by freeze casting and temperature gradient-guided thermally-induced phase separation. Morphology analysis of cross-sections revealed significantly smaller pore sizes for radially (68.0 ± 20.3 μm) and axially aligned (69.9 ± 24.1 μm) scaffolds compared to those of the random scaffold. At 18 weeks post-implantation in rabbits with osteochondral defects, axially and radially aligned scaffolds, especially the latter, favored cell migration and infiltration, resulting in faster cartilage regeneration rate. The combination of freeze casting with other biofabrication techniques, like electrospinning, could further tune pore characteristics of the final products, providing benefits for both *in vitro* and *in vivo* cell behavior. Lee et al. performed cold-plate electrospinning with PCL and SF nanoparticles (SP) aiming at the fabrication of macroporous matrices for artificial dermis applications (Figure 1.15A-B).[390] The presence of SP in PCL nanofibers endowed the composites with enhanced interconnected pore size, porosity, and hydrophilicity. The scaffolds were implanted into full-thickness skin defects in rat wound models. Their structural and physicochemical properties resulted in more efficient cell infiltration and collagen deposition, leading in turn to faster wound healing rate compared to that of pure PCL matrices 20 days post-implantation. PCL/SP composites showed comparable wound healing rate to the commercial Matriderm® collagen artificial dermis, while their sufficient structural support resulted in reduced contracture and scar formation (Figure 1.15C).

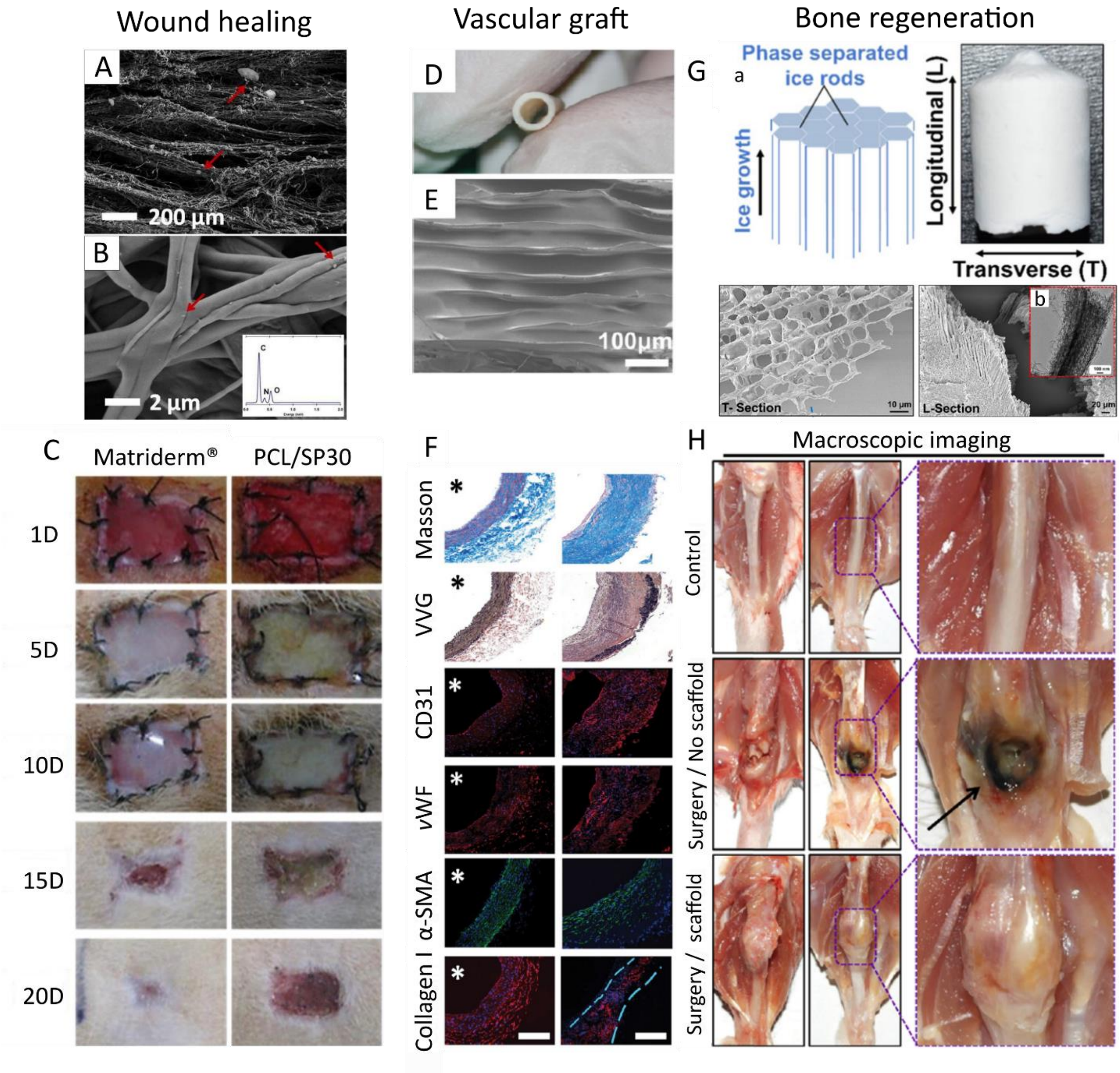

Figure 1.15 *In vivo* implantation of freeze casted scaffolds. (A-B) SEM images of fibrous PCL/SP30 (PCL with 30% SF nanoparticles) scaffold. EDS analysis is shown in the inset. (C) Macroscopic images of wound healing process in rat wound model with commercialized artificial dermis (Matriderm®) and PCL/SP30 scaffold. (D) Vascular scaffold consisting of an inner layer of freeze casted SF/gelatin surrounded by an electrospun poly (ε-caprolactone) (PCL) outer sheath. (E) Lamellar inner surface of freeze casted graft. (F) Cross-sections of lamellar (∗) and non-lamellar grafts with histological staining for collagen (blue) and elastin (black), and immunofluorescent staining for CD 31 (red), vWF (red), α- SMA (green), and collagen I (red), respectively. (G) Macroscopic and microscopic images of freeze casted

silica/SF scaffold with honeycomb structure. (H) Macroscopic images of the implant site of rat femur 25 days post-implantation. (A-C) Reprinted from ref[390], Copyright (2016), with permission from Elsevier. (D-F) Adapted with permission from ref[391]. Copyright (2019) American Chemical Society. (G-H) Adapted with permission from ref[386]. Copyright (2019) American Chemical Society.

Freeze casted scaffolds topography is also an important factor for their evaluation as suitable *in vivo* implants. As discussed earlier, Yang et al. found that the sole existence of well distributed nanoridges on a SF film induced hMSCs differentiation to osteoblasts.[378] After one month's implantation into subcutaneous dorsum sites of rats, a higher amount of calcified tissue was formed on nanoridged films than on flat ones, while this difference was more easily observed when hMSCs were pre-seeded on the films. Besides, more organized fibrous tissues containing more collagen deposition were observed around nanoridged films than around flat films, both for pre-seeded or not films. Expression of osteopontin and osteocalcin was found at the outer surface of nanoridged films, even without seeded hMSCs. The same result confirming the formation of bone-like tissue was also observed on flat films, but only when seeded with hMSCs. Therefore, nanoridges *per se* on SF films could promote bone formation both *in vitro* and *in vivo*. Wang et al.[391] elaborated small diameter vascular grafts composed of an electrospun PCL outer sheath and an freeze casted and freeze-dried SF/gelatin inner layer (Figure 1.15D). The inner surface exhibited a lamellar structure with height of 10 μm, thickness of 200 nm, and average gap between two lamellae of 20 μm (Figure 1.15E). Mechanical properties (including elastic response, burst pressure and elongation at break) and stability in PBS buffer of PCL-coated scaffolds were enhanced, compared to those of scaffolds without the PCL sheath. The presence of lamellae on the inner surface not only inhibited significantly the adhesion and activation of platelets, but promoted the growth and alignment of endothelial cells as well, compared to non-lamellar grafts. Furthermore, scaffolds with lamellar topography could maintain good antithrombosis properties and high blood flow within 3 months' implantation in rabbit carotid artery defect models. The well-organized elastin, collagen, and muscle fibers, as well as the expression of relative proteins on the lamellar grafts confirmed the ability of the scaffolds to conduct *in situ* endothelialization (Figure 1.15F).

The integration of bioactive additives during the preparation of starting solutions or suspensions prior to the freeze casting process, can favour tissue engineering applications. As previously mentioned, bone-oriented materials hold a dominant position among *in vivo* implantations. This application could benefit from the introduction of bioactive compounds in the base material to promote more efficient integration and/or post-operative controlled drug release. A hybrid aerogel fabricated via freeze casting, followed by supercritical drying, was recently reported, using a sol-gel assembly of organosilane (tetraethyl orthosilicate) and SF (Figure 1.15G).[386] The silica-SF scaffold immersed in a cold bath at -196 °C at a constant rate of 33 $cm.h^{-1}$ exhibited micro-honeycomb hierarchical pore structures with macropore and mesopore sizes of ∼18 μm and ∼17 nm respectively and showed the lowest bulk density (ρ_b = 0.075 g cm^{-3}) and the highest Young's modulus (ε = 7.3 MPa) along the freezing direction. Regarding the *in vitro* biological properties, this scaffold was considered as clinically implantable as it showed augmented protein adsorption, minimal effect on human red blood cells lysis, bone-like Hap crystals formation on its surface, and MG-63 osteoblasts attachment and proliferation. Macroscopic images of implants dissected 25 days post-surgery, demonstrated significant bone tissue regeneration around and inside the implants in the defect sites induced in rat models (Figure 1.15H). Another scaffold used for bone tissue engineering involves mineralized collagen fibers, derived from collagen and apatite (Col-Ap) suspensions in a modified simulated body fluid promoting collagen self-assembly and *in situ* apatite precipitation.[388] These suspensions were submitted to either random, either unidirectional controlled freezing, leading to equiaxed and lamellar structure, respectively. By varying the initial collagen concentration (1.0, 2.0, and 3.0 $g.L^{-1}$), precipitated apatite content was ∼54, ∼35 and ∼18% respectively (hence the scaffolds Col-Ap-54, -35, and -18). Analyzing the equiaxed scaffolds, with the increase of apatite content, decreased average pore size and porosity were observed under the same freezing conditions. The composition of Col-Ap-35 equiaxed scaffolds with pore sizes of ∼82 μm had greater similarity with natural bone, therefore they were tested as *in vivo* implants. Scaffolds loaded with murine calvarial cells (mCOBs) were implanted in cranial defects of mouse models. After 4 weeks' implantation, the defect was repaired, with more than 90% of the area filled with newly formed bone.

The examples listed above are not exhaustive. They provide however, a quick survey of the relevance of freeze casted materials in *in vivo* settings and thus their potential to address different tissue engineering challenges. Freeze casting endows scaffolds with controlled microstructures, mechanical properties and bioactivity, contributing to effective tissue regenerations upon implantation. One aspect that is worth mentioning is, for a given scaffold, the coherence between cell behavior *in vitro* and *in vivo.* Such results seem to confirm the increased physiological relevance of freeze casted 3D cell culture scaffolds as suitable model to predict the cellular response *in vivo*.

1.4 Encapsulation during freeze casting in biomaterials design

One of the key phenomena occurring during freeze casting is the segregation of the solutes towards the interstitial space defined by ice crystals due to the insolubility of most molecular and ionic species in ice.[393,394] The case of suspended particles is more complex and has been extensively discussed in the literature from different perspectives due to its relevance in a wide range of domains, from geophysics to biology and engineering.[313,395–398] The fate of stable suspended particles in a given solvent when meeting an advancing freezing front can be either engulfment (into ice), rejection from the ice front or encapsulation in between the growing ice crystals. Many factors play a role in these different scenarios such as the ice front velocity, the particle size or the particles density among others. The relevance of such phenomena in cryobiology has been anticipated in the early 1980s with a series of groundbreaking works devoted to understand the interaction between suspended cells and moving ice fronts.[399,400]

The first observations of the interaction between suspended cells and moving ice fronts followed, in particular with an interest in the fate of erythrocytes during directional freezing.[318,401,402] Under directional freezing, red blood cells were mostly entrapped in the interdendritic regions, especially at high ice front velocities. This results led the authors to hypothesize that, upon freezing in saline medium, high osmotic pressure due to solute concentration or the mechanical stress from the ice crystals caused cell death.[318,403] Interestingly, they observed that cells were uniformly distributed and showed higher viability when glycerol was added.[318] They suggested that the reason behind is that glycerol could inhibit the formation of ice crystals and reduce the mechanical stresses that cells experience. Similar effects were later observed with high concentration of trehalose[403] and dimethyl sulfoxide (DMSO)[20]. Also sperm cells derived from different species such as donkey[404], bull[405], and killer whale[406] have been cryoprotected with directional freezing and resulted in successful fertilization after artificial insemination. For instance, bull semen was collected from ten Holstein–Friesian bulls and protected in commercialized Berliner Cryomedium supplemented with 7% v/v glycerol via directional freezing.[20] Compared with fresh sperm, thawed samples showed more than 75% viability and comparable acrosome integrity and similar sperm morphology. It was also shown that controlled ice nucleation during slow freezing is not necessary for directional freezing in view of viability and other functional analysis, which indicates that directional freezing could reduce costs and save energy during cell cryoprotection.

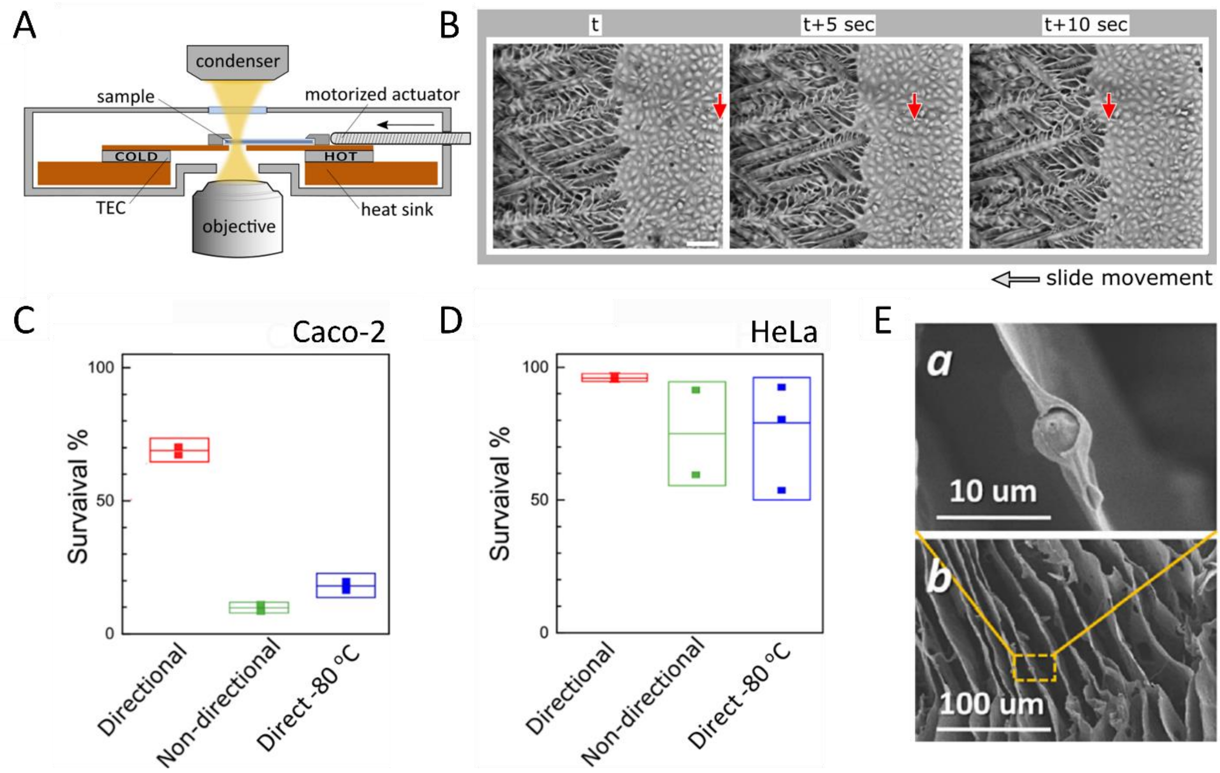

Figure 1.16 (A) Schematic illustration of translational cryostage. This stage is integrated with a microscope which can *in situ* observe freezing behavior when sample is moved by a motorized actuator from hot to cold side. (B) Representative images of ice front propagation in IEC-18 epithelial cell suspension (in 10% DMSO). The red arrows indicate one cell gradually being frozen when sample is moved. Survival rate based on flow cytometry for Caco-2 (C) and HeLa cell (D) after combination of directional freezing and gradual cooling, non-directional gradual cooling (1 °C.min^{-1}) and direct freezing at -80 °C freezer. (E) SEM images of lamellar alginate foams with encapsulated yeast cells. Scale bar, 100 μm (B). (A-D) Adapted from ref[317]. (E) Adapted from ref[17].

This technique could also be applied for the cryopreservation of adherent cells, such as neuron-like cells[407] and intestinal epithelium IEC-18 cells[317]. More specifically, Bahari et al.[317] applied two-stage freezing to IEC-18 cells in the presence of DMSO: a) translational cryostage for directional freezing (Figure 1.16A) to approximately -8 °C at various speeds, followed by gradual freezing to -20 °C at 1.2 $°C.min^{-1}$, and b) liquid nitrogen cooling stage for cooling to -80 °C at 0.5/1 $°C.min^{-1}$. During directional freezing the increase of velocity (Figure 1.16B) and DMSO concentration resulted in more branches and narrower width of the ice crystals. The protocol with velocity of 30 $\mu m.s^{-1}$ in directional freezing, liquid nitrogen gradual freezing at 0.5 $°C.min^{-1}$, and DMSO concentration more than 7.5% was able to maintain the round morphology of IEC-18 cells. The same conditions were applied for the cryopreservation of HeLa and Caco2 cells. Their viability was higher when protected via directional freezing than that of samples processed either with nondirectional but controlled freezing rate, or directly in -80 °C (Figure 1.16C-D).

Directional freezing could also promote the formation of uniform ice crystals reducing the effect of supercooling and osmotic stress on cells. Apart from cells, directional freezing has already been used for the cryopreservation of small tissues, like ovary[21,22,408] and liver[24] in the presence of cryoprotectant agents like DMSO and ethylene glycol. However, these agents could induce harmful effects to cells like decreased DNA stability, especially at high concentrations.[409]

Another alternative to reduce mechanical stress is the use of biopolymers instead of toxic cryoprotectants such as DMSO to protect cell entities via freeze casting. Our group found that alginate could be successfully applied to protect *Saccharomyces cerevisiae* without using any toxic chemicals.[17] Mixtures of alginate and yeast cells were uni-directionally freeze casted and rehydrated; cell viability was evaluated through cells' metabolic activity. The obtained results showed that yeast cells were mostly trapped into well-aligned alginate lamellae (Figure 1.16E) and retained their metabolic activity, thus indicating the existence of viable yeast cells in dried alginate foams. The entrapment of cells during ice growth and possible viscosity drag caused by alginate pave a way to novel cryopreservation approach via freeze casting, that will be developed in chapters 3 and 4. The use of biocompatible polymers could not only alleviate the potential mechanical stress generated during freezing, but also improve entrapment efficiency within the viscous polymer phase.

Merging of directional freezing technology – that was known in the cryobiology domain – with the developments that rose from a different community, that of freeze casting, has widened the possibility to understand the fundamental physicochemical processes endured by cells during freezing. The anisotropy of freeze casting/directional freezing provides an opportunity to probe the interaction between the medium being frozen and its interaction with growing ice crystals, a feat inaccessible to a standard freezing setup. In particular, the controlled freezing environment and the possibility to integrate it into other characterization instruments has enabled to determine, for the first time, the pressure generated in between ice crystals and how it depends with the freezing rate.[410] These results that directly depend on the intersection between directional freezing and freeze casting will provide much needed insight to tackle the cryopreservation of ever more sensitive biological entities.

The following chapters will address the fabrication of biomaterials using freeze casting as main strategy. The chosen examples follow the same path that has been discussed here, building up from relatively straightforward freeze casting of biopolymer matrix as a drug release device (Chapter 2), to the encapsulation of increasingly labile biological entities such as yeast cells (Chapter 3) and Red Blood cells (Chapter 4).

Chapter 2

Redesigning silk as antimicrobial macroporous patches

Chapter 2 is to be submitted as *Kankan Qin, Rui F.P. Pereira, Thibaud Coradin, Veronica Z. Bermudez and Francisco M. Fernandes* "Redesigning silk as antimicrobial macroporous patches" to Materials Today Bio.

2.1 Introduction

Silk is one of the most sophisticated and unique soft materials found in nature. It is characterized by a precise coaxial structuration of a silk fibroin (SF) core and a silk sericin (SS) sheath that envelopes the former. Historically, the use of silk in biomedical applications dates back to the Greek and Roman civilizations who bundled up spider silk fibers for wound treatment[411]. Nowadays, the use of silk as a high-tech fiber is widespread in clinical practice, and plays a pivotal role in suturing[412], plastic and internal surgery[413]. From its early use to the current applications, a myriad of approaches have been proposed to extract the highest potential out of this natural material. Reverse engineering silk – which consists in separating the SF from the SS fractions – has been claimed as an attractive strategy to fabricate SF films, foams, fibers and meshes. Using porous SF materials has been particularly attractive in wound healing[414] due to suitable cell attachment and migration both *in vitro*[415] and *in vivo*[416]. Silk-based wound dressing materials have, to the best of our knowledge, been solely built from degummed (SS-free) silk. Silk sericin's largely accepted immunogenic role has limited the development of SS-containing silk materials for biomedical applications.[417] This shortcoming has been, however, challenged over the past decade with a growing body of work both in academic and clinical contexts[418–422] where the potential of SS has been emphasized. Combining recent knowledge on SS with the widely explored solution processing routes to fabricate SF materials[423] opens an interesting pathway to redesign silk biomaterials based on their native composition and topology.

Similarly to bone, skin or wood, silk's extraordinary macroscopic performance correlates positively with the mesoscopic hierarchical structure of its respective fibers, as recently pointed out by Qiu *et al.*[424]. According to these authors five levels of structural hierarchy may be identified in silk: (level 1) amino acid sequence within the protein molecules; (level 2) secondary structure (regular hydrogen bonding pattern between the amine and carboxyl groups yielding α-helices, β-sheets and β-turns); (level 3) intermolecular β-crystallites; (level 4) molecular β-crystal network (nanofibrils[425]), in which amorphous chains bond the β-crystallites together along a nano-fishnet topology; and (level 5) nanofibrils network (multi-domain system). It has been argued that the outstanding mechanical properties of silk materials originate from the nano-fishnet topology structure of the β-crystallites in the molecular-scale crystal networks, and from the strong friction among nanofibrils in the mesoscopic nanofibrils network[424].

As discussed in Chapter 1, ice-templating (also known as freeze casting) has evolved from a ceramics-oriented process devoted to the fabrication of lightweight materials to one of the most promising routes to fabricate aligned macroporous biomaterials from biopolymer solutions[8,13,301,313,315,426]. Ice-templating of SF has been previously proposed for the fabrication of biocompatible 3D aligned scaffolds for tissue engineering applications[385,427], in particular because of the scaffolds' ability to promote cell contact guiding. However, beyond cell guiding, the aligned macroporous channels generated by ice-templating also configure an effective capillary transport system[301] that could be beneficial for the clearance of exudates between the wound and the patch external surface during healing.

Here we propose an unprecedented approach to fabricate a silk dermal patch with redesigned macroporosity in which the native topological assembly of both proteins is preserved (SS@SF). Such constructs are obtained after a three-step process: *i*. ice-templating of aqueous SF solution, ensuring a controlled macroporous structure; *ii*. methanol (MeOH)-induced enhancement of the β-sheet domain content of SF, and *iii*. coating of SF with a SS sheath to yield a reconstructed 3D silk material. The SS@SF core-shell system obtained represents a suitable 3D cage to encapsulate and deliver Rifamycin, a bactericidal hydrophilic molecule that works by binding to – and inhibiting – the DNA-dependent RNA polymerase[428].

The present SS@SF platform was tested as an antibiotic delivery system under the form of disk patches, an attractive vector for the delivery of topical drugs[429,430]. The fabrication of patches for the topic delivery of antibiotics is of the utmost relevance for the prevention and treatment of many primary cutaneous bacterial infections, but finds particular relevance in the treatment of chronic wounds, such as neuropathic[431], venous[432], pressure[433], and diabetic[434] ulcers, which affect millions of patients each year.

Here, we took advantage of the methanol (MeOH) stabilization step to load silk fibroin (SF) foams with rifamycin before achieving a subsequent coating with silk sericin sheath (SS). Resulting SS@SF foams show superhydrophobicity comparable to methanol-processed foams (SF-MeOH). Sericin coating helps to retain more rifamycin and freezing rate for foam fabrication tunes its release kinetics in aqueous solution. Long-term antibacterial activity on agar plate nominates these silk matrices as good candidates for developing antibacterial dermal patches.

2.2 Results and discussion

2.2.1 Porosity control in SF foams

Porosity plays a critical role in the performance of antimicrobial dermal patches. It dictates the material's mechanical and liquid transport properties, two key characteristics in ensuring the patch cohesiveness and its ability to extract exudates from the underneath wound. To address the need to fabricate porous patches with a controlled macroporous texture, we performed uniaxial ice-templating experiments involving different SF solution concentrations and cooling rates. We prepared SF foams from 2.5, 5.0 and 7.5 wt.% SF aqueous solutions at three different cooling rates (1, 10 and 100 °C/min). Samples obtained from 2.5 wt.% SF solutions were too fragile to withstand handling and were subsequently discarded from further studies. Both 5.0 and 7.5 wt.% SF solutions originated foams with lamellar pore section morphology, as evidenced in the Scanning Electron Microscopy (SEM) images obtained from slices cut perpendicular to the ice growth direction (Figure 2.1A). Both SF concentrations yielded comparable pore sizes, as deduced from the wall-to-wall distance (measured from each pore minimum Feret diameter). As discussed elsewhere, for ice templating, polymer concentration usually correlates positively with the mechanical properties of otherwise comparable foams. [301] Producing foams whose pore sections are invariant with the polymer initial concentration allows thus to independently modulate the mechanics of the foams without altering the pore dimensions. In contrast, the impact of the cooling rate on the characteristic pore size was marked. The average pore wall-to-wall distances (smallest axis of each pore section) decreased from 90 to 70 µm ([SF] = 5.0 wt.%) and from 100 to 60 µm ([SF] = 7.5 wt.%) with increasing cooling rate (Figure 2.1B). The full wall-to-wall distance data, obtained by SEM image analysis (N > 180), are plotted next to the boxplots in Figure 2.1B for a detailed account of the dispersion of the measured average distances. These results suggest that it is possible to selectively control the average pore size of biopolymer foams by playing with SF concentration and cooling rate. In this work we have selected the materials obtained from 5.0 wt.% SF aqueous solution for the elaboration of antimicrobial patches.

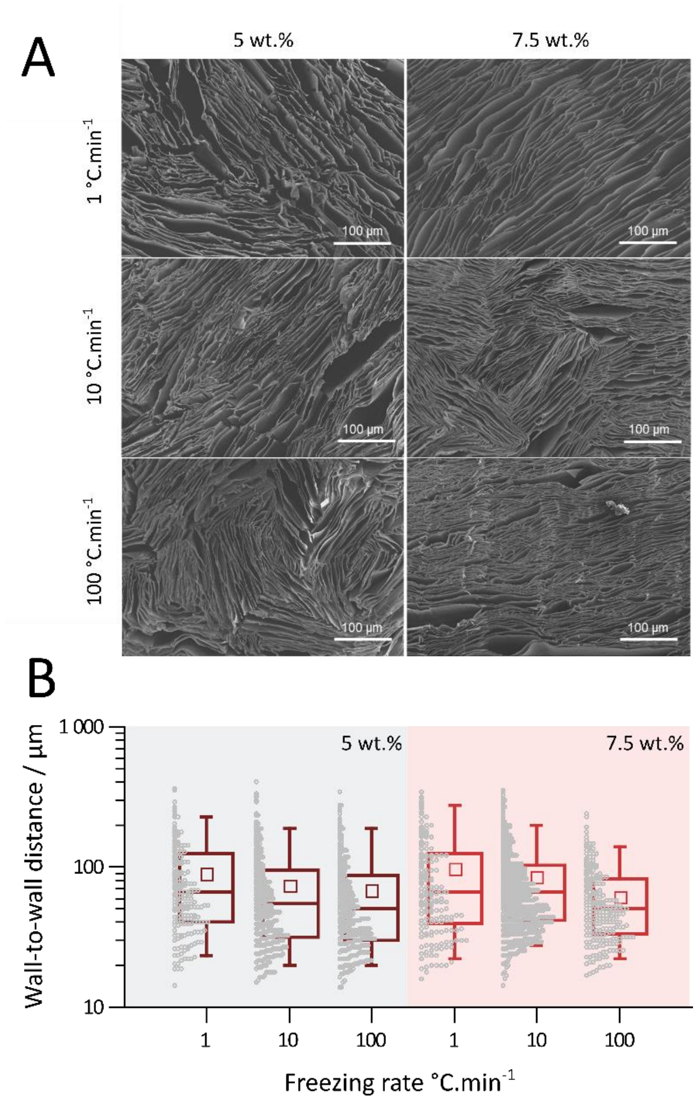

Figure 2.1 The macroporous structure of ice-templated SF foams is defined by the cooling rate. A) SEM images of SF foams obtained via ice-templating of 5.0 and 7.5 wt.% SF aqueous solutions at 1, 10 and 100 °C.min^{-1}. B) Pore wall-to-wall distances determined by analysis of SEM images after thresholding in FIJI software[435]. Boxplots display the 10th, 25th, 50th, 75th and 90th percentiles, and the average values are marked with square symbols. The individual data points measured from image analysis are displayed in grey to the left of the boxplot.

2.2.2 Stabilization of SF foams

Given that the application of antimicrobial patches regards a humid environment, one of the central requirements that needs to be fulfilled by the material is water insolubility. Unlike most biomaterials processing routes, ice-templating is particularly useful to preserve the structural and molecular integrity of biopolymers[13]. This feature, commonly considered an advantage to shape temperature-sensitive systems, also means that the intrinsic properties of SF – such as its water solubility – are not modified during the process.

Owing to the strong hydrogen bonding interactions and hydrophobic nature, β-sheet crystallites favor water insolubility, whereas random coils and α-helices promote water solubility[436–438]. The control of the hydrophilic–lipophilic balance (HLB) in the SF environment, mediated by small molecules, allows fine-tuning the structure of the SF protein, thus enabling to engineer its surface properties[439]. In SF the transformation of random coils into β-sheet structures is facilitated in the presence of MeOH, with HLB = 7.95[440,441].

To induce the formation of β-sheets, SF foams were exposed to MeOH after freeze-drying. The as-prepared materials preserved the macroporous texture, as demonstrated by SEM (Figure 2.2A) where both the pore section aspect ratio and the SF walls' thickness remained unchanged. The formation of additional β-sheet domains was tracked by Fourier Transform Infrared (FTIR) spectroscopy (Figure 2.2B). The intensity maximum of the broad and non-resolved characteristic amide I band at 1643 cm^{-1} indicates a predominance of random coil conformations in the SF foams. Upon MeOH treatment, the intensity maximum shifted to 1625 cm^{-1} and a shoulder emerged at 1699 cm^{-1}. These spectral events reveal the occurrence of β-sheet structures[442,443]. The stability of SF-MeOH in aqueous media was confirmed by the absence of significant redispersion of the foams soaked in water for at least 4 days (data not shown).

2.2.3 Re-designing silk

To promote the formation of a reconstructed 3D silk material, the SF-MeOH foams were coated with a SS envelope to reproduce silk's native composition and topological arrangement (SS@SF). The obtained SS@SF foams retained the macroporous structure defined through the previous ice-templating and MeOH-exposure processing steps, respectively (Figure 2.2A). The higher magnification SEM image (right panel, third row of Figure 2.2A) depicts the foams after SS coating. The walls of the SS@SF foams do not display any noticeable change in terms of thickness when compared to SF-MeOH, suggesting that the SS layer thickness is negligible compared to the SF walls. The characteristic amide I FTIR spectroscopic signature of the β-sheet secondary structure is not significantly modified in SS@SF (1623 and 1699 cm^{-1} events) with respect to SF-MeOH. The co-occurrence of the SS and SF fractions could be further evidenced by confocal microscopy (Figure 2.2C). SF could be directly imaged by Second Harmonic Generation (SHG), whose signal is a characteristic feature of the co-alignement of non-centrosymetric protein secondary structures (α-helices and β-sheets). To ascertain the presence of SS in SS@SF foams, SS was grafted with RITC and subsequently coated onto the surface of SF-MeOH by immersion for 2 hours. The left panel in Figure 2.2C was obtained by exciting SF-MeOH samples under a confocal microscope at λ_{ex} = 880 nm and collecting the emission signal at λ_{em} = 440 nm, corresponding to the frequency doubling characteristic of SHG. In the right panel of Figure 2.2C, SS@SF foam display SHG signal and RITC fluorescence endowed by the SF crystallites and RITC-grafted SS respectively, suggesting a successful coating. The two channels' pixel intensity at each plane correlates positively (SHG signal from the β-sheet domains of SF and fluorescence from the RITC-SS moiety) as determined from the co-localization analysis using FIJI software[435]. Data correlation was analyzed after an automated thresholding of both channels using the Costes algorithm (SHG/SF max. threshold = 34 and RITC-SS max. threshold = 31 for 256 gray levels [444]. Figure 2.2D depicts the two-dimensional correlation heatmap obtained from co-localization analysis. Pearson's correlation coefficient – that ranges between -1 for anticorrelation to 1 for perfect correlation – was equal to 0.55 which may relate to signal intensity difference between the two channels [445]. Manders' tM1 parameter[446] was equal to 0.61, which indicates the high fraction of SF voxels (above threshold) that are colocalized with SS voxels (above threshold). These results show that after automatic thresholding (that eliminates the large number of background voxels) there is an extensive coverage of SF structures by SS.

We further analyzed the hydrophobicity of SF-MeOH and SS@SF foams by water contact angle at the surface of the foams. Both foams show high angle value (~150°) (Figure 2.2E), indicating a superhydrophobic surface. The formation of β-sheet crystallites [447,448] should confer a hydrophobic character to the SF-MeOH foam. Noticeably, despite the extensive coverage detected by co-localization, the hydrophilic SS fraction had no significant influence on the hydrophobicity of the foams. The foams' surface topography that arises from the oriented porosity, seems to play a more pronounced role on superhydrophobicity as described by Wenzel's model[449] than the components' molecular hydrophilic/hydrophobic character. In fact, foams with similar pore size lead to comparable surface hydrophobicity regardless of sericin coating. For an antibacterial patch, the hydrophobicity could prevent bacterial adhesion on the surface and thus reduce the possibility of wound infection from atmosphere.[450]

One aspect that is often disregarded when considering antibacterial dermal patches is that of their deformability under strain. In fact, in order to develop antibacterial dermal patches that display optimal adhesion to the wound, the mechanical solicitation induced by the deformation of skin should be taken into account. We performed a compliance test for both SF-MeOH and SS@SF hydrated foams adhered on the surface of polydimethylsiloxane (PDMS) substrates that were stretched to mimic the stretch ratio of skin (c.a. 20-30% depending on the body area in human skin[451]) (Figure 2.2F). The stretch ratio of the foams was plotted against the PDMS stretch ratio to extract the compliance of the hydrated foams under strain induced by the PDMS substrate. Regardless of freezing rate and sericin-coating, all foams exhibited good compliance when PDMS was stretched to 10%, above which foams exhibited lower stretch ratio than the substrate. When the PDMS was stretched to 25% (close to the normal arm skin surface strain[451]), the foams were stretched by approximately 14%. Although the literature on dermal patches seems to lack the quantification of their ability to accommodate the skin (or a skin model) stretching without detachment, we believe such measure are central to provide an idea of the conditions under which the patches can be applied without mechanical stabilization by adhesives. Although the patches do not deform to the same extent as the skin model beneath, the SF-based patches did not detach when the substrate was stretched up to 30%, suggesting their suitability to accommodate normal mechanical solicitation induced by skin without requiring a supplementary protective layer.

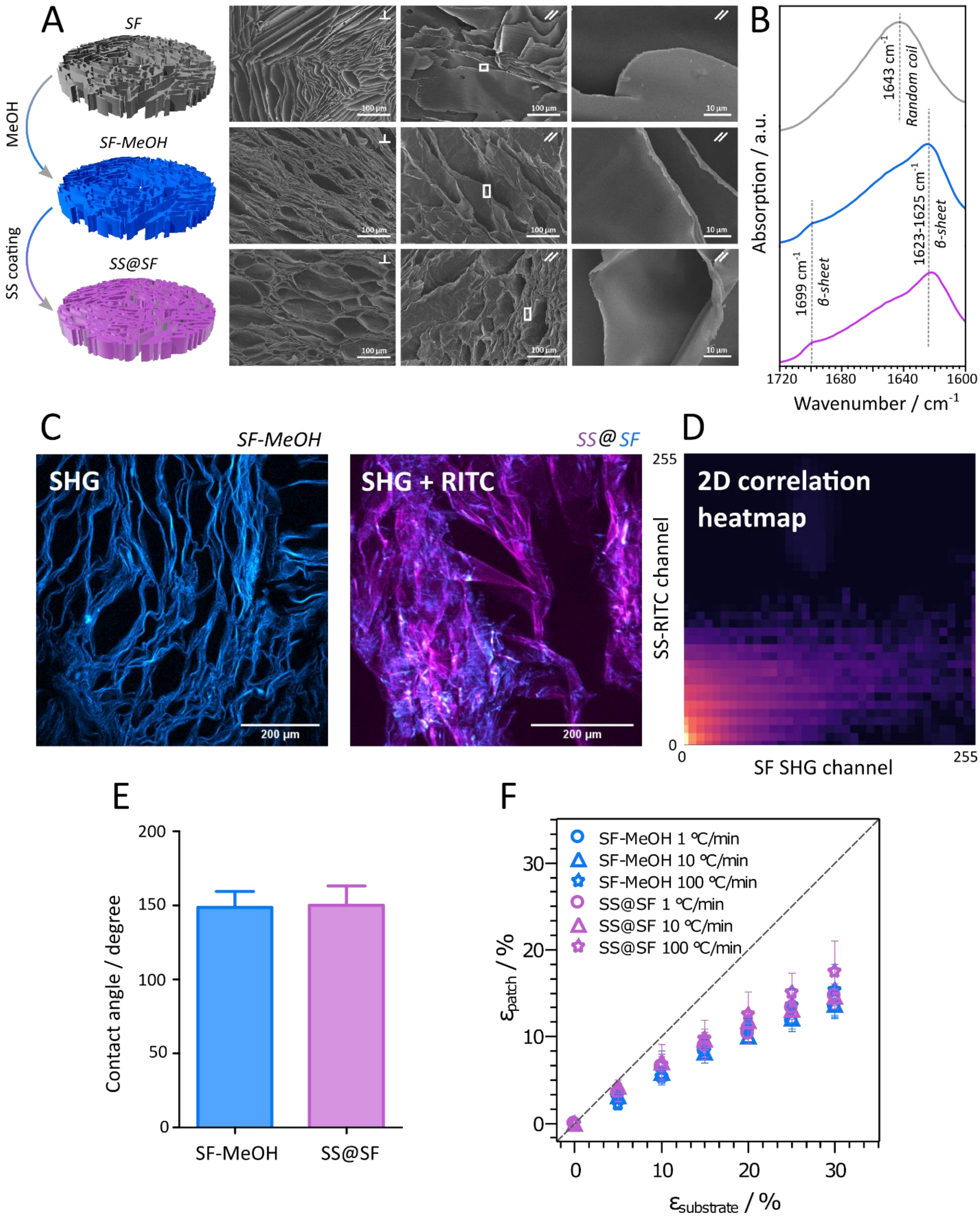

Figure 2.2 The modification of SF foams with SS following a methanol treatment step preserves the macroscopic, superhydrophobic and mechanical properties, while promoting a

major change in the protein’s tertiary structure. A) Scheme of SF-based foams modification process and corresponding SEM images at 5.0 wt.%, obtained at 10 °C.min^{-1}. B) FTIR spectra of amide I band region of SF foams after freeze casting (grey line), after MeOH treatment (blue line) and following SS deposition (violet line). C) Confocal microscopy of SF-MeOH (left panel) and SS@SF (right panel) foams fabricated at 10 °C.min^{-1}. Scale bar, 100 µm. Blue channel was obtained from second harmonic generation (SHG) signal from the β-sheet domains in SF. Violet channel codes for SS grafted with rhodamine isothyocyanate (RITC). D) 2D correlation heatmap between blue (SF) and violet (SS) channel. E) Contact angle of SF-MeOH and SS@SF foams obtained at 10 °C.min^{-1} cooling rate. F) Compliance test of SF-MeOH and SS@SF, fabricated at 1 (circle symbols), 10 (triangle symbols) and 100 °C.min^{-1} (star symbols) cooling rate. Blue and violet symbols represent SF-MeOH and SS@SF, respectively.

2.2.4 Tuning rifamycin release kinetics

To ascertain their applicability as antibacterial patches, SF foams were loaded with Rifamycin (Rif) in dissolved in MeOH (Figure 2.3A). The loading efficiency was *ca*. 1.75 wt.% and did not depend on the freezing rate (Figure 2.3B). After immersion of the foams in an aqueous solution containing SS, the loading dropped to *ca*. 0.5 wt. % and showed a decrease with increasing freezing rate. Foams immersed in a SS-free aqueous solution displayed smaller drug retention (< 0.25 wt. %). This result clearly states the importance of the SS coating as it allows to i) minimize the drug leaching and ii) tune the drug loading according with the freezing rates. It can be hypothesized that the deposition of SS on the surface of SF-MeOH foams minimizes the desorption of Rif during water immersion. Increasing freezing rates – that result in decreased pore wall-to-wall distance (Figure 2.1B) and consequently in higher specific surface area – may require a longer period for full SS coating of the foam’s internal surface, leaving time for drug desorption.

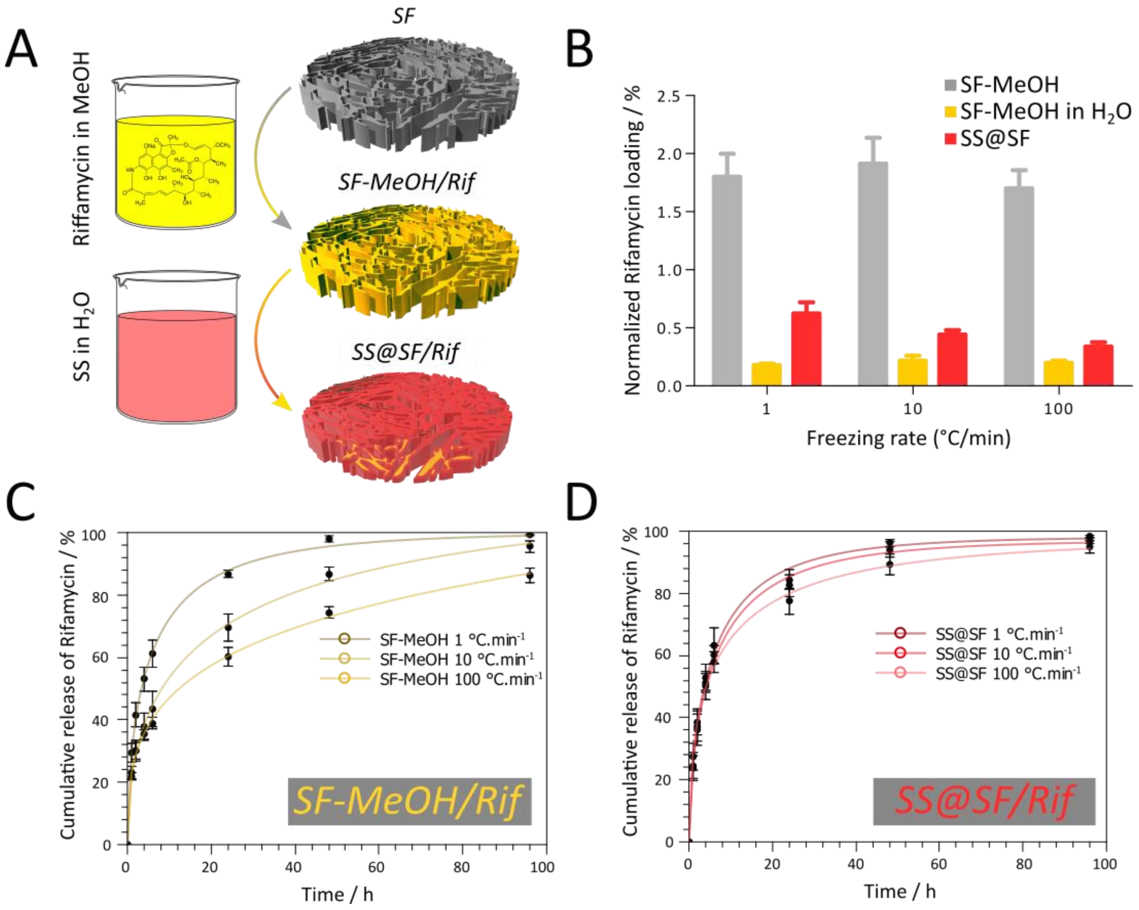

Figure 2.3 Antibiotic release behavior in SF-MeOH and SS@SF foams is dictated by SS coating. A) Rifamycin loading process in SF foam after MeOH treatment and SS coating. B) Initial Rifamycin loading in SF-MeOH (white column), after soaking SF-MeOH 2 h in H_2O (yellow column) and after soaking SS@SF 2 h in SS solution (red column), as function of freezing rate. C, D) Rifamycin release profiles in aqueous media from Rifamycin-loaded SF-MeOH (left panel) and SS@SF (right panel). Release profiles are fitted to the Weibull function. Yellow and red lines represent release from SF-MeOH and SS@SF, respectively. Darker lines correspond to foams prepared at 1 °C.min^{-1}, intermediate lines to 10 °C.min^{-1} and lighter lines to 100 °C.min^{-1}. Lines between experimental data points are exclusively a guide to the eye.

The kinetics of Rif release were studied for both SF-MeOH and SS@SF foams prepared at different freezing rates. All foams kept releasing Rif for 96 hours. The release profile showed a typical three-stage release profile: i) a burst release at the beginning, ii) a slower stage in the middle and iii) a plateau at the end. Given the similar Rif content within the SF-MeOH foams (Figure 2.3B), tuning freezing rate during foam fabrication could regulate the release kinetics in aqueous media (Figure 2.3C). Compared to SF-MeOH foams, SS@SF foams showed faster Rif release kinetics. This effect can be explained by the higher loading of Rif in SS@SF foams that generates a higer gradient between the drug-rich foam core and the solution. The effect of freezing rate on Rif release for SS@SF foams is thus difficult to assess since the loading capacity varies strongly (Figure 2.3D). To gain further insight on the release behavior, we applied three common drug release models (Higuchi, Korsmeyer-Peppas and Weibull model). Fitting curves (Figure S1) and summary of the results (Table 1) suggest that the Weibull model describes the release profile more accurately than the other models considered.

Table 1. Rifamycin release analysis according to Higuchi, Korsmeyer-Peppas and Weibull models

Sample	Freezing rate (°C.min^{-1})	Higuchi model $y = Ax^{0.5} + B$		Korsmeyer-Peppas model $y = Ax^{B} + C$			Weibull model $y = M_0(1 - e^{(-kx)^n})$		
		A	*r²*	*A*	*B*	*r²*	*k*	*n*	*r²*
SF-MeOH	1	9.4 ± 1.8	0.820	39.7 ± 7.8	0.223 ± 0,036	0.969	0.145 ± 0.001	0.547 ± 0.02	0.999
SF-MeOH	10	9.5 ± 1.1	0.931	26.5 ± 3.8	0.295 ± 0.027	0.990	0.039 ± 0.010	0.482 ± 0.03	0.999
SF-MeOH	100	8.13 ± 0.89	0.933	24.3 ± 1.4	0.282 ± 0.011	0.998	0.003 ± 0.005	0.343 ± 0.03	0.999
SS@SF	1	9.5 ± 1.8	0.819	38.2 ± 9.2	0.231 ± 0,044	0.956	0.157 ± 0.017	0.620 ± 0.05	0.997
SS@SF	10	9.4 ± 1.7	0.832	36.5 ± 8.5	0.237 ± 0.043	0.960	0.143 ± 0.014	0.606 ± 0.04	0.998
SS@SF	100	8.8 ± 1.6	0.836	36.6 ± 5.9	0.224 ± 0.030	0.978	0.122 ± 0.020	0.489 ± 0.03	0.998

In this model,

$$y = M_0(1 - e^{(-kx)^n})$$

y corresponds to the cumulative release of the active principle, M_0 corresponds to total amount of drug released, k corresponds to the release rate constant and n corresponds to the structure-related parameter. In all cases, n was less than 0.75, indicating a Fickian diffusion-dominated release from cylindrical pores.[452] Compared to the release from SF-MeOH foams, SS@SF foams exhibited a relatively higher k at a given freezing rate. This faster release constant could be partially due to the higher Rif loading. SF-MeOH foams possessed similar Rif loading, but significantly different release rate with varying fabrication speed. Increasing freezing rate from 1 to 100 °C.min^{-1} reduced release rate k by approximately 50 times. This could be associated to the physical characteristics of matrix, such as porosity and pore size distribution[452,453] as well as with the possible erosion of matrix[454]. The reduced pore section observed for high freezing rate foams is likely to limit the diffusion of Rif out of foams and therefore delay the release kinetics. To explore the role of the protein's dissolution in the drug release, we've conducted protein quantification in the liquid medium for SF-MeOH and SS@SF during 96h. For SS@SF foams, the dissolution of silk proteins during release experiments displayed a similar profile as Rif release (Figure 2.4), indicating its essential role on antibiotic release. In parallel, the similar dissolution of silk fibroin from SF-MeOH foams in water suggests that the limited solubility of MeOH-treated SF determines the total protein in solution rather than the foams' morphology. Altogether, both SS coating and freezing rate played a positive role in improving Rif initial loading within foams. These parameters can thus act as effective lever to modulate indirectly the release profile from SF-based foams.

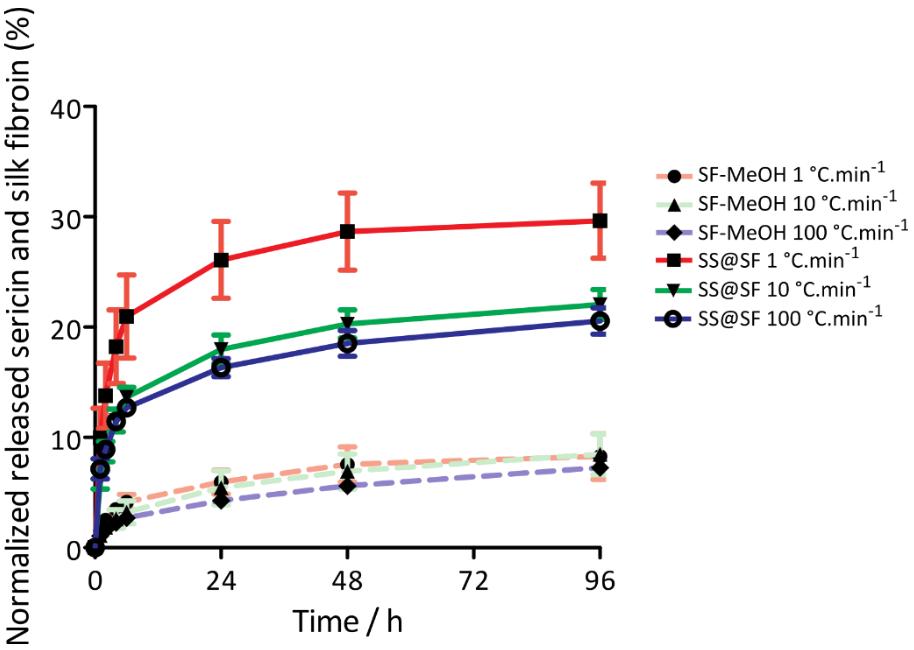

Figure 2.4 Normalized silk protein release during drug release test. Dot lines and solid lines represent SF-MeOH and SS@SF (5 wt.% SF was fabricated at -1/10/100 °C.min^{-1}), respectively. Light red, SF-MeOH (SF was fabricated at -1 °C.min^{-1}); light green, SF-MeOH (SF was fabricated at -10 °C.min^{-1}); light blue, SF-MeOH (SF was fabricated at -100 °C.min^{-1}); red, SS@SF (SF was fabricated at -1 °C.min^{-1}); green, SS@SF (SF was fabricated at -10 °C.min^{-1}); blue, SS@SF (SF was fabricated at -100 °C.min^{-1}).

Finally, we performed Kirby–Bauer test[455] to validate the antibacterial behavior of Rif against *S. aureus* (Figure 2.5). Inhibition zone diameter is the main indicator to describe the antibacterial activity of the materials. In comparison to previous studies in solution, Rif has to diffuse through the agar gel and bacteria growth inhibition requires that antibiotic concentration is larger than its Minimum Inhibitory Concentration (MIC). Thus, the kinetics profiles resulting from the disc method are expected to be delayed compared to spectrophotometric titration of antibiotics released in solution. Moreover, SS@SF foams exhibited a longer duration of Rif release (~ 9 days) compared to the one from SF-MeOH foams (~ 4 days) and increased freezing rate led to lower cumulative inhibition radius and thus less Rif release. Besides, variation of the freezing rate failed to tune Rif release kinetics on solid agar plate for SF-MeOH foams contrary to what was observed in solution. The different Rif release kinetics at varying freezing rate for SS@SF foams should thus be ascribed to the difference of initial Rif loading (Figure 2.2B).

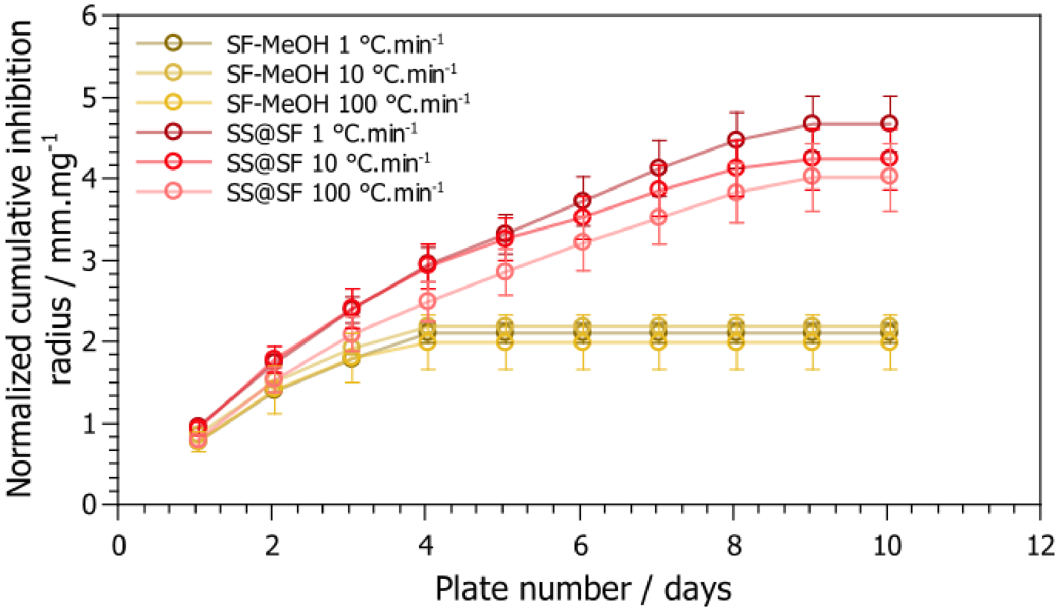

Figure 2.5 Kirby–Bauer test of Rifamycin-loaded SF-MeOH and SS@SF foams (5.0 wt.% SF prepared at 1, 10 and 100 °C.min^{-1}). Cumulative and inhibition zones' radius at each plate. Yellow and red lines represent release from SF-MeOH and SS@SF, respectively. Darker lines correspond to foams prepared at 1 °C.min^{-1}, intermediate lines to 10 °C.min^{-1} and lighter lines to 100 °C.min^{-1}. Lines between experimental data points are exclusively a guide to the eye.

2.2.5 Discussion

Altogether, it is possible to obtain silk fibroin foams with oriented pores whose size decreases with increasing freezing rate. However, after treatment with MeOH – which stabilizes the SF matrix – in the presence of rifamycin, freezing rate has no impact neither on the foam stability in aqueous solution nor on the antibiotic loading. It does impact on the rifamycin release kinetics in solution but not in a solid form, probably because the low initial loading may limit antibiotic accumulation above its MIC. Deposition of a silk sericin coating has no significant impact on the material porosity but allows to improve the short-term retention of rifamycin in water. The resulting loading of the reconstituted silk foams is the highest for the lowest freezing rate, *i.e.* the larger pores, suggesting some influence of sericin diffusion on the coating extent.

Drug release studies in solution showed that the lowest freezing rate also leads to fastest delivery rates for both uncoated and coated foams. However, unexpectedly, release was faster for coated ones. Parallel studies of the protein release from the foams in fact indicated that sericin was also leaching, suggesting that the two processes, *i.e.* coating degradation and antibiotic release were correlated.

Nevertheless, when the antibacterial properties of the foams were evaluated in the solid form, much better performances were obtained for the reconstructed silk foams, which we attribute to the higher initial rifamycin loading compared to fibroin-only samples. It can also be pointed out that, compared to the solution studies, the leaching of the sericin molecules may be slower within the agarose gel environment, allowing the coating to play a protective role over a longer period of time.

In this perspective, it is well-established that, for wound repair, 2 to 10 days are needed for reconstructing connective tissue and new blood vessel networks that are essential for subsequent tissue remodeling.[456] During this period, prevention from bacterial infection is necessary. Assuming that our testing methodology by the disc method is representative of the working environment of antibacterial patches on skin, our reconstructed silk-based antibacterial patches achieved ~9 days’ continuous release of antibiotics, meeting this demand.

2.3 Conclusions

In this work, we have studied the coating of silk fibroin macroporous scaffolds by sericin to reconstruct silk matrices that could act as antibacterial dermal patches. Macroporosity, as generated by freeze-casting, could be tuned by the freezing rate. Treatment of silk fibroin foams with MeOH not only allowed to obtain superhydrophobic materials with suitable compliance in skin-like conditions but also to load rifamycin. Sericin coating allowed for retention of higher antibiotic loading than non-coated foams, resulting in materials exhibiting antibacterial properties in a solid hydrated environment over more than 1 week. These re-designed silk materials have a clear interest as antibacterial dressings for clinical applications but optimization of pore size and organization as well as identification of alternative methodologies to achieve more stable sericin coatings are still necessary.

2.4 Materials and Methods

2.4.1 Preparation of SF aqueous solution.

Preparation and purification of SF was performed according to the protocol published previously.[423] Firstly, *Bombyx mori* cocoons (5.0 g) was cut into small pieces and degummed by boiling them for 30 min in a 0.02 M Na2CO3 (obtained from SIGMA-ALDRICH) solution. After that, the fibers were rinsed several times with distilled water, squeezed out to remove the excess water, and finally dried overnight in a fume hood. Secondly, SF was immersed into 9.3 M LiBr (obtained from SIGMA-ALDRICH) solution (ratio, 1 g: 4 mL) and then incubated at 60 °C for 4 h. 3.5 kDa membrane (obtained from ThermoFisher Scientific) was used in the dialysis of the SF solution during 2 days. The final SF solution was recovered and stored at 4 °C.

2.4.2 Fabrication of SF foam.

2.5, 5.0 and 7.5 wt.% of SF solutions were freeze-casted at 1, 10 and 100 $°C.min^{-1}$ with unidirectional freezing home-made setup[301]. Briefly, 2 mL sample solution was pipetted into a plastic tube disposed onto a temperature-controlled copper rod and a thermal controller was used to precisely control the temperature gradient. After stabilizing for 3 min, the temperature was decreased from 20 to −80 °C at a controlled freezing rate. Once the temperature reached −80 °C, sample was recovered and then freeze-dried (ALPHA 2-4 LD, Bioblock Scientific) for 24 h.

2.4.3 Sericin-coating of SF foam.

Firstly, 100 mL of 10 $mg.mL^{-1}$ silk sericin (SS, obtained from SIGMA-ALDRICH) in carbonate buffer (pH 9.3) was mixed with 1 mL of 1 $mg.mL^{-1}$ rhodamine-B isothiocyanate (RITC, obtained from SIGMA-ALDRICH) in N,N-dimethylformamide (obtained from SIGMA-ALDRICH) overnight. The mixture was then dialyzed to deionized water with 3.5 kDa cutoff membrane (obtained from ThermoFisher Scientific) for two days. Dialysis water was changed every 4 h. RITC-SS was recovered by freeze-drying the dialyzed solution for 24 h.

Prior to SS coating, SF foams (5.0 wt.%, 10 °C.min^{-1}) were immersed in methanol for 2 h and freeze-dried for 2 h, which resulted in SF-MeOH foams. Subsequently, SS coated SF foams (SS@SF) were obtained by immersing for 2h the SF-MeOH foams into 2 wt% SS/RITC-SS aqueous solution and then drying it at 37 °C in an oven for 24 h.

2.4.4 Scanning electronic microscope.

Morphological analysis was performed in a Hitachi S-3400N SEM (Japan) at 10 kV. Scaffolds were cut along and perpendicularly to the main freezing direction and then sputtered with a 10 nm gold layer on the surface in order to improve its conductivity. Image analysis was performed by Image J software.

2.4.5 Confocal microscopy.

SF non-centrosymmetric structures (determined by their SHG signal) and fluorescence signal of RITC-SS coating on SF foams were analyzed on a Leica SP5 upright confocal, multiphoton laser scanning microscope in order to get information about the SS distributions inside the foam. Image processing was performed with Image J software. Co-localisation analysis was performed using the Coloc2 plugin that performs Costes[444] auto-threshold analysis to define the signal-rich voxels in each channel followed by Manders[446] and Pearson analysis[445].

2.4.6 Fourier-transform infrared spectroscopy (FTIR).

SF, SF-MeOH, SS@SF foams were analyzed by FTIR using a PerkinElmer spectrum 400 with attenuated total reflection (ATR) accessories. All spectra were recorded in the 4000 to 400 cm^{-1} range by averaging 4 scans and a resolution of 1 cm^{-1}. The amide I band range (1600-1720 cm^{-1}) was also extracted for the discussion of secondary structures of silk proteins.

2.4.7 Drug release in aqueous solution.

SF foams (5.0 wt.%, at 1, 10 and 100 °C.min^{-1}) were directly immersed into 1 mg.mL^{-1} Rifamycin methanolic solution for 2 h and then freeze-dried for 24 h. Half of the samples were subsequently disposed into H_2O for 2 h and the other half in 2 wt.% SS aqueous solution for 2 h. All foams were then dried in an oven at 37 °C. The dried samples were then disposed into 3 mL of H_2O and the release of Rifamycin and proteins were detected at 445 and 280 nm respectively with a UV-vis spectrometer (UVIKONXL SECOMAM). Three replicates were performed for each condition. The release profile was fitted with three models (Higuchi, Korsmeyer-Peppas, Weibull) in Qtiplot software.

2.4.8 *Kirby–Bauer* disc diffusion test.

5 wt.% SF scaffolds fabricated at 1, 10 and 100 °C.min^{-1} were immersed into 1 mg.mL^{-1} rifamycin methanolic solution for 2 h, freeze-dried, and cut into around 1 mm slices. Half of the samples were put into H_2O and the other half in 2 wt.% SS aqueous solution for 2 h. All samples were dried in an oven at 37 °C. The dried slices were disposed on the surface of agar culture plate pre-cultured with 10^7 cells.mL^{-1} *Staphylococcus aureus*. The plates were incubated at 30 °C for 24 h and then the inhibition zone was measured. The sample disks were then transferred onto a new agar culture plate with pre-cultured bacteria for another 24 h. The inhibition zone at the second day was measured. The same procedures were performed until no inhibition zone appeared, except for the fifth plate since it took five days for transferring to the following plate. Data analysis was performed by Graphpad Prism software.

2.4.9 Contact angle.

Surface properties of SF and SS@SF foams (5.0 wt.%, at 10 °C.min^{-1}) were analyzed using a Drop Shape Analyzer – DSA30 (KRÜSS GmbH, Germany). Foams were firstly fixed with a glass coverslip and then disposed on a movable platform. 2 µl H_2O was pipetted on the surface of the samples and the image was taken immediately after drop stabilization on the surface of the foams. The contact angle was analyzed using DSA4 software. Samples were triplicated.

2.4.10 Compliance test.

SF and SS@SF foams (5.0 wt.%) fabricated at 1, 10 and 100 °C.min^{-1} were cut into disk-shaped pieces with height of approximately 1 mm. The samples were then immersed for 2 h in H_2O and 2% wt.% SS solution, respectively. Subsequently, wet samples were disposed on the surface of a PDMS substrate that was stretched to different ratios (5.0%, 10%, 15%, 20%, 25% and 30%). Relative deformation of the substrate and the sample were measured by video analysis using predefined marks on both the substrate and the sample to infer local strain. Three samples were analyzed for each condition.

Chapter 3

Unveiling cells' local environment during cryopreservation by correlative in situ spatial and thermal analyses

This work is under revision as *Kankan Qin, Corentin Eschenbrenner, Felix Ginot, Dmytro Dedovets, Thibaud Coradin, Sylvain Deville, Francisco M. Fernandes* "Unveiling Cells' Local Environment During Cryopreservation by Correlative In Situ Spatial and Thermal Analyses" in the Journal of Physical Chemistry Letters.

3.1 Introduction

For decades, cryopreservation has been the pivotal strategy in preserving functional living matter for extended periods of time. The ability to overcome the lifespan of individual cells, cell assemblies or tissues has enabled much of the recent advances in fundamental cell biology, cell therapies and tissue engineering[457] along with the clinical breakthroughs in reproductive biology[458], and more generally all cases where the use of immortalized cell lines is not suitable. Cryopreservation is generally attained via two seemingly opposite approaches whose common purpose is to prevent the deleterious effects, direct or not, of water solidification on cells: *vitrification* and *slow freezing* methods.[457] *Vitrification* consists in a liquid-solid transition of water – intra- and extracellular – to an amorphous (vitreous) state by rapidly cooling (up to 10^6 °C.min^{-1})[459] below the glass transition temperature, preventing ice crystallization and thus minimizing cryoinjury.[460] Conversely, *slow freezing* methods, that involve programmed temperature decrease, are nowadays widely applied for cryopreservation of cells and tissues[461,462]. Beyond their technical differences, both *vitrification* and *slow freezing* strategies rely on an entangled set of thermodynamic and kinetic parameters that blur the analysis of the freezing phenomena. In addition, their respective success is determined by the viability and/or vitality of cells and tissues that are frozen in presence of pCPAs such as DMSO which may impose cytotoxic response by cells.[463–466] The challenges in establishing causal effects between the physico-chemical freezing parameters and the biological responses have diverted the main research efforts towards a different direction, *i.e.* formulating new freezing media that maximizes cell viability to the stresses imposed by freezing and thawing.

Strategies to inhibit or minimize ice crystals formation while reducing the harmful effects of most pCPAs (*e.g.* DMSO, glycerol) were proposed by lowering the later concentrations in presence of non-permeating cryoprotectant agents (npCPAs).[467] Also sucrose and trehalose were found to accelerate dehydration of cells by altering intra- and extracellular osmotic pressures, which to some extent reduces the possibility of intracellular ice growth.[468,469] Recently, antifreeze proteins (AFPs) that present ice recrystallization inhibition (IRI) properties have also been applied as freezing media[470], but immunological and toxicological issues are still concerns for their clinical use[471,472]. To circumvent these issues AFP mimics such as Poly(vinyl alcohol) (PVA) have been used for animal cell[473] and bacteria[471] cryopreservation as biocompatible alternatives endued with IRI properties. Complex carbohydrates such as hydroxyethyl starch (HES)[474,475], alginate[476–478] or synthetic polyampholytes[479] have been adopted in the field of cell cryopreservation either with other pCPAs or alone. More radical solutions have also been proposed such as the use of metal-organic frameworks[480] armors around cells to prevent damage by ice crystals or hydroxyapatite nanoparticles[469] as vehicles to promote the internalization of CPAs. In most of the preceding cases, may they be classical solutions such as DMSO or more sophisticated solutions such as AFPs, one question remains open. What is the local composition of the vicinity of cells during freezing?

Here we address that question by using a very simple freezing medium, sodium alginate solution in water, to focus on the cellular environment during the freezing process. We adapted the directional freezing method developed by Dedovets *et al.*[481] to investigate the interaction between suspended *S. cerevisiae* cells and a moving freezing front in presence of a polysaccharide salt solution. These observations are combined with the analysis of the water-sodium alginate phase diagram obtained by Differential Scanning Calorimetry (DSC) to draw a more complete picture of the freezing environment experienced by *S. cerevisiae* cells throughout the freezing process. Directional freezing has been previously applied to observe red blood cells during freezing[482] and to preserve adherent cells[483] as well as ovarian[408], liver[24] and heart[484] tissue in complex pCPA-containing media. In this work directional freezing provides a controlled freezing environment with clearly defined thermal boundary conditions, steady freezing rate, and the ability to investigate *in situ* the interaction between cells and the freezing front. These conditions enable to bridge the kinetic and thermodynamic events occurring during freezing to create a more complete view of *S. cerevisiae* environment prior, during and after interaction with the freezing front. Moreover, we demonstrate that despite the slow freezing approach and the absence of pCPAs, the effective segregation between pure ice crystals, and an increasingly concentrated phase, rich in cells and alginate, leads to a cellular local environment characterized by a vitreous behavior whose predominance correlates positively with yeast viability.

3.2 Results

3.2.1 Thermodynamics of freezing media

Most compounds soluble in water are practically insoluble in hexagonal ice (I_h). This implies that most solutes are segregated from ice crystals during water freezing.[393,485] Under specific conditions, also particles[398] and even cells[399,476,482] in suspension segregated towards the interstitial space defined by the newly formed ice crystals. The consequence of such segregation step is central in cryobiology since it determines the local composition of the cellular environment during freezing, an information that was experimentally unavailable and conceptually overlooked.

Figure 3.1a illustrates the path of an individual cell (in cyan) at two key moments that are defined by the solute concentration changes. To characterize the increasingly concentrated media generated during ice growth a binary phase diagram of sodium alginate in water was established using DSC (Figure 3.1b). The freezing temperature T_f was determined at the onset of the exothermic crystallization peak for polymer volume fractions, ϕ_p ranging from 0.025 to 0.65 in consecutive freezing and heating cycle at 10 °C.min^{-1} (Figure S5). According to Flory's theory, the freezing point of a polymer solution with high polymerization degree (N >>> 1) can be described by equation 3.1,[486]

$$T_f = \frac{1 + \frac{w}{\Delta H}\phi_p^2}{\frac{1}{T^0} - \frac{R}{\Delta H}\left(\ln\left(1-\phi_p\right)+\phi_p\right)} \qquad (eq.3.1)$$

where w is the regular solution interaction parameter in J.mol^{-1}, ΔH is the water melting enthalpy (ΔH = 6007 J.mol^{-1}), ϕ_p is the polymer volume fraction and R is the Boltzman constant in J.K^{-1}. For $\phi > 0.54$ no exothermic peak corresponding to water freezing was detected at -10 °C.min^{-1}, suggesting that for high polymer content compositions no ice crystallization occurred within the detection limit of the DSC. The lack of detectable freezing events is in good agreement with the glass transition temperatures calculated for the ice-alginate system defined by Gordon-Taylor equation[486] (eq. 2),

$$T_g = \frac{T_{gw}\phi_w + kT_{gp}\phi_p}{\phi_w + k\phi_p} \qquad (eq.\ 3.2)$$

Where T_g corresponds to the glass transition temperature for a given composition, T_{gw} = -137.15 °C is the pure ice glass transition temperature, T_{gp} = 120 °C is the polymer glass transition temperature and k is an empirical parameter fixed to 0.5 as discussed elsewhere for other polysaccharide systems[486]. The full phase diagram of the alginate/water binary system is depicted in Figure 3.1b. As reported for similar polysaccharide systems[486], upon cooling at 10 °C.min^{-1}, sodium alginate solutions (s) below $\phi < 0.54$ tend to segregate into a pure ice phase (i) along with an increasingly concentrated solution phase (s). If the mixture is cooled below the temperature defined by the intersection between T_f and T_g then a vitreous (v) or glassy phase is formed whose composition is defined by the same intersection between T_f and T_g.

From another set of DSC experiments we quantified the ice volume fraction ϕ_{ice} from the integral of the ice melting enthalpy in alginate-water binary mixtures. From the values of ϕ_{ice} obtained, we determined the volume fraction of non-frozen water associated with the polymer for each alginate concentration. Figure 3.1c depicts the evolution of the non-frozen water volume fraction (local ϕ_{water}) and alginate volume fraction (local $\phi_{alginate}$) in between ice crystals after freezing different alginate-water binary mixtures from room temperature to -80 °C at 10 °C.min^{-1}. The local composition in between ice crystals was found to be independent of the initial alginate-water composition up to $\phi = 0.6$ (dark grey and magenta data points). Above this alginate volume fraction no ice melting endotherm was detected upon heating the samples from -80 °C to 40 °C, suggesting that no ice crystallization took place during freezing. Under these circumstances all water was considered as non-freezing water (a thorough discussion of the nature of freezable and non-freezable water in presence of polysaccharides is available elsewhere and is beyond the scope of this work[486]). As a consequence, no phase segregation occurred and the local composition of the polymer-rich phase after freezing was similar to the initial mixtures (lighter grey and magenta data points). The intersection between the liquidus curve and the glass transition curves (Figure 3.1b) thus defines the local composition of the segregated phase for $\phi < 0.6$. This critical polymer volume fraction will be referred to hereafter as ϕ_{crit}. For all practical uses in cell cryopreservation, polysaccharide concentrations is lower than ϕ_{crit}. The consequences from a cryopreservation standpoint are important since these data suggests that regardless of the initial concentration of polymer (provided that $\phi < \phi_{crit}$), the composition of the local environment surrounding cells is independent of the initial polymer concentration and is defined solely by the intersection between T_f and T_g.

Since the initial composition of alginate solutions we used in the cell cryopreservation experiments was limited to $\phi = 0.025$ (vertical dotted line in Figure 3.1b), and because the thermal gradient in the directional freezing setup is linear, it is possible to transpose the data from the phase diagram to establish the composition of the cell surroundings from room temperature to -80 °C during freezing. Such an analogy enables to describe both the temperature and composition of the ice/alginate solution/vitreous phase throughout the full freezing process. We thus define two moments that separate different polymer concentration around individual cells during freezing. At t_1 (Figure 3.1a) the cell surroundings evolved from a fixed polysaccharide concentration defined by the initial water-alginate mixture to experience an increase in local polymer concentration until this concentration reached ϕ_{crit} at t_2 (Figure 3.1a). At t_2 alginate concentration in the cells' surrounding became constant and equivalent to the vitreous mixture of alginate and water defined by ϕ_{crit}.

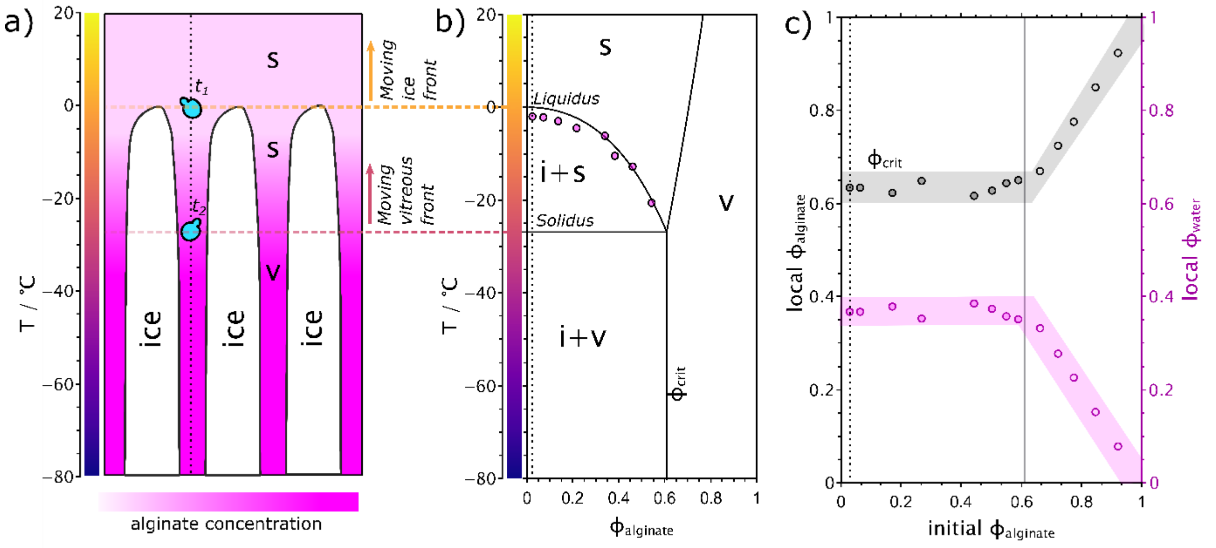

Figure 3.1 Phase segregation of alginate/water solution (*s*) during directional freezing enables controlled phase separation into ice (*i*) and a vitreous phase (*v*). **a**) Diagram of the freezing

profile and phase separation during ice growth. At t_1, cells are brought into contact with the freezing front and enter the interstitial space defined by ice crystals. Between t_1 and t_2 cells experience an increasingly concentrated solution phase that co-exists with ice. When the composition and temperature of the interstitial space attain ϕ_{crit}, defined as the intersection between the liquidus and T_g lines, the cells become entrapped in a vitreous phase. **b**) Phase diagram of alginate/water solution. Magenta points describe the cryoscopic depression of alginate/water mixtures as determined by DSC at 10 °C.min^{-1}. Liquidus curve is defined by equation 2 and theoretical T_g calculated according to Gordon Taylor model is defined by equation 3. **c**) The composition of segregated phase upon freezing according to initial alginate concentration. Non-freezing water contained in the segregated phase, in magenta, is determined by the difference between the total amount of water in the solution and the amount of water determined by the melting enthalpy of the frozen fraction. In black, alginate composition in the segregated phase according to the initial alginate volume fraction.

3.2.2 Local concentration of alginate between ice crystals

It is commonly admitted that each cell type displays optimum viability at a specific freezing rate. The bell-shaped curves that describe cell viability according to freezing rate, have supported this empirical statement and have provided much needed guidance in the definition of the best cryopreservation protocols for different cell types.[487,488] The description of the viability according to the freezing rate is, however, a limited tool in providing insight into the different phenomena occurring during cryopreservation. As shown above, the composition of the interstitial zones, and thus the cellular environment during freezing, depends on the intersection point between T_f and T_g. The liquidus curve describes a purely thermodynamic transition whose characteristic temperature for a given composition is not expected to change with the freezing rate. The glass transition is, on the contrary, strongly dependent on the heating and cooling rates[489]. Faster cooling rates are expected to move T_g to higher temperatures, which changes the intersection point between T_f and T_g and thus impacts on ϕ_{crit}, the composition of the vitreous phase. In the following experiments we have controlled the ice front velocity as a strategy to modulate the freezing rate in the directional freezing setups. To ascertain the impact of ice front velocity on the phase segregation between ice and alginate/water glass during freezing, an alginate solution marked with rhodamine B was frozen under the confocal microscope setup depicted in Figure 3.2a at 10, 20, 30 and 50 µm.s^{-1}. Two dimensional image sequences of the freezing phenomena were acquired and stabilized at the moving front. Figure 3.2b represents a section of a still image used to calculate the volume fraction of ice according to the distance to the ice front for the different ice front velocities. At least ten consecutive images were treated (Figure S6) for each ice front velocity. From the integration of the ice zones (in black) the ice volume fraction as a function of the distance to the ice front was determined. Figure 3.2c describes the progression of the ice volume fraction, ϕ_{ice}, along the x direction according to the ice front velocity. From the moving ice front point towards the cold element, ϕ_{ice} grows rapidly to attain a relatively stable regime at around 400 µm from the ice front. The ice volume fraction at the plateau zone is independent of the ice front velocity for 10 and 20 µm.s^{-1}. As the ice front velocity increases from 20 to 50 µm.s^{-1}, ϕ_{ice} at the plateau decreases from 0.91 to 0.79, respectively. While this difference may seem of little relevance to understand the local environment of cells during freezing, the conversion to local alginate concentration in the interstitial zones is revelatory. In figure 3.2d, for highest ice front velocity (50 µm.s^{-1}), the local alginate concentration evolves from 4 wt.% to attain a stable regime at around 20 wt.%. For the lower ice front velocities (10 and 20 µm.s^{-1}) a mostly linear trend indicates that the local concentration of alginate evolves from 4 wt.% to 40 wt.% within the first 600 µm. The intermediate ice front velocity, 30 µm.s^{-1} yields a mostly linear alginate concentration variation with the distance to the ice front, reaching 26 wt.% at 600 µm. These results clearly indicate that the local environment surrounding cells during directional freezing is largely controlled by the ice front velocity. The difference in alginate concentration profile evidenced in Figure 3.2.d can be further explained by the fact that the lowest temperature available in the confocal setup is -8 °C. At high ice front velocities the T_g is higher and the intersection between the liquidus line and T_g is readily accessible at moderate temperatures such as -8 °C. This leads to reaching a plateau in composition under the confocal microscope as observed for 50 µm.s^{-1}. At lower velocities the intersection between the liquidus line and T_g can only be accessed at lower temperatures, leading the experiment not to attain the steady state regime. While this limitation is present and relevant in the confocal setup it was fully eliminated in the cell freezing setup used later in this work where the cold plate can go as low as -100 °C.

Another aspect that was accessible from the previous data relates to how the variation of alginate concentration occurs with time, for different ice front velocities, from t_1 onwards. Figure 3.2e describes the local alginate concentration increase within the accessible field view under the confocal microscope setup, from the ice front to 600 µm. For low velocities, the concentration increase was progressive but reached high alginate concentration (up to 40 wt.%). At higher ice front velocities the alginate concentration increase was sharper but reached a far more limited local concentration (20 wt.%). Figure 3.2f depicts the initial concentration increase immediately after t_1. The slopes of the linear fits show a marked difference in the initial concentration variation ranging from 1.3 to 7.1 wt%.s^{-1} for 10 and 50 µm.s^{-1}, respectively.

It is thus reasonable to hypothesize that, in directional freezing, the ice front velocity can play two major roles impacting cell behavior. The first is related with the final composition of the vitreous alginate-water phase surrounding the cells that varies from 20 to 40 wt% by solely modifying the ice front velocity from 50 to 10 µm.s^{-1}, respectively. This may account for important variations in cell viability since the hydration of the storage medium will, in the present water-polysaccharide system in the absence of pCPAs, define the osmotic pressure difference between the intra- and extracellular media of the cells after t_2. The second role of the ice front velocity is related with the rate at which the polymer concentration changes from t_1 onwards. Assuming that suspended cells will, prior to interaction with the freezing front, be at osmotic equilibrium with the alginate solution ($\phi = 0.025$, 4 wt%), the ice front velocity determines the rate at which cells will be drawn to an osmotic out-of-equilibrium situation.

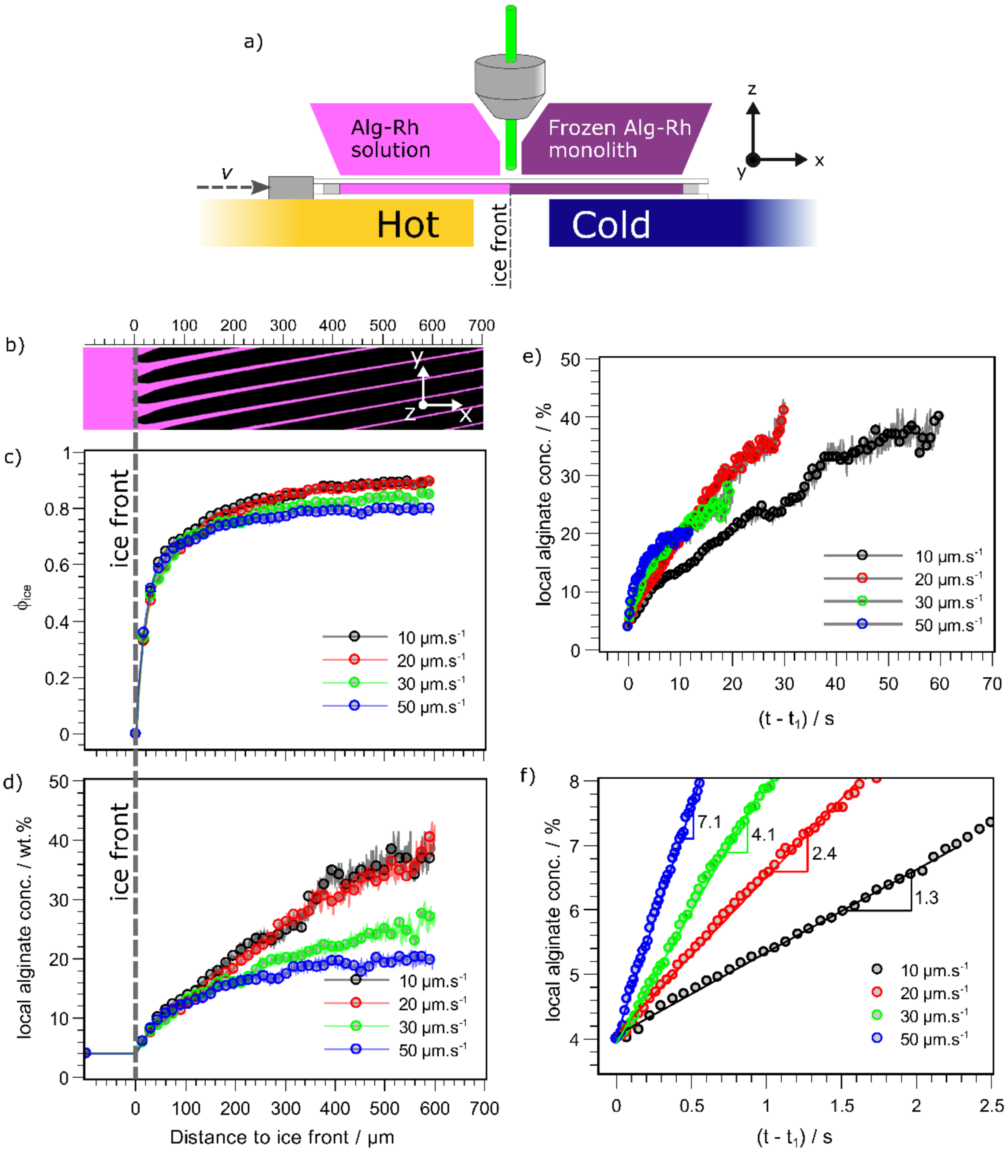

Figure 3.2 The composition of the interstitial space between ice crystals is determined by the linear freezing velocity. **a**) The freezing setup available under the confocal microscope enables to follow the freezing front at different linear velocities ranging from 10 to 50 μm.s^{-1}. **b**) Frame of the freezing front under the confocal microscope. In magenta, rhodamine B-grafted alginate; in black, ice. **c**) Ice volume fraction varies with the distance to the freezing front. Alginate/water segregated volume between ice crystals according to the ice front distance. Data is obtained from the integration of the volμme of ice crystals from the confocal microscopy obtained at 10 μm.s^{-1}, placed above the graph. **d**) Alginate concentration can be calculated as a function of the distance to the freezing front assuming a zero solubility in the ice fraction. e) Local alginate concentration evolution over time after interaction with the ice

front (t_1). f) Initial moments of the alginate concentration evolution over time after interaction with the ice moving front.

The local environment of cells during freezing is determined by a diverse range of conditions that extend beyond the local concentration of polymer, as discussed so far. Another particularly important aspect is the fate of cells during their interaction with the freezing front. As reported previously[476], yeast cells are observed covered in a polysaccharide envelope, regardless of the ice front velocity used in the directional freezing (Figure S7). However, to establish a quantitative relationship between cell viability and ice front velocity we should ensure that the ratio of cells that end up within the interstitial space defined by ice crystals (*i.e*. enveloped in alginate) over those being engulfed directly by ice is independent of the ice front velocity.

3.2.3 Cell viability

To determine the physical environment of suspended *S. cerevisiae* cells during freezing the home-built directional freezing setup[476] (Figure 3.3a) was used to freeze yeast cell suspensions at different ice front velocities. The three dimensional image of the freezing front zone, depicted in Figure 3.3b illustrates how ice crystals (unmarked, white) segregate both alginate solution (marked with Rhodamine B (Rh-Alg), coded in magenta) and *S. cerevisiae* cells (marked with FUN1 dye, coded in cyan) to form domains of 4-6 µm in the y direction (after the ice crystal is fully formed, bottom of the image) separated by ice crystals ranging between 20 and 50 µm in the y direction (see Figure S6). From the 3D rendered image, yeast cells appear covered by a magenta layer (rhodamine B in alginate), indicating the absence of direct contact between the cell wall with ice crystals. This observation was further confirmed by a sequential imaging of cells exposed to an ice front moving at 10 $\mu m.s^{-1}$. Figure 3.3c depicts nine sequential fluorescence 2D images of the freezing front before, during and after the interaction of two suspended cells with the moving freezing front. Two different outcomes were identified: encapsulation in the interstitial space defined by ice crystals (white arrows) and engulfment of the cells in the ice crystals (yellow arrows). The images in Figure 3.3c were chosen due to the co-occurrence of both cases and are not representative of the whole sample. Statistical analysis of the encapsulation efficiency of yeast cells ($n > 200$) by the moving ice front (Figure 3.3d) performed on image sequences obtained at 10 and 50 $\mu m.s^{-1}$

yielded more than 85% of cells were encapsulated in the alginate-rich zones, regardless of the ice front velocity.

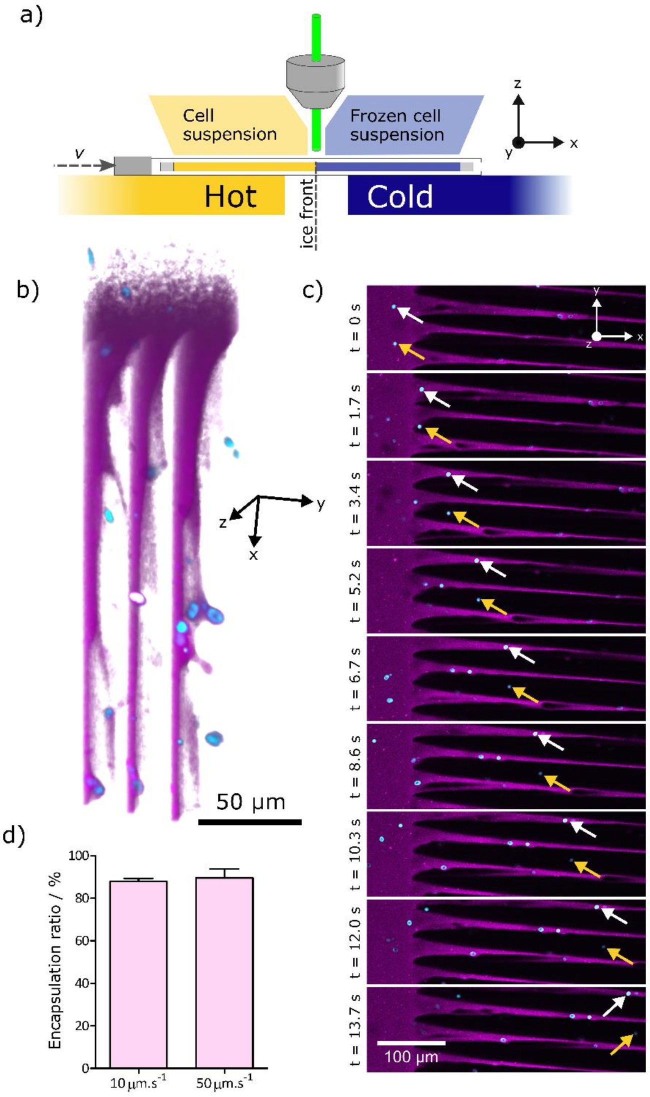

Figure 3.3 *In situ* directional freezing observation using confocal microscopy enables tracking the fate of individual *S. cerevisiae* cells at different ice front velocities. **a**) Directional freezing stage used to freeze cells under the confocal microscope. **b**) Three-dimensional rendered image of the freezing front region of a yeast cell suspension in alginate. Yeast cells (cyan) was stained with FUN1 dye, alginate was stained with Rhodamine B (magenta) and ice was unmarked (same color as background, white). **c**) Sequential 2D fluorescence imaging of the freezing front of yeast cells suspension frozen at 10 µm.s^{-1}. Fluorophore exclusion zones

are occupied by ice (black). **d**) Statistic analysis of encapsulation efficiency for individual yeast cells at 10 and 50 µm.s^{-1} freezing front velocity.

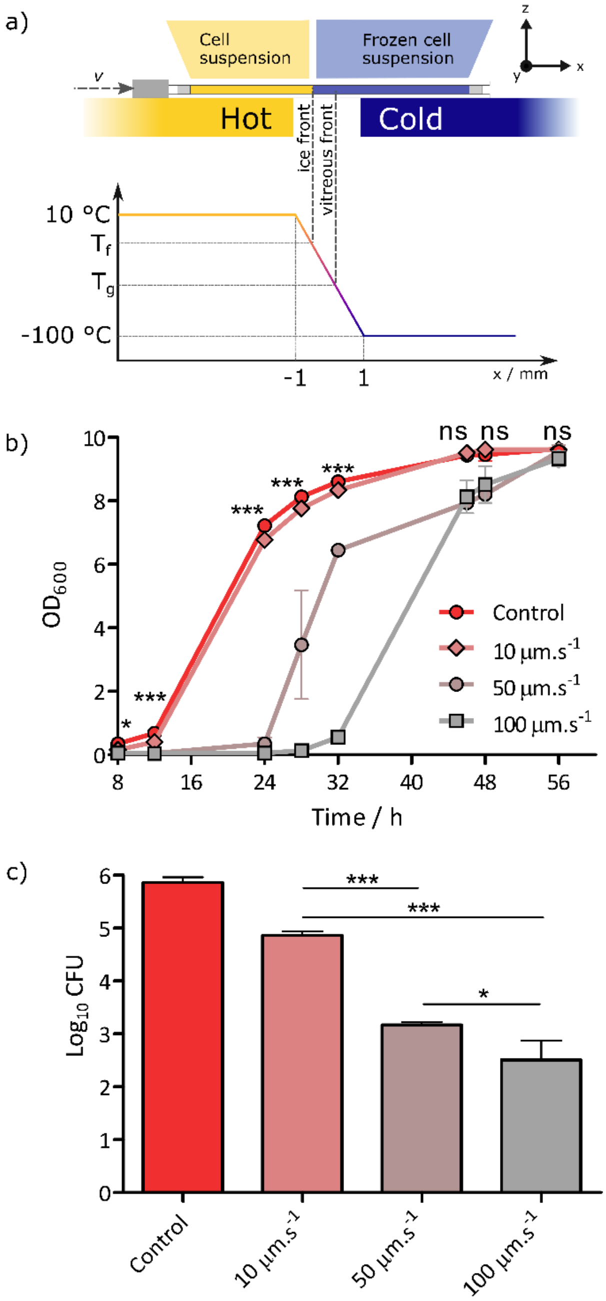

Figure 3.4 Ice front velocity determines yeast viability. **a**) Directional freezing setup used for freezing yeast cells suspended in alginate. **b**) Optical density of yeast suspension after directional freezing, thawing and re-culture in YPD suspension. **c**) Colony forming units of *S. cerevisiae* determined by plate counting performed immediately after thawing.

As shown above, the freezing conditions determine the polymer concentration and the velocity at which this concentration is attained based solely on the velocity of the freezing front. To ascertain if ice front velocity did translate into different cell viability when applied to yeast cell suspensions a dedicated directional freezing setup was built to control the freezing step between well-defined thermal boundary conditions closer to the temperatures relevant in cryopreservation (Figure 3.4a). *S. cerevisiae* cells suspended in alginate solution were placed between glass coverslips separated by a 500 µm spacer and moved from the hot block (T_H = 10 °C) towards the cold block (T_C = -100 °C) at different linear velocities. To ascertain the impact of the ice front velocity on the viability of *S. cerevisiae* cells during freezing, three ice front velocities, 10, 50 and 100 µm.s^{-1}, were used. Experimental data describing the cooling rate according to the ice front velocity is available in the supporting information (Figure S8). The growth curves of yeast cells were obtained in liquid growth conditions after directional freezing followed by controlled quick thawing to 37°C (Figure 3.4b). The viability results support previous findings on the inverse dependency of cell viability with freezing rate.[487,488,490] When frozen at 10 µm.s^{-1} (5 °C.min^{-1}) *S. cerevisiae* cell suspensions ($1.5 \cdot 10^7$ cells.mL^{-1}) display significantly faster growth kinetics than at higher ice front velocities (and freezing rates). Though significantly different from the control up to 32h, the characteristic growth curve of cell suspensions frozen at 10 µm.s^{-1} follow the control growth curve closely. This behavior is also observed for different cell densities ranging from $1.5 \cdot 10^6$ to $1.5 \cdot 10^8$ cells.mL^{-1} (Figure 3.5). As the ice front velocities increased from 10 to 50 and 100 µm.s^{-1} the cells' growth kinetics decreased in a monotonic manner indicating the inverse dependence between cell viability and the physico-chemical conditions determined by the ice front progression. These results were further confirmed by plate counting after a freeze-thawing process (Figure. 3.4c). The colony forming units determined by plate counting also decreased monotonically with ice front velocity.

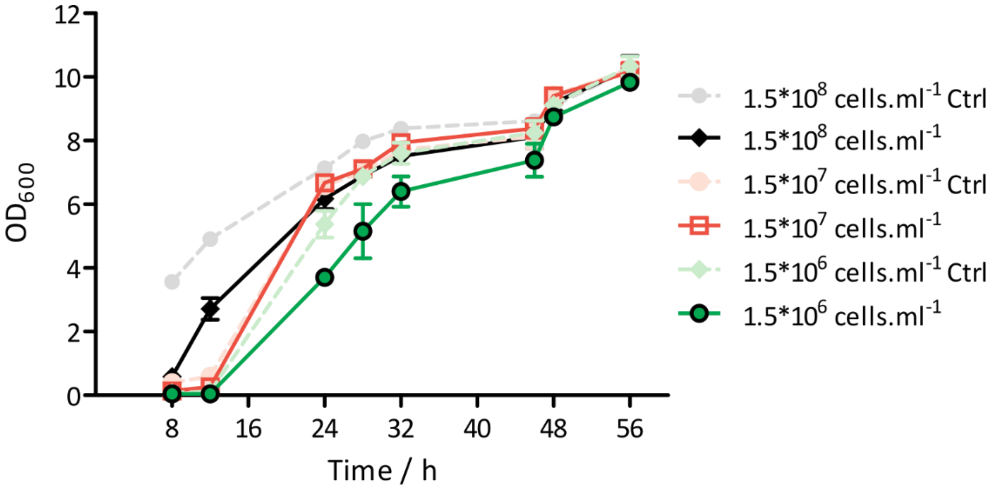

Figure 3.5 *S. cerevisiae* cell growth profiles with different initial cell densities (from $1.5 \cdot 10^6$ to $1.5 \cdot 10^8$ cells.mL^{-1}). Dot and light line, indicating control group without being frozen. Solid and dark line, indicating experimental group after subsequently freezing (10 µm.s^{-1}), thawing and re-culturing.

3.2.4 Membrane integrity and apoptosis

In yeast cells, cell death can be caused by extremely harsh microenvironments or regulated cell death.[491] Apoptosis, one important type of regulated cell death, can be induced by two main factors: 1) exogenous triggers like chemical or physical stresses; 2) endogenous triggers due to lethal signal transduction pathways.[492] Apoptotic markers such as DNA fragmentation, phosphatidylserine externalization and caspases activation, enable characterization of yeast apoptotic behavior.[493,494] Another essential marker of cell death is membrane disintegration. Thus, in order to further understand the reasons behind the limited viability of *Saccharomyces cerevisiae* in freeze-casting conditions, we firstly analyze the membrane integrity by using propidium iodide (PI). PI can bind to double stranded DNA of cells whose membrane is damaged while it remains excluded for cells with intact membrane. We have then detected apoptosis with double staining (PI and Annexin-FITC that binds to phosphatidylserine).

In figure 3.6a, the control (fresh yeast cells) shows higher membrane integrity (approximately 90%) than directionally frozen samples, as expected. However, the extent of membrane integrity loss is not proportional to the ice front velocity. There is a significant decrease of intact cell ratio from 10 to 50 μm.s^{-1}, but this ratio then increases at 100 μm.s^{-1}. Therefore the delayed growth profile and lower cell colony numbers measured at higher ice front velocity (Figure 3.4) found after reculturing frozen and thawed yeast cannot be explained by the disruption of cell membrane integrity alone.

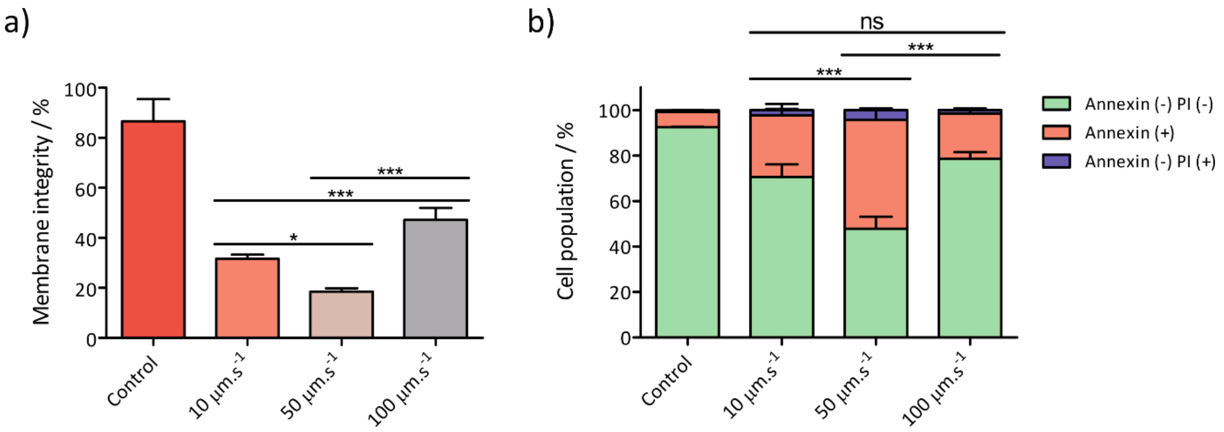

Figure 3.6 Membrane integrity and apoptotic behavior of *S. cerevisiae* depend on ice front velocity. **a**) FACS analysis of membrane integrity (PI staining). **b**) Apoptotic analysis with annexin and PI double staining. * indicates significance ($P<0.05$); *** indicates significance ($P<0.01$); ns indicates no significance.

Apoptosis analysis revealed a similar trend to membrane integrity (Figure 3.6b). In this analysis, annexin (-) PI (-) group indicates living cells, annexin (+) group indicates cells experiencing apoptotic behavior and annexin (-) PI (+) group indicates cells whose membrane disruption is not caused by an apoptotic behavior. Varying ice front velocity from 10 to 50 μm.s^{-1} significantly lows down the ratio of living cell and increases apoptotic cell ratio. Percentage of apoptotic cell for samples frozen at 100 μm.s^{-1} was lower than the one frozen at 50 μm.s^{-1}, while being comparable to samples frozen at 10 μm.s^{-1}. Noticeably, the PI (-) cell groups at varying ice front velocity are all higher than the counterpart in membrane integrity test (Figure 3.6a). This difference could be due to the removal of cells with broken membrane during the cell wall dissolution process that is essential prior to yeast apoptosis experiment.

Another possible reason lies in the relatively long processing time of apoptosis tests (~ 3 h) leading to higher ratio of PI stained yeast cells. In summary, compared to 50 $\mu m.s^{-1}$, cells frozen at 10 $\mu m.s^{-1}$ showed higher membrane integrity, increased ratio of living cells and decreased ratio of apoptotic cells, which is associated with the higher cell viability. However, 100 $\mu m.s^{-1}$ led to similar living cell ratio and even slightly higher ratio of cells with intact membrane, which is insufficient to explain the lower cell viability (Figure 3.4).

3.3 Discussion

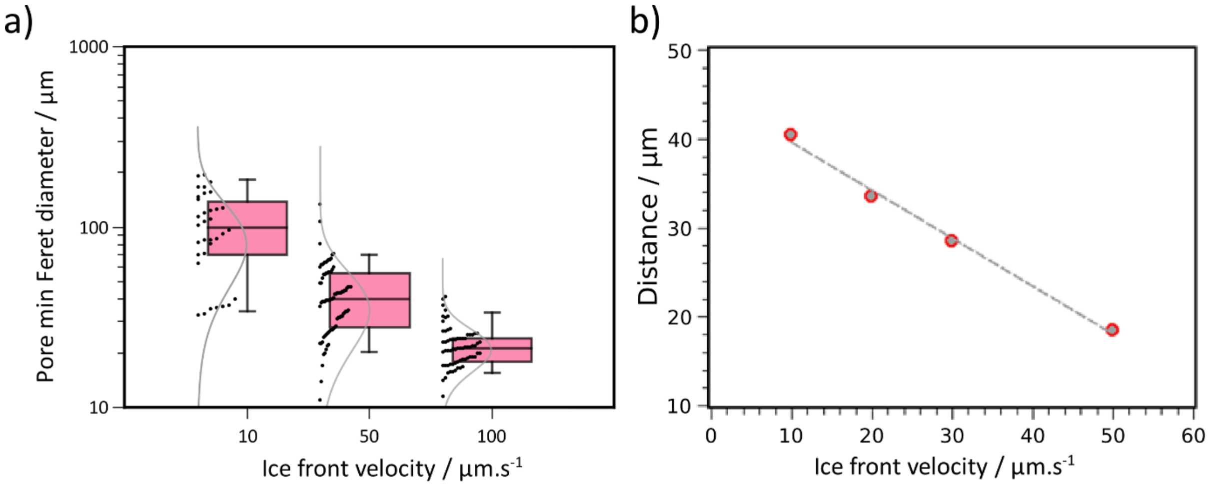

Figure 3.7 a) Minimum Feret diameter of pores performed on binarized images using FIJI software according to SEM images in Figure S3.3. Moustache boxplots depict the median (center), 1st and 3rd quartiles (bottom and top of boxes, respectively) and 10th and 90th percentile of the distribution (lower and superior moustache limits, respectively) for each ice front velocity. Black dots correspond to individual measurements (N>36). Fitting gamma function are juxtaposed with the boxplots and depicted to the left of each box. b) Periodic distances obtained by FFT analysis of confocal image stacks (n > 10) at different ice front velocities.

Establishing a strict causal relationship between yeast viability and the composition of the cell surroundings determined by the ice front velocity is not possible since a wide range of other parameters are simultaneously at play. The pressure formed in between ice crystals during ice templating and its dependence with ice front velocity cannot be discarded. Recent results suggest that the pressure generated during ice templating of a lamellar glycolipid can attain values in the kbar range.[410] Although only two ice front velocities were tested (9 and 15 µm.s^{-1}), the pressure values do stand in the critical range for eukaryotic cells (between 1 and 3 kbar).[495] It is likely that a wider ice front velocity range may translate into significantly different interstitial pressures with repercussions in cell viability. Also the morphology of the ice crystals formed during freezing are markedly different depending on the ice front velocity. The minimum Feret diameter of the macroporous alginate structures observed under SEM after freeze drying (Figure 3.7a) and the periodic distances obtained under the confocal microscope (Figure 3.7b) are relevant measures to describe the wall-to-wall distance of the lamellar pores generated by the growth of ice crystals. The inverse scaling between ice crystals size and ice front velocity observed here is a common behavior described for ice-templating of a variety of systems ranging from biopolymers[301,476] to ceramic slurries[2,343]. While the morphological feature may seem of little relevance to cell viability, the size and distribution of ice crystals within the sample may have significant impact during thawing of the samples, notably on their likelihood to endure recrystallization, a key aspect in cell injury.

Nevertheless, we have here minimized the unknown variables usually associated with cryopreservation by selecting a freezing setup with clearly defined boundary conditions that can be reproduced under a confocal microscope to draw a clearer picture of the cellular environment during freezing. We can therefore unveil, in a detailed manner, how the medium surrounding each cell evolves during freezing and how the ice front velocity determines the composition of the cell environment. Based on the water-alginate phase diagram we introduce the notion of *vitreous moving front* as a key element to understand how the medium concentration evolves over time during freezing. Of especial importance is the impact of the ice front velocity on the evolution of the concentration of the polymer solute surrounding cells. Increasing the ice front velocity led to a lower concentration of alginate within the interstitial space where cells are confined. This evolution could lead to a lower osmotic pressure difference between the extracellular and the intracellular spaces and thus to less osmotic stress. In this regard, fast ice front velocity would seem a favorable condition to maximize cell viability. However, an attentive look at the initial solute concentration rate of change between t_1 and t_2 shows very large variation, up to 7.1 wt%.s^{-1}, at high velocity, whereas this value was as low as 1.7 wt%.s^{-1} for slower ones. We hypothesize that this slow rate of solute concentration change is a central parameter behind the increased viability of cells frozen at 10 µm.s^{-1}. Higher rates may not allow to reach an equilibrium state between the intra- and extracellular osmotic forces, leading to an excess of cytoplasmic water and therefore inefficient inhibition of intracellular ice growth by solute/crowding effects.

However, compared to the result of growth profile and cell viability via cell colony counting, membrane integrity and apoptotic behavior of cryopreserved cells show different profiles at high ice front velocity. After freezing at 10 μm.s^{-1}, cells show higher membrane integrity and express more apoptotic proteins than those at 50 μm.s^{-1}. At 100 μm.s^{-1}, the higher membrane integrity and lower expression of apoptotic proteins could not explain the delayed cell growth profiles and lower cell colony numbers (Figure 3.4b).

In literature, cold environment induces a Viable But Non Culturable (VBNC) state for *Vibrio vulnificu*[496] and *Vibrio cholera*[497,498] bacteria. Although a cold-induced VBNC behavior has not been observed in *S. cerevisiae*, it was reported as a response to other stresses such as SO_2-rich environments[499]. Therefore, we can hypothesize that, rather than temperature, it is the sudden change of alginate concentration at high ice front velocity (Figure 3.2f) during directional freezing that induces VBNC for *S. cerevisiae*. In VBNC state, cells are alive but cannot multiply themselves, and thus show growth rate but high membrane integrity and low amount of cells with apoptotic behavior. Prior to apoptosis analysis, the freezing, thawing and cell wall dissolution steps are necessary, but these steps may exert increased stresses on cells, introducing some artefacts in the measurements. Hence, future works could involve other indexes such as ROS accumulations and DNA degradations[492] with the apoptosis analysis for further unveiling the effect of freezing process on yeast cell behaviors.

3.4 Conclusions

Coupling microscopic observation during directional freezing of cells with the thermal analysis of the freezing medium enabled to characterize the cell local environment during freezing. To the best of our knowledge, describing the composition of the freezing media surrounding cells during freezing has never been accomplished. Here we experimentally quantify the evolution of the concentration of a polysaccharide-based medium during freezing and we establish that its final concentration is independent from its initial concentration in solution below a critical value. We describe the vitreous nature of the polysaccharide surrounding cells as it accumulates in the interstitial space defined by ice crystals. Most transformations in concentration occur between the time points that mediate between the passage of the moving ice front and the moving vitreous front, a concept we introduce for the first time. Due to the eminently kinetic nature of the vitreous transition, we prove that the different composition of the cell surroundings depends on the ice front velocity used during freezing.

These results provide a more detailed insight into the osmotic stress endured by cells during cryopreservation, an information that has remained elusive up to now. Furthermore, the correlative approach developed here should allow to achieve a deeper understanding of the freezing mechanisms of biological materials and provide quantitative data to rationalize cell survival during cryopreservation, an essential step to achieve better freezing protocols in absence of toxic cryoprotectants. Membrane integrity and apoptotic behavior analysis do not show a clear relationship with ice front velocity, which may due to an induction to Viable But Non Culturable (VBNC) state for yeast cells. Given multiple stresses (freezing, thawing and cell wall dissolution), other markers such as ROS accumulations and DNA degradations could be integrated with apoptosis analysis in order to further understand the effect of freezing on yeast cell behaviors.

3.5 Materials and Methods

3.5.1 Differential Scanning Calorimetry (DSC)

DSC was performed to study the thermal behavior of alginate/water mixtures. In a typical experiment, 20 mg of different composition varying from 4 wt.% to 80 wt.% were sealed in aluminum crucibles and left to homogenize for one week at ambient temperature. To analyze the fraction of frozen water, samples were cooled to -80 °C at -10 °C.min^{-1} followed by heating back to room temperature. The ice melt endotherm was analyzed to understand the local composition of composition of the final system. The comparison between ice melting endotherm integration and the amount of introduced water allowed the quantification of the amount of non-freezing water associated with the polymer fraction according with the initial alginate concentration. To describe the cryoscopic depression, samples were cyclically cooled to -80 °C and heated back the temperature corresponding to the middle of the melt endotherm. Upon each cycle the return temperature between heating and cooling ramps was shifted of 0.5 °C towards lower temperatures to overcome supercooling. All DSC analysis were performed in a TA Instruments Q20 DSC instrument coupled with a cooling flange.

3.5.2 Directional freezing under confocal microscopy

The confocal microscopy system designed to inspect the ice front during directional freezing[481] was composed of a temperature controller connected to two independent Peltier elements (ET-127-10-13, Adaptive, purchased from RS Components, France) coupled with a controlled XY stage. The distance between the thermal elements was 2 mm. The freezing process was observed under a Confocal Laser Scanning Platform Leica TCS SP8 (Leica Microsystems SAS, Germany). For the analysis of the polymer fraction, rhodamine B (0.1 mM) was dissolved in 4 wt% alginate solution. The obtained fluorescent solution was injected inside Hele-Shaw cells. The filled Hele-Shaw cell were moved from the hot to the cold Peltier elements (temperature ranged from 12 to -8 °C) by a stepper motor at 10, 20, 30 and 50 μm.s^{-1} linear velocities. The ice crystal and corresponding segregated polymer volume fractions were analyzed with FIJI software[500]. For cell imaging during freezing, *S. cerevisiae* cells (around $1.5\cdot10^{7}$ cells.mL^{-1}) stained with LIVE/DEAD™ Yeast Viability Kit (L7009, ThermoFisher

Scientific) were mixed with alginate solution in presence of Rhodamine B (0.1 mM) for 30 minutes. The samples were then imaged during freezing as they crossed the thermal gradient at 10 and 50 µm.s^{-1}. Image analysis was performed using Fiji software[500]. The encapsulation efficiency of yeast cells (stained by SYTO 9 and propidium iodide (PI), both obtained from Thermo Fisher Scientific) was obtained from counting cells trapped inside of alginate walls or ice column (n > 200).

Confocal image treatment for volume fraction analysis: Image sequences of at least 10 consecutive frames were treated with a 2pixel median filter and rotated so that the ice front was horizontal. A 600*600 Gaussian blur filter was applied to each frame to extract a background intensity mask. Initial images were then divided by the obtained masks. A drift correction was applied using a movie stabilization macro by Nicholas Schneider (available from https://github.com/NMSchneider/fixTranslation-Macro-for-ImageJ/blob/master/NMS_fixTranslation_ver1.ijm) to stabilize the ice moving front. Image sequences were cropped to remove stabilization artifacts at the image edges. All images extended for at least 600 µm below the ice front. Image sequences were subsequently binarized using a Huang threshold between 0 and 39, rotated by 90° and their profile integrated.

3.5.3 Cell culture

10 mg of dry *Saccharomyces cerevisiae* cells (obtained from SIGMA-ALDRICH) were suspended in 1 ml pH 7.2 PBS solution. Subsequently 10 µl of cell suspension were pipetted into 10 ml Yeast Extract Peptone Dextrose (YPD) culture medium. Cell suspensions were then placed in an incubator at 30 °C, 150 rpm for 30 hours. Cells were harvested after centrifugation at 6000 rpm for 10 minutes and resuspended in 0.9 wt.% NaCl solution for the following experiments.

3.5.4 Directional freezing of yeast cells

The setup was composed of two temperature-controlled aluminum plates (12×10×1.5 cm) used as cold (T_C = -100 ± 5 °C) and hot element (T_H = 10 ± 2 °C) and a motor used to slide the samples between both aluminum plates. The cold plate was refrigerated via a copper element plunged into liquid Nitrogen. The hot plate was controlled by a circulating flow of water from a nearby temperature controlled bath. The distance between the two plates was set to 2 mm. Mixture of 4 wt.% alginate sodium salt aqueous solution and yeast cells (final concentration, $1.5 \cdot 10^{7}$ cells.ml^{-1}) was stabilized for 30 minutes at room temperature and injected into a sample holder (a glass coverslip sealed with a 500 µm culture chamber from Thermo Fisher Scientific). Prior to freezing, a stabilization period (30 mins. At T_H) was systematically applied for the samples to attain thermal equilibrium, upon which the samples moved at 10, 50 or 100 µm.s^{-1} from the hot to the cold element. Once the sample was fully frozen and reached the edge of the cold element it was stored at -80 °C for 12 h. The frozen samples were fully thawed in a water bath at 37 °C for 15 seconds. To ascertain cell regrowth after freezing and thawing, 120 µl of each thawed solution was dispersed into 10 ml fresh YPD broth medium and incubated at 30 °C, 150 rpm. Aliquots were drawn at 8, 12, 24, 28, 32, 48, 56 h and optical density at 600 nm was tracked using a UV spectrometer (UVIKONXL SECOMAM). Three replicates were performed for each ice front velocity. Directional freezing was performed at different cell densities, ranging from $1.5 \cdot 10^{6}$ to $1.5 \cdot 10^{8}$ cells.mL^{-1}. The same freezing, sampling and the subsequent OD measurement procedures described above were applied. Three replicates were performed for each cell density.

3.5.5 Cell viability assay

Cell viability assay was performed by plate counting. The frozen samples (*ca.* 300 µL) obtained after directional freezing were taken out from the -80 °C freezer and thawed in a water bath at 37 °C for 15 seconds. Subsequently, 120 µl of the samples were centrifuged at 6000 rpm and resuspended in 200 µl 0.9 wt.% NaCl solution. Samples were diluted to 1/10, 1/100 and 1/1000X. For plate counting, 100 µl of each of the diluted samples were pipetted onto the YPD agar surface (three replicates for each condition) and spreaded with a sterile plastic cell spreader. Agar plates were then put inside an incubator at 30 °C for 24 h and cell colonies were counted by visual inspection.

3.5.6 Flow cytometry

For membrane integrity, 200 µl thawed samples were centrifuged at 6000 rpm for 10 min and resuspended in 300 µl 0.9% NaCl solution. Cells were then stained with propidium iodide (PI, 1 µg/ml) in dark for 10 min at ambient temperature and analyzed with LSRFortessa flow cytometer (from Becton Dickinson). For apoptotic analysis, sample preparation were performed according to the previous published papers[501,502]. Briefly, the thawed and resuspended samples were washed twice in sorbitol buffer and then 120 U lyticase and 23 µl β-Glucuronidase/Arylsulfatase were used to digest yeast cell walls in dark for 2 h at 30 °C. Subsequently, cells were centrifuged and washed twice with binding buffer. 100 µl binding buffer was used to resuspend the cells. 5 µl annexin-FITC (obtained from Thermo Fisher Scientific) and 1 µl PI (500 $\mu g.mL^{-1}$) were incubated with the cell solutions in dark at ambient temperature for 20 min. Finally, flow cytometry analysis was performed with LSRFortessa flow cytometer (from Becton Dickinson) followed by adding extra 200 µl binding buffer.

3.5.7 Scanning Electron Microscope (SEM)

After directional freezing, samples were freeze-dried (ALPHA 2-4 LD, Bioblock Scientific, 0.1 mbar, at condenser temperature -80 °C) for 24 hours. The dried foams were cut perpendicular to the ice front growth direction (revealing the pores' cross section) and parallel to the ice growth direction (revealing the pores' alignment) and fixed to a metal SEM holder using carbon tape. Samples were sputtered with 10 nm gold layer and imaged on a Hitachi S-3400N scanning electron microscope at 10 kV beam acceleration voltage. Subsequent SEM image analysis were performed with FIJI software[500].

3.5.8 Conversion between mass and volume fraction

The conversion between mass and volume fraction assuming a zero volume change of mixing is given below,

$$\emptyset_p = \frac{\rho_w}{\rho_p\left(\frac{1}{x_w^{wt}-1}-1\right)+\rho_w} \qquad (eq.\ 3.3)$$

where x_w^{wt} is the water mass fraction and ρ_w and ρ_p are the water and polymer density, respectively.

Chapter 4

Red blood cell cryopreservation by directional freezing

4.1 Introduction

Long term preservation of cells and tissues outside of their natural environment is extremely challenging. Such limitations are particularly striking when it comes to red blood cells whose relevance in hemorrhage, anemia or other life-threatening conditions is paramount. In USA alone, approximately 57000 blood components per day are clinically transfused and among them red blood cell (RBC) accounts more than 60%.[503] Aside from RBC production from hematopoietic stem cells[504] – which is still not applied as a source of RBC in clinical practice – there is no alternative to dispose of RBC other than to collect blood from healthy donors and store it during its short life span in blood bags (< 49 days).[25] As briefly discussed in the previous chapter, cryopreservation is central to fields such as reproductive medical practice[458,505] and cell and tissue banking[506,507]. It can significantly extend the conservation time of blood products but requires the use of cryoprotection agents such as most commonly used glycerol[508] or even more toxic compounds such as DMSO[509]. Using cryopreservation as a strategy to preserve RBCs is, for the moment, not allowed for civilian medical practice. The potential toxicity effects of cryoprotection agents[409] and the need for complexed deglycerolization process[510,511] are still major concerns hampering the implementation of cryopreservation in clinical practice. Recent results have shown the ability to optimize glycerol-based cryopreservation systems by minimizing the concentration of glycerol[509,512] and by exploring potential substitutes[473,480,513,514] to alleviate or solve the adverse effects of glycerol.

One of such strategies is to mimic those found in nature. Polar fish and plants express antifreeze glycoproteins and antifreeze proteins (AF(G)Ps) to protect themselves from environmental low-temperature damage.[515,516] The reasons lie in the intrinsic property of AFPs, that inhibit ice recrystallization, enabling good cell survival to cryoinjury. Several research groups synthesized and applied those proteins to protect cells during cryopreservation. But the immunological and toxicological issues of AF(G)Ps for the cryopreserved cells still limit their application.[471,472] AFP mimics have proven useful in reducing the toxicity while simultaneously maintain AFP's ice growth inhibition properties. An important example is that of polyvinyl alcohol (PVA) which significantly improves RBC recovery especially when combined with other polymers such as hydroxyethyl starch and synthetic polymer.[473,474,517] Trehalose that naturally protects cells from multiple adversities such as cold, desiccation and osmotic stresses, has been regarded as one biocompatible candidate for RBC protection.[518,519] Co-existence of intra- and extracellular trehalose is essential for its efficient cryoprotective role, but the general absence of endogenous trehalose synthesis pathway and its impermeability through plasma membrane limit its application.[520,521] Researchers found that carriers such as liposomes[522,523] and functional particles[469,514] could increase the intracellular level of trehalose, leading to high recovery of cryopreserved erythrocytes. Besides vectors for the transport of trehalose, other compounds such as Zr-based metal organic framework[480], quantum dots[524], and amino acids[525] have been proposed as cryoprotective agents for RBCs. Albumin, one important component in whole blood, acts not only as a good membrane stabilizer, but also as an antioxidant to eliminate free radicals.[526–529] In 1976, Blank et al.[526] found that albumin could protect spermatozoa by adsorbing onto the surface of plasma membrane. Since then, it has been widely applied to the cryoprotection of sperm.[530–532] Albumin alone or combined with other components also enabled cryoprotection of other cell types, such as nerve cell[533] and RBC[534–537]. The presence of albumin significantly improved recovery of RBCs, but the poor post-transfusion efficiency is still a concern.[536,537]

Commercial cryopreservation protocol for RBCs involves slow freezing in presence of high concentration of glycerol.[538] Vitrification via rapid freezing avoids ice formation during solidification and has been applied for erythrocytes cryo-protection as well but is difficult to implement for practical sample volumes (i.e. beyond the mL range).[480,539] For instance, Liu et al.[539] synthesized trehalose-functional (glyco) peptides to protect cells in liquid nitrogen and achieved final cell survival up to 75%. As one of the slow freezing techniques, directional freezing enabled cell and tissue protection for clinical applications.[21,404,483] Thawed donkey sperm after directional freezing showed high motility ratio and successful pregnancy after artificial insemination.[404] Fifteen years ago, Ishiguro et al.[482] explored RBC behavior during directional freezing and found that glycerol could alleviate mechanical interactions between cells and ice crystals whereas antifreeze proteins acted in an opposite way by modifying ice crystallographic structure. Recently, our group successfully applied directional freezing to cryoprotect *Saccharomyces cerevisiae* in presence of alginate instead of common toxic reagents and simultaneously unveiled local environments surrounding cells during cryopreservation.[540] The survival of yeast cells was proved relative to the thermal behaviors of alginate.

Here, we use bovine serum albumin (BSA) to protect red blood cells during directional freezing. We hypothesize that the introduction of BSA protects cells from being damaged during freezing. Moreover, as Albumin is naturally present in blood, its use as a cryoprotectant should simplify the cell purification procedure prior to clinical usage. Our approach may thus open an interesting pathway to promote the cryopreservation of blood products since the logistic hurdles inherent deglycerolization – such as the use of blood processing setup like COBE® 2991 – could be entirely avoided.

4.2 Results

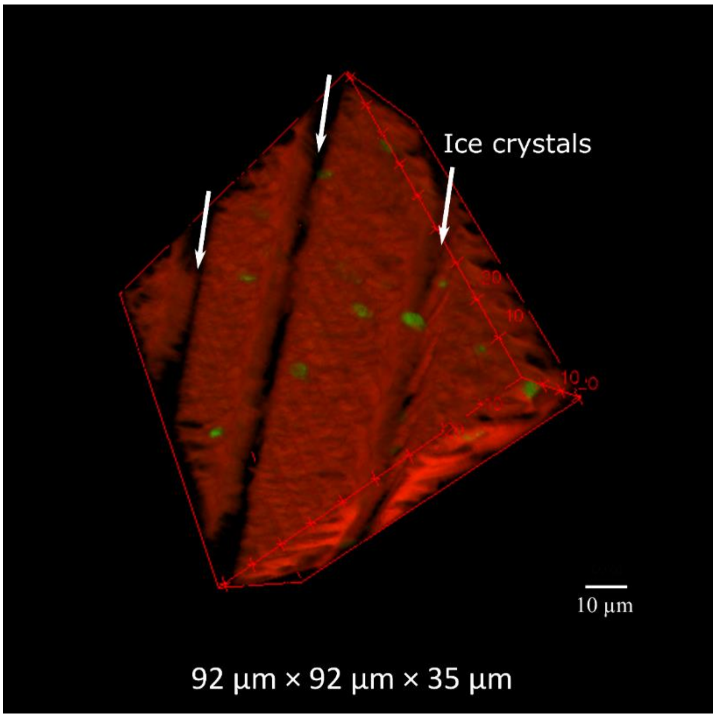

Figure 4.1 Confocal image of BSA (ϕ_{BSA} = 0.28) foams with encapsulated RBCs after directionally freezing (at 100 µm.s^{-1}) and freeze-drying. White arrows, indicate ice crystals; green color, calcein-stained RBCs; red color, rhodamine B/BSA.

Directional freezing can make use of regular ice growth along one direction to encapsulate cells into the ice interstices and has been applied for cryopreservation of sperm[404,406,541] and neuron-like cells[407]. In our previous work, we applied directional freezing to cryopreserve *Saccharomyces cerevisiae* in presence of sole alginate (polysaccharide) without harmful permeating cryoprotectant agents.[540] We unveiled local physico-chemical environment surrounding cells during freezing by coupling DSC and *in situ* microscopic analysis and revealed a relationship between composition of the cells' vicinity and final cell viability. Albumin is a major component of whole blood and has been found beneficial for cell viability during cryopreservation[531,533]. Here, mixtures of RBCs and BSA were directionally frozen at varying ice front velocities. Thermal gradient between cold and hot blocks induced ice formation once sample chamber was moved to the point where the freezing point is. Since cells and polymers are insoluble in ice, they segregate, ending up in the interstitial space[9,476]. The continuous movement of the sample towards the cold block promotes continuous ice crystal growth, leading to two separated phases: ice phase and BSA-rich phase with encapsulated RBCs (Figure 4.1) Directional freezing enabled encapsulation of most RBCs into BSA-rich phase when initial $\phi_{BSA} = 0.28$.

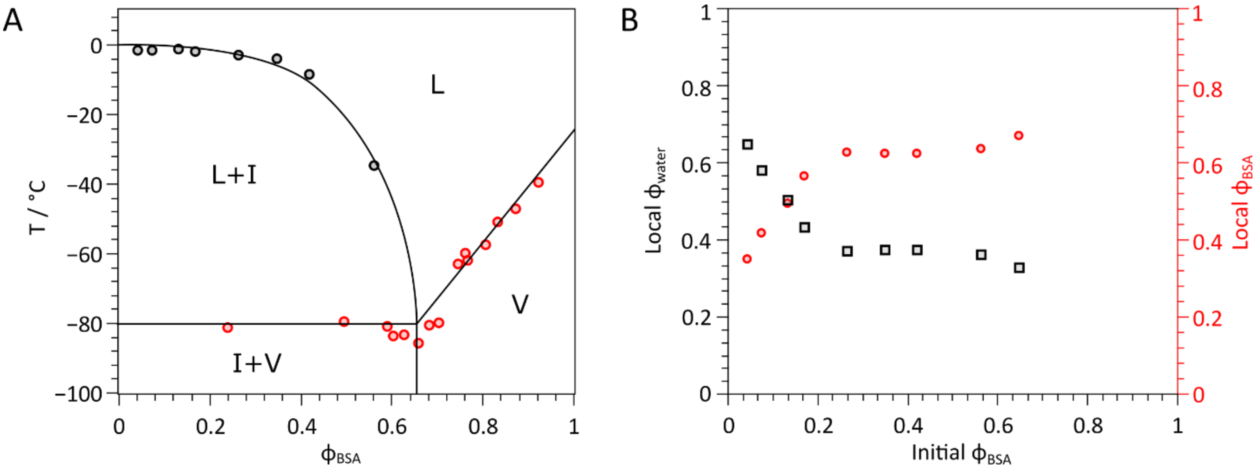

Figure 4.2 Composition diagram of BSA in water obtained from DSC data analysis of crystallization temperature and Tg data from Panagopoulou's work[542] (A) and local BSA-rich phase between ice crystals at varying initial BSA volume fraction (B). For local BSA-rich phase, volume fraction of local water (nonfreezing water) and BSA were calculated.

4.2.1 Behavior of BSA solutions during freezing

As shown previously with alginate, data from Differential Scanning Calorimetry analysis that combines the crystallization behavior of a polymer/water system, together with the Tg, enables to describe the cell environment during freezing. In Figure 4.2A we depict the composition diagram for BSA/water mixtures. The crystallization temperature was determined from consecutive DSC cooling cycles (Figure S9). The return point between the heating and cooling ramps was progressively adjusted to eliminate the supercooling effect on crystallization temperature. Increased initial BSA volume fraction (ϕ_{BSA}) resulted in decreased crystallization temperature as expected. The crystallization temperature firstly stayed stable at around -2 °C when ϕ_{BSA} was below 0.16, and began to decrease to -35 °C with the increase of volume fraction. Above 0.56, crystallization temperature was undetectable, which is consistent with published BSA crystallization profile[542]. Gradually concentrated BSA reduces its crystallization temperature, which may protect cells from being damaged during cryopreservation. Tg according to the BSA-water composition – taken from available data in the literature obtained using the same cooling/heating velocities (10 $°C.min^{-1}$) – completes the composition diagram. The intersection between Tc and Tg is found around $\phi_{BSA} = 0.65$ which indicates the expected composition of the BSA-rich domains at 10 $°C.min^{-1}$. Upon freezing, ice crystals rejected BSA molecules into ice interstices, leading to a BSA-rich phase, in which we further analyzed the local ϕ_{water} (non-freezing water volume fraction) and local ϕ_{BSA}. Increased initial ϕ_{BSA} led to two different profiles for BSA-rich phase (Figure 4.2B). Between 0.04 to 0.27, increased initial ϕ_{BSA} resulted in a dramatic drop of local ϕ_{water} from 0.58 to 0.30, while in parallel local ϕ_{BSA} increased approximately by a factor of two. When the initial ϕ_{BSA} was beyond 0.27, local ϕ_{BSA} reached a plateau, indicating a constant composition of the BSA-rich phase. This plateau is fully consistent with the local composition inferred from the intersection between Tc and Tg. Interestingly, the Tg data for BSA volume fractions beneath the intersection point is constant, further supporting the fixed local concentration of BSA that arises from the phase segregation. Unfortunately, Tg data in the lower BSA volume fraction was unavailable in the literature to explain the initial variation of local composition of the interstitial space described in Figure 4.2B. In the following experiments, we directionally froze RBCs with varied BSA volume fractions from 0.04 to 0.28 that mostly belongs to the decreased local ϕ_{water} profile. Our previous research revealed that local ϕ_{water} in alginate-rich phase has a strong influence on the viability of cryopreserved yeast cell.[540] Thus we hypothesize that the decreased local ϕ_{water} in BSA-rich phase could be an important factor for RBCs cryosurvival.

4.2.2 RBC cryosurvival after directional freezing

Directional freezing of RBCs in presence of BSA was performed based on our previously described platform[540]. Broken red blood cells release hemoglobin that is visibly reddish and easily detected with UV spectrum at 541 nm[469,543]. Increased ϕ_{BSA} resulted in improved cell recovery that was further enhanced at higher ice front velocity. (Figure 4.3) From 0.04 to 0.28, cell recovery was increased from~18% to ~30% at 10 μm s^{-1} while ~38% to ~95% at 100 μm s^{-1}. The positive role of concentrated BSA on cell recovery was further confirmed in figure S10. Among all volume fractions, higher ice front velocity led to improved cell recovery, especially when ϕ_{BSA} = 0.28, approximately by a factor of three when varying ice front velocity from 10 to 100 μm s^{-1}. After thawing and centrifuging, non-lysed RBCs were pelleted at the bottom of the tube and simultaneously hemoglobin was released from broken cells, leading to red color in the supernatant. For negative control, fresh sample showed almost no cell hemolysis as could be seen from the colorless supernatant. Samples processed in other conditions presented red color except for ϕ_{BSA} = 0.28 at 50 and 100 μm s^{-1}, confirming the positive role of highly concentrated BSA systems on RBC recovery.

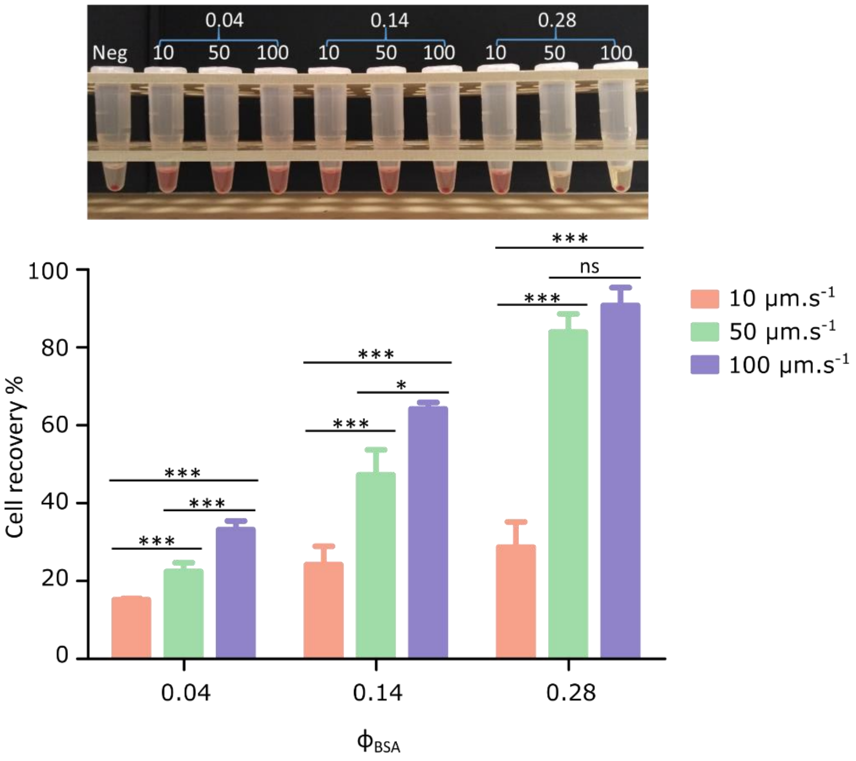

Figure 4.3 RBCs recovery after directional freezing with varying ϕ_{BSA} (0.04, 0.14 and 0.28) at varying ice front velocities. Upper panel: image of centrifuged samples after freeze-thawing process. Red color is due to released hemoglobin from lysed cells. Neg, stand for negative

control, obtained without being frozen. Lower panel: Cell recovery after freezing and thawing.

Cell density used in these experiments (10^8 cells mL^{-1}) was 50 times lower than physiological density (~5×10^9 cells mL^{-1}) in human body. In the literature, cell density was found essential for final cryosurvival.[544] To account for this effect we performed another test with cell density of 5×10^9 cells mL^{-1} at 100 μm s^{-1} (Figure 4.4). Cells frozen with BSA volume fraction of 0.28 showed the highest recovery (~80%), which further confirm the beneficial effects of highly concentrated BSA on cell survival during directional freezing. However, a relatively lower survival compared to samples with 10^8 cells mL^{-1} was observed, that may be ascribed to the increased mechanical stresses between cells.

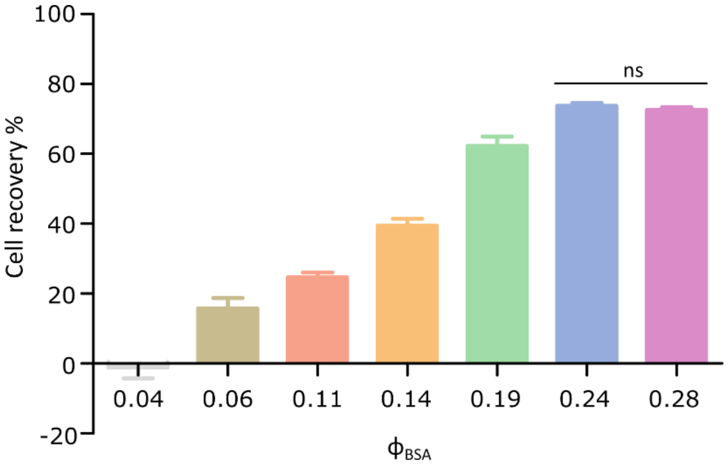

Figure 4.4 Cell recovery when directionally freezing RBCs (5×10^9 cells mL^{-1}) at 100 μm s^{-1}. ns, indicates no significant difference.

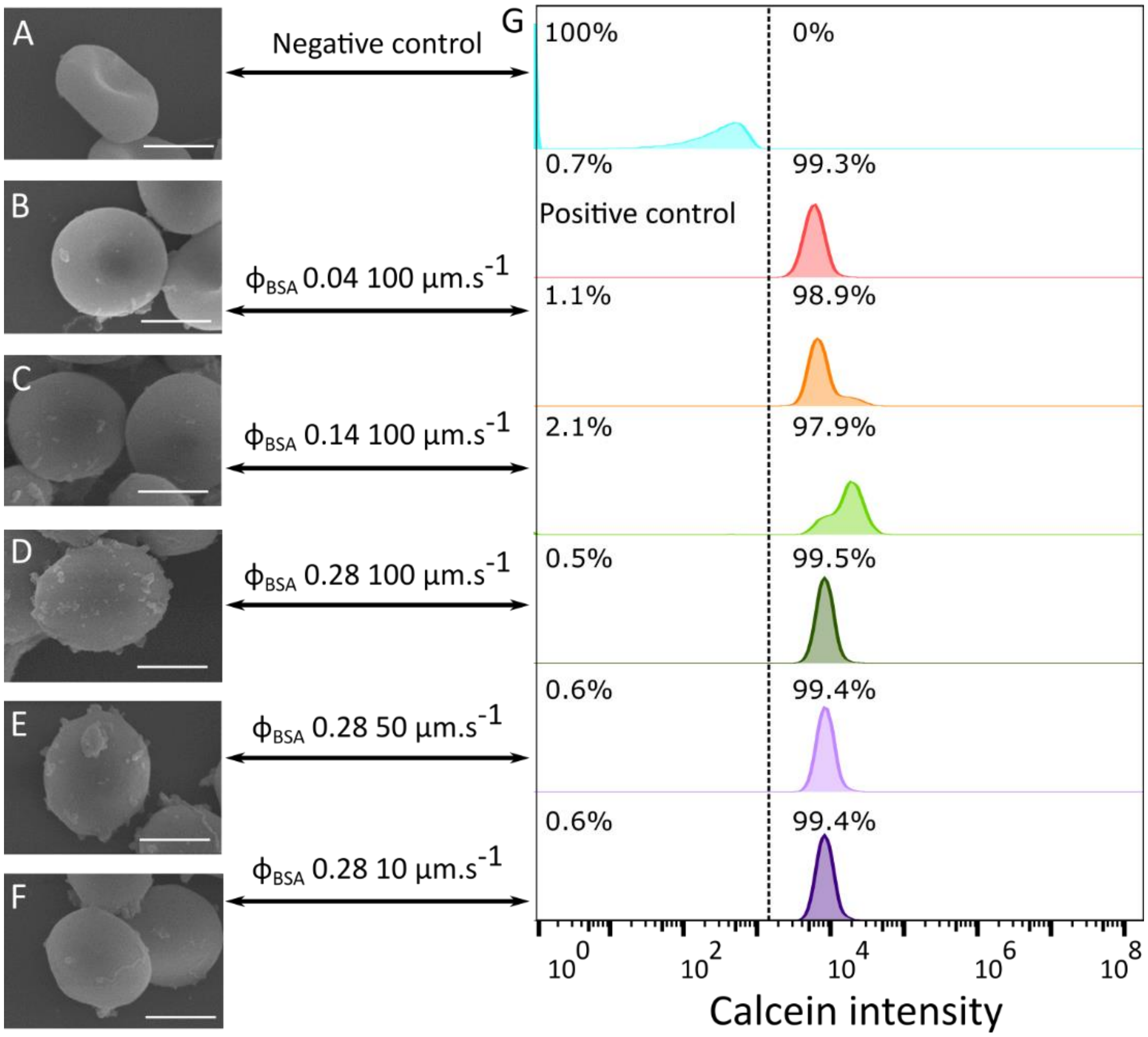

Figure 4.5 SEM and Flow cytometry of RBCs after freezing and thawing. RBCs were stained with Calcein-AM for flow cytometry. Negative and positive control, indicates calcein non-stained and stained cells without experiencing freezing. Varied BSA volume fraction and ice front velocities were applied to experimental groups. Scale bar, 2 µm.

4.2.3 Red blood cell quality

While the previous experiments allowed for determining the amount of RBCs with preserved membrane integrity, it was necessary to gain further insights on the physiological state of recovered cells. For this purpose, SEM and flow cytometry were performed on cells after freezing and thawing. Healthy RBCs displayed biconcave shape that confer them high flexibility and high capacity for oxygen delivery.[545–547] In Figure 4.5A, a majority of fresh RBCs showed biconcave disc shape, as expected. Cells frozen at 100 µm s^{-1} in presence of low fraction of BSA (ϕ_{BSA} = 0.04 and 0.14) exhibited similar shape as fresh samples (Figure 4.5B-C). For high volume fraction groups, a majority of thawed cells shown disc shape in absence of the concave feature, and there were a small part of cells exhibiting a morphological alteration to slightly spherical form (Figure 4.5D and Figure S11). Varying ice front velocity did not significantly alter the shape of RBCs when ϕ_{BSA} = 0.28 (Figure 4.5E-F). Calcein-AM, a non-fluorescent cell-permeant dye that is converted to green-fluorescent calcein by intracellular esterases in living cells[548], was used for flow cytometry test. In figure 4.5G, negative (non-stained fresh cells) and positive (stained fresh cells) control had an apparent separate fluorescence intensity, easier for the gating of experimental group. Regardless of experimental conditions (BSA concentration and ice front velocity), more than 97% cells showed high calcein intensity. That indicates that, after resuspending, most of the recovered RBCs have esterase activity and thus are alive. In other words, the slightly altered RBCs shape does not affect their esterase activity. Forward scatter gating in flow cytometry analysis is commonly regarded as an index of cell size.[549] For experimental groups, thawed RBCs showed similar median cell size compared to positive control, except for those frozen in presence of ϕ_{BSA} = 0.14 (at 100 µm s^{-1}) with slightly smaller size. (Figure 4.6A-B) Considering both cell recovery and quality, more than 95% RBCs exhibited intact membranes with metabolic activities and similar cell size compared to control after being cryopreserved via directional freezing with ϕ_{BSA} = 0.28 at 100 µm s^{-1}.

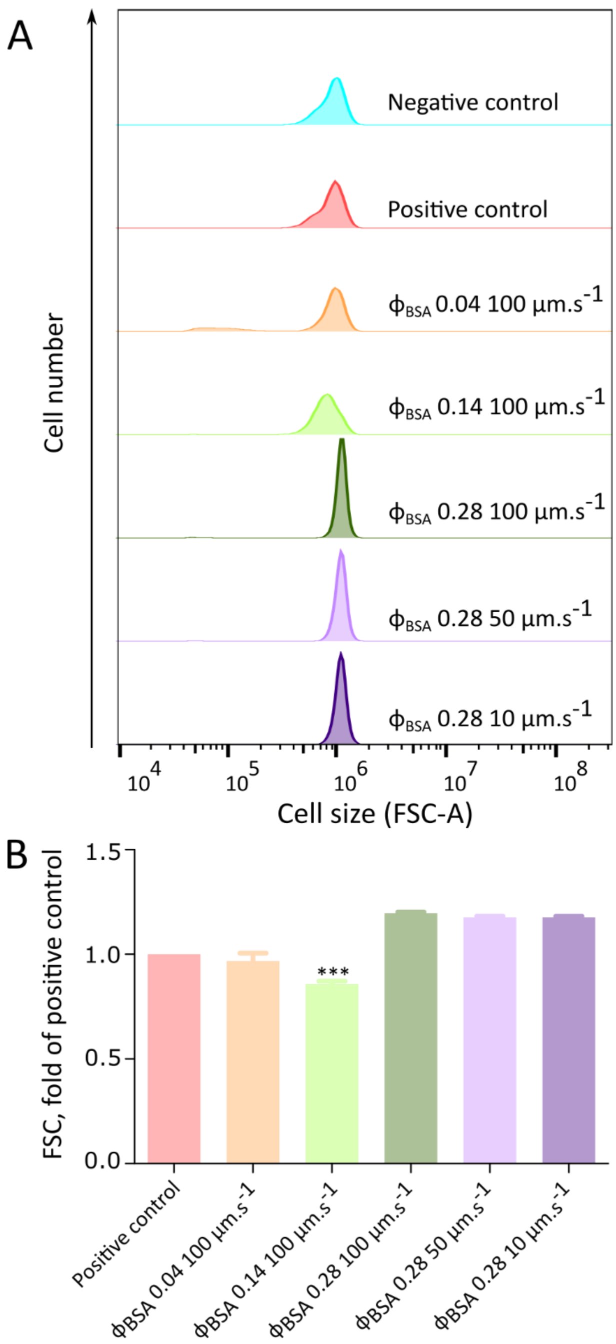

Figure 4.6 (A) Cell size (FSC-A) of Calcein-stained RBCs. (B) Cell size comparison between positive control (fresh cell) and cryopreserved cells. Cells frozen with ϕ_{BSA} 0.14 showed significantly smaller size than fresh cells. ***, indicates $P<0.01$.

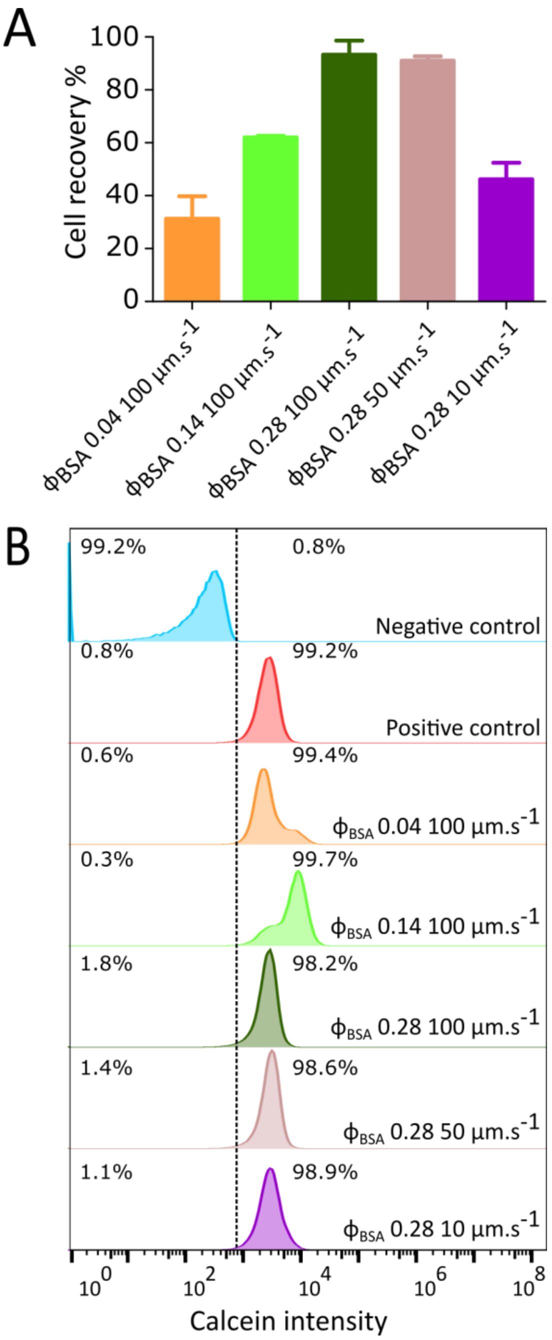

Figure 4.7 Cell recovery (A) and flow cytometry (B) of RBCs after 106 days' storage in freezer.

As described earlier, the limited life span of RBCs even in presence of additives (< 49 days)[550] leads to high demand of daily blood donors. Here, we performed RBC cryopreservation by directional freezing and stored them into -80°C freezer over three months (106 days). In figure 4.7A, cell recovery followed a same survival trend with the one after 1 day’s preservation. RBCs survival could be improved with increased BSA content and further enhanced at higher ice front velocity. After 106 days, the group obtained with a 0.28 volume fraction at 100 μm.s^{-1} showed ~95% survival comparable to the samples thawed after 1 day’s storage. (Figure S12) Further calcein staining (Figure 4.7B) indicated that more than 98% cells presented esterase activity regardless of freezing conditions. Among all the experimental group, size of thawed cells was similar with the positive control except for 0.14 volume fraction group with smaller size. (Figure 4.8) Thus, directional freezing in presence of BSA (ϕ_{BSA} = 0.28) allows a two times longer preservation in freezer without significantly affecting cell viability and vitality than the approved preservation duration of red blood cells (49 days).

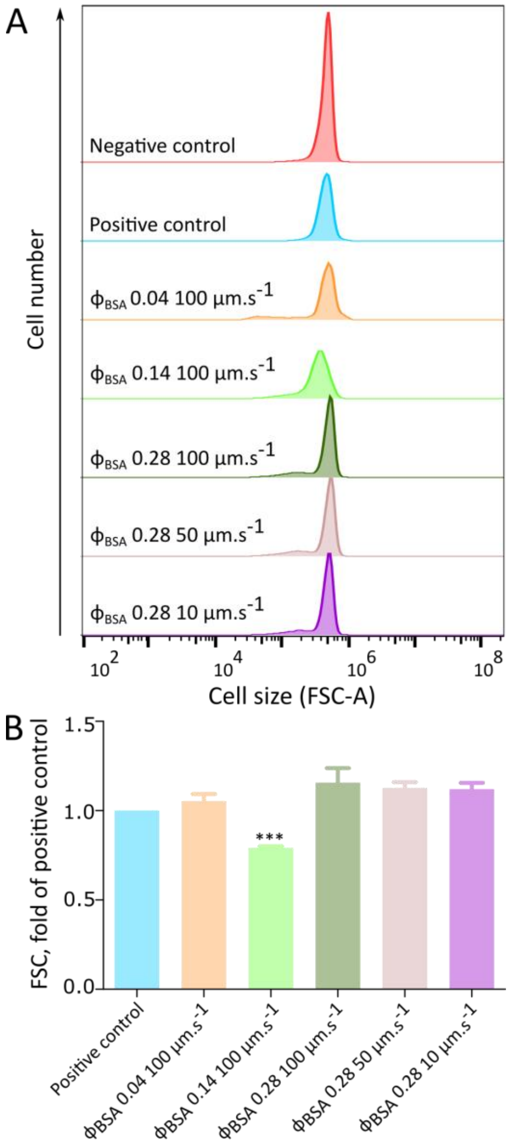

Figure 4.8 (A) Cell size (FSC-A) of Calcein-stained RBCs RBCs after 106 days' preservation in -80°C freezer. (B) Cell size comparison between positive control (fresh cell) and cryopreserved cells. ***, indicates significant difference at P<0.01.

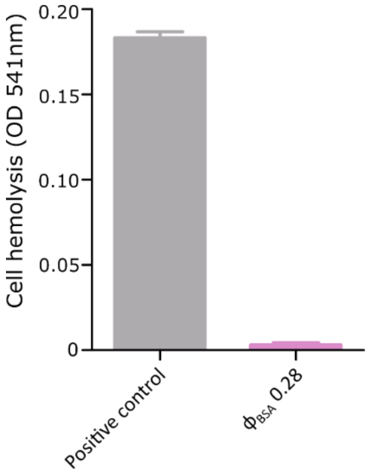

Figure 4.9 Resuspending efficiency of thawed cells followed by freezing at 100 μm.s^{-1}. Positive control, absorbance of hemolysis in deionized H_2O with same amount of cells compared to the one in presence of BSA.

In conventional cryopreservation of RBCs, time-consuming deglycerolization process has harmful effects on final cell quality.[511,551] For the sake of clinical applications, resuspending efficiency of freeze-thawed cells should be taken into account in order to get highly concentrated cell suspension equivalent to physiological cell density. In figure 4.9, almost no hemolysis (absorbance at 541 nm, less than 0.005) occurred after resuspending thawed cells (ϕ_{BSA} = 0.28, at 100 μm s^{-1}) compared to the positive control, i.e. whole hemolysis of RBCs. In other words, the cells could be cryopreserved in a relatively diluted state, but once needed, those cells could be thawed, concentrated and then applied in specific solutions without time-consuming and harmful post-purification of cells.

4.3 Discussion

Correlation between local ϕ_{BSA} in the BSA-rich phase and cell recovery is presented in Figure 4.10, highlighting a positive effect of high local BSA volume fraction on cell recovery. This can be explained considering that high local ϕ_{BSA} causes high osmotic pressure on cells so that more intracellular water tends to diffuse out of cells, decreasing the possibility of cryoinjury due to intracellular ice formation[552]. Sufficient water efflux from RBCs due to exposure to high local BSA content could also reduce the likelihood of intracellular supercooling that was regarded as one main contributor to the intracellular ice formation[553]. Zakharov et al.[554] found via high-resolution synchrotron X-ray diffraction that ice crystals in BSA solution could preserve their crystal size on partial melting, indicating an ice recrystallization inhibition property for BSA. Thus higher amount of BSA (especially when $\phi_{BSA} = 0.28$) may protect cells from being damaged during thawing process.

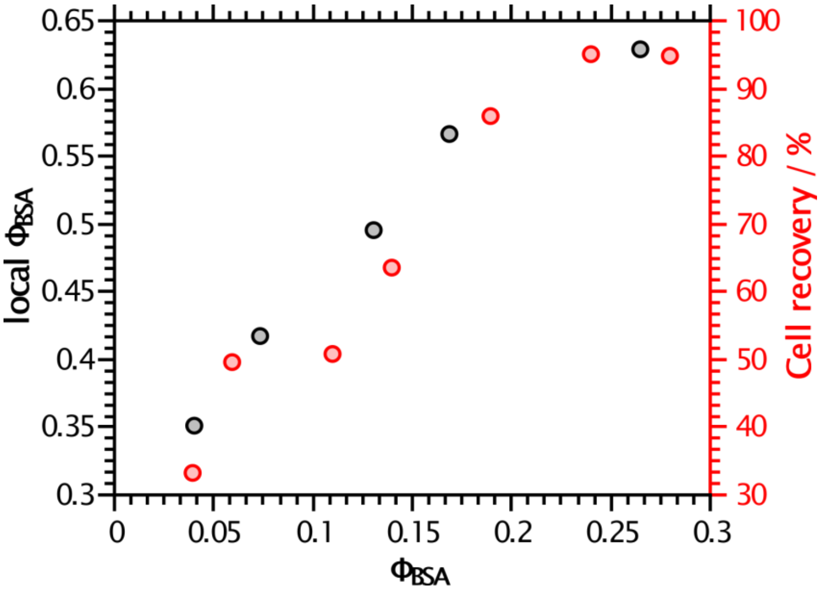

Figure 4.10 Cell recovery during directional freezing vs local ϕ_{BSA} in BSA-rich phase according to DSC analysis. Columns represent cell recovery after thawing and red points indicate local ϕ_{BSA} in BSA-rich phase during freezing.

Highly concentrated BSA is also likely to enhance encapsulation ratio of RBCs due to its high viscosity[540] and may also protect RBCs from the mechanical stresses[482] induced by freezing step since albumin could adsorb onto the surface of cell membranes[526]. Anti-oxidative property of BSA probably play a role in the high cell recovery since other antioxidants have proven useful for enhanced survival of sheep RBCs[555]. Interestingly, varying speed did not significantly change local ϕ_{water} and ϕ_{BSA} in the BSA-rich phase between ice crystals (Figure 4.11), while the increased ice front velocity resulted in improved cell recovery (Figure 4.3). Previous results indicate that increased freezing rate resulted in smaller ice crystals[483], which could probably increase the melting speed during thawing process, leading to less possibility of ice recrystallizations and thus higher cell recovery. Further analysis of *in situ* nonfreezing water state in BSA-rich phase between ice crystals during freezing may help to explain the protection mechanism of BSA during directional freezing.

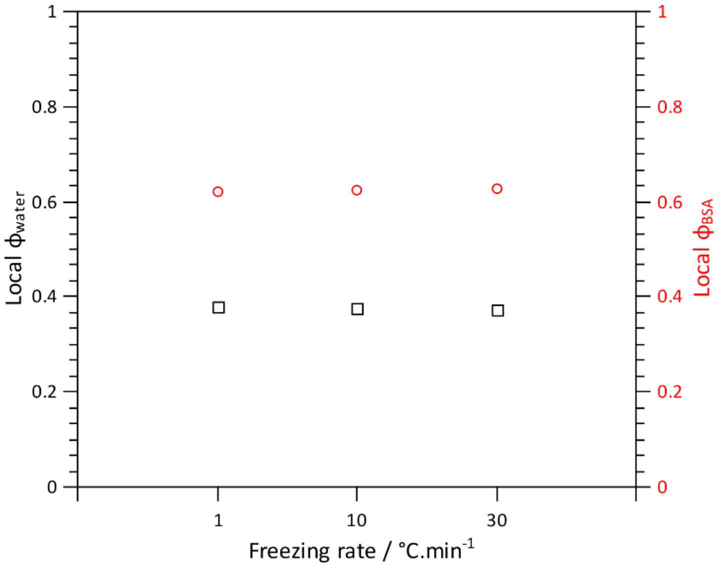

Figure 4.11 Local ϕ_{BSA} and ϕ_{water} in BSA-rich phase after freezing BSA (ϕ_{BSA} = 0.28) at varying freezing rates.

Noticeably, directional freezing process did not change the secondary structure of BSA regardless of freezing conditions as confirmed by circular dichroism. As shown in Figure

4.12, CD analysis shown two peaks at ~208 and ~221 nm, typical for α helix. At varying ice front velocity, BSA showed no significant difference for its secondary structure compared to controls. The peak intensity variations were due to the concentration difference that could be seen from the high-tension voltage spectra.

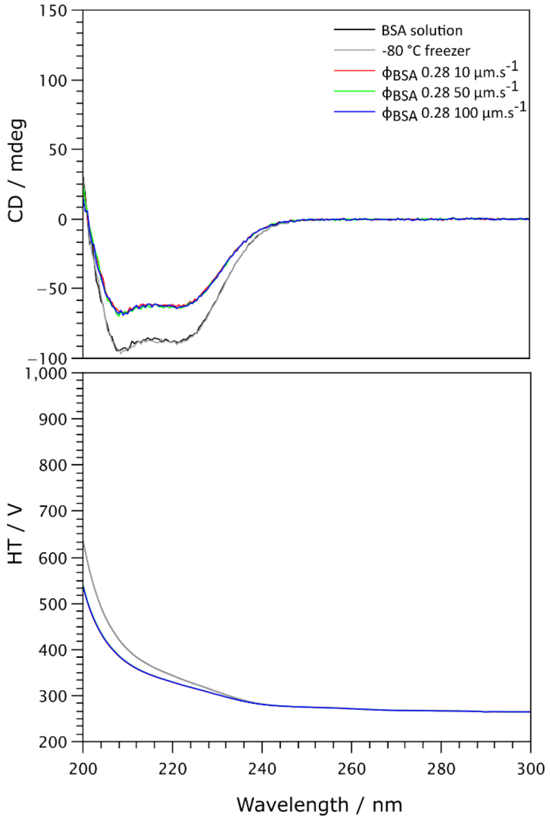

Figure 4.12 CD spectrum of BSA before and after freezing. BSA without experiencing freezing process and with freezing in -80 °C freezer were regarded as controls.

Considering the quality of RBCs, a similar disc-based shape was displayed for both fresh cells and thawed cells experiencing directional freezing in presence of low BSA volume fractions (0.04 and 0.14), while a slightly spherical morphology was observed for cells frozen with high ϕ_{BSA} (0.28). High initial volume fraction led to high local ϕ_{BSA} and thus high dehydration degree for cells. In that case, cells probably need long time to adjust themselves to the normal shape after being thawed, while our immediate preparation of SEM cell samples ceased the recovery process. To alleviate shape alteration, addition of plasma proteins (such as fibrinogen) in suspending medium could be a good option since those proteins could help RBCs retain their normal shape[535,556]. Increasing ice front velocity did not significantly change the cell shape (Figure 4.6), which is likely due to the stable local ϕ_{BSA} at varying freezing speed. It has been previously reported that the morphological alteration of glutaraldehyde-fixed red blood cells do not correlate with cell adenosine triphosphate (ATP) level and 24-h post-transfusion survival.[557] Further metabolic activity analysis based on esterase indicated that more than 95% retained RBCs after freezing and thawing are alive regardless of experimental conditions. Considering viability and quality of RBCs, the 0.28 BSA volume fraction group showed good cryosurvival and led to similar cell size compared to fresh cells. The comparable recovery and viability of thawed RBCs after 1-day and 106-day storage enabled us to extend the preservation time of RBCs from commonly accepted 49 days to 106 days. Given physiological cell density, the low hemolysis rate when resuspending thawed cells provides a simple tool to enrich RBCs for post-transfusion. For the sake of practical applications, RBCs mechanics and functional analysis (such as CD35 expression and intracellular nitric oxide level) will have to be explored.

Compared to previously utilized alginate/water system for yeast cryopreservation[540], BSA/water mixture showed a similar phase diagram and dramatically different compositions for the polymer-rich phase. The polymer content in alginate-rich phase is stable regardless of initial polymer concentrations and can be tuned by varying ice front velocity. However, for BSA-rich phase, increasing initial ϕ_{BSA} resulted in increased local ϕ_{BSA} until around 0.28, followed by a stable BSA concentration profile. Varying ice front velocity did not affect the BSA content within BSA-rich phase. During directional freezing, most cells are encapsulated into polymer phase, thus the composition of polymer-rich phase regulates the physical environment surrounding cells. Correlations between composition of polymer-rich phase and final cell recovery can be established based on directional freezing and polymer thermal analysis during freezing and simultaneously provides useful information for selecting future cryoprotectants.

4.4 Conclusions

In this work, we applied directional freezing in presence of BSA, the major component in whole blood, to cryoprotect red blood cells without addition of harmful cryoprotectant agents. Results show that increasing proportion of BSA results in enhanced cell recovery up to ϕ_{BSA} = 0.28, at which more than 95% cells were kept intact. Although a slight morphological alteration occurred, flow cytometry revealed that thawed cells are metabolically alive and exhibit similar size compared to fresh RBCs. Surprisingly, we found that after 106 days of storage in -80 °C freezer, thawed cells showed survival rates comparable to cells stored for 1day, indicating that our cryopreservation technique via directional freezing offer preservation of RBCs for a two times longer period than approved preservation duration of red blood cells. Furthermore, low hemolysis during resuspension should enable an easier processing step compared to usual cryoprotectant withdrawing prior to clinical usage. Extension to human RBCs and further analysis of the physiological activity of recovered cells are now necessary to assess the full potential of this technology in alleviating the urgent demand of daily blood donor.

4.5 Materials and methods

4.5.1 Cell cryopreservation

Sheep red blood cells (RBCs) stored in 1:1 Alsever's solution (purchased from Alliance Bio Expertise Company, France) were centrifuged at 600 g, 4 °C for 10 mins, then supernatant was replaced with the same volume of 0.9 wt.% sodium chloride solution. The same step was repeated three times. Subsequently, RBCs were diluted into varied bovine serum albumin (BSA, obtained from SIGMA-ALDRICH) volume fractions from 0.04 to 0.28 to get final concentration of 10^8 cells.mL^{-1}. Directional freezing was applied to freeze RBCs as previously described[540]. In brief, mixture of RBCs and BSA was injected into a sample holder which was then moved from a hot plate to a cold plate at different ice front velocities (10/50/100 µm.s^{-1}). Once sample was entirely located onto the cold plate, it was disposed into -80 °C freezer overnight. Besides, several ϕ_{BSA} (0.04, 0.06, 0.11, 0.14, 0.19, 0.24 and 0.28) were applied for RBCs cryopreservation at 100 µm s^{-1}. The next day, the frozen chamber was thawed on a thermostatic plate at 45 °C for ~15s and then 200 µL cell solution was taken out and centrifuged to get the supernatant. 100 µl supernatant was disposed into 96 wells plate for absorbance detection at 541 nm (A_s). Non-frozen cell mixtures were centrifuged and the absorbance of supernatants were detected as A_{sn}. RBCs were diluted into deionized H_2O and freeze-thawed three times for achieving total hemolysis of cells, the supernatant was subsequently detected as positive control (A_p). Negative control was obtained by detecting supernatant of cell mixtures in 0.9 wt.% sodium chloride (A_n).

$$\text{Cell recovery}\ \% = 100 - (\mathrm{As} - \mathrm{Asn})/(\mathrm{Ap} - \mathrm{An}) * 100$$

Physiological cell density (5×10^9 cells.mL^{-1}) was applied with varied BSA volume fractions (0.04, 0.06, 0.11, 0.14, 0.19, 0.24 and 0.28). The same freezing, thawing and detection performed as previously described.

ϕ_{BSA} 0.04 and 0.14 at 100 µm.s^{-1} and ϕ_{BSA} 0.28 at 10/50/100 µm.s^{-1} were applied for directional freezing of RBCs (10^8 cells.mL^{-1}). Subsequently, frozen samples were preserved in -80°C freezer for 106 days. After thawing, cell recovery was detected as previously described.

4.5.2 Cell resuspending efficiency

10^8 cells.mL^{-1} RBCs with ϕ_{BSA} 0.28 were frozen at 100 µm.s^{-1} and thawed with the method used above. Thawed cells were centrifuged and washed once with 1% w/v proline for removing hemoglobin residues and lysed cell fragments. Supernatant of cell solution after resuspending in proline solution was then analyzed with UV at 541 nm in order to obtain the resuspending efficiency after cryopreservation. Positive control was determined from the absorbance of RBCs totally lysed in deionized H_2O.

4.5.3 Flow cytometry

The freeze-thawed RBCs were pipetted into 1.5 mL Eppendorf tube and centrifuged to obtain cell pellets which were then washed three times with 1% w/v L-proline solution (obtained from SIGMA-ALDRICH). RBCs were then stained with 10 µM Calcein-AM (purchased from Thermo-Fisher) at 37 °C for 45 min and analyzed in Flow cytometer (Accuri^{TM} C6, BD Biosciences, USA) with 488 nm laser excitation and 530/30 nm filter. Around 60000 events were processed for each sample. Stained and non-stained fresh cells were regarded as positive and negative control, respectively. FlowJo-V10 software was used for the analysis.

4.5.4 Scanning Electron Microscope (SEM)

Freezing and thawing process were performed according to 4.4.1 section. Thawed cells were then washed for 5 times in 1% proline solution in order to remove BSA residues. 800 µL proline solution was used to resuspend RBCs and 200 µL 5% glutaraldehyde solution was then dropwisely added to the cell solution. The mixture was agitating for 2 h and centrifuged for pelleting RBCs. Subsequently, 50, 60, 70, 80, 90 and 100% ethanol solutions were used to dehydrate cells (10 min each). Finally, one drop of cell solution was pipetted and dried onto a glass coverslip that was attached on a SEM holder using carbon tape. 10 nm golden powder was sputtered on the sample. SEM image was captured on a Hitachi S-3400N scanning electron microscope (10 kV beam acceleration voltage) and image analysis was performed in Fiji software[435].

4.5.5 Differential Scanning Calorimetry (DSC)

Around 15 mg of BSA/water mixture varying from 0.04 to 0.73 volume fraction were sealed in aluminum crucibles. Crystallization temperature detection and nonfreezing water analysis were performed according to our previously published article[540]. Briefly, typical DSC experiment was performed with cooling process from 20 to -80 °C at 10 °C.min^{-1}, followed by heating back to a temperature at which a normal freezing step without supercooling was achieved. To analyze frozen water, ice melt endotherm was calculated from a typical DSC heating cycle from -80 °C to 60 °C. Nonfreezing water fraction could be obtained from the difference between initial water content and frozen water mass. Subsequently, local water and BSA volume fraction could be analyzed for BSA-rich phase between ice crystals. All experiments were performed in a TA Instruments Q20 DSC instrument coupled with a cooling flange. The following analysis was performed in TA Universal Analysis software.

4.5.6 Confocal microscopy

Red blood cells were firstly stained with 10 µM Calcein-AM (purchased from Thermo-Fisher) at 37 °C for 45 min and mixed with BSA (volume fraction 0.04, 0.14 and 0.28) in presence of Rhodamine B (0.1 mM). The same directional freezing procedures were applied to the mixture of RBCs and BSA. Frozen samples were freeze-dried for 24 h in a freeze-drier (ALPHA 2-4 LD, Bioblock Scientific). One piece of dried foam was then disposed on a glass slide, immersed in oil and covered with another coverslip. Another droplet of oil was used for microscope observation under 40× objective. Image capture was performed under a Leica SP5 upright confocal and image analysis was done via Fiji[435].

4.5.7 Circular dichroism (CD) spectrum

The sample cryopreservation protocols were applied to ϕ_{BSA} 0.28 at 10, 50 and 100 µm.s^{-1}. Fresh and thawed BSA solution were then diluted to 0.5 mg.mL^{-1}, spectrum was measured from 195 to 300 nm at room temperature with 1 mm thick quartz cuvettes on a JASCO J810 spectropolarimeter. Accumulation was set for three times. Three replicates were performed for each sample.

General conclusions and perspectives

Controlling the porous architecture of biomaterials is a major lever for optimizing their tissue repair properties. Plenty of options such as 3D printing (for example, stereolithography), porogen-based techniques (like solvent casting/particle leaching, freeze casting, *etc*) and electrospinning are available to achieve this goal. Among them, freeze casting (also called ice templating) has been proved as a good approach for making porous scaffolds as it is amenable to a wide range of materials, does not require the use of high temperature or organic solvent and allows to create macropores with tailored size and orientation. In this context, a first part of this PhD work was devoted to the application of freeze-casting to the re-design of silk matrices and their use as drug delivery systems. However, the very low temperature conditions of this technique make it *a priori* less adapted to cell encapsulation, although cellularized biomaterials are of particular interest in tissue engineering. An important step towards this challenging goal is to understand how the freeze-casting process impact cell viability. This has been the central question addressed in the second part of this thesis, focusing on the encapsulation of *Saccharomyces cerevisiae* yeast cells. This work led us to consider that freeze-casting may also be suited as a cryo-preservation technique, where the porous matrix is not considered as a scaffold but as a temporary storage environment. This approach was initiated in the third part of my PhD, focusing on the cryo-preservation of red blood cells.

For the biomimetic silk matrix, our home-made freeze casting device enabled fabrication of biocompatible silk fibroin foams with different concentrations. The unidirectional growth of ice crystals led to well-aligned pores along the gradient after sublimation. Pore geometry could be tuned by varying cooling rate. The combination of matrix stabilization by methanol and drug-loading procedures resulted in rifamycin-loaded water-insoluble matrices enabling subsequent sericin-coating and slow release of antibiotics. More specifically, the sericin coating played a positive role in improving rifamycin retention within foams, while varying freezing rate tuned its release kinetics, which may be ascribed to the variation of pore wall-to-wall distance. Such reconstituted silk matrices enabled long term release (up to 9 days) of the antibiotics and efficient antibacterial properties against *Staphylococcus aureus*. Combined with their relatively good compliance, the tunable antibiotic release properties in both aqueous and agar plate of these re-designed silk matrices make them good candidates for to develop dermal patches. In future, *in vitro* and *in vivo* tests should be performed with these biocompatible and structure-controllable silk composites to explore this application. From a wider perspective, these results indicate that the intrinsic characteristics of the freeze-casting technique such as low temperature and aqueous processing conditions could enable the fabrication of multi-phasic materials (for instance, polymer-hydroxyapatite composite for bone repair) and the simultaneous incorporation of bioactive molecules, such as growth factors, leading to fabrication of multifunctional porous biomaterials.

Foreseeing applications in cell encapsulation, the physicochemical environments surrounding cells during freezing has been studied by a combination of directional freezing under confocal microscope and differential scanning calorimetry analysis. A model system consisting of the well-characterized polysaccharide alginate and of robust *S. cerevisiae* yeasts was selected. We established phase diagram of alginate based on experimental freezing point and theoretical glass transition temperature during freezing. In that case, alginate final concentration was a constant regardless of its initial concentrations when temperature is below a critical value, the cross point of freezing temperature curve and glass transition curve. Vitreous alginate located in the interstices between ice crystals was revealed and was supposed to surround cells. *In situ* analysis of the freezing events of alginate indicated that the composition of vitreous alginate, and therefore cell environment, could be tuned with varied ice front velocities. Increasing the ice front velocity led to a higher change rate of alginate concentrations at the beginning of the freezing event that may be far away from the equilibrium between intra- and extracellular osmotic forces. The following directional freezing experiments evidenced that the viability of yeast cells decreases with increasing ice front velocity, which was confirmed by plate counting of thawed cells. Preliminary studies of the physiological state of the yeast cells led apparently-divergent information at high ice front velocity, suggesting that they may enter a viable non-culturable state during the freezing process in these conditions. Altogether the here-developed tool allows for correlating the kinetics and thermodynamics features of the biopolymer under-freezing and may further be applied to a wide variety of other (bio)-polymers of interest. Meanwhile, there are still many questions unanswered about the impact of these features on the cell behavior, which are expected to depend on the considered cell type.

This latter point was emphasized in our studies devoted to red blood cells cryopreservation. In this part, the considered biopolymer was albumin, a key blood component that could act both as antioxidant reagent and cell membrane stabilizer. Directional freezing enabled high cell recovery (more than 95%) at 100 µm.s^{-1} with 50% albumin. Increasing albumin concentration led to higher cell recovery, that was further enhanced by increasing ice front velocity. Cell vitality test via flow cytometry showed that intact cells after freezing and thawing were metabolically alive. After 106 days, the cell recovery and vitality were comparable to those that were stored for 1 day. In other words, our directional freezing approach extends the preservation time from commonly approved 49 days to 106 days without affecting cell recovery. Thermal analysis indicated that the amount of non-freezing water remaining associated to interstitial albumin decreased with initial protein concentration, which should allow to reach a suitable osmotic equilibrium. Thus, compared to the yeast/alginate system, high ice front velocities are here more favorable to cell survival.

In summary, we have demonstrated here that directional freezing in presence of biocompatible polymers is not only a versatile technique to prepare macroporous scaffolds but is also a promising approach for the long-term cryopreservation of cells without any potentially-toxic additional cryoprotectant. Our studies have suggested that it could constitute a quite universal strategy but that both the cell type and the nature of the biopolymer, which is often dictated by the targeted use of stored cells, define the optimal processing conditions, such as polymer concentration or ice front velocity. This points out that, in addition to the further development of coupled/correlative techniques allowing for a better understanding of the physico-chemical evolution of the system under freezing, more biological insights on the response of cells to cold conditions are required to progress in this field.

Freeze casting enables porous material fabrication and cell encapsulation (and/or cryopreservation). We can thus image that freezable cellularized materials with controlled geometry and well retained cell recovery could probably be obtained via freeze casting in terms of tissue engineering or other biomedical applications. This kind of material has several main advantages: 1) diverse selection of material types because of the simple processing conditions; 2) easy approach for introducing cells or other bioactive molecules (growth factors, for instance); 3) lamellar structures enabling efficient exchange of nutrients and metabolites. However, how to keep cells alive during freezing and how to stabilize thawed matrix without affecting cell recovery are challenges that remain to be addressed.

Abbreviations

ABS	Acrylonitrile butadiene styrene
AFPs	Antifreeze proteins
aNSCs	Adult neural stem cells
BC	Bovine chondrocytes
BMG	Bulk metallic glass
CAD	Computer-aided design
CaSi	Calcium silicate
CT	Computed Tomography
DAPI	4’-6-diamidino-2’-phenylindole
DCPD	Dicalcium phosphate dihydrate
DEF	Diethyl fumarate
DMSO	Dimethylsulfoxide
FAs	Focal adhesions
FBs	Fibrillar adhesions
HA	Hyaluronic acid
Hap	Hydroxyapatite
hASCs	Human adipose-derived stem cells
HES	Hydroxyethyl starch
hFOB	Human fetal osteoblasts
HT29	Human colorectal adenocarcinoma monolayer cell
HUVECs	Human umbilical vein endothelial cells
Irgacure 184	1-hydroxycyclohexyl phenyl ketone
Irgacure 2959	2-hydroxy-1-[4-(hydro- xyethoxy) phenyl]-2-methyl-1-propanone
Irgacure 651	2,2-dimethoxy-2-phenylacetophenone
LAP	lithium phenyl-2,4,6-trimethylbenzoylphosphinate
LFs	Ligament fibroblasts
LVEC	Human embryonic germ cells
MIC	Minimum Inhibitory Concentration
NAs	Nascent adhesions

NHDFs	Normal human dermal fibroblasts
PAA	Polyacrylamide
PANI	Polyaniline
PCL	Poly (ε- caprolactone)
PDMS	Polydimethylsiloxane
PEG-co-PDP	Poly(ethylene glycol-co-depsipeptide)
PEG-DA	Poly (ethylene glycol) diacrylate
PEGDMA	Poly(ethylene glycol) dimethacrylate
PHBV	Poly (3-hydroxybutyrate-co-3-hydroxyvalerate)
PLGA	Poly(lactic-co-glycolic acid)
PLLA	Poly (L-lactide)
PMMA	Poly(methyl methacrylate)
PPF	Polypropylene fumarate
PU	Polyurethane
PVA	Poly(vinyl alcohol)
rBMSCs	Rat bone marrow stromal cells
SaOs2	Human osteoblastic cell
SHG	Second Harmonic Generation
SIRC	Corneal epithelial cells
UV	Ultraviolet
β-TCP	β-tricalcium phosphate

Supplementary data

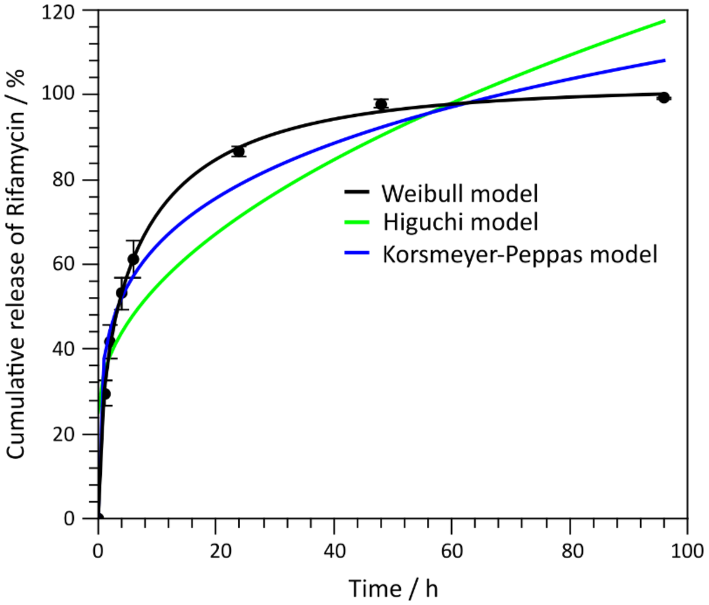

Figure S1 Fitting curves of rifamycin release from SF-MeOH foams (5 wt.% SF was fabricated at 1 °C.min^{-1}). Black dots, experimental data; green line, Higuchi fitting curve; blue line, Korsmeyer-Peppas fitting curve; black line, Weibull fitting curve.

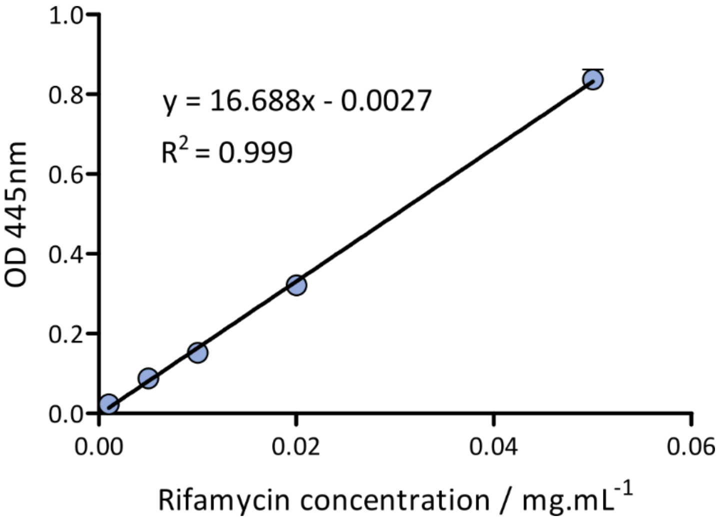

Figure S2 Calibration curve of rifamycin in methanol solution.

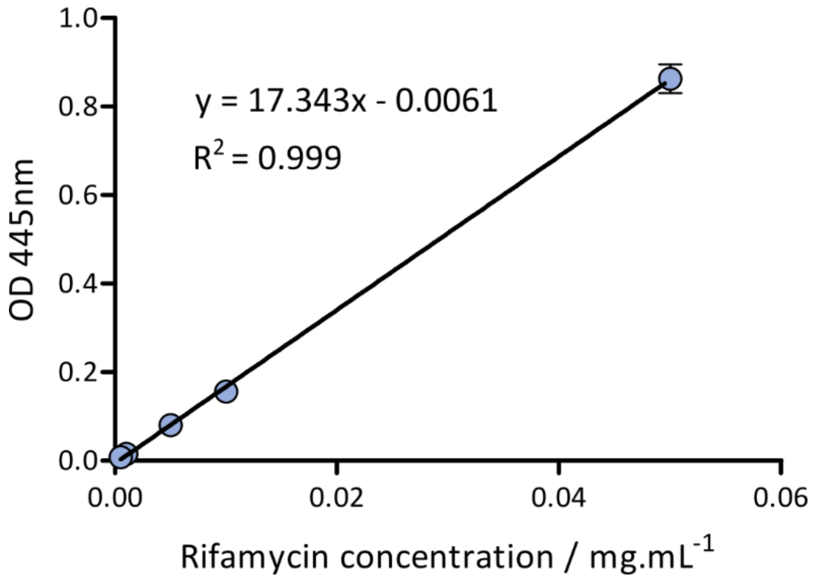

Figure S3 Calibration curve of rifamycin in H_2O.

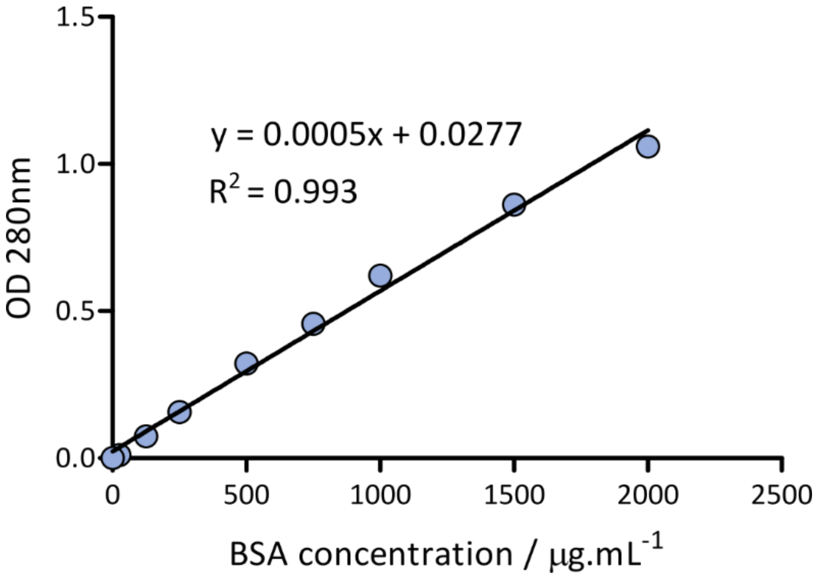

Figure S4 Calibration curve of bovine serum albumin in H_2O.

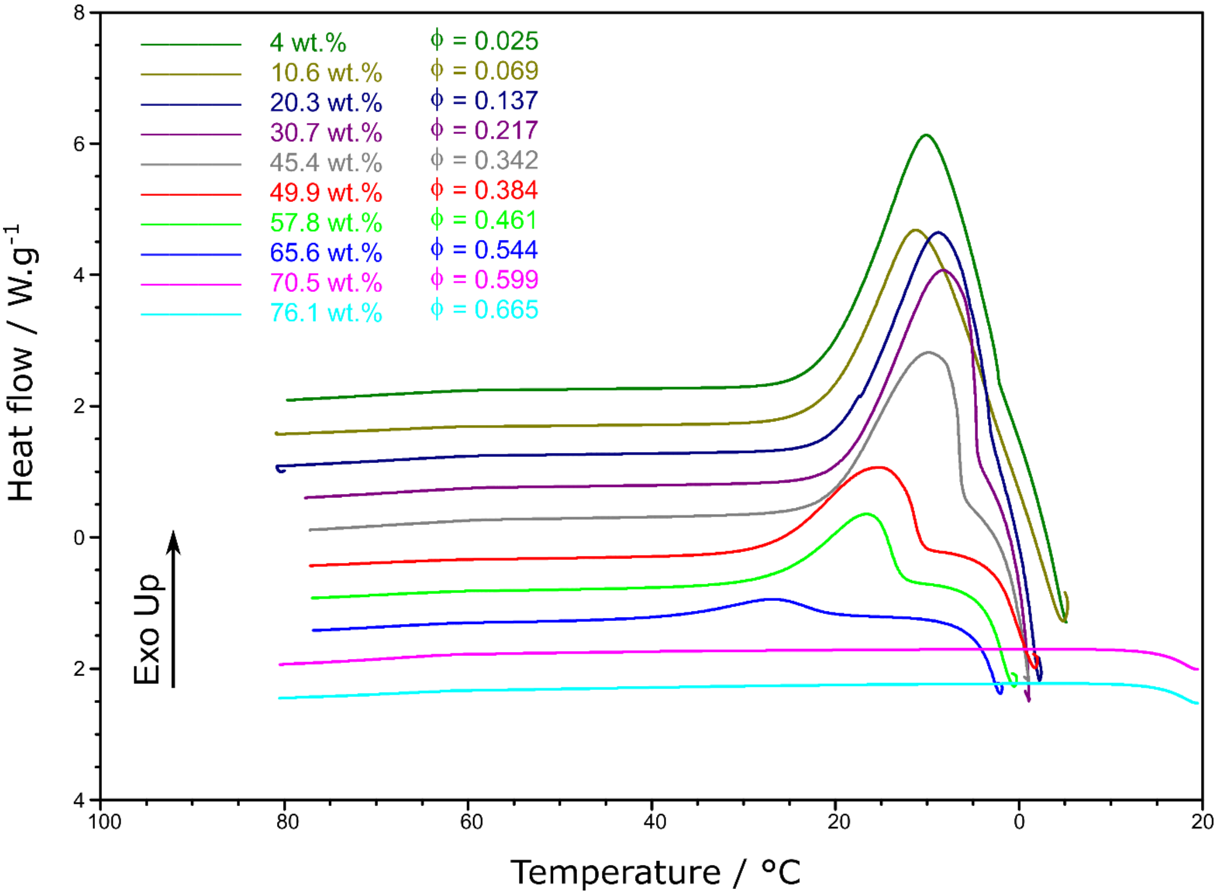

Figure S5. Cooling Differential Scanning Calorimetry scans obtained at 10 °C.min^{-1} for alginate/water binary mixtures ranging from 4 to 76.1 wt.% in alginate.

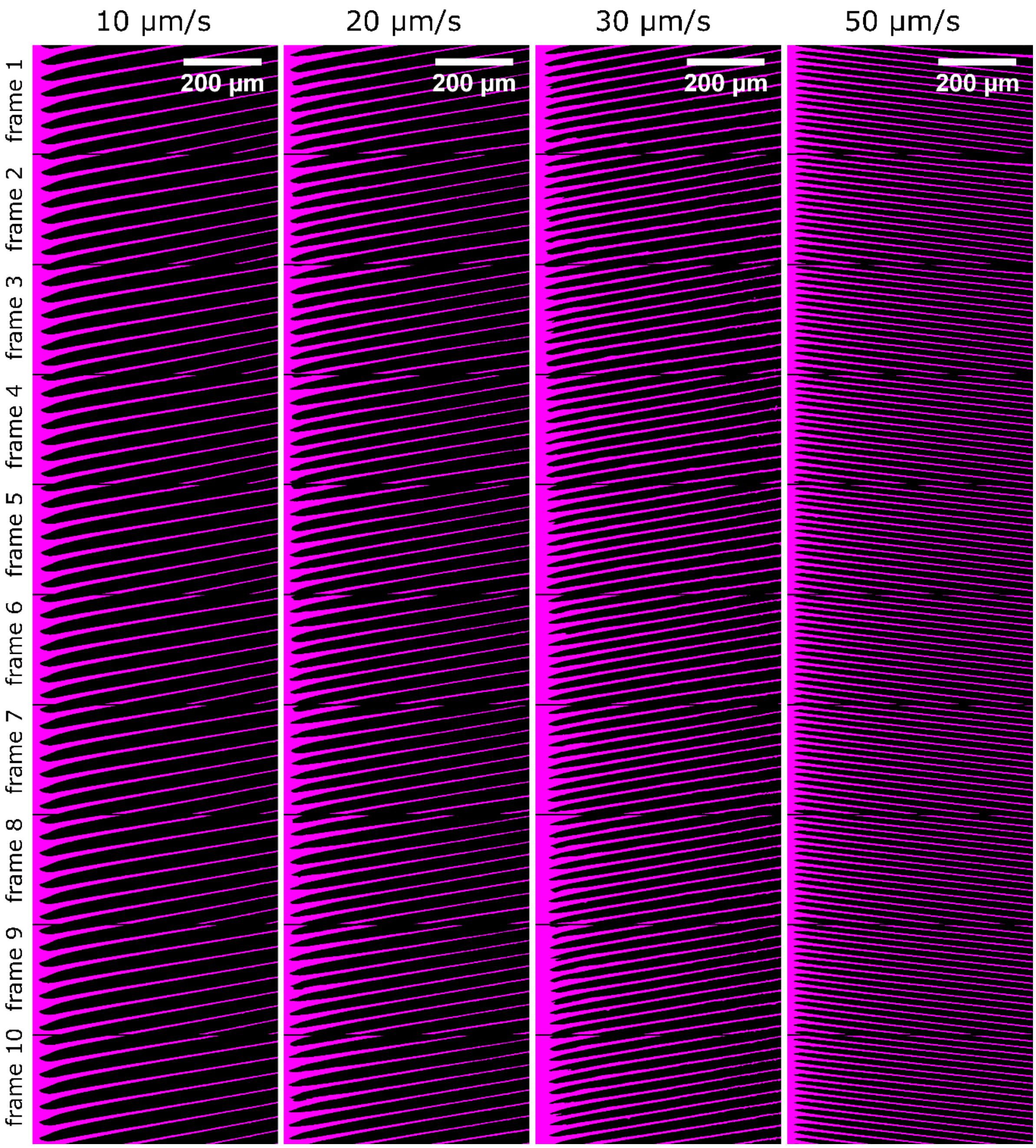

Figure S6. Examples of sequential frames used for the extraction of ice volume fraction at different ice front velocities

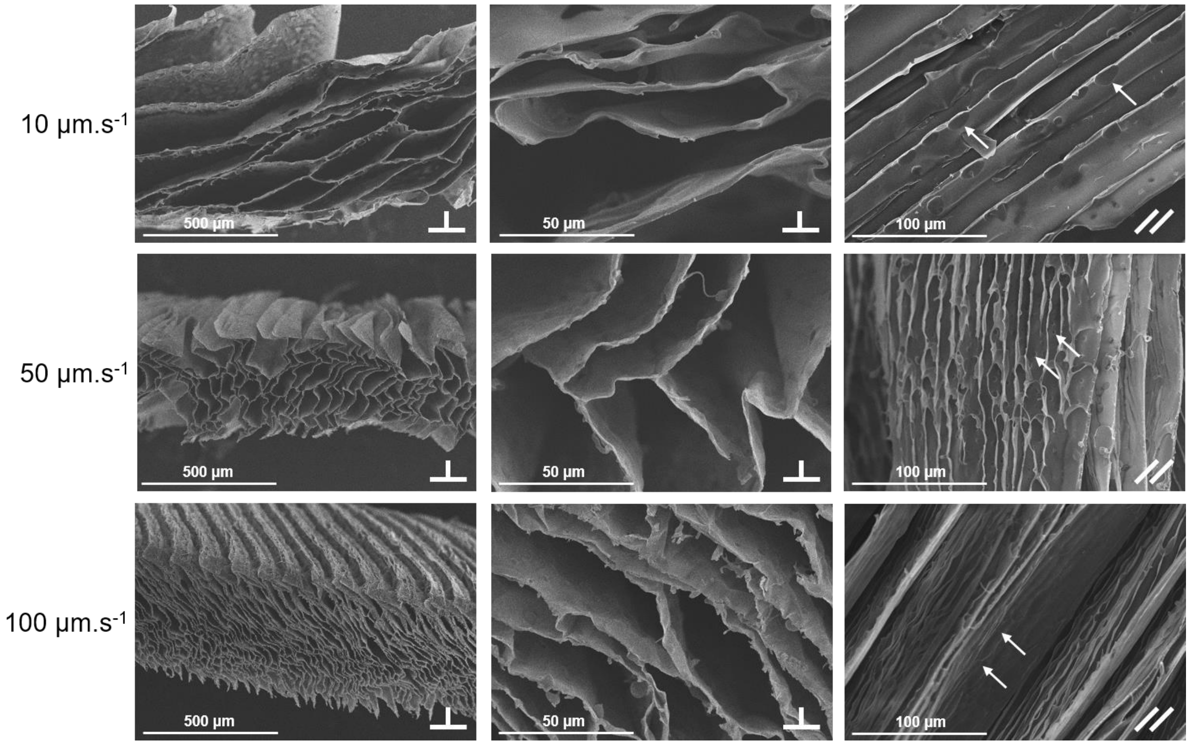

Figure S7 SEM micrographs of lyophilized alginate/cell foams prepared by directional freezing at different ice front velocities. Sample sections were cut perpendicular to the ice front growth direction. White arrows, indicate encapsulated yeast cells.

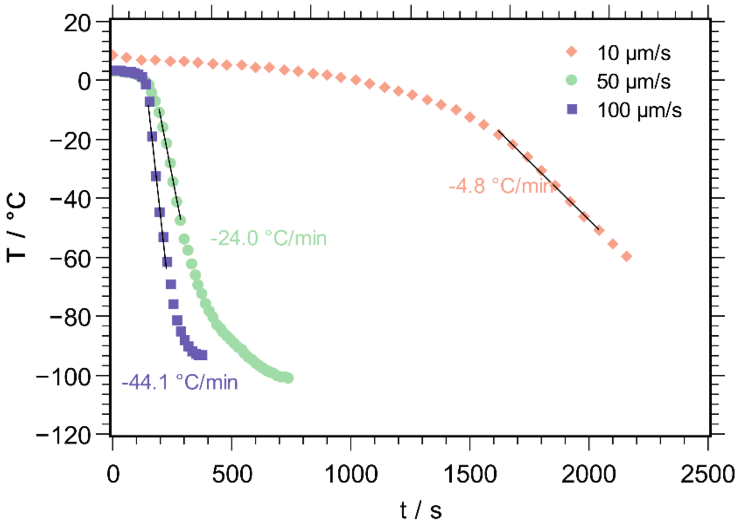

Figure S8 Temperature variation at different ice front velocities in the home-made directional freezing setup.

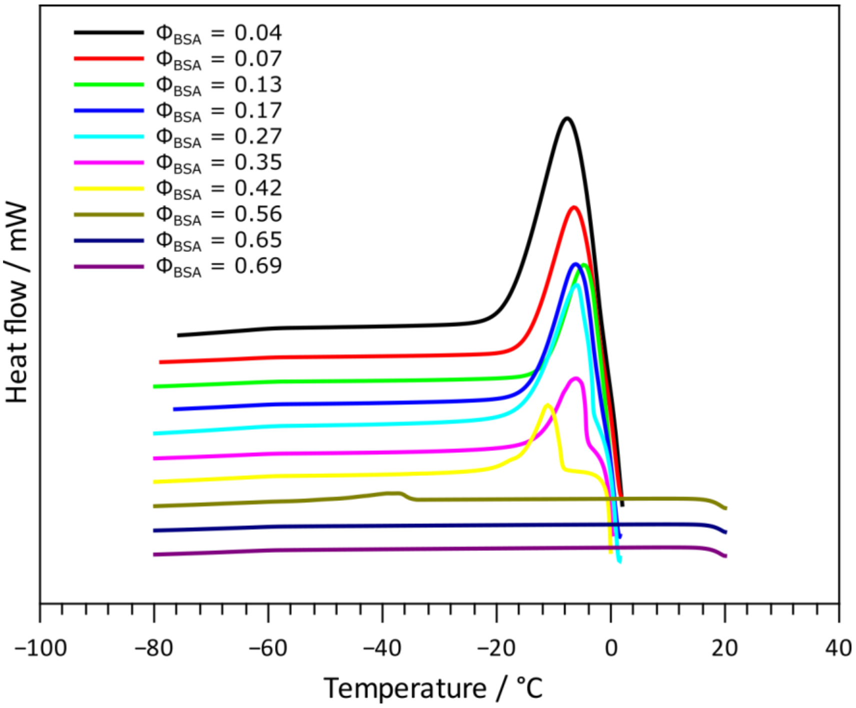

Figure S9 DSC cooling scan of BSA aqueous solution ranging from 0.04 to 0.69 volume fraction.

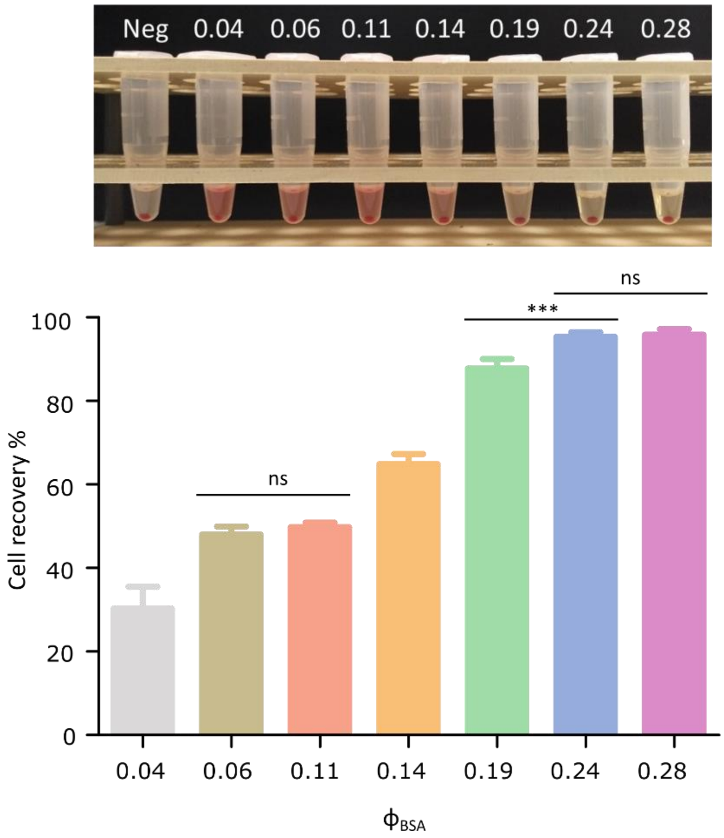

Figure S10 Cell recovery after directionally freezing with varying BSA volume fractions (from 0.04 to 0.28) at 100 μm s^{-1}. ns, indicates no significant difference; ***, indicates significant difference at P<0.01.

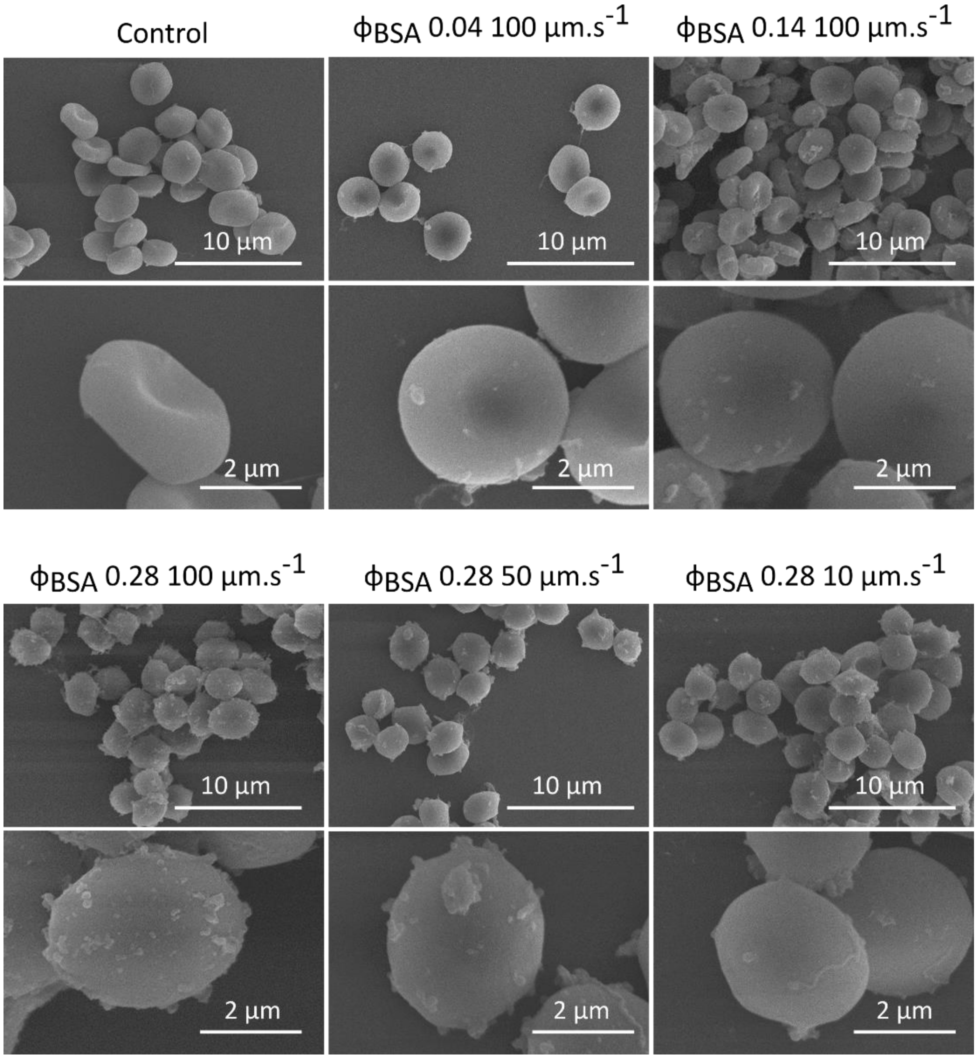

Figure S11 SEM images of thawed cells after directionally freezing at varied ice front velocities in presence of different amount of BSA (volume fraction of 0.04,0.14 and 0.28).

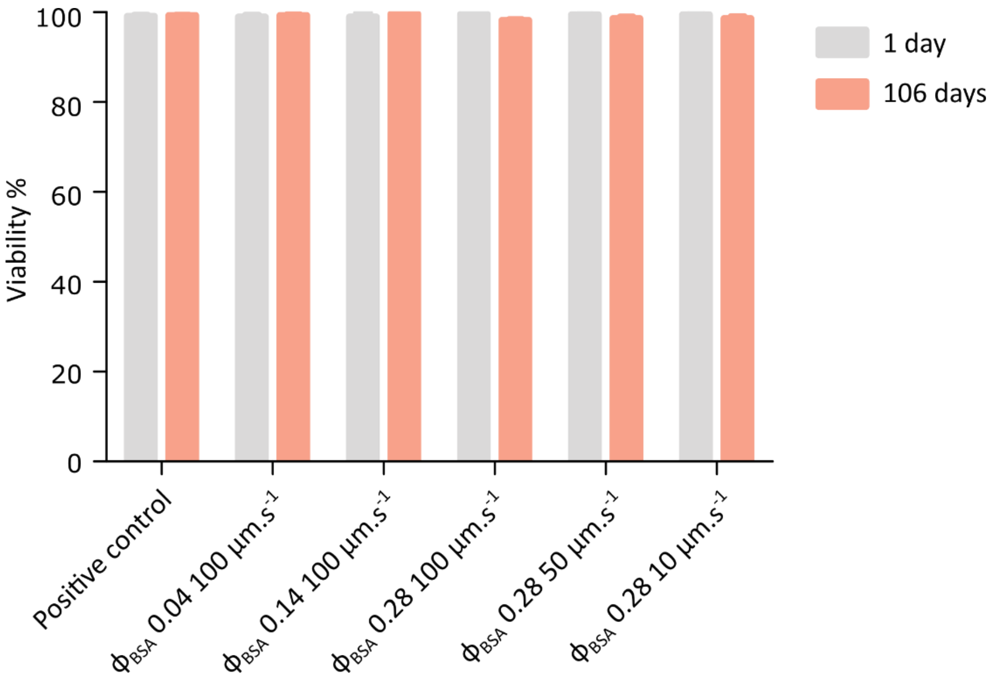

Figure S12 RBC viability after 1 day and 106 days' storage in -80°C freezer after directional freezing.

Résumé en Français

En ingénierie tissulaire, les biomatériaux doivent posséder certaines propriétés essentielles telles que la porosité, la résistance mécanique, la biocompatibilité et l'acceptation immunitaire. Ces paramètres vont impacter sur certains comportements cellulaires (par exemple, la migration, la prolifération et la différenciation). Afin d'obtenir un échafaudage de structure idéale, de nombreuses techniques ont été explorées, telles que l'impression en 3D (ex. la stéréolithographie), les techniques à base de porogènes (comme le coulage par solvant, la lixiviation des particules, le freeze-casting, *etc*) et l'électrofiltration. Parmi celles-ci, le freeze-casting s'est avéré être une bonne approche pour la fabrication d'échafaudages poreux en raison de sa biocompatibilité et de la grande porosité qui en résulte. Le freeze-casting a été bien étudié pour la fabrication de matériaux poreux anisotropes qui pourraient être appliqués dans de nombreux domaines, tels que l'ingénierie tissulaire, les dispositifs de stockage d'énergie et les capteurs. Depuis la publication de l'article de Deville en 2006, l'exploration de cette technique s'est développée, passant des matériaux biomimétiques (nacre et os, par exemple) aux matériaux multifonctionnels. Divers « éléments de construction » (comme les nanofibres, les nanoparticules, les macromolécules, *etc*) ont été étudiés pour fabriquer des matériaux ayant différentes structures et/ou différentes fonctions. Bien que des solvants tels que l'eau, le camphène, l'alcool tert-butylique et le CO2 liquide aient été étudiés pour disperser les blocs de construction, seule la suspension aqueuse sera abordée dans cette thèse. L'ensemble de ces éléments fait l'objet du premier chapitre, bibliographique, de cette thèse.

La soie, un matériau naturel aux excellentes propriétés mécaniques, possède des structures sophistiquées avec un noyau en fibroine de soie (SF) entouré d'une gaine en séricine de soie (SS). La SF a été transformée en plusieurs types de matériaux (hydrogels, éponges, fibres et constructions imprimées en 3D) pour des études *in vitro* et *in vivo*. En dépit des effets immunogènes communément admis, la séricine de soie a été bien étudiée dans le cadre de recherches universitaires et cliniques. Dans le deuxième chapitre de ce manuscrit, nous avons appliqué la technique de freeze-casting à la matrice de soie par ingénierie inverse avec du SF et du SS séparés afin d'obtenir des patchs dermiques antibactériens. Pour la matrice de soie biomimétique, notre dispositif fait maison a permis de fabriquer des mousses de SF biocompatibles avec différentes concentrations à des vitesses de refroidissement variables. La croissance unidirectionnelle des cristaux de glace a permis d'obtenir les pores finaux bien alignés le long du gradient, avant d’effectuer la sublimation de la glace. La géométrie des pores a pu être ajustée en faisant varier la vitesse de refroidissement, ce qui est essentiel pour une pénétration réussie des cellules dans les échafaudages lors la colonisation cellulaire (**Figure 1**).

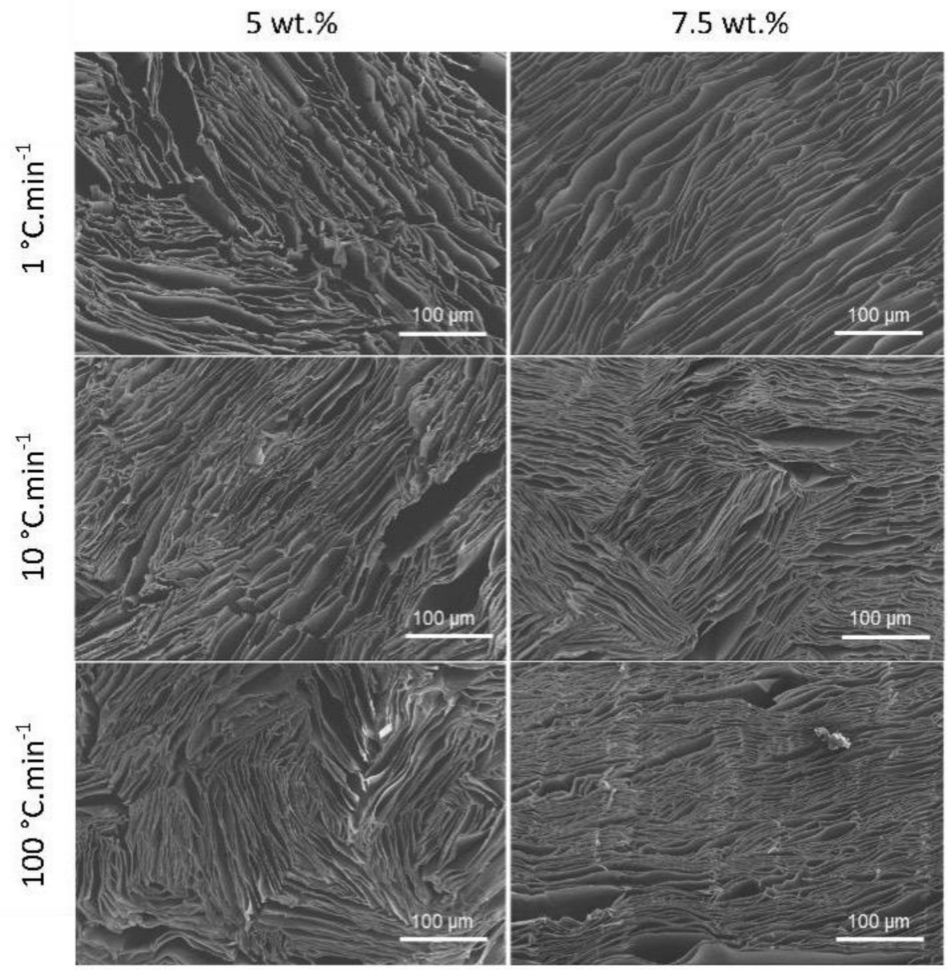

Figure 1. Images de microscopie à balayage de matrices de fibroïne de soie de concentration initiale 5 et 7.5 % (en masse) après freeze-casting à trois vitesses de refroidissement (1, 10 et 100 °C.min^{-1}). Barre d’échelle : 100 µm.

La combinaison des procédures de stabilisation de la matrice et de chargement des médicaments a permis d'obtenir une matrice insoluble dans l'eau et chargée de rifamycine, ce qui a permis le revêtement ultérieur de séricine et la libération aqueuse d'antibiotiques. Une charge élevée d'antibiotiques a été obtenue avec 1,5 µg par mg de composite. En outre, la gaine de séricine a permis de retenir davantage de rifamycine, dont la quantité diminue lorsque la vitesse de refroidissement augmente. L'augmentation de la vitesse de congélation pendant la préparation de la mousse a entraîné une réduction du taux de libération. Un taux de congélation plus élevé a entraîné une réduction de la distance entre les pores et les parois, ce qui est susceptible d'entraver la diffusion de la molécule à partir des mousses et donc de retarder la cinétique de libération. Ainsi, le revêtement a joué un rôle positif dans l'amélioration de la rétention de la rifamycine dans les mousses, tandis que la variation de la vitesse de congélation a permis de réguler la cinétique de libération de Rif en solution aqueuse. En outre, les mousses SS@SF ont permis une libération à long terme (jusqu'à 9 jours) de la rifamycine et des propriétés antibactériennes efficaces contre Staphylococcus aureus. La libération continue d'antibiotiques est nécessaire pour prévenir les infections bactériennes pendant et après une opération chirurgicale. La libération d'antibiotiques contre les bactéries en milieu aqueux et sur gélose permet à la matrice de soie remaniée d'être un bon candidat pour devenir un patch cutané antibactérien.

Le freeze-casting permet également l'encapsulation (ou la cryopréservation) des cellules et des tissus. La cryopréservation, en tant que technique unique permettant de prolonger la durée de vie des cellules et des tissus, a permis des avancées dans des domaines tels que la biologie cellulaire fondamentale, l'ingénierie tissulaire, *etc*. En raison des effets néfastes des cryoprotecteurs commerciaux (tels que le glycérol et le diméthyl sulfoxyde) sur le long terme, d'autres substituts potentiels (par exemple, les protéines, les polysaccharides, les polymères synthétiques) ont été explorés. Mais l'environnement physico-chimique entourant les cellules pendant la congélation est encore mal connue. La congélation directionnelle, un des types de congélation, implique un gradient thermique horizontal conduisant à la formation de glace lorsque l'échantillon est déplacé du côté chaud vers le côté froid. Pendant la congélation, les bio-entités et les milieux de congélation sont expulsés et emprisonnés entre les cristaux de glace. Comme la congélation directionnelle est traçable au microscope, elle permet d'explorer le comportement des cellules in situ pendant la congélation. Ainsi, une combinaison de congélation directionnelle sous microscope confocal et d'analyse calorimétrique différentielle à balayage a été réalisée pour révéler les environnements environnants les levures *Saccharomyces cerevisiae* pendant la congélation et les interactions in situ entre les cellules et le front de congélation. L'alginate a été choisi comme le biopolymère biocompatible cryoprotecteur. Nous avons établi un diagramme de phase de l'alginate basé sur le point de congélation expérimental et la température de transition vitreuse théorique pendant la congélation. Dans ce cas, la concentration finale de l'alginate était une constante indépendamment de ses concentrations initiales lorsque la température est inférieure à une valeur critique, de la courbe de température du point de congélation et de la courbe de transition vitreuse. La présence d'un alginate vitreux situé dans les interstices entre les cristaux de glace et entourant les cellules a été révélée. L'analyse *in situ* des événements de congélation de l'alginate a indiqué que la composition de l'alginate vitreux pouvait être régulée par des vitesses de front de glace variées, ce qui signifie que l'environnement cellulaire change à des vitesses de front de glace différentes. L'augmentation de la vitesse du front de glace a conduit à un taux de changement plus élevé des concentrations d'alginate au début des événements de congélation, ce qui peut être très éloigné des conditions d'équilibre entre les forces osmotiques intra et extracellulaires. La congélation directionnelle réalisée avec un dispositif fait maison a permis de constater que la viabilité des cellules de levure était inversement liée à la vitesse du front de glace, ce qui a été confirmé par le comptage sur gel des cellules décongelées (**Figure 2**).

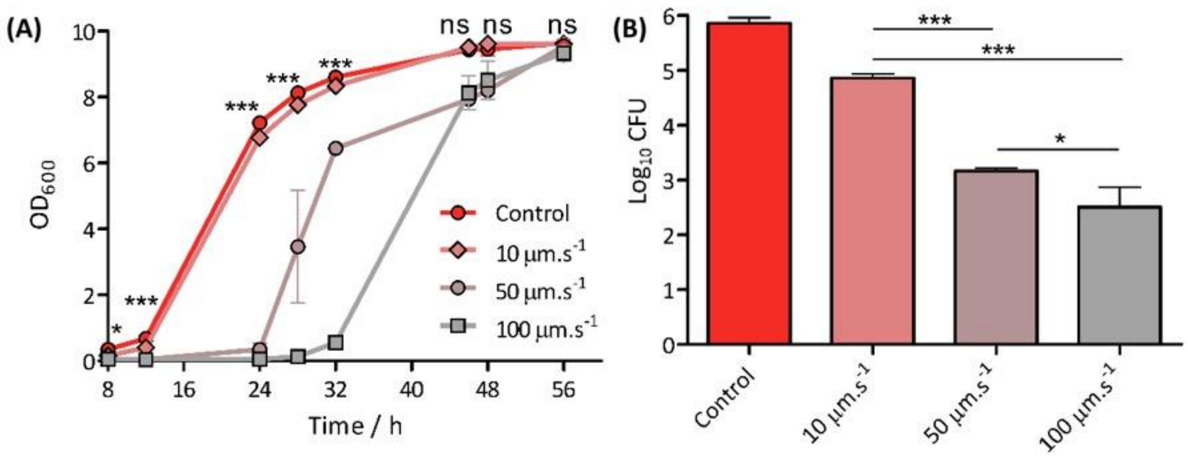

Figure 2. Influence de la vitesse du front de glace sur la survie des cellules de levure déterminée après décongélation par (A) croissance en milieu liquide et (B) comptage sur boîte.

La faible vitesse d'évolution de la concentration en alginate peut expliquer le taux de cryosurvie plus élevé à faible vitesse du front de glace. En résumé, nous avons obtenu une compréhension approfondie de la relation entre l'environnement cellulaire et la cryosurvie finale en couplant l'observation in situ et l'analyse thermique du milieu de congélation. Cette approche fournit un outil utile pour explorer de nouveaux milieux de congélation, ce qui devrait permettre d'améliorer encore le processus de cryopréservation sans ajouter de cryoprotecteurs toxiques, avec de multiples applications cliniques. Ces études et résultats sont rassemblés dans le Chapitre 3.

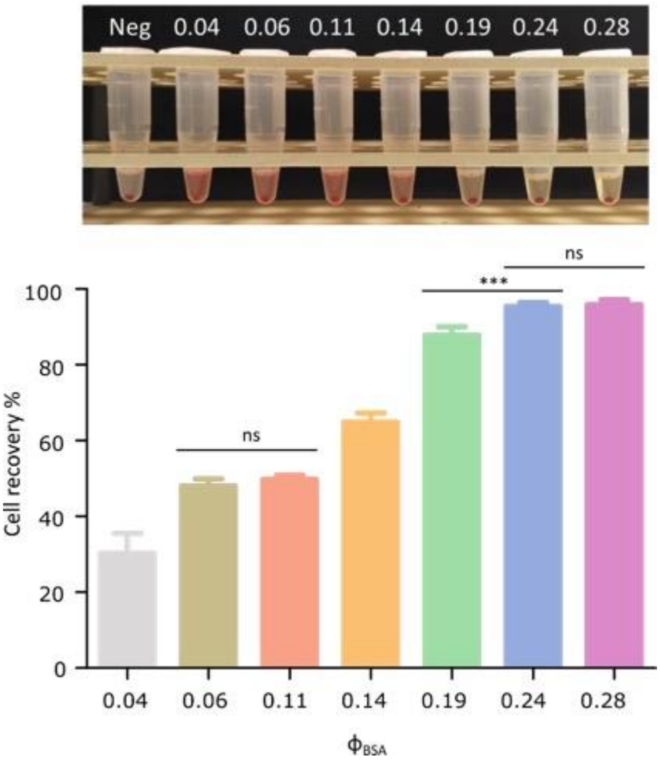

Figure 3. Influence de la fraction volumique d'albumine (Φ_{BSA}) sur le taux de récupération des globules rouges (la photo au-dessus du graph montre la variation correspondant de l'aspect des échantillons)

Le globule rouge est considéré comme un produit sanguin non substitué en cas d'hémorragie et d'anémie mortelles lors d'une utilisation chirurgicale et on a longtemps essayé de prolonger sa durée de conservation. Bien que divers cryoprotecteurs se soient avérés utiles, leur toxicité et les processus complexes de leur retrait avant utilisation des cellules restent problématiques. L'albumine, un composant important du sang, pourrait également agir comme réactif antioxydant et stabilisateur de la membrane cellulaire. Dans le chapitre 4, nous montrons qu'il est possible d'obtenir un taux de récupération cellulaire élevée (plus de 95%) à une vitesse de

100 μm.s^{-1} avec 50% d'albumine. L'augmentation de la concentration d'albumine a conduit à une récupération cellulaire plus élevée qui a été encore améliorée par l'augmentation de la vitesse du front de glace (**Figure 3**).

Le test de viabilité cellulaire par cytométrie de flux a montré une vitalité cellulaire élevée, indiquant que les cellules intactes après la congélation et la décongélation étaient métaboliquement actives. Après une conservation de 106 jours, la récupération et la vitalité des cellules étaient comparables à celles d'une conservation d'un jour. L'analyse thermique de l'albumine a indiqué que l'eau non congelée restant à l'intérieur de l'albumine interstitielle entre les cristaux de glace diminuait avec l'augmentation de la concentration initiale en protéine, ce qui entraîne des forces osmotiques suffisantes pour que l'eau intracellulaire s'écoule et donc une possibilité moindre de formation de glace intracellulaire. La combinaison de la congélation directionnelle et de l'albumine biocompatible offre un nouveau paradigme pour la cryopréservation des globules rouges, permettant une cryosurvie élevée des globules rouges et une durée de vie prolongée.

En conclusion, la congélation directionnelle en présence de polymères biocompatibles a été appliquée avec succès pour l'élaboration de biomatériaux antimicrobiens et pour la cryopréservation de levures et des globules rouges. Il ne fait aucun doute que cette approche pourrait servir de stratégie commune pour la cryoconservation future des cellules et des tissus mais les fonctionnalités des cellules après la congélation et la décongélation doivent encore être vérifiées pour des applications pratiques.

Bibliography

1. Mathew, A. P., Augustine, R., Kalarikkal, N. & Thomas, S. Tissue engineering: Principles, recent trends and the future. in *Nanomedicine and Tissue Engineering: State of the Art and Recent Trends* 31–82 (CRC Press, 2016).

2. Deville, S., Saiz, E., Nalla, R. K. & Tomsia, A. P. Freezing as a Path to Build Complex Composites. *Science* **311**, 515–518 (2006).

3. Zeng, X. *et al.* Facile Preparation of Superelastic and Ultralow Dielectric Boron Nitride Nanosheet Aerogels via Freeze-Casting Process. *Chem. Mater.* **27**, 5849–5855 (2015).

4. Shao, Y. *et al.* 3D Freeze-Casting of Cellular Graphene Films for Ultrahigh-Power-Density Supercapacitors. *Adv. Mater.* **28**, 6719–6726 (2016).

5. Si, Y. *et al.* Ultralight Biomass-Derived Carbonaceous Nanofibrous Aerogels with Superelasticity and High Pressure-Sensitivity. *Adv. Mater.* **28**, 9512–9518 (2016).

6. Xu, H. *et al.* Ultralight Cellular Foam from Cellulose Nanofiber/Carbon Nanotube Self-Assemblies for Ultrabroad-Band Microwave Absorption. *ACS Appl. Mater. Interfaces* **11**, 22628–22636 (2019).

7. Mohee, L., Offeddu, G. S., Husmann, A., Oyen, M. L. & Cameron, R. E. Investigation of the intrinsic permeability of ice-templated collagen scaffolds as a function of their structural and mechanical properties. *Acta Biomater.* **83**, 189–198 (2019).

8. Yin, K., Divakar, P. & Wegst, U. G. K. Freeze-casting porous chitosan ureteral stents for improved drainage. *Acta Biomater.* **84**, 231–241 (2019).

9. Christoph, S. *et al.* Ice-templating beet-root pectin foams: Controlling texture, mechanics and capillary properties. *Chem. Eng. J.* **350**, 20–28 (2018).

10. Bai, Y. *et al.* High Ion Transport within a Freeze-Casted Gel Film for High-Rate Integrated Flexible Supercapacitors. *ACS Appl. Mater. Interfaces* **11**, 43294–43302 (2019).

11. Zhang, Y., Zhang, L., Zhang, G. & Li, H. Naturally Dried Graphene-Based

Nanocomposite Aerogels with Exceptional Elasticity and High Electrical Conductivity. *ACS Appl. Mater. Interfaces* **10**, 21565–21572 (2018).

12. Wang, Q. *et al.* An All-Freeze-Casting Strategy to Design Typographical Supercapacitors with Integrated Architectures. *Small* **14**, (2018).

13. Rieu, C. *et al.* Topotactic Fibrillogenesis of Freeze-Cast Microridged Collagen Scaffolds for 3D Cell Culture. *ACS Appl. Mater. Interfaces* **11**, 14672–14683 (2019).

14. Nyström, G., Fong, W. K. & Mezzenga, R. Ice-Templated and Cross-Linked Amyloid Fibril Aerogel Scaffolds for Cell Growth. *Biomacromolecules* **18**, 2858–2865 (2017).

15. Guex, A. G. *et al.* Highly porous scaffolds of PEDOT:PSS for bone tissue engineering. *Acta Biomater.* **62**, 91–101 (2017).

16. Riblett, B. W., Francis, N. L., Wheatley, M. A. & Wegst, U. G. K. Ice-templated scaffolds with microridged pores direct DRG neurite growth. *Adv. Funct. Mater.* **22**, 4920–4923 (2012).

17. Christoph, S., Kwiatoszynski, J., Coradin, T. & Fernandes, F. M. Cellularized Cellular Solids via Freeze-Casting. *Macromol. Biosci.* **16**, 182–187 (2016).

18. Kremenska, Y. *et al.* Dimethyl Sulfoxide Has an Impact on Epigenetic Profile in Mouse Embryoid Body. *Stem Cells* **24**, 2549–2556 (2006).

19. D'Alessandro, A., Rossetti, R., Zolla, L., Pallotta, V. & D'Amici, G. M. Red blood cell processing for cryopreservation: from fresh blood to deglycerolization. *Blood Cells, Mol. Dis.* **48**, 226–232 (2012).

20. Fuller, R. & Devireddy, R. V. The effect of two different freezing methods on the immediate post-thaw membrane integrity of adipose tissue derived stem cells. *Int. J. Heat Mass Transf.* **51**, 5650–5654 (2008).

21. Maffei, S., Pennarossa, G., Brevini, T. A. L., Arav, A. & Gandolfi, F. Beneficial effect of directional freezing on in vitro viability of cryopreserved sheep whole ovaries and

ovarian cortical slices. *Hum. Reprod.* **29**, 114–124 (2014).

22. Maffei, S. *et al.* Direct comparative analysis of conventional and directional freezing for the cryopreservation of whole ovaries. *Fertil. Steril.* **100**, 1122–1131 (2013).

23. Arav, A. *et al.* Ovarian function 6 years after cryopreservation and transplantation of whole sheep ovaries. *Reprod. Biomed. Online* **20**, 48–52 (2010).

24. Gavish, Z., Ben-Haim, M. & Arav, A. Cryopreservation of whole murine and porcine livers. *Rejuvenation Res.* **11**, 765–772 (2008).

25. Scott, K. L., Lecak, J. & Acker, J. P. Biopreservation of red blood cells: Past, present, and future. *Transfus. Med. Rev.* **19**, 127–142 (2005).

26. Hollister, S. J. Porous scaffold design for tissue engineering. *Nature Materials* **4**, 518–524 (2005).

27. Langer, R. & Vacanti, J. P. Tissue Engineering. *Science* **260**, 920–926 (1993).

28. Kim, Y. S., Smoak, M. M., Melchiorri, A. J. & Mikos, A. G. An Overview of the Tissue Engineering Market in the United States from 2011 to 2018. *Tissue Engineering - Part A* **25**, 1–8 (2019).

29. Ruoslahti, E. & Pierschbacher, M. D. New perspectives in cell adhesion: RGD and integrins. *Science* **238**, 491–497 (1987).

30. Allison L. Berrier and Kenneth M. Yamada. Cell–Matrix Adhesion. *J. Cell. Physiol.* **207**, 581–588 (2007).

31. Linder, S. The matrix corroded: podosomes and invadopodia in extracellular matrix degradation. *Trends Cell Biol.* **17**, 107–117 (2007).

32. Gumbiner, B. M. Cell adhesion: The molecular basis of tissue architecture and morphogenesis. *Cell* **84**, 345–357 (1996).

33. Abercrombie, M., Heaysman, J. E. M. & Pegrum, S. M. The locomotion of fibroblasts

in culture. IV. Electron microscopy of the leading lamella. *Exp. Cell Res.* **67**, 359–367 (1971).

34. Abercrombie, M. Fibroblasts. *J Clin Pathol Suppl (R Coll Pathol)* **12**, 1–6 (1978).

35. Curtis, A. S. G. The mechanism of adhesion of cells to glass. A Study by Interference Reflection Microscopy. *J. Cell Biol.* **20**, 199–215 (1964).

36. Luo, B., Carman, C. V & Springer, T. A. Structural Basis of Integrin Regulation and Signaling. *Annu. Rev. Immunol.* 619–647 (2007).

37. Huang, X. Z. *et al.* Inactivation of the integrin β6 subunit gene reveals a role of epithelial integrins in regulating inflammation in the lungs and skin. *J. Cell Biol.* **133**, 921–928 (1996).

38. Johnson, M. S., Lu, N., Denessiouk, K., Heino, J. & Gullberg, D. Integrins during evolution: Evolutionary trees and model organisms. *Biochim. Biophys. Acta - Biomembr.* **1788**, 779–789 (2009).

39. Anderson, L. R., Owens, T. W. & Naylor, M. J. Structural and mechanical functions of integrins. *Biophys. Rev.* **6**, 203–213 (2014).

40. Bachmann, M., Kukkurainen, S., Hytönen, V. P. & Wehrle-Haller, B. Cell Adhesion by Integrins. *Physiol. Rev.* **99**, 1655–1699 (2019).

41. Jian-Ping Xiong, Thilo Stehle, Simon L. Goodman, and M. A. A. New insights into the structural basis ofintegrin activation. *Blood* **102**, 1155–1159 (2003).

42. Puklin-Faucher, E., Gao, M., Schulten, K. & Vogel, V. How the headpiece hinge angle is opened: New insights into the dynamics of integrin activation. *J. Cell Biol.* **175**, 349–360 (2006).

43. Takagi, J., Petre, B. M., Walz, T. & Springer, T. A. Global conformational earrangements in integrin extracellular domains in outside-in and inside-out signaling. *Cell* **110**, 599–611 (2002).

44. Arnold, M. *et al.* Activation of integrin function by nanopatterned adhesive interfaces. *ChemPhysChem* **5**, 383–388 (2004).

45. Tsimbouri, P. M., McNamara, L. E., Alakpa, E. V., Dalby, M. J. & Turner, L. A. *Cell-Material Interactions*. *Tissue Engineering: Second Edition* (2014).

46. Reddy, K. B., Smith, D. M. & Plow, E. F. Analysis of fyn function in hemostasis and αllbβ3-integrin signaling. *J. Cell Sci.* **121**, 1641–1648 (2008).

47. Bouvard, D., Pouwels, J., De Franceschi, N. & Ivaska, J. Integrin inactivators: Balancing cellular functions in vitro and in vivo. *Nat. Rev. Mol. Cell Biol.* **14**, 432–444 (2013).

48. Stukel, J. M. & Willits, R. K. Mechanotransduction of neural cells through cell-substrate interactions. *Tissue Engineering - Part B: Reviews* **22**, 173–182 (2016).

49. Roca-Cusachs, P., Iskratsch, T. & Sheetz, M. P. Finding the weakest link-exploring integrin-mediated mechanical molecular pathways. *Journal of Cell Science* **125**, 3025–3038 (2012).

50. Kim, J. *et al.* Nanotopographical manipulation of focal adhesion formation for enhanced differentiation of human neural stem cells. *ACS Appl. Mater. Interfaces* **5**, 10529–10540 (2013).

51. Yang, K. *et al.* Multiscale, hierarchically patterned topography for directing human neural stem cells into functional neurons. *ACS Nano* **8**, 7809–7822 (2014).

52. Bachir, A. I. *et al.* Integrin-associated complexes form hierarchically with variable stoichiometry in nascent adhesions. *Curr. Biol.* **24**, 1845–1853 (2014).

53. Cavalcanti-Adam, E. A. *et al.* Cell spreading and focal adhesion dynamics are regulated by spacing of integrin ligands. *Biophys. J.* **92**, 2964–2974 (2007).

54. Sun, Z., Guo, S. S. & Fässler, R. Integrin-mediated mechanotransduction. *Journal of Cell Biology* **215**, 445–456 (2016).

55. Dudziak, D. *et al.* Differential antigen processing by dendritic cell subsets in vivo. *Science* **315**, 107–111 (2007).

56. Sun, Z. *et al.* Kank2 activates talin, reduces force transduction across integrins and induces central adhesion formation. *Nat. Cell Biol.* **18**, 941–953 (2016).

57. Zamir, E. *et al. Dynamics and segregation of cell-matrix adhesions in cultured fibroblasts*. *NATURE CELL BIOLOGY* **2**, (2000).

58. Sun, Z., Guo, S. S. & Fässler, R. Integrin-mediated mechanotransduction. **215**, (2016).

59. Chen, L., Yan, C. & Zheng, Z. Functional polymer surfaces for controlling cell behaviors. *Materials Today* **21**, 38–59 (2018).

60. Fusco, S., Panzetta, V., Embrione, V. & Netti, P. A. Crosstalk between focal adhesions and material mechanical properties governs cell mechanics and functions. *Acta Biomater.* **23**, 63–71 (2015).

61. Wu, X. *et al.* Reversible hydrogels with tunable mechanical properties for optically controlling cell migration. *Nano Res.* **11**, 5556–5565 (2018).

62. Chao, P. hsiu G., Sheng, S. C. & Chang, W. R. Micro-composite substrates for the study of cell-matrix mechanical interactions. *J. Mech. Behav. Biomed. Mater.* **38**, 232–241 (2014).

63. Cornwell, K. G., Lei, P., Andreadis, S. T. & Pins, G. D. Crosslinking of discrete self-assembled collagen threads: Effects on mechanical strength and cell-matrix interactions. *J. Biomed. Mater. Res. - Part A* **80**, 362–371 (2007).

64. Cameron, A. R., Frith, J. E. & Cooper-White, J. J. The influence of substrate creep on mesenchymal stem cell behaviour and phenotype. *Biomaterials* **32**, 5979–5993 (2011).

65. Saha, K. *et al.* Substrate modulus directs neural stem cell behavior. *Biophys. J.* **95**, 4426–4438 (2008).

66. Floren, M. *et al.* Human mesenchymal stem cells cultured on silk hydrogels with

variable stiffness and growth factor differentiate into mature smooth muscle cell phenotype. *Acta Biomater.* **31**, 156–166 (2016).

67. Das, R. K. & Zouani, O. F. A review of the effects of the cell environment physicochemical nanoarchitecture on stem cell commitment. *Biomaterials* **35**, 5278–5293 (2014).

68. Tse, J. R. & Engler, A. J. Stiffness gradients mimicking in vivo tissue variation regulate mesenchymal stem cell fate. *PLoS One* **6**, (2011).

69. Zhang, Q., Yu, Y. & Zhao, H. The effect of matrix stiffness on biomechanical properties of chondrocytes. *Acta Biochim. Biophys. Sin. (Shanghai).* **48**, 958–965 (2016).

70. Saxena, S. *et al.* Microgel film dynamics modulate cell adhesion behavior. *Soft Matter* **10**, 1356–1364 (2014).

71. Parandakh, A., Anbarlou, A., Tafazzoli-Shadpour, M., Ardeshirylajimi, A. & Khani, M. M. Substrate topography interacts with substrate stiffness and culture time to regulate mechanical properties and smooth muscle differentiation of mesenchymal stem cells. *Colloids Surfaces B Biointerfaces* **173**, 194–201 (2019).

72. Petersen, A., Joly, P., Bergmann, C., Korus, G. & Duda, G. N. The impact of substrate stiffness and mechanical loading on fibroblast-induced scaffold remodeling. *Tissue Eng. - Part A* **18**, 1804–1817 (2012).

73. Arahira, T. & Todo, M. Effects of osteoblast-like cell seeding on the mechanical properties of porous composite scaffolds. *Adv. Compos. Mater.* **24**, 79–90 (2015).

74. Rowland, C. R., Colucci, L. A. & Guilak, F. Fabrication of anatomically-shaped cartilage constructs using decellularized cartilage-derived matrix scaffolds. *Biomaterials* **91**, 57–72 (2016).

75. Dos Santos, E. A., Farina, M., Soares, G. A. & Anselme, K. Chemical and topographical influence of hydroxyapatite and β-tricalcium phosphate surfaces on

human osteoblastic cell behavior. *J. Biomed. Mater. Res. - Part A* **89**, 510–520 (2009).

76. Liu, X. *et al.* Surface Chemical Gradient Affects the Differentiation of Human Adipose-Derived Stem Cells via ERK1/2 Signaling Pathway. *ACS Appl. Mater. Interfaces* **7**, 18473–18482 (2015).

77. Liu, X. & Wang, S. Three-dimensional nano-biointerface as a new platform for guiding cell fate. *Chemical Society Reviews* **43**, 2385–2401 (2014).

78. Zhao, C., Han, P., Ji, W. & Zhang, X. Enhanced mechanical properties and in vitro cell response of surface mechanical attrition treated pure titanium. *J. Biomater. Appl.* **27**, 113–118 (2012).

79. Zhang, Y. *et al.* Combined Chemical Groups and Topographical Nanopattern on the Poly(ϵ-Caprolactone) Surface for Regulating Human Foreskin Fibroblasts Behavior. *ACS Appl. Mater. Interfaces* **8**, 7720–7728 (2016).

80. Schlie, S., Fadeeva, E., Koch, J., Ngezahayo, A. & Chichkov, B. N. Femtosecond laser fabricated spike structures for selective control of cellular behavior. *J. Biomater. Appl.* **25**, 217–233 (2010).

81. Park, J. Y., Lee, D. H., Lee, E. J. & Lee, S. H. Study of cellular behaviors on concave and convex microstructures fabricated from elastic PDMS membranes. *Lab Chip* **9**, 2043–2049 (2009).

82. Mills, C. A. *et al.* Directional alignment of MG63 cells on polymer surfaces containing point microstructures. *Small* **3**, 871–879 (2007).

83. Bruekers, S. M. C. *et al.* Fibrin-fiber architecture influences cell spreading and differentiation. *Cell Adhesion and Migration* **10**, 495–504 (2016).

84. Liu, X. *et al.* The co-effect of surface topography gradient fabricated via immobilization of gold nanoparticles and surface chemistry via deposition of plasma polymerized film of allylamine/acrylic acid on osteoblast-like cell behavior. *Appl. Surf. Sci.* **473**, 838–847 (2019).

85. Yang, D. *et al.* Promoting Cell Migration in Tissue Engineering Scaffolds with Graded Channels. *Advanced Healthcare Materials* (2017). doi:10.1002/adhm.201700472

86. Mandal, B. B. & Kundu, S. C. Cell proliferation and migration in silk fibroin 3D scaffolds. *Biomaterials* **30**, 2956–2965 (2009).

87. Bai, H. *et al.* Biomimetic gradient scaffold from ice-templating for self-seeding of cells with capillary effect. *Acta Biomater.* **20**, 113–119 (2015).

88. Shen, Y. *et al.* Effect of surface chemistry on the integrin induced pathway in regulating vascular endothelial cells migration. *Colloids Surfaces B Biointerfaces* **126**, 188–197 (2015).

89. Liu, X. *et al.* Adipose stem cells controlled by surface chemistry. *J. Tissue Eng. Regen. Med.* **7**, 112–117 (2013).

90. Nakaoka, R., Yamakoshi, Y., Isama, K. & Tsuchiya, T. Effects of surface chemistry prepared by self-assembled monolayers on osteoblast behavior. *J. Biomed. Mater. Res. - Part A* **94**, 524–532 (2010).

91. Schweikl, H. *et al.* Proliferation of osteoblasts and fibroblasts on model surfaces of varying roughness and surface chemistry. *J. Mater. Sci. Mater. Med.* **18**, 1895–1905 (2007).

92. Delalat, B., Goreham, R. V., Vasilev, K., Harding, F. J. & Voelcker, N. H. Subtle changes in surface chemistry affect embryoid body cell differentiation: Lessons learnt from surface-bound amine density gradients. *Tissue Eng. - Part A* **20**, 1715–1725 (2014).

93. Keselowsky, B. G., Collard, D. M. & García, A. J. Surface chemistry modulates focal adhesion composition and signaling through changes in integrin binding. *Biomaterials* **25**, 5947–5954 (2004).

94. Keselowsky, B. G., Collard, D. M. & García, A. J. *Surface chemistry modulates fibronectin conformation and directs integrin binding and specificity to control cell*

adhesion. (2003).

95. Bain, L. E. *et al.* Surface topography and chemistry shape cellular behavior on wide band-gap semiconductors. *Acta Biomater.* **10**, 2455–2462 (2014).

96. Bergholt, N. L. *et al.* Surface chemistry, substrate, and topography guide the behavior of human articular chondrocytes cultured in vitro. *J. Biomed. Mater. Res. - Part A* **106**, 2805–2816 (2018).

97. Hyun, J., Chen, J., Setton, L. A. & Chilkoti, A. Patterning cells in highly deformable microstructures: Effect of plastic deformation of substrate on cellular phenotype and gene expression. *Biomaterials* **27**, 1444–1451 (2006).

98. Burke, G. A. *et al.* Osteoblast-like cell response to calcium phosphate coating chemistry and morphology on etched silicon surfaces. *J. Mater. Sci. Mater. Med.* **23**, 835–851 (2012).

99. Zheng, Z. *et al.* The behavior of MC3T3-E1 cells on chitosan/poly-L-lysine composite films: Effect of nanotopography, surface chemistry, and wettability. *J. Biomed. Mater. Res. - Part A* **89**, 453–465 (2009).

100. Lapointe, V. L. S., Fernandes, A. T., Bell, N. C., Stellacci, F. & Stevens, M. M. Nanoscale Topography and Chemistry Affect Embryonic Stem Cell Self-Renewal and Early Differentiation. *Adv. Healthc. Mater.* **2**, 1644–1650 (2013).

101. Christoph, S. Elaboration par freeze-casting de matériaux poreux hybrides cellularisés pour la bioremédiation des sols. (Sorbonne University, 2017).

102. Leong, K. F., Cheah, C. M. & Chua, C. K. Solid freeform fabrication of three-dimensional scaffolds for engineering replacement tissues and organs. *Biomaterials* **24**, 2363–2378 (2003).

103. Ligon, S. C., Liska, R., Stampfl, J., Gurr, M. & Mülhaupt, R. Polymers for 3D Printing and Customized Additive Manufacturing. *Chem. Rev.* **117**, 10212–10290 (2017).

104. Tolochko, N. K. *et al.* Absorptance of powder materials suitable for laser sintering. *Rapid Prototyping Journal* **6**, 155–160 (2000).

105. Kumar, S. Selective laser sintering: A qualitative and objective approach. *Jom* **55**, 43–47 (2003).

106. Shivalkar, Saurabh, and S. S. Solid Freeform Techniques Application in Bone Tissue Engineering for Scaffold Fabrication. (2016).

107. Mazzoli, A. Selective laser sintering in biomedical engineering. *Medical & Biological Engineering & Computing* **51**, 245–256 (2013).

108. Eosoly, S., Brabazon, D., Lohfeld, S. & Looney, L. Selective laser sintering of hydroxyapatite/poly-e-caprolactone scaffolds. *Acta Biomaterialia* **6**, 2511–2517 (2010).

109. Du, Y. *et al.* Selective laser sintering scaffold with hierarchical architecture and gradient composition for osteochondral repair in rabbits. *Biomaterials* **137**, 37–48 (2017).

110. Wiria, F. E., Leong, K. F., Chua, C. K. & Liu, Y. Poly-e-caprolactone/hydroxyapatite for tissue engineering scaffold fabrication via selective laser sintering. *Acta Biomater.* **3**, 1–12 (2007).

111. Liao, H.-T., Lee, M.-Y., Tsai, W.-W., Wang, H. & Lu, W.-C. Osteogenesis of adipose-derived stem cells on polycaprolactone- β -tricalcium phosphate scaffold fabricated via selective laser sintering and surface coating with collagen type I. *Journal of Tissue Engineering and Regenerative Medicine* **10**, E337–E353 (2016).

112. Xia, Y. *et al.* Selective laser sintering fabrication of nano-hydroxyapatite/poly-ε-caprolactone scaffolds for bone tissue engineering applications. *International journal of nanomedicine* **8**, 4197–213 (2013).

113. Zhou, W. Y., Lee, S. H., Wang, M., Cheung, W. L. & Ip, W. Y. Selective laser sintering of porous tissue engineering scaffolds from poly(L-lactide)/carbonated

hydroxyapatite nanocomposite microspheres. *Journal of Materials Science: Materials in Medicine* **19**, 2535–2540 (2008).

114. Roskies, M. *et al.* Improving PEEK bioactivity for craniofacial reconstruction using a 3D printed scaffold embedded with mesenchymal stem cells. *Journal of Biomaterials Applications* **31**, 132–139 (2016).

115. Shuai, C. *et al.* Characterization and bioactivity evaluation of (polyetheretherketone/polyglycolicacid)-hydroyapatite scaffolds for tissue regeneration. *Materials* **9**, (2016).

116. Shuai, C. *et al.* Silane modified diopside for improved interfacial adhesion and bioactivity of composite scaffolds. *Molecules* **22**, (2017).

117. Shuai, C. *et al.* Tailoring properties of porous Poly (vinylidene fluoride) scaffold through nano-sized 58s bioactive glass. *Journal of Biomaterials Science, Polymer Edition* **27**, 97–109 (2016).

118. Huang, W. *et al.* MgO whiskers reinforced poly(vinylidene fluoride) scaffolds. *RSC Advances* **6**, 108196–108202 (2016).

119. Shuai, C. *et al.* Nanodiamond reinforced polyvinylidene fluoride/bioglass scaffolds for bone tissue engineering. *Journal of Porous Materials* **24**, 249–255 (2017).

120. Shuai, C., , Wang Guo , Chengde Gao, Y. Y., , Yong Xu , Long Liu, Tian Qin, H. S. & , Sheng Yang, Pei Feng, and P. W. Calcium Silicate Improved Bioactivity and Mechanical Properties of Poly(3-hydroxybutyrate-co-3-hydroxyvalerate) Scaffolds. (2017).

121. Duan, S. *et al.* Microstructure evolution and mechanical properties improvement in liquid-phase-sintered hydroxyapatite by laser sintering. *Materials* **8**, 1162–1175 (2015).

122. Shuai, C. *et al.* Mechanical and structural characterization of diopside scaffolds reinforced with graphene. *Journal of Alloys and Compounds* **655**, 86–92 (2016).

123. Gao, C., Zhuang, J., Li, P., Shuai, C. & Peng, S. Preparation of micro/nanometer-sized porous surface structure of calcium phosphate scaffolds and the influence on biocompatibility. *Journal of Materials Research* **29**, 1144–1152 (2014).

124. Shuai, C. *et al.* Polyetheretherketone/poly (glycolic acid) blend scaffolds with biodegradable properties. *Journal of Biomaterials Science, Polymer Edition* **27**, 1434–1446 (2016).

125. Salmoria, G. V., Klauss, P., Paggi, R. A., Kanis, L. A. & Lago, A. Structure and mechanical properties of cellulose based scaffolds fabricated by selective laser sintering. *Polymer Testing* **28**, (2009).

126. Brunello, G. *et al.* Powder-based 3D printing for bone tissue engineering. *Biotechnology Advances* **34**, 740–753 (2016).

127. Kosorn, W. *et al.* PCL/PHBV blended three dimensional scaffolds fabricated by fused deposition modeling and responses of chondrocytes to the scaffolds. *Journal of Biomedical Materials Research - Part B Applied Biomaterials* **105**, 1141–1150 (2017).

128. Nyberg, E., Rindone, A., Dorafshar, A. & Grayson, W. L. Comparison of 3D-Printed Poly-ε-Caprolactone Scaffolds Functionalized with Tricalcium Phosphate, Hydroxyapatite, Bio-Oss, or Decellularized Bone Matrix <sup/>. *Tissue Engineering Part A* **23**, 503–514 (2017).

129. Wang, S. J. *et al.* Thermogel-coated poly(ε-caprolactone) composite scaffold for enhanced cartilage tissue engineering. *Polymers* **8**, (2016).

130. Habib, F. N., Nikzad, M., Masood, S. H. & Saifullah, A. B. M. Design and Development of Scaffolds for Tissue Engineering Using Three-Dimensional Printing for Bio-Based Applications. *3D Printing and Additive Manufacturing* **3**, 119–127 (2016).

131. Lara-Padilla, H., Mendoza-Buenrostro, C., Cardenas, D., Rodriguez-Garcia, A. & Rodriguez, C. A. Influence of controlled cooling in bimodal scaffold fabrication using polymers with different melting temperatures. *Materials* **10**, (2017).

132. Heo, D. N. *et al.* Enhanced bone tissue regeneration using a 3D printed microstructure incorporated with a hybrid nano hydrogel. *Nanoscale* **9**, 5055–5062 (2017).

133. Yen, H. J., Tseng, C. S., Hsu, S. H. & Tsai, C. L. Evaluation of chondrocyte growth in the highly porous scaffolds made by fused deposition manufacturing (FDM) filled with type II collagen. *Biomedical Microdevices* **11**, 615–624 (2009).

134. Idaszek, J., Bruinink, A. &¬więszkowski, W. Delayed degradation of poly(lactide-co-glycolide) accelerates hydrolysis of poly(??-caprolactone) in ternary composite scaffolds. *Polymer Degradation and Stability* **124**, 119–127 (2016).

135. Ostrowska, B., Di Luca, A., Moroni, L. & Swieszkowski, W. Influence of internal pore architecture on biological and mechanical properties of three-dimensional fiber deposited scaffolds for bone regeneration. *Journal of Biomedical Materials Research - Part A* **104**, 991–1001 (2016).

136. Shor, L., Gu¨ ceri, S., Wen, X., Gandhi, M. & Sun, W. Fabrication of three-dimensional polycaprolactone/hydroxyapatite tissue scaffolds and osteoblast-scaffold interactions in vitro. *Biomaterials* **28**, 5291–5297 (2007).

137. Rai, B. *et al.* Differences between in vitro viability and differentiation and in vivo bone-forming efficacy of human mesenchymal stem cells cultured on PCL-TCP scaffolds. *Biomaterials* **31**, 7960–7970 (2010).

138. Hung, B. P. *et al.* Three-Dimensional Printing of Bone Extracellular Matrix for Craniofacial Regeneration. *ACS Biomaterials Science and Engineering* **2**, 1806–1816 (2016).

139. Yoshinari, M., Matsuzaka, K. & Inoue, T. Surface modification by cold-plasma technique for dental implants-Bio-functionalization with binding pharmaceuticals. *Japanese Dental Science Review* **47**, 89–101 (2011).

140. Nowicki, M. A., Castro, N. J., Plesniak, M. W. & Zhang, L. G. 3D printing of novel osteochondral scaffolds with graded microstructure. *Nanotechnology* **27**, 1–10 (2016).

141. Wu, J. *et al.* Gradient biomaterials and their influences on cell migration. *Interface Focus* **2**, 337–355 (2012).

142. Sardella, E. *et al.* Improving Internal Cell Colonization of Porous Scaffolds with Chemical Gradients Produced by Plasma Assisted Approaches. *ACS Appl. Mater. Interfaces* **9**, 4966–4975 (2017).

143. Wang, X., Jiang, M., Zhou, Z., Gou, J. & Hui, D. 3D printing of polymer matrix composites: A review and prospective. *Composites Part B: Engineering* **110**, 442–458 (2017).

144. Lee, J. W., Kim, J. Y. & Cho, D.-W. Solid Free-form Fabrication Technology and Its Application to Bone Tissue Engineering. *International journal of stem cells* **3**, 85–95 (2010).

145. Yuan, B., Zhou, S.-Y. & Chen, X.-S. Rapid prototyping technology and its application in bone tissue engineering. *J. Zhejiang Univ. Sci. B* **18**, 303–315 (2017).

146. Raeisdasteh Hokmabad, V., Davaran, S., Ramazani, A. & Salehi, R. Design and fabrication of porous biodegradable scaffolds: a strategy for tissue engineering. *J. Biomater. Sci. Polym. Ed.* **28**, 1797–1825 (2017).

147. Du, D. *et al.* Microstereolithography-Based Fabrication of Anatomically Shaped Beta-Tricalcium Phosphate Scaffolds for Bone Tissue Engineering. *BioMed Research International* **2015**, (2015).

148. Zsedenyi, A. *et al.* Gold nanoparticle-filled biodegradable photopolymer scaffolds induced muscle remodeling: in vitro and in vivo findings. *Materials Science and Engineering C* **72**, 625–630 (2017).

149. Accardo, A. *et al.* Multiphoton Direct Laser Writing and 3D Imaging of Polymeric Freestanding Architectures for Cell Colonization. *Small* **13**, (2017).

150. Shanjani, Y., Pan, C. C., Elomaa, L. & Yang, Y. A novel bioprinting method and system for forming hybrid tissue engineering constructs. *Biofabrication* **7**, 045008

(2015).

151. Wang, Z. *et al.* A simple and high-resolution stereolithography-based 3D bioprinting system using visible light crosslinkable bioinks. *Biofabrication* **7**, 045009 (2015).

152. Mondschein, R. J., Kanitkar, A., Williams, C. B., Verbridge, S. S. & Long, T. E. Polymer structure-property requirements for stereolithographic 3D printing of soft tissue engineering scaffolds. *Biomaterials* **140**, 170–188 (2017).

153. Cheng, Y.-L., Chen, Y.-W., Wang, K. & Shie, M.-Y. Enhanced adhesion and differentiation of human mesenchymal stem cell inside apatite-mineralized/poly(dopamine)-coated poly(?-caprolactone) scaffolds by stereolithography. *J. Mater. Chem. B* **4**, 6307–6315 (2016).

154. Shie, M. Y. *et al.* 3D printing of cytocompatible water-based light-cured polyurethane with hyaluronic acid for cartilage tissue engineering applications. *Materials* **10**, (2017).

155. Lee, S.-J. *et al.* Development of Novel 3D Printed Scaffolds with Core-shell Nanoparticles for Nerve Regeneration. *IEEE Transactions on Biomedical Engineering* **9294**, 1–1 (2016).

156. Elomaa, L. *et al.* Preparation of poly(e-caprolactone)-based tissue engineering scaffolds by stereolithography Laura. *Acta Biomaterialia* **7**, 3850–3856 (2011).

157. Guillaume, O. *et al.* Surface-enrichment with hydroxyapatite nanoparticles in stereolithography-fabricated composite polymer scaffolds promotes bone repair. *Acta Biomaterialia* **54**, 386–398 (2017).

158. Zhou, X. *et al.* 3D bioprinted graphene oxide-incorporated matrix for promoting chondrogenic differentiation of human bone marrow mesenchymal stem cells. *Carbon* **116**, 615–624 (2017).

159. Castro, N. J., O'Brien, J. & Zhang, L. G. Integrating biologically inspired nanomaterials and table-top stereolithography for 3D printed biomimetic osteochondral scaffolds. *Nanoscale* **7**, 14010–14022 (2015).

160. Williams, C. G., Malik, A. N., Kim, T. K., Manson, P. N. & Elisseeff, J. H. Variable cytocompatibility of six cell lines with photoinitiators used for polymerizing hydrogels and cell encapsulation. *Biomaterials* **26**, 1211–1218 (2005).

161. Farkas, B., Dante, S. & Brandi, F. Photoinitiator-free 3D scaffolds fabricated by excimer laser photocuring. *Nanotechnology* **28**, 034001 (2017).

162. Cvetkovic, C., Rich, M. H., Raman, R., Kong, H. & Bashir, R. A 3D-printed platform for modular neuromuscular motor units. *Microsystems & Nanoengineering* **3**, 17015 (2017).

163. Zhu, W. *et al.* Direct 3D bioprinting of prevascularized tissue constructs with complex microarchitecture. *Biomaterials* **124**, 106–115 (2017).

164. Arcaute, K., Mann, B. K. & Wicker, R. B. Stereolithography of three-dimensional bioactive poly(ethylene glycol) constructs with encapsulated cells. *Annals of Biomedical Engineering* **34**, 1429–1441 (2006).

165. Chan, V., Zorlutuna, P., Jeong, J. H., Kong, H. & Bashir, R. Three-dimensional photopatterning of hydrogels using stereolithography for long-term cell encapsulation. *Lab on a Chip* **10**, 2062 (2010).

166. Mapili, G., Lu, Y., Chen, S. & Roy, K. Laser-layered microfabrication of spatially patterned functionalized tissue-engineering scaffolds. *Journal of Biomedical Materials Research - Part B Applied Biomaterials* **75**, 414–424 (2005).

167. Elomaa, L. *et al.* Three-dimensional fabrication of cell-laden biodegradable poly(ethylene glycol-co-depsipeptide) hydrogels by visible light stereolithography. *J. Mater. Chem. B* **3**, 8348–8358 (2015).

168. Lin, H. *et al.* Application of visible light-based projection stereolithography for live cell-scaffold fabrication with designed architecture. *Biomaterials* **34**, 331–339 (2013).

169. Hosoya, K. & Fréchet, J. M. J. Influence of the seed polymer on the chromatographic properties of size monodisperse polymeric separation media prepared by a multi-step

swelling and polymerization method. *J. Polym. Sci. Part A Polym. Chem.* **31**, 2129–2141 (1993).

170. Conoscenti, G. *et al.* PLLA scaffolds produced by thermally induced phase separation (TIPS) allow human chondrocyte growth and extracellular matrix formation dependent on pore size. *Mater. Sci. Eng. C* **80**, 449–459 (2017).

171. van der Smissen, A. *et al.* Artificial extracellular matrices support cell growth and matrix synthesis of human dermal fibroblasts in macroporous 3D scaffolds. *J. Tissue Eng. Regen. Med.* **11**, 1390–1402 (2017).

172. Rodríguez-Pérez, E., Lloret Compañ, A., Monleón Pradas, M. & Martínez-Ramos, C. Scaffolds of Hyaluronic Acid-Poly(Ethyl Acrylate) Interpenetrating Networks: Characterization and In Vitro Studies. *Macromol. Biosci.* **16**, 1147–1157 (2016).

173. Intranuovo, F. *et al.* Plasma modification of PCL porous scaffolds fabricated by solvent-casting/particulate-leaching for tissue engineering. *Plasma Process. Polym.* **11**, 184–195 (2014).

174. Martínez-pérez, C. a, Olivas-armendariz, I., Castro-carmona, J. S. & García-casillas, P. E. Scaffolds for Tissue Engineering Via Thermally Induced Phase Separation. *Adv. Regen. Med.* 275–294 (2011).

175. Janik, H. & Marzec, M. A review: Fabrication of porous polyurethane scaffolds. *Mater. Sci. Eng. C* **48**, 586–591 (2015).

176. Heijkants, R. G. J. C. *et al.* Preparation of a polyurethane scaffold for tissue engineering made by a combination of salt leaching and freeze-drying of dioxane. *J. Mater. Sci.* **41**, 2423–2428 (2006).

177. de Lima, J. A. & Felisberti, M. I. Porous polymer structures obtained via the TIPS process from EVOH/PMMA/DMF solutions. *J. Memb. Sci.* **344**, 237–243 (2009).

178. Bacakova, L., Filova, E., Parizek, M., Ruml, T. & Svorcik, V. Modulation of cell adhesion, proliferation and differentiation on materials designed for body implants.

Biotechnol. Adv. **29**, 739–767 (2011).

179. Büyüköz, M., Erdal, E. & Alsoy Altinkaya, S. Nanofibrous gelatine scaffolds integrated with nerve growth factor-loaded alginate microspheres for brain tissue engineering. *J. Tissue Eng. Regen. Med.* **12**, e707–e719 (2017).

180. Gandolfi, M. G. *et al.* Polylactic acid-based porous scaffolds doped with calcium silicate and dicalcium phosphate dihydrate designed for biomedical application. *Mater. Sci. Eng. C* **82**, 163–181 (2018).

181. Thomson, R. C., Shung, A. K., Yaszemski, M. J. & Mikos, A. G. *Polymer Scaffold Processing. Principles of Tissue Engineering* (Elsevier Inc., 2000).

182. Carfì Pavia, F. *et al.* Modulation of physical and biological properties of a composite PLLA and polyaspartamide derivative obtained via thermally induced phase separation (TIPS) technique. *Mater. Sci. Eng. C* **67**, 561–569 (2016).

183. Salerno, A., Fernández-Gutiérrez, M., San Román Del Barrio, J. & Domingo, C. Bio-safe fabrication of PLA scaffolds for bone tissue engineering by combining phase separation, porogen leaching and scCO2 drying. *J. Supercrit. Fluids* **97**, 238–246 (2015).

184. Salerno, A., Guarino, V., Oliviero, O., Ambrosio, L. & Domingo, C. Bio-safe processing of polylactic-co-caprolactone and polylactic acid blends to fabricate fibrous porous scaffolds for in vitro mesenchymal stem cells adhesion and proliferation. *Mater. Sci. Eng. C* **63**, 512–521 (2016).

185. Mikos, A. G. & Temenoff, J. S. Formation of highly porous biodegradable scaffolds for tissue engineering. *Electronic Journal of Biotechnology; Vol 3, No 2 (2000)* **3**, 1995–2000 (2000).

186. Draghi, L., Resta, S., Pirozzolo, M. G. & Tanzi, M. C. Microspheres leaching for scaffold porosity control. *Journal of Materials Science: Materials in Medicine* **16**, 1093–1097 (2005).

187. Grenier, S., Sandig, M. & Mequanint, K. Polyurethane biomaterials for fabricating 3D porous scaffolds and supporting vascular cells. *Journal of Biomedical Materials Research - Part A* **82**, 802–809 (2007).

188. Zhang, Z. Z. *et al.* Role of scaffold mean pore size in meniscus regeneration. *Acta Biomater.* **43**, 314–326 (2016).

189. Perez, R. A. & Mestres, G. Role of pore size and morphology in musculo-skeletal tissue regeneration. *Mater. Sci. Eng. C* **61**, 922–939 (2016).

190. Bacakova, L., Filova, E., Parizek, M., Ruml, T. & Svorcik, V. Modulation of cell adhesion, proliferation and differentiation on materials designed for body implants. *Biotechnol. Adv.* **29**, 739–767 (2011).

191. Pamula, E. *et al.* The influence of pore size on colonization of poly(L-lactide-glycolide) scaffolds with human osteoblast-like MG 63 cells in vitro. *J. Mater. Sci. Mater. Med.* **19**, 425–435 (2008).

192. Murphy, C. M., Duffy, G. P., Schindeler, A. & O’Brien, F. J. Effect of collagen-glycosaminoglycan scaffold pore size on matrix mineralization and cellular behavior in different cell types. *J. Biomed. Mater. Res. - Part A* **104**, 291–304 (2016).

193. Sin, D. *et al.* Polyurethane (PU) scaffolds prepared by solvent casting/particulate leaching (SCPL) combined with centrifugation. *Mater. Sci. Eng. C* **30**, 78–85 (2010).

194. Stoppato, M. *et al.* Effects of silk fibroin fiber incorporation on mechanical properties, endothelial cell colonization and vascularization of PDLLA scaffolds. *Biomaterials* **34**, 4573–4581 (2013).

195. Moschouris, K., Firoozi, N. & Kang, Y. The application of cell sheet engineering in the vascularization of tissue regeneration. *Regenerative Medicine* **11**, 559–570 (2016).

196. Nomi, M., Atala, A., De Coppi, P. & Soker, S. Principals of neovascularization for tissue engineering. *Molecular Aspects of Medicine* **23**, 463–483 (2002).

197. Liao, C.-J. *et al.* Fabrication of porous biodegradable polymer scaffolds using a solvent merging/particulate leaching method. *J. Biomed. Mater. Res.* **59**, 676–681 (2002).

198. Murphy, W. L., Dennis, R. G., Kileny, J. L. & Mooney, D. J. Salt fusion: an approach to improve pore interconnectivity within tissue engineering scaffolds. *Tissue engineering* **8**, 43–52 (2002).

199. Deng, Y. *et al.* A novel akermanite/poly (lactic-co-glycolic acid) porous composite scaffold fabricated via a solvent casting-particulate leaching method improved by solvent self-proliferating process. *Regen. Biomater.* **4**, 233–242 (2017).

200. Nam, Y. S., Yoon, J. J. & Park, T. G. A novel fabrication method of macroporous biodegradable polymer scaffolds using gas foaming salt as a porogen additive. *Journal of Biomedical Materials Research* **53**, 1–7 (2000).

201. Jing, X., Mi, H. Y. & Turng, L. S. Comparison between PCL/hydroxyapatite (HA) and PCL/halloysite nanotube (HNT) composite scaffolds prepared by co-extrusion and gas foaming. *Materials Science and Engineering C* **72**, 53–61 (2017).

202. Barbetta, A., Gumiero, A., Pecci, R., Bedini, R. & Dentini, M. Gas-in-liquid foam templating as a method for the production of highly porous scaffolds. *Biomacromolecules* **10**, 3188–3192 (2009).

203. Yoon, J. J. & Park, T. G. Degradation behaviors of biodegradable macroporous scaffolds prepared by gas foaming of effervescent salts. *J. Biomed. Mater. Res.* **55**, 401–408 (2001).

204. Dehghani, F. & Annabi, N. Engineering porous scaffolds using gas-based techniques. *Curr. Opin. Biotechnol.* **22**, 661–666 (2011).

205. Barbetta, A., Rizzitelli, G., Bedini, R., Pecci, R. & Dentini, M. Porous gelatin hydrogels by gas-in-liquid foam templating. *Soft Matter* **6**, 1785 (2010).

206. Costantini, M. *et al.* Correlation between porous texture and cell seeding efficiency of gas foaming and microfluidic foaming scaffolds. *Mater. Sci. Eng. C* **62**, 668–677

(2016).

207. Kim, S. H., Kim, J. E., Kim, S. H. & Jung, Y. Substance P/dexamethasone-encapsulated PLGA scaffold fabricated using supercritical fluid process for calvarial bone regeneration. *J. Tissue Eng. Regen. Med.* **11**, 3469–3480 (2017).

208. Moghadam, M. Z., Hassanajili, S., Esmaeilzadeh, F., Ayatollahi, M. & Ahmadi, M. Formation of porous HPCL/LPCL/HA scaffolds with supercritical CO2 gas foaming method. *Journal of the Mechanical Behavior of Biomedical Materials* **69**, 115–127 (2017).

209. Huang, E. *et al.* A novel route to the generation of porous scaffold based on the phase morphology control of co-continuous poly(ε-caprolactone)/polylactide blend in supercritical CO 2. *Polymer (Guildf).* **118**, 163–172 (2017).

210. Bhamidipati, M., Scurto, A. M. & Detamore, M. S. The Future of Carbon Dioxide for Polymer Processing in Tissue Engineering. *Tissue Eng. Part B Rev.* **19**, 221–232 (2013).

211. Zhu, X. H., Lee, L. Y., Jackson, J. S. H., Tong, Y. W. & Wang, C. H. Characterization of porous poly(D,L-Lactic-co-glycolic Acid) sponges fabricated by supercritical CO2 gas-foaming method as a scaffold for three-dimensional growth of hep3b cells. *Biotechnology and Bioengineering* **100**, 998–1009 (2008).

212. Quirk, R. A., France, R. M., Shakesheff, K. M. & Howdle, S. M. Supercritical fluid technologies and tissue engineering scaffolds. *Curr. Opin. Solid State Mater. Sci.* **8**, 313–321 (2004).

213. Barry, J. J. a, Silva, M. M. C. G., Popov, V. K., Shakesheff, K. M. & Howdle, S. M. Supercritical carbon dioxide: putting the fizz into biomaterials. *Philos. Trans. A. Math. Phys. Eng. Sci.* **364**, 249–261 (2006).

214. Kuang, T. *et al.* Facile preparation of open-cellular porous poly (L-lactic acid) scaffold by supercritical carbon dioxide foaming for potential tissue engineering applications. *Chem. Eng. J.* **307**, 1017–1025 (2017).

215. White, L. J., Hutter, V., Tai, H., Howdle, S. M. & Shakesheff, K. M. The effect of processing variables on morphological and mechanical properties of supercritical CO2 foamed scaffolds for tissue engineering. *Acta Biomaterialia* **8**, 61–71 (2012).

216. Ginty, P. J. *et al.* Mammalian cell survival and processing in supercritical CO2. *Proc. Natl. Acad. Sci. U. S. A.* **103**, 7426–7431 (2006).

217. Ginty, P. J. *et al.* A supercritical CO2 injection system for the production of polymer/mammalian cell composites. *J. Supercrit. Fluids* **43**, 535–541 (2008).

218. Cheng, J., Jun, Y., Qin, J. & Lee, S. H. Electrospinning versus microfluidic spinning of functional fibers for biomedical applications. *Biomaterials* **114**, 121–143 (2017).

219. Asti, A. & Gioglio, L. Natural and synthetic biodegradable polymers: different scaffolds for cell expansion and tissue formation. *Int. J. Artif. Organs* **37**, 187–205 (2014).

220. Doshi, J. & Reneker, D. H. Electrospinning process and applications of electrospun fibers. *Conference Record of the 1993 IEEE Industry Applications Conference Twenty-Eighth IAS Annual Meeting* **35**, 151–160 (1993).

221. Bhardwaj, N. & Kundu, S. C. Electrospinning: A fascinating fiber fabrication technique. *Biotechnology Advances* **28**, 325–347 (2010).

222. Wang, S. *et al.* Fabrication and morphology control of electrospun poly(γ-glutamic acid) nanofibers for biomedical applications. *Colloids and Surfaces B: Biointerfaces* **89**, 254–264 (2012).

223. Wang, S. *et al.* Design of electrospun nanofibrous mats for osteogenic differentiation of mesenchymal stem cells. *Nanomedicine Nanotechnology, Biol. Med.* **14**, 2505–2520 (2017).

224. Li, Y., Lim, C. T. & Kotaki, M. Study on structural and mechanical properties of porous PLA nanofibers electrospun by channel-based electrospinning system. *Polymer (United Kingdom)* **56**, 572–580 (2015).

225. Zhang, Z., Hu, J. & Ma, P. X. Nanofiber-based delivery of bioactive agents and stem cells to bone sites. *Advanced Drug Delivery Reviews* **64**, 1129–1141 (2012).

226. Li, D., Ouyang, G., McCann, J. T. & Xia, Y. Collecting electrospun nanofibers with patterned electrodes. *Nano Letters* **5**, 913–916 (2005).

227. Ju, Y. M. *et al.* Electrospun vascular scaffold for cellularized small diameter blood vessels: A preclinical large animal study. *Acta Biomater.* **59**, 58–67 (2017).

228. Zhao, Q., Lu, W. W. & Wang, M. Modulating the release of vascular endothelial growth factor by negative-voltage emulsion electrospinning for improved vascular regeneration. *Mater. Lett.* **193**, 1–4 (2017).

229. Song, W. *et al.* Corona Discharge: A Novel Approach to Fabricate Three-Dimensional Electrospun Nanofibers for Bone Tissue Engineering. *ACS Biomater. Sci. Eng.* **3**, 1146–1153 (2017).

230. Nam, J., Huang, Y., Agarwal, S. & Lannutti, J. Improved Cellular Infiltration in Electrospun Fiber via Engineered Porosity. *Tissue Engineering* **13**, 2249–2257 (2007).

231. Skotak, M., Ragusa, J., Gonzalez, D. & Subramanian, A. Improved cellular infiltration into nanofibrous electrospun cross-linked gelatin scaffolds templated with micrometer-sized polyethylene glycol fibers. *Biomedical Materials* **6**, 055012 (2011).

232. Ehler, E. & Jayasinghe, S. N. Cell electrospinning cardiac patches for tissue engineering the heart. *Analyst* **139**, 4449–4452 (2014).

233. Inozemtseva, O. A. *et al.* Electrospinning of functional materials for biomedicine and tissue engineering. *Russian Chemical Reviews* **84**, 251–274 (2015).

234. Ren, K., Wang, Y., Sun, T., Yue, W. & Zhang, H. Electrospun PCL/gelatin composite nanofiber structures for effective guided bone regeneration membranes. *Mater. Sci. Eng. C* **78**, 324–332 (2017).

235. Wang, C. *et al.* Two-phase electrospinning to incorporate growth factors loaded

chitosan nanoparticles into electrospun fibrous scaffolds for bioactivity retention and cartilage regeneration. *Mater. Sci. Eng. C* **79**, 507–515 (2017).

236. Kai, D., Prabhakaran, M. P., Jin, G., Tian, L. & Ramakrishna, S. Potential of VEGF-encapsulated electrospun nanofibers for in vitro cardiomyogenic differentiation of human mesenchymal stem cells. *J. Tissue Eng. Regen. Med.* **11**, 1002–1010 (2017).

237. Wang, J. *et al.* Evaluation of the potential of rhTGF- β3 encapsulated P(LLA-CL)/collagen nanofibers for tracheal cartilage regeneration using mesenchymal stems cells derived from Wharton's jelly of human umbilical cord. *Mater. Sci. Eng. C* **70**, 637–645 (2017).

238. Zhang, S., Jiang, G., Prabhakaran, M. P., Qin, X. & Ramakrishna, S. Evaluation of electrospun biomimetic substrate surface-decorated with nanohydroxyapatite precipitation for osteoblasts behavior. *Mater. Sci. Eng. C* **79**, 687–696 (2017).

239. Kuttappan, S., Mathew, D. & Nair, M. B. Biomimetic composite scaffolds containing bioceramics and collagen/gelatin for bone tissue engineering - A mini review. *International Journal of Biological Macromolecules* **93**, 1390–1401 (2016).

240. Salifu, A. A., Lekakou, C. & Labeed, F. H. Electrospun oriented gelatin-hydroxyapatite fiber scaffolds for bone tissue engineering. *J. Biomed. Mater. Res. - Part A* **105**, 1911–1926 (2017).

241. Qazi, T. H., Rai, R. & Boccaccini, A. R. Tissue engineering of electrically responsive tissues using polyaniline based polymers: A review. *Biomaterials* **35**, 9068–9086 (2014).

242. Mitra, J., Jain, S., Sharma, A. & Basu, B. Patterned growth and differentiation of neural cells on polymer derived carbon substrates with micro/nano structures in vitro. *Carbon* **65**, 140–155 (2013).

243. Jain, S., Sharma, A. & Basu, B. Vertical electric field stimulated neural cell functionality on porous amorphous carbon electrodes. *Biomaterials* **34**, 9252–9263 (2013).

244. Xu, J., Xie, Y., Zhang, H., Ye, Z. & Zhang, W. Fabrication of PLGA/MWNTs composite electrospun fibrous scaffolds for improved myogenic differentiation of C2C12 cells. *Colloids Surfaces B Biointerfaces* **123**, 907–915 (2014).

245. Manchineella, S. *et al.* Pigmented Silk Nanofibrous Composite for Skeletal Muscle Tissue Engineering. *Adv. Healthc. Mater.* **5**, 1222–1232 (2016).

246. Wang, L., Wu, Y., Hu, T., Guo, B. & Ma, P. X. Electrospun conductive nanofibrous scaffolds for engineering cardiac tissue and 3D bioactuators. *Acta Biomater.* **59**, 68–81 (2017).

247. Stout, D. A., Yoo, J., Santiago-Miranda, A. N. & Webster, T. J. Mechanisms of greater cardiomyocyte functions on conductive nanoengineered composites for cardiovascular applications. *Int. J. Nanomedicine* **7**, 5653–5669 (2012).

248. Dvir, T. *et al.* Nanowired three-dimensional cardiac patches. *Nat. Nanotechnol.* **6**, 720–725 (2011).

249. Thrivikraman, G., Mallik, P. K. & Basu, B. Substrate conductivity dependent modulation of cell proliferation and differentiation in vitro. *Biomaterials* **34**, 7073–7085 (2013).

250. Townsend-Nicholson, A. & Jayasinghe, S. N. Cell electrospinning: A unique biotechnique for encapsulating living organisms for generating active biological microthreads/scaffolds. *Biomacromolecules* **7**, 3364–3369 (2006).

251. Kim, M. *et al.* Highly porous 3D nanofibrous scaffolds processed with an electrospinning/laser process. *Curr. Appl. Phys.* **14**, 1–7 (2014).

252. Sarioglu, O. F., Keskin, N. O. S., Celebioglu, A., Tekinay, T. & Uyar, T. Bacteria encapsulated electrospun nanofibrous webs for remediation of methylene blue dye in water. *Colloids Surfaces B Biointerfaces* **152**, 245–251 (2017).

253. Lancu??ki, A. *et al.* Design of starch-formate compound fibers as encapsulation platform for biotherapeutics. *Carbohydr. Polym.* **158**, 68–76 (2017).

254. Jayasinghe, S. N. Cell electrospinning: a novel tool for functionalising fibres, scaffolds and membranes with living cells and other advanced materials for regenerative biology and medicine. *Analyst* **138**, 2215 (2013).

255. Wang, X. *et al.* 3D bioprinting technologies for hard tissue and organ engineering. *Materials (Basel).* **9**, 1–23 (2016).

256. Martínez Ávila, H., Schwarz, S., Rotter, N. & Gatenholm, P. 3D bioprinting of human chondrocyte-laden nanocellulose hydrogels for patient-specific auricular cartilage regeneration. *Bioprinting* **1**–**2**, 22–35 (2016).

257. Dababneh, A. B. & Ozbolat, I. T. Bioprinting Technology: A Current State-of-the-Art Review. *J. Manuf. Sci. Eng.* **136**, 061016 (2014).

258. Murphy, S. V. & Atala, A. 3D bioprinting of tissues and organs. *Nature biotechnology* **32**, 773–785 (2014).

259. Christensen, K. *et al.* Freeform inkjet printing of cellular structures with bifurcations. *Biotechnology and Bioengineering* **112**, 1047–1055 (2015).

260. Alan, F.-J. *et al.* Bioprinting of human pluripotent stem cells and their directed differentiation into hepatocyte-like cells for the generation of mini-livers in {3D}. *Biofabrication* **7**, 44102 (2015).

261. Xu, C., Chai, W., Huang, Y. & Markwald, R. R. Scaffold-free inkjet printing of three-dimensional zigzag cellular tubes. *Biotechnology and Bioengineering* **109**, 3152–3160 (2012).

262. Skardal, A. *et al.* Bioprinted Amniotic Fluid-Derived Stem Cells Accelerate Healing of Large Skin Wounds. *STEM CELLS Translational Medicine* **1**, 792–802 (2012).

263. Yanez, M. *et al.* In vivo assessment of printed microvasculature in a bilayer skin graft to treat full-thickness wounds. *Tissue Eng Part A* **21**, 224–233 (2015).

264. Hoch, E., Hirth, T., Tovar, G. E. M. & Borchers, K. Chemical tailoring of gelatin to

adjust its chemical and physical properties for functional bioprinting. *Journal of Materials Chemistry B* **1**, 5675 (2013).

265. Compaan, A. M., Christensen, K. & Huang, Y. Inkjet Bioprinting of 3D Silk Fibroin Cellular Constructs Using Sacrificial Alginate. *ACS Biomaterials Science and Engineering* **3**, 1519–1526 (2017).

266. Cui, X., Breitenkamp, K., Finn, M. G. G., Lotz, M. & D'Lima, D. D. Direct human cartilage repair using three-dimensional bioprinting technology. *Tissue Engineering Part A* **18**, 1304–1312 (2012).

267. Gao, G. *et al.* Bioactive nanoparticles stimulate bone tissue formation in bioprinted three-dimensional scaffold and human mesenchymal stem cells. *Biotechnology Journal* **9**, 1304–1311 (2014).

268. Gao, G., Yonezawa, T., Hubbell, K., Dai, G. & Cui, X. Inkjet-bioprinted acrylated peptides and PEG hydrogel with human mesenchymal stem cells promote robust bone and cartilage formation with minimal printhead clogging. *Biotechnology Journal* **10**, 1568–1577 (2015).

269. Cui, X., Breitenkamp, K., Lotz, M. & D'Lima, D. Synergistic action of fibroblast growth factor-2 and transforming growth factor-beta1 enhances bioprinted human neocartilage formation. *Biotechnology and Bioengineering* **109**, 2357–2368 (2012).

270. Gao, G. *et al.* Improved properties of bone and cartilage tissue from 3D inkjet-bioprinted human mesenchymal stem cells by simultaneous deposition and photocrosslinking in PEG-GelMA. *Biotechnology Letters* **37**, 2349–2355 (2015).

271. Pereira, R. F. & Bártolo, P. J. 3D bioprinting of photocrosslinkable hydrogel constructs. *Journal of Applied Polymer Science* **132**, (2015).

272. Cui, X. F., Dean, D., Ruggeri, Z. M. & Boland, T. Cell Damage Evaluation of Thermal Inkjet Printed Chinese Hamster Ovary Cells. *Biotechnology and Bioengineering* **106**, 963–969 (2010).

273. Lorber, B., Hsiao, W., Hutchings, I. & Martin, K. Adult rat retinal ganglion cells and glia can be printed by piezoelectric inkjet printing. *Biofabrication* **6**, 15001 (2014).

274. Vyas, C. *et al.* Engineering the vasculature with additive manufacturing. *Curr. Opin. Biomed. Eng.* **2**, 1–13 (2017).

275. Sears, N. A., Seshadr, D. R., Dhavalikar, P. S. & Cosgriff-Hernandez, E. A review of three-diementional printing in tissue engineering. *Tissue Eng. Part B Rev.* **22**, 298–310 (2016).

276. Cui, X. & Boland, T. Human microvasculature fabrication using thermal inkjet printing technology. *Biomaterials* **30**, 6221–6227 (2009).

277. Xu, T. *et al.* Complex heterogeneous tissue constructs containing multiple cell types prepared by inkjet printing technology. *Biomaterials* **34**, 130–139 (2013).

278. Ng, W. L., Yeong, W. Y. & Naing, M. W. Polyelectrolyte gelatin-chitosan hydrogel optimized for 3D bioprinting in skin tissue engineering. *International Journal of Bioprinting* **2**, (2016).

279. Johnson, B. N. *et al.* 3D Printed Anatomical Nerve Regeneration Pathways. *Advanced Functional Materials* **25**, 6205–6217 (2015).

280. Merceron, T. K. *et al.* A 3D bioprinted complex structure for engineering the muscle–tendon unit. *Biofabrication* **7**, 035003 (2015).

281. Duan, B., Hockaday, L. A., Kang, K. H. & Butcher, J. T. 3D Bioprinting of heterogeneous aortic valve conduits with alginate/gelatin hydrogels. *Journal of Biomedical Materials Research - Part A* **101 A**, 1255–1264 (2013).

282. Zhang, Y. S. *et al.* Bioprinting 3D microfibrous scaffolds for engineering endothelialized myocardium and heart-on-a-chip. *Biomaterials* **110**, 45–59 (2016).

283. You, F. *et al.* 3D Printing of Porous Cell-Laden Hydrogel Constructs for Potential Applications in Cartilage Tissue Engineering. *ACS Biomaterials Science and*

Engineering **2**, 1200–1210 (2016).

284. Huang, Y., Zhang, X., Gao, G., Yonezawa, T. & Cui, X. 3D bioprinting and the current applications in tissue engineering. (2017). doi:10.1002/biot.201600734

285. Billiet, T., Gevaert, E., De Schryver, T., Cornelissen, M. & Dubruel, P. The 3D printing of gelatin methacrylamide cell-laden tissue-engineered constructs with high cell viability. *Biomaterials* **35**, 49–62 (2014).

286. Zhao, Y., Li, Y., Mao, S., Sun, W. & Yao, R. The influence of printing parameters on cell survival rate and printability in microextrusion-based 3D cell printing technology. *Biofabrication* **7**, 045002 (2015).

287. Zhang, Y., Yu, Y. & Ozbolat, I. T. Direct Bioprinting of Vessel-Like Tubular Microfluidic Channels. *Journal of Nanotechnology in Engineering and Medicine* **4**, 020902 (2013).

288. Markstedt, K. *et al.* 3D bioprinting human chondrocytes with nanocellulose-alginate bioink for cartilage tissue engineering applications. *Biomacromolecules* **16**, 1489–1496 (2015).

289. Lee, V. K. *et al.* Creating perfused functional vascular channels using 3D bio-printing technology. *Biomaterials* **35**, 8092–8102 (2014).

290. Schuurman, W. *et al.* Bioprinting of hybrid tissue constructs with tailorable mechanical properties. *Biofabrication* **3**, 021001 (2011).

291. Jia, W. *et al.* Direct 3D bioprinting of perfusable vascular constructs using a blend bioink. *Biomaterials* **106**, 58–68 (2016).

292. Kolesky, D. B. *et al.* 3D bioprinting of vascularized, heterogeneous cell-laden tissue constructs. *Advanced Materials* **26**, 3124–3130 (2014).

293. Kang, H.-W. *et al.* A 3D bioprinting system to produce human-scale tissue constructs with structural integrity. *Nature Biotechnology* **34**, 312–319 (2016).

294. Nakamura, M., Iwanaga, S., Henmi, C., Arai, K. & Nishiyama, Y. Biomatrices and biomaterials for future developments of bioprinting and biofabrication. *Biofabrication* **2**, 014110 (2010).

295. Gao, Q., He, Y., Fu, J. zhong, Liu, A. & Ma, L. Coaxial nozzle-assisted 3D bioprinting with built-in microchannels for nutrients delivery. *Biomaterials* **61**, 203–215 (2015).

296. Zhang, Y. *et al.* In vitro study of directly bioprinted perfusable vasculature conduits. *Biomater. Sci.* **3**, 134–143 (2015).

297. Visser, J. *et al.* Biofabrication of multi-material anatomically shaped tissue constructs. *Biofabrication* **5**, 035007 (2013).

298. Li, J., Chen, M., Fan, X. & Zhou, H. Recent advances in bioprinting techniques: Approaches, applications and future prospects. *Journal of Translational Medicine* **14**, (2016).

299. Deville, S. Freeze-casting of porous biomaterials: Structure, properties and opportunities. *Materials (Basel).* **3**, 1913–1927 (2010).

300. Gutiérrez, M. C., Ferrer, M. L. & Del Monte, F. Ice-templated materials: Sophisticated structures exhibiting enhanced functionalities obtained after unidirectional freezing and ice-segregation- induced self-assembly. *Chem. Mater.* **20**, 634–648 (2008).

301. Christoph, S. *et al.* Ice-templating beet-root pectin foams : Controlling texture , mechanics and capillary properties. *Chem. Eng. J.* **350**, 20–28 (2018).

302. Munch, E. *et al.* Tough, Bio-Inspired Hybrid Materials. *Science* **322**, 1516–1520 (2008).

303. Huang, C. *et al.* Ultra-Tough Inverse Artificial Nacre Based on Epoxy-Graphene by Freeze-Casting. *Angew. Chem. Int. Ed.* **131**, 7718–7722 (2019).

304. Wicklein, B. *et al.* Thermally insulating and fire-retardant lightweight anisotropic foams based on nanocellulose and graphene oxide. *Nat. Nanotechnol.* **10**, 277–283

(2015).

305. Deville, S. Freeze-casting of porous ceramics: A review of current achievements and issues. *Adv. Eng. Mater.* **10**, 155–169 (2008).

306. Xie, M. *et al.* Flexible and active self-powered pressure, shear sensors based on freeze casting ceramic-polymer composites. *Energy Environ. Sci.* **11**, 2919–2927 (2018).

307. Zhang, Y., Roscow, J., Xie, M. & Bowen, C. High piezoelectric sensitivity and hydrostatic figures of merit in unidirectional porous ferroelectric ceramics fabricated by freeze casting. *J. Eur. Ceram. Soc.* **38**, 4203–4211 (2018).

308. Gutiérrez, M. C. *et al.* Hydrogel scaffolds with immobilized bacteria for 3D cultures. *Chem. Mater.* **19**, 1968–1973 (2007).

309. Singh, G. & Soundarapandian, S. Effect of particle size and freezing conditions on freeze-casted scaffold. *Ceram. Int.* **45**, 11633–11638 (2019).

310. Xie, L. *et al.* High porosity Ca-α-SiAlON ceramics with rod-like grains fabricated by freeze casting and pressureless sintering. *J. Eur. Ceram. Soc.* **39**, 2036–2041 (2019).

311. Zhang, H., Long, J. & Cooper, A. I. Aligned porous materials by directional freezing of solutions in liquid CO2. *J. Am. Chem. Soc.* **127**, 13482–13483 (2005).

312. Scotti, K. L. & Dunand, D. C. Freeze casting – A review of processing, microstructure and properties via the open data repository, FreezeCasting.net. *Prog. Mater. Sci.* **94**, 243–305 (2018).

313. Wegst, U. G. K., Schecter, M., Donius, A. E. & Hunger, P. M. Biomaterials by freeze casting. *Philos. Trans. R. Soc. A Math. Phys. Eng. Sci.* **368**, 2099–2121 (2010).

314. Mallick, K. K. Freeze casting of porous bioactive glass and bioceramics. in *Journal of the American Ceramic Society* **92**, (2009).

315. Francis, N. L. *et al.* An ice-templated, linearly aligned chitosan-alginate scaffold for neural tissue engineering. *J. Biomed. Mater. Res. - Part A* **101**, 3493–3503 (2013).

316. Arav, A. & Saragusty, J. Directional freezing of sperm and associated derived technologies. *Anim. Reprod. Sci.* **169**, 6–13 (2016).

317. Bahari, L., Bein, A., Yashunsky, V. & Braslavsky, I. Directional freezing for the cryopreservation of adherent mammalian cells on a substrate. *PLoS One* **13**, 1–17 (2018).

318. Ishiguro, H. & Rubinsky, B. Mechanical interactions between ice crystals and red blood cells during directional solidification. *Cryobiology* **31**, 483–500 (1994).

319. Chaunier, L. *et al.* Material extrusion of plant biopolymers: Opportunities & challenges for 3D printing. *Addit. Manuf.* **21**, 220–233 (2018).

320. Lama, M. *et al.* Self-Assembled Collagen Microparticles by Aerosol as a Versatile Platform for Injectable Anisotropic Materials. *Small* **1902224**, 1–8 (2019).

321. Wegst, U. G. K., Bai, H., Saiz, E., Tomsia, A. P. & Ritchie, R. O. Bioinspired structural materials. *Nat. Mater.* **14**, 23–36 (2015).

322. Luz, G. M. & Mano, J. F. Biomimetic design of materials and biomaterials inspired by the structure of nacre. *Philos. Trans. R. Soc. A Math. Phys. Eng. Sci.* **367**, 1587–1605 (2009).

323. Yao, H. Bin, Ge, J., Mao, L. B., Yan, Y. X. & Yu, S. H. 25th anniversary article: Artificial carbonate nanocrystals and layered structural nanocomposites inspired by nacre: Synthesis, fabrication and applications. *Adv. Mater.* **26**, 163–188 (2014).

324. Currey, J. D. Mechanical properties of mother of pearl in tension. *Proc. R. Soc. London - Biol. Sci.* **196**, 443–463 (1977).

325. Wei, H., Ma, N., Shi, F., Wang, Z. & Zhang, X. Artificial nacre by alternating preparation of layer-by-layer polymer films and CaCO3 strata. *Chem. Mater.* **19**, 1974–1978 (2007).

326. Podsiadlo, P. *et al.* Ultrastrong and stiff layered polymer nanocomposites. *Science* **318**,

80–83 (2007).

327. Lin, W., Wang, C. an, Le, H., Long, B. & Huang, Y. Special assembly of laminated nanocomposite that mimics nacre. *Mater. Sci. Eng. C* **28**, 1031–1037 (2008).

328. Wat, A. *et al.* Bioinspired nacre-like alumina with a bulk-metallic glass-forming alloy as a compliant phase. *Nat. Commun.* **10**, (2019).

329. Garnier, M. J. & Dunand, D. C. Ni-Al2O3 nacre-like composites through hot-pressing of freeze-cast foams. *Mater. Sci. Eng. A* **743**, 190–196 (2019).

330. Guo, R. F., Guo, N., Shen, P., Yang, L. K. & Jiang, Q. C. Effects of ceramic lamellae compactness and interfacial reaction on the mechanical properties of nacre-inspired Al/Al2O3–ZrO2 composites. *Mater. Sci. Eng. A* **718**, 326–334 (2018).

331. Bouville, F. *et al.* Strong, tough and stiff bioinspired ceramics from brittle constituents. *Nat. Mater.* **13**, 508–514 (2014).

332. Launey, M. E. *et al.* Designing highly toughened hybrid composites through nature-inspired hierarchical complexity. *Acta Mater.* **57**, 2919–2932 (2009).

333. Yang, J. *et al.* Photodriven Shape-Stabilized Phase Change Materials with Optimized Thermal Conductivity by Tailoring the Microstructure of Hierarchically Ordered Hybrid Porous Scaffolds. *ACS Sustain. Chem. Eng.* **6**, 6761–6770 (2018).

334. Picot, O. T. *et al.* Using graphene networks to build bioinspired self-monitoring ceramics. *Nat. Commun.* **8**, (2017).

335. Lian, G. *et al.* Vertically Aligned and Interconnected Graphene Networks for High Thermal Conductivity of Epoxy Composites with Ultralow Loading. *Chem. Mater.* **28**, 6096–6104 (2016).

336. Mao, L. B. *et al.* Synthetic nacre by predesigned matrix-directed mineralization. *Science* **354**, 107–110 (2016).

337. Hing, K. A. Bone repair in the twenty-first century: Biology, chemistry or engineering?

Philosophical Transactions of the Royal Society A: Mathematical, Physical and Engineering Sciences **362**, 2821–2850 (2004).

338. Reznikov, N., Shahar, R. & Weiner, S. Bone hierarchical structure in three dimensions. *Acta Biomater.* **10**, 3815–3826 (2014).

339. Eckstein, F. *et al.* Sex differences of human trabecular bone microstructure in aging are site-dependent. *J. Bone Miner. Res.* **22**, 817–824 (2007).

340. Burrows, M., Liu, D., Moore, S. & McKay, H. Bone microstructure at the distal tibia provides a strength advantage to males in late puberty: An HR-pQCT study. *J. Bone Miner. Res.* **25**, 1423–1432 (2010).

341. Deville, S. Ice-templating, freeze casting: Beyond materials processing. *Journal of Materials Research* **28**, 2202–2219 (2013).

342. Ryan, T. M. & Krovitz, G. E. Trabecular bone ontogeny in the human proximal femur. *J. Hum. Evol.* **51**, 591–602 (2006).

343. Deville, S., Saiz, E. & Tomsia, A. P. Freeze casting of hydroxyapatite scaffolds for bone tissue engineering. *Biomaterials* **27**, 5480–5489 (2006).

344. Reed, S. *et al.* Macro- and micro-designed chitosan-alginate scaffold architecture by three-dimensional printing and directional freezing. *Biofabrication* **8**, (2016).

345. Song, X. *et al.* Biomimetic 3D Printing of Hierarchical and Interconnected Porous Hydroxyapatite Structures with High Mechanical Strength for Bone Cell Culture. *Adv. Eng. Mater.* **21**, 1800678 (2018).

346. Jung, J. Y. *et al.* 3D Printed Templating of Extrinsic Freeze-Casting for Macro-Microporous Biomaterials. *ACS Biomater. Sci. Eng.* **5**, 2122–2133 (2019).

347. Clearfield, D., Nguyen, A. & Wei, M. Biomimetic multidirectional scaffolds for zonal osteochondral tissue engineering via a lyophilization bonding approach. *J. Biomed. Mater. Res. - Part A* **106**, 948–958 (2018).

348. Pek, Y. S., Gao, S., Arshad, M. S. M., Leck, K. J. & Ying, J. Y. Porous collagen-apatite nanocomposite foams as bone regeneration scaffolds. *Biomaterials* **29**, 4300–4305 (2008).

349. Kameo, Y., Sakano, N. & Adachi, T. Theoretical concept of cortical to cancellous bone transformation. *Bone Reports* 100260 (2020).

350. Zhou, X., Novotny, J. E. & Wang, L. Anatomic variations of the lacunar-canalicular system influence solute transport in bone. *Bone* **45**, 704–710 (2009).

351. Qiu, S., Fyhrie, D. P., Palnitkar, S. & Sudhaker Rao, D. Histomorphometric assessment of Haversian canal and osteocyte lacunae in different-sized osteons in human rib. *Anat. Rec. - Part A Discov. Mol. Cell. Evol. Biol.* **272**, 520–525 (2003).

352. Bidan, C. M. *et al.* Geometry as a Factor for Tissue Growth: Towards Shape Optimization of Tissue Engineering Scaffolds. *Adv. Healthc. Mater.* **2**, 186–194 (2013).

353. Rumpler, M., Woesz, A., Dunlop, J. W. C., van Dongen, J. T. & Fratzl, P. The effect of geometry on three-dimensional tissue growth. *J. R. Soc. Interface* **5**, 1173–1180 (2008).

354. Engler, A. J., Sen, S., Sweeney, H. L. & Discher, D. E. Matrix Elasticity Directs Stem Cell Lineage Specification. *Cell* **126**, 677–689 (2006).

355. Palchesko, R. N., Lathrop, K. L., Funderburgh, J. L. & Feinberg, A. W. In vitro expansion of corneal endothelial cells on biomimetic substrates. *Sci. Rep.* **5**, 7955 (2015).

356. Pawelec, K. M., Husmann, A., Best, S. M. & Cameron, R. E. Ice-templated structures for biomedical tissue repair: From physics to final scaffolds. *Applied Physics Reviews* **1**, 021301 (2014).

357. Figueiredo, L. *et al.* Assessing glucose and oxygen diffusion in hydrogels for the rational design of 3D stem cell scaffolds in regenerative medicine. *J. Tissue Eng.*

Regen. Med. **12**, 1238–1246 (2018).

358. Malda, J. *et al.* Oxygen Gradients in Tissue-Engineered PEGT/PBT Cartilaginous Constructs: Measurement and Modeling. *Biotechnol. Bioeng.* **86**, 9–18 (2004).

359. Yang, D. *et al.* Promoting Cell Migration in Tissue Engineering Scaffolds with Graded Channels. *Adv. Healthc. Mater.* **6**, 1700472 (2017).

360. Shamir, E. R. & Ewald, A. J. Three-dimensional organotypic culture: Experimental models of mammalian biology and disease. *Nat. Rev. Mol. Cell Biol.* **15**, 647–664 (2014).

361. Husmann, A., Pawelec, K., Burdett, C., Best, S. & Cameron, R. Numerical simulations to determine the influence of mould design on ice-templated scaffold structures. *J. Biomed. Eng. Informatics* **1**, 47 (2015).

362. Pawelec, K. M., Husmann, A., Best, S. M. & Cameron, R. E. A design protocol for tailoring ice-templated scaffold structure. *J. R. Soc. Interface* **11**, (2014).

363. Thibert, E. & Dominé, F. Thermodynamics and Kinetics of the Solid Solution of HNO $_3$ in Ice. *J. Phys. Chem. B* **102**, 4432–4439 (1998).

364. Thibert, E. & Dominé, F. *Thermodynamics and Kinetics of the Solid Solution of HCl in Ice*. (1997).

365. Asuncion, M. C. T., Goh, J. C. H. & Toh, S. L. Anisotropic silk fibroin/gelatin scaffolds from unidirectional freezing. *Mater. Sci. Eng. C* **67**, 646–656 (2016).

366. Meurice, E. *et al.* Osteoblastic cells colonization inside beta-TCP macroporous structures obtained by ice-templating. *J. Eur. Ceram. Soc.* **36**, 2895–2901 (2016).

367. Ghorbani, F., Zamanian, A., Kermanian, F. & Shamoosi, A. A bioinspired 3D shape olibanum-collagen-gelatin scaffolds with tunable porous microstructure for efficient neural tissue regeneration. *Biotechnol. Prog.* **36**, e2918 (2019).

368. Semyari, H. *et al.* Fabrication and characterization of collagen–hydroxyapatite-based

composite scaffolds containing doxycycline via freeze-casting method for bone tissue engineering. *J. Biomater. Appl.* **33**, 501–513 (2018).

369. Cheng, Z., Zhao, K. & Wu, Z. P. Structure control of hydroxyapatite ceramics via an electric field assisted freeze casting method. *Ceram. Int.* **41**, 8599–8604 (2015).

370. Liu, B. *et al.* Improved osteoblasts growth on osteomimetic hydroxyapatite/BaTiO3 composites with aligned lamellar porous structure. *Mater. Sci. Eng. C* **61**, 8–14 (2016).

371. Giraud Guille, M. M., Nassif, N. & Fernandes, F. M. Collagen-based Materials for Tissue Repair, from Bio-inspired to Biomimetic. in *Materials Design Inspired by Nature: Function Through Inner Architecture* 107–127 (2013).

372. Davidenko, N., Campbell, J. J., Thian, E. S., Watson, C. J. & Cameron, R. E. Collagen-hyaluronic acid scaffolds for adipose tissue engineering. *Acta Biomater.* **6**, 3957–3968 (2010).

373. Beri, P. *et al.* Biomaterials to model and measure epithelial cancers. *Nat. Rev. Mater.* **3**, 418–430 (2018).

374. Xu, S. *et al.* The role of collagen in cancer: From bench to bedside. *J. Transl. Med.* **17**, 1–22 (2019).

375. Campbell, J. J., Husmann, A., Hume, R. D., Watson, C. J. & Cameron, R. E. Development of three-dimensional collagen scaffolds with controlled architecture for cell migration studies using breast cancer cell lines. *Biomaterials* **114**, 34–43 (2017).

376. Zehbe, R., Goebbels, J., Ibold, Y., Gross, U. & Schubert, H. Three-dimensional visualization of in vitro cultivated chondrocytes inside porous gelatine scaffolds: A tomographic approach. *Acta Biomater.* **6**, 2097–2107 (2010).

377. Arabi, N., Zamanian, A., Rashvand, S. N. & Ghorbani, F. The Tunable Porous Structure of Gelatin–Bioglass Nanocomposite Scaffolds for Bone Tissue Engineering Applications: Physicochemical, Mechanical, and In Vitro Properties. *Macromol. Mater. Eng.* **303**, (2018).

378. Yang, M., Shuai, Y., Sunderland, K. S. & Mao, C. Ice-Templated Protein Nanoridges Induce Bone Tissue Formation. *Adv. Funct. Mater.* **27**, 1–9 (2017).

379. Ghorbani, F., Zamanian, A. & Nojehdehian, H. Effects of pore orientation on in-vitro properties of retinoic acid-loaded PLGA/gelatin scaffolds for artificial peripheral nerve application. *Mater. Sci. Eng. C* **77**, 159–172 (2017).

380. Lien, S. M., Ko, L. Y. & Huang, T. J. Effect of pore size on ECM secretion and cell growth in gelatin scaffold for articular cartilage tissue engineering. *Acta Biomater.* **5**, 670–679 (2009).

381. Farokhi, M., Mottaghitalab, F., Fatahi, Y., Khademhosseini, A. & Kaplan, D. L. Overview of Silk Fibroin Use in Wound Dressings. *Trends in Biotechnology* **36**, 907–922 (2018).

382. Thurber, A. E., Omenetto, F. G. & Kaplan, D. L. In vivo bioresponses to silk proteins. *Biomaterials* **71**, 145–157 (2015).

383. Wang, Y., Kim, H. J., Vunjak-Novakovic, G. & Kaplan, D. L. Stem cell-based tissue engineering with silk biomaterials. *Biomaterials* **27**, 6064–6082 (2006).

384. Shokrollahi, H., Salimi, F. & Doostmohammadi, A. The fabrication and characterization of barium titanate/akermanite nano-bio-ceramic with a suitable piezoelectric coefficient for bone defect recovery. *J. Mech. Behav. Biomed. Mater.* **74**, 365–370 (2017).

385. Mandal, B. B., Gil, E. S., Panilaitis, B. & Kaplan, D. L. Laminar Silk Scaffolds for Aligned Tissue Fabrication. *Macromol. Biosci.* **13**, 48–58 (2013).

386. Maleki, H. *et al.* Mechanically Strong Silica-Silk Fibroin Bioaerogel: A Hybrid Scaffold with Ordered Honeycomb Micromorphology and Multiscale Porosity for Bone Regeneration. *ACS Appl. Mater. Interfaces* **11**, 17256–17269 (2019).

387. Feng, X. *et al.* Influence of pore architectures of silk fibroin/collagen composite scaffolds on the regeneration of osteochondral defects in vivo. *J. Mater. Chem. B* **8**,

391–405 (2019).

388. Xia, Z. *et al.* Fabrication and characterization of biomimetic collagen-apatite scaffolds with tunable structures for bone tissue engineering. *Acta Biomater.* **9**, 7308–7319 (2013).

389. Yin, K. *et al.* Freeze-cast Porous Chitosan Conduit for Peripheral Nerve Repair. in *MRS Advances* **3**, 1677–1683 (Materials Research Society, 2018).

390. Lee, J. M. *et al.* Three dimensional poly(ε-caprolactone) and silk fibroin nanocomposite fibrous matrix for artificial dermis. *Mater. Sci. Eng. C* **68**, 758–767 (2016).

391. Wang, Z. *et al.* Remodeling of a Cell-Free Vascular Graft with Nanolamellar Intima into a Neovessel. *ACS Nano* **13**, 10576–10586 (2019).

392. Leong, M. F., Rasheed, M. Z., Lim, T. C. & Chian, K. S. In vitro cell infiltration and in vivo cell infiltration and vascularization in a fibrous, highly porous poly(D,L-lactide) scaffold fabricated by cryogenic electrospinning technique. *J. Biomed. Mater. Res. - Part A* **91**, 231–240 (2009).

393. Thibert, E. & Dominé, F. Thermodynamics and kinetics of the solid solution of HCl in ice. *J. Phys. Chem. B* **101**, 3554–3565 (1997).

394. Thibert, E. & Dominé, F. Thermodynamics and kinetics of the solid solution of HNO3 in ice. *J. Phys. Chem. B* **102**, 4432–4439 (1998).

395. Corte, A. E. Vertical migration of particles in front of a moving freezing plane. *J. Geophys. Res.* **67**, 1085–1090 (1962).

396. Dedovets, D. & Deville, S. Multiphase imaging of freezing particle suspensions by confocal microscopy. *J. Eur. Ceram. Soc.* **38**, 2687–2693 (2018).

397. Saint-Michel, B., Georgelin, M., Deville, S. & Pocheau, A. Interaction of Multiple Particles with a Solidification Front: From Compacted Particle Layer to Particle

Trapping. *Langmuir* **33**, 5617–5627 (2017).

398. Deville, S. Understanding the Freezing of Colloidal Suspensions: Crystal Growth and Particle Redistribution. in *Freezing Colloids: Observations, Principles, Control, and Use: Applications in Materials Science, Life Science, Earth Science, Food Science, and Engineering* 91–170 (Springer, Cham, 2017).

399. Bronstein, V. L., Itkin, Y. A. & Ishkov, G. S. Rejection and capture of cells by ice crystals on freezing aqueous solutions. *J. Cryst. Growth* **52**, 345–349 (1981).

400. Körber, C. Phenomena at the advancing ice—liquid interface: Solutes particles and biological cells. *Q. Rev. Biophys.* **21**, 229–298 (1988).

401. Rubinsky, B. & Ikeda, M. *A Cryomicroscope Using Directional Solidification for the Controlled Freezing of Biological Material*. *CRYOBIOLOGY* **22**, (1985).

402. Ishiguro, H. & Koike, K. Three-dimensional behavior of ice crystals and biological cells during freezing of cell suspensions. in *Annals of the New York Academy of Sciences* **858**, 235–244 (1998).

403. Hubel, A., Darr, T. B., Chang, A. & Dantzig, J. Cell partitioning during the directional solidification of trehalose solutions. *Cryobiology* **55**, 182–188 (2007).

404. Saragusty, J., Lemma, A., Hildebrandt, T. B. & Göritz, F. Follicular size predicts success in artificial insemination with frozen-Thawed sperm in donkeys. *PLoS One* **12**, (2017).

405. Saragusty, J., Osmers, J. H. & Hildebrandt, T. B. Controlled ice nucleation-Is it really needed for large-volume sperm cryopreservation? *Theriogenology* **85**, 1328–1333 (2016).

406. Robeck, T. R. *et al.* In vitro sperm characterization and development of a sperm cryopreservation method using directional solidification in the killer whale (Orcinus orca). *Theriogenology* **76**, 267–279 (2011).

407. Uemura, M. & Ishiguro, H. Freezing behavior of adherent neuron-like cells and morphological change and viability of post-thaw cells. *Cryobiology* **70**, 122–135 (2015).

408. Arav, A. *et al.* Ovarian function 6 years after cryopreservation and transplantation of whole sheep ovaries. *Reprod. Biomed. Online* **20**, 48–52 (2010).

409. Best, B. P. Cryoprotectant Toxicity: Facts, Issues, and Questions. *Rejuvenation Res.* **18**, 422–436 (2015).

410. Baccile, N. *et al.* Unveiling the Interstitial Pressure between Growing Ice Crystals during Ice-Templating Using a Lipid Lamellar Probe. *J. Phys. Chem. Lett.* **11**, 1989–1997 (2020).

411. Holland, C., Numata, K., Rnjak-Kovacina, J. & Seib, F. P. The Biomedical Use of Silk: Past, Present, Future. *Advanced Healthcare Materials* **8**, (2019).

412. The renaissance of silk in surgery. *JAMA - J. Am. Med. Assoc.* **113**, 1417 (1939).

413. Clemens, M. W. *et al.* Clinical application of a silk fibroin protein biologic scaffold for abdominal wall fascial reinforcement. *Plast. Reconstr. Surg. - Glob. Open* **2**, 1–10 (2014).

414. Gil, E. S., Panilaitis, B., Bellas, E. & Kaplan, D. L. Functionalized Silk Biomaterials for Wound Healing. *Adv. Healthc. Mater.* **2**, 206–217 (2013).

415. Min, B. M., Jeong, L., Lee, K. Y. & Park, W. H. Regenerated silk fibroin nanofibers: Water vapor-induced structural changes and their effects on the behavior of normal human cells. *Macromol. Biosci.* **6**, 285–292 (2006).

416. Sugihara, A. *et al.* Promotive effects of a silk fibroin and polarized hydroxyapatite on epidermal recovery from full-thickness skin wounds (44552). *Proc. Soc. Exp. Biol. Med.* **225**, 58–64 (2000).

417. Pecquet, C. Allergic reactions to insect secretions. *European Journal of Dermatology*

23, 767–773 (2013).

418. Kunz, R. I., Brancalhão, R. M. C., Ribeiro, L. D. F. C. & Natali, M. R. M. Silkworm Sericin: Properties and Biomedical Applications. *BioMed Research International* **2016**, (2016).

419. Gilotra, S., Chouhan, D., Bhardwaj, N., Nandi, S. K. & Mandal, B. B. Potential of silk sericin based nanofibrous mats for wound dressing applications. *Mater. Sci. Eng. C* **90**, 420–432 (2018).

420. Chen, C. S. *et al.* Three-Dimensionally Printed Silk-Sericin-Based Hydrogel Scaffold: A Promising Visualized Dressing Material for Real-Time Monitoring of Wounds. *ACS Appl. Mater. Interfaces* **10**, 33879–33890 (2018).

421. Mandal, B. B., Priya, A. S. & Kundu, S. C. Novel silk sericin/gelatin 3-D scaffolds and 2-D films: Fabrication and characterization for potential tissue engineering applications. *Acta Biomater.* **5**, 3007–3020 (2009).

422. Zhang, Y. Q. Applications of natural silk protein sericin in biomaterials. *Biotechnol. Adv.* **20**, 91–100 (2002).

423. Rockwood, D. N. *et al.* Materials fabrication from Bombyx mori silk fibroin. *Nat. Protoc.* **6**, 1612–1631 (2011).

424. Qiu, W., Patil, A., Hu, F. & Liu, X. Y. Hierarchical Structure of Silk Materials Versus Mechanical Performance and Mesoscopic Engineering Principles. *Small* **15**, (2019).

425. Ling, S., Kaplan, D. L. & Buehler, M. J. Nanofibrils in nature and materials engineering. *Nat. Rev. Mater.* **3**, (2018).

426. Jaafar, Z. *et al.* Plant Cell wall inspired Xyloglucan/Cellulose Nanocrystals Aerogels Produced By Freeze-Casting. *Carbohydr. Polym.* **247**, 116544 (2020).

427. Oliveira, A. L. *et al.* Aligned silk-based 3-D architectures for contact guidance in tissue engineering. *Acta Biomater.* **8**, 1530–1542 (2012).

428. Maslow, M. J. & Portal-Celhay, C. Rifamycins. in *Mandell, Douglas, and Bennett's Principles and Practice of Infectious Diseases* 337–349 (Elsevier, 2019).

429. Sarheed, O., Ahmed, A., Shouqair, D. & Boateng, J. Antimicrobial Dressings for Improving Wound Healing. in *Wound Healing - New insights into Ancient Challenges* (InTech, 2016).

430. Helary, C. *et al.* Evaluation of dense collagen matrices as medicated wound dressing for the treatment of cutaneous chronic wounds. *Biomater. Sci.* **3**, 373–382 (2015).

431. Panasci, K. Burns and Wounds. in *Acute Care Handbook for Physical Therapists (Fourth Edition)* 283–311 (2014).

432. Kamel, R. A., Ong, J. F., Eriksson, E., Junker, J. P. E. & Caterson, E. J. Tissue engineering of skin. *Journal of the American College of Surgeons* **217**, 533–555 (2013).

433. Smith, D. M. *et al.* Evaluation of the bacterial diversity of Pressure ulcers using bTEFAP pyrosequencing. *BMC Med. Genomics* **3**, (2010).

434. Gianino, E., Miller, C. & Gilmore, J. Smart wound dressings for diabetic chronic wounds. *Bioengineering* **5**, (2018).

435. Schindelin, J. *et al.* Fiji: An open-source platform for biological-image analysis. *Nature Methods* **9**, 676–682 (2012).

436. Jin, H. J. *et al.* Water-stable silk films with reduced β-sheet content. *Adv. Funct. Mater.* **15**, 1241–1247 (2005).

437. Lu, Q. *et al.* Water-insoluble silk films with silk I structure. *Acta Biomater.* **6**, 1380–1387 (2010).

438. Lu, S. *et al.* Insoluble and flexible silk films containing glycerol. *Biomacromolecules* **11**, 143–150 (2010).

439. Lu, S. *et al.* The influence of the hydrophilic-lipophilic environment on the structure of

silk fibroin protein. *J. Mater. Chem. B* **3**, 2599–2606 (2015).

440. Tsukada, M., Freddi, G., Monti, P., Bertoluzza, A. & Kasai, N. Structure and molecular conformation of tussah silk fibroin films: Effect of methanol. *J. Polym. Sci. Part B Polym. Phys.* **33**, 1995–2001 (1995).

441. Chen, X. *et al.* Conformation transition kinetics of regenerated Bombyx mori silk fibroin membrane monitored by time-resolved FTIR spectroscopy. *Biophys. Chem.* **89**, 25–34 (2001).

442. Hu, X., Kaplan, D. & Cebe, P. Determining beta-sheet crystallinity in fibrous proteins by thermal analysis and infrared spectroscopy. *Macromolecules* **39**, 6161–6170 (2006).

443. Barth, A. Infrared spectroscopy of proteins. *Biochimica et Biophysica Acta - Bioenergetics* **1767**, 1073–1101 (2007).

444. Costes, S. V. *et al.* Automatic and quantitative measurement of protein-protein colocalization in live cells. *Biophys. J.* **86**, 3993–4003 (2004).

445. Dunn, K. W., Kamocka, M. M. & McDonald, J. H. A practical guide to evaluating colocalization in biological microscopy. *Am. J. Physiol. - Cell Physiol.* **300**, 723–742 (2011).

446. Manders, E. M. M., Verbeek, F. J. & Aten, J. A. Measurement of co-localization of objects in dual-colour confocal images. *J. Microsc.* **169**, 375–382 (1993).

447. Wang, L. *et al.* Interfacial rheology of natural silk fibroin at air/water and oil/water interfaces. *Langmuir* **28**, 459–467 (2012).

448. Lefèvre, T., Rousseau, M. E. & Pézolet, M. Protein secondary structure and orientation in silk as revealed by Raman spectromicroscopy. *Biophys. J.* **92**, 2885–2895 (2007).

449. Han, T. Y., Shr, J. F., Wu, C. F. & Hsieh, C. Te. A modified Wenzel model for hydrophobic behavior of nanostructured surfaces. *Thin Solid Films* **515**, 4666–4669 (2007).

450. Poonguzhali, R., Khaleel Basha, S. & Sugantha Kumari, V. Fabrication of asymmetric nanostarch reinforced Chitosan/PVP membrane and its evaluation as an antibacterial patch for in vivo wound healing application. *Int. J. Biol. Macromol.* **114**, 204–213 (2018).

451. Maiti, R. *et al.* In vivo measurement of skin surface strain and sub-surface layer deformation induced by natural tissue stretching. *J. Mech. Behav. Biomed. Mater.* **62**, 556–569 (2016).

452. Gbureck, U., Vorndran, E., Müller, F. A. & Barralet, J. E. Low temperature direct 3D printed bioceramics and biocomposites as drug release matrices. *J. Control. Release* **122**, 173–180 (2007).

453. Xing, K. *et al.* Dual-Stimulus-Triggered Programmable Drug Release and Luminescent Ratiometric pH Sensing from Chemically Stable Biocompatible Zinc Metal-Organic Framework. *ACS Appl. Mater. Interfaces* **10**, 22746–22756 (2018).

454. Csapó, E. *et al.* Cross-linked and hydrophobized hyaluronic acid-based controlled drug release systems. *Carbohydr. Polym.* **195**, 99–106 (2018).

455. Kung, M. L. *et al.* Biomimetic polymer-based Ag nanocomposites as a antimicrobial platform. *Appl. Mater. Today* **4**, 31–39 (2016).

456. Barnes, L. A. *et al.* Mechanical Forces in Cutaneous Wound Healing: Emerging Therapies to Minimize Scar Formation. *Advances in Wound Care* **7**, 47–56 (2018).

457. Jang, T. H. *et al.* Cryopreservation and its clinical application. *Integr. Med. Res.* **6**, 12–18 (2017).

458. Yokonishi, T. *et al.* Offspring production with sperm grown in vitro from cryopreserved testis tissues. *Nat. Commun.* **5**, 1–6 (2014).

459. Bald, W. B. On crystal size and cooling rate. *J. Microsc.* **143**, 89–102 (1986).

460. Fahy, G. M. & Wowk, B. Principles of cryopreservation by vitrification. in

Cryopreservation and freeze-drying protocols. Methods in Molecular Biology (Methods and Protocols) 21–82 (Springer, New York, NY, 2015).

461. Suzuki, N. *et al.* Successful fertility preservation following ovarian tissue vitrification in patients with primary ovarian insufficiency. *Hum. Reprod.* **30**, 608–615 (2015).

462. Kawamura, K. *et al.* Hippo signaling disruption and Akt stimulation of ovarian follicles for infertility treatment. *Proc. Natl. Acad. Sci.* **110**, 17474–17479 (2013).

463. Kita, H., Okamoto, K., Kushima, R., Kawauchi, A. & Chano, T. Dimethyl sulfoxide induces chemotherapeutic resistance in the treatment of testicular embryonal carcinomas. *Oncol. Lett.* **10**, 661–666 (2015).

464. Pal, R., Mamidi, M. K., Das, A. K. & Bhonde, R. Diverse effects of dimethyl sulfoxide (DMSO) on the differentiation potential of human embryonic stem cells. *Arch. Toxicol.* **86**, 651–661 (2012).

465. Galvao, J. *et al.* Unexpected low-dose toxicity of the universal solvent DMSO. *FASEB J.* **28**, 1317–1330 (2014).

466. Alessandrino, E. P. *et al.* Adverse events occurring during bone marrow or peripheral blood progenitor cell infusion: Analysis of 126 cases. *Bone Marrow Transplant.* **23**, 533–537 (1999).

467. Seo, J. M. *et al.* Cryopreservation of amniotic fluid-derived stem cells using natural cryoprotectants and low concentrations of dimethylsulfoxide. *Cryobiology* **62**, 167–173 (2011).

468. Gurruchaga, H. *et al.* Advances in the slow freezing cryopreservation of microencapsulated cells. *J. Control. Release* **281**, 119–138 (2018).

469. Stefanic, M. *et al.* Apatite nanoparticles strongly improve red blood cell cryopreservation by mediating trehalose delivery via enhanced membrane permeation. *Biomaterials* **140**, 138–149 (2017).

470. Biggs, C. I. *et al.* Polymer mimics of biomacromolecular antifreezes. *Nat. Commun.* **8**, 1–12 (2017).

471. Hasan, M., Fayter, A. E. R. & Gibson, M. I. Ice Recrystallization Inhibiting Polymers Enable Glycerol-Free Cryopreservation of Microorganisms. *Biomacromolecules* **19**, 3371–3376 (2018).

472. Graham, B. *et al.* Polyproline as a Minimal Antifreeze Protein Mimic That Enhances the Cryopreservation of Cell Monolayers. *Angew. Chem. Int. Ed.* **129**, 16157–16160 (2017).

473. Mitchell, D. E., Lovett, J. R., Armes, S. P. & Gibson, M. I. Combining Biomimetic Block Copolymer Worms with an Ice-Inhibiting Polymer for the Solvent-Free Cryopreservation of Red Blood Cells. *Angew. Chem. Int. Ed.* **55**, 2801–2804 (2016).

474. Deller, R. C., Vatish, M., Mitchell, D. A. & Gibson, M. I. Glycerol-Free Cryopreservation of Red Blood Cells Enabled by Ice-Recrystallization-Inhibiting Polymers. *ACS Biomater. Sci. Eng.* **1**, 789–794 (2015).

475. Blood, R. *et al.* A Comparative Study of the Effects of Glycerol and Hydroxyethyl Starch in Canine. *J. Vet. Med. Sci.* **66**, 1543–1547 (2004).

476. Christoph, S., Kwiatoszynski, J., Coradin, T. & Fernandes, F. M. Cellularized Cellular Solids via Freeze-Casting. *Macromol. Biosci.* **16**, 182–187 (2016).

477. Liu, X., Zhao, G., Chen, Z., Panhwar, F. & He, X. Dual Suppression Effect of Magnetic Induction Heating and Microencapsulation on Ice Crystallization Enables Low-Cryoprotectant Vitrification of Stem Cell–Alginate Hydrogel Constructs. *ACS Appl. Mater. Interfaces* **10**, 16822–16835 (2018).

478. Cao, Y. *et al.* The Unusual Properties of Polytetrafluoroethylene Enable Massive-Volume Vitrification of Stem Cells with Low-Concentration Cryoprotectants. *Adv. Mater. Technol.* **4**, 1–14 (2019).

479. Stubbs, C., Bailey, T. L., Murray, K. & Gibson, M. I. Polyampholytes as Emerging

Macromolecular Cryoprotectants. *Biomacromolecules* **21**, 7–17 (2020).

480. Zhu, W. *et al.* Metal-Organic Framework Nanoparticle-Assisted Cryopreservation of Red Blood Cells. *J. Am. Chem. Soc.* **141**, 7789–7796 (2019).

481. Dedovets, D., Monteux, C. & Deville, S. Five-dimensional imaging of freezing emulsions with solute effects. *Science* **360**, 303–306 (2018).

482. Ishiguro, H. & Rubinsky, B. Mechanical interactions between ice crystals and red blood cells during directional solidification. *Cryobiology* **31**, 483–500 (1994).

483. Bahari, L., Bein, A., Yashunsky, V. & Braslavsky, I. Directional freezing for the cryopreservation of adherent mammalian cells on a substrate. *PLoS One* **13**, 1–17 (2018).

484. Elami, A. *et al.* Successful restoration of function of frozen and thawed isolated rat hearts. *J. Thorac. Cardiovasc. Surg.* **135**, 666–673 (2008).

485. Tajima, Y., Matsuo, T. & Suga, H. Calorimetric study of phase transition in hexagonal ice doped with alkali hydroxides. *J. Phys. Chem. Solids* **45**, 1135–1144 (1984).

486. Kocherbitov, V. The nature of nonfreezing water in carbohydrate polymers. *Carbohydr. Polym.* **150**, 353–358 (2016).

487. Mazur, P. Freezing of living cells: mechanisms and implications. *The American journal of physiology* **247**, C125–C142 (1984).

488. Mazur, P. & Schmidt, J. J. Interactions of cooling velocity, temperature, and warming velocity on the survival of frozen and thawed yeast. *Cryobiology* **5**, 1–17 (1968).

489. Moynihan, C. T., Easteal, A. J. & Wilder, J. Dependence of the Glass Transition Temperature on Heating and Cooling Rate. *J. Phys. Chem.* **78**, 2673–2677 (1974).

490. Mazur, P. Cryobiology: The Freezing of Biological Systems. *Science* **168**, 939–949 (1970).

491. Carmona-Gutierrez, D. *et al.* Guidelines and recommendations on yeast cell death nomenclature. *Microbial Cell* **5**, 4–31 (2018).

492. Carmona-Gutierrez, D. *et al.* Apoptosis in yeast: Triggers, pathways, subroutines. *Cell Death and Differentiation* **17**, 763–773 (2010).

493. Ludovico, P. *et al. Saccharomyces cerevisiae commits to a programmed cell death process in response to acetic acid*. *Microbiology* **147**, (2001).

494. Madeo, F. *et al.* Apoptosis in yeast. *Current Opinion in Microbiology* **7**, 655–660 (2004).

495. Frey, B. *et al.* Cells Under Pressure – Treatment of Eukaryotic Cells with High Hydrostatic Pressure, from Physiologic Aspects to Pressure Induced Cell Death. *Curr. Med. Chem.* **15**, 2329–2336 (2008).

496. Weichart, D., Mcdougald, D., Jacobs, D. & Kjelleberg, S. In situ analysis of nucleic acids in cold-induced nonculturable Vibrio vulnificus. *Appl. Environ. Microbiol.* **63**, 2754–2758 (1997).

497. Asakura, H. *et al.* Gene expression profile of Vibrio cholerae in the cold stress-induced viable but non-culturable state. *Environ. Microbiol.* **9**, 869–879 (2007).

498. González-Escalona, N., Fey, A., Höfle, M. G., Espejo, R. T. & Guzmán, C. A. Quantitative reverse transcription polymerase chain reaction analysis of Vibrio cholerae cells entering the viable but non-culturable state and starvation in response to cold shock. *Environ. Microbiol.* **8**, 658–666 (2006).

499. Salma, M., Rousseaux, S., Sequeira-Le Grand, A., Divol, B. & Alexandre, H. Characterization of the Viable but Nonculturable (VBNC) State in Saccharomyces cerevisiae. *PLoS One* **8**, 2–12 (2013).

500. Schneider, C. A., Rasband, W. S. & Eliceiri, K. W. NIH Image to ImageJ: 25 years of image analysis. *Nature Methods* **9**, 671–675 (2012).

501. Herker, E. *et al.* Chronological aging leads to apoptosis in yeast. *J. Cell Biol.* **164**, 501–507 (2004).

502. Madeo, F., Fröhlich, E. & Fröhlich, K. U. A yeast mutant showing diagnostic markers of early and late apoptosis. *J. Cell Biol.* **139**, 729–734 (1997).

503. Facts About Blood Needs. *American Red Cross* Available at: https://www.redcrossblood.org/donate-blood/how-to-donate/how-blood-donations-help/blood-needs-blood-supply (accessed May 30, 2020).

504. Giarratana, M. C. *et al.* Proof of principle for transfusion of in vitro-generated red blood cells. *Blood* **118**, 5071–5079 (2011).

505. Tucker, M. J. & Liebermann, J. *Vitrification in assisted reproduction, second edition*. *Vitrification in Assisted Reproduction, Second Edition* (CRC Press, 2015).

506. Karimi-Busheri, F. & Weinfeld, M. *Biobanking and Cryopreservation of Stem Cells*. **951**, (Springer, 2016).

507. Pegg, D. E. The preservation of tissues for transplantation. *Cell and Tissue Banking* **7**, 349–358 (2006).

508. Henkelman, S., Noorman, F., Badloe, J. F. & Lagerberg, J. W. M. Utilization and quality of cryopreserved red blood cells in transfusion medicine. *Vox Sanguinis* **108**, 103–112 (2015).

509. Pogozhykh, D. *et al.* Exploring the possibility of cryopreservation of feline and canine erythrocytes by rapid freezing with penetrating and non-penetrating cryoprotectants. *PLoS One* **12**, (2017).

510. Lusianti, R. E., Benson, J. D., Acker, J. P. & Higgins, A. Z. Rapid removal of glycerol from frozen-thawed red blood cells. *Biotechnol. Prog.* **29**, 609–620 (2013).

511. Liu, J. *et al.* Deglycerolization of red blood cells: A new dilution-filtration system. *Cryobiology* **81**, 160–167 (2018).

512. Briard, J. G. *et al.* Small molecule ice recrystallization inhibitors mitigate red blood cell lysis during freezing, transient warming and thawing. *Sci. Rep.* **6**, 2–11 (2016).

513. Poisson, J. S., Acker, J. P., Briard, J. G., Meyer, J. E. & Ben, R. N. Modulating Intracellular Ice Growth with Cell-Permeating Small-Molecule Ice Recrystallization Inhibitors. *Langmuir* **35**, 7452–7458 (2019).

514. Zhang, Y. *et al.* Cold-Responsive Nanoparticle Enables Intracellular Delivery and Rapid Release of Trehalose for Organic-Solvent-Free Cryopreservation. *Nano Lett.* **19**, 9051–9061 (2019).

515. Harding, M. M., Anderberg, P. I. & Haymet, A. D. J. 'Antifreeze' glycoproteins from polar fish. *European Journal of Biochemistry* **270**, 1381–1392 (2003).

516. Bravo, L. A. & Griffith, M. Characterization of antifreeze activity in Antarctic plants. *J. Exp. Bot.* **56**, 1189–1196 (2005).

517. Deller, R. C., Vatish, M., Mitchell, D. A. & Gibson, M. I. Synthetic polymers enable non-vitreous cellular cryopreservation by reducing ice crystal growth during thawing. *Nat. Commun.* **5**, 1–7 (2014).

518. Crowe, J. H. & Crowe, L. M. Preservation of mammalian cells - Learning nature's tricks. *Nature Biotechnology* **18**, 145–146 (2000).

519. Elbein, A. D., Pan, Y. T., Pastuszak, I. & Carroll, D. New insights on trehalose: A multifunctional molecule. *Glycobiology* **13**, (2003).

520. Wolkers, W. F., Tablin, F. & Crowe, J. H. *From anhydrobiosis to freeze-drying of eukaryotic cells*. *Comparative Biochemistry and Physiology Part A* **131**, (2002).

521. Toner, M. & Kocsis, J. *Storage and Translational Issues in Reparative Medicine*. *Ann. N.Y. Acad. Sci* **961**, (2002).

522. Stoll, C., Holovati, J. L., Acker, J. P. & Wolkers, W. F. Synergistic effects of liposomes, trehalose, and hydroxyethyl starch for cryopreservation of human

erythrocytes. *Biotechnol. Prog.* **28**, 364–371 (2012).

523. Holovati, J. L., Gyongyossy-Issa, M. I. C. & Acker, J. P. Effects of trehalose-loaded liposomes on red blood cell response to freezing and post-thaw membrane quality. *Cryobiology* **58**, 75–83 (2009).

524. Bai, G. *et al.* Oxidized Quasi-Carbon Nitride Quantum Dots Inhibit Ice Growth. *Adv. Mater.* **29**, (2017).

525. Yang, J. *et al.* Exploring the Potential of Biocompatible Osmoprotectants as Highly Efficient Cryoprotectants. *ACS Appl. Mater. Interfaces* **9**, 42516–42524 (2017).

526. Blank, M., Soo, L. & Britten, J. S. *Adsorption of Albumin on Rabbit Sperm Membranes*. *J. Membrane Biol* **29**, (1976).

527. Roche, M., Rondeau, P., Singh, N. R., Tarnus, E. & Bourdon, E. The antioxidant properties of serum albumin. *FEBS Letters* **582**, 1783–1787 (2008).

528. Dashtestani, F., Ghourchian, H. & Najafi, A. Albumin coated copper-cysteine nanozyme for reducing oxidative stress induced during sperm cryopreservation. *Bioorg. Chem.* **80**, 621–630 (2018).

529. Uysal, O. & Bucak, M. N. Effects of oxidized glutathione, bovine serum albumin, cysteine and lycopene on the quality of frozen-thawed ram semen. *Acta Vet. Brno* **76**, 383–390 (2007).

530. Lee, W.-H. *et al.* Effects of α-Linolenic Acid and Bovine Serum Albumin on Frozen-thawed Boar Sperm Quality during Cryopreservation. *Reprod. Dev. Biol.* **40**, 33–37 (2016).

531. Rosato, M. P. & Iaffaldano, N. Cryopreservation of rabbit semen: Comparing the effects of different cryoprotectants, cryoprotectant-free vitrification, and the use of albumin plus osmoprotectants on sperm survival and fertility after standard vapor freezing and vitrification. *Theriogenology* **79**, 508–516 (2013).

532. Amidi, F., Farshad, A. & Khor, A. K. Effects of cholesterol-loaded cyclodextrin during freezing step of cryopreservation with TCGY extender containing bovine serum albumin on quality of goat spermatozoa. *Cryobiology* **61**, 94–99 (2010).

533. González Porto, S. A. *et al.* The addition of albumin improves Schwann cells viability in nerve cryopreservation. *Cell Tissue Bank.* **19**, 507–517 (2018).

534. Quan, G. B. *et al.* Intracellular sugars improve survival of human red blood cells cryopreserved at -80°C in the presence of polyvinyl pyrrolidone and human serum albumin. *Cryo-Letters* **28**, 95–108 (2007).

535. Baar, S. Albumin and Hydroxy-Ethyl Starch in the Cryopreservation of Red Cells—an In Vitro Study. *Transfusion* **13**, 73–83 (1973).

536. STRUMIA, M. M. & STRUMIA, P. V. Recovery and survival of human red blood cells frozen with albumin, dextran and lactose-albumin. in *International Society of Blood Transfusion* **19**, 61–68 (Karger Publishers, 1964).

537. Strumia, M. M. *et al.* Effect of Lactose, Dextran and Albumin on Recovery and Survival of Frozen Red Cells. *Transfusion* **5**, 399–411 (1965).

538. Lagerberg, J. W. Cryopreservation of red blood cells. in *Cryopreservation and Freeze-Drying Protocols.* 353–367 (Springer, New York, NY, 2015).

539. Liu, B., Zhang, Q., Zhao, Y., Ren, L. & Yuan, X. Trehalose-functional glycopeptide enhances glycerol-free cryopreservation of red blood cells. *J. Mater. Chem. B* **7**, 5695–5703 (2019).

540. Qin, K. *et al.* Unveiling cells' local environment during cryopreservation by correlative in situ spatial and thermal analyses. 1–31

541. Si, W. *et al.* Directional freezing as an alternative method for cryopreserving rhesus macaque (Macaca mulatta) sperm. *Theriogenology* **74**, 1431–1438 (2010).

542. Panagopoulou, A. *et al.* Glass transition and dynamics in BSA-water mixtures over

wide ranges of composition studied by thermal and dielectric techniques. *Biochim. Biophys. Acta - Proteins Proteomics* **1814**, 1984–1996 (2011).

543. Lynch, A. L., Chen, R. & Slater, N. K. H. PH-responsive polymers for trehalose loading and desiccation protection of human red blood cells. *Biomaterials* **32**, 4443–4449 (2011).

544. Wagner, C. T., Burnett, M. B., Livesey, S. A. & Connor, J. Red blood cell stabilization reduces the effect of cell density on recovery following cryopreservation. *Cryobiology* **41**, 178–194 (2000).

545. Guest, M. M., Bond, T. P., Cooper, R. G. & Derrick, J. R. Red Blood Cells: Change in Shape in Capillaries. *Science* **142**, 1319–1321 (1963).

546. Mohandas, N. & Gallagher, P. G. Red cell membrane: Past, present, and future. *Blood* **112**, 3939–3948 (2008).

547. El Assal, R. *et al.* Bio-inspired cryo-ink preserves red blood cell phenotype and function during nanoliter vitrification. *Adv. Mater.* **26**, 5815–5822 (2014).

548. Boehm, D. *et al.* Caspase-3 Is Involved in the Signalling in Erythroid Differentiation by Targeting Late Progenitors. *PLoS One* **8**, (2013).

549. Miettinen, T. P. & Björklund, M. Cellular Allometry of Mitochondrial Functionality Establishes the Optimal Cell Size. *Dev. Cell* **39**, 370–382 (2016).

550. Flegel, W. A., Natanson, C. & Klein, H. G. Does prolonged storage of red blood cells cause harm? *British Journal of Haematology* **165**, 3–16 (2014).

551. Chang, A., Kim, Y., Hoehn, R., Jernigan, P. & Pritts, T. Cryopreserved packed red blood cells in surgical patients: past, present, and future. *Blood Transfus.* **15**, 341–347 (2016).

552. Prickett, R. C., Marquez-Curtis, L. A., Elliott, J. A. W. & McGann, L. E. Effect of supercooling and cell volume on intracellular ice formation. *Cryobiology* **70**, 156–163

(2015).

553. Ross-Rodriguez, L. U., Elliott, J. A. W. & McGann, L. E. Investigating cryoinjury using simulations and experiments. 1: TF-1 cells during two-step freezing (rapid cooling interrupted with a hold time). *Cryobiology* **61**, 38–45 (2010).

554. Zakharov, B. *et al.* Ice Recrystallization in a Solution of a Cryoprotector and Its Inhibition by a Protein: Synchrotron X-Ray Diffraction Study. *J. Pharm. Sci.* **105**, 2129–2138 (2016).

555. Alotaibi, N. A. S., Slater, N. K. H. & Rahmoune, H. Salidroside as a novel protective agent to improve red blood cell cryopreservation. *PLoS One* **11**, (2016).

556. Talstad, I. Protection of Blood Cells by Plasma Proteins. *Acta Med. Scand.* **190**, 145–148 (1971).

557. Barbul, A. *et al.* Nanoparticle-Decorated Erythrocytes Reveal That Particle Size Controls the Extent of Adsorption, Cell Shape, and Cell Deformability. *ACS Appl. Nano Mater.* **1**, 3785–3799 (2018).

Qin Kankan – Thèse de doctorat - 2020

Applications du freeze casting dans la fabrication de biomatériaux et la cryoconservation de cellules

Résumé :

En ingénierie tissulaire, les biomatériaux doivent posséder certaines propriétés essentielles telles que la porosité, la résistance mécanique, la biocompatibilité et l'acceptation immunitaire. Le freeze-casting s'est avéré être une bonne approche pour la fabrication d’échafaudages poreux en raison de sa biocompatibilité et de la grande porosité qui en résulte (Chapitre 1). Dans le Chapitre 2, nous avons appliqué la technique de freeze-casting à la matrice de soie par ingénierie inverse avec du fibroine de soie et du sericine de soie séparés afin d'obtenir des patchs dermiques antibactériens. Le freeze-casting permet également l'encapsulation (ou la cryopréservation) des cellules et des tissus. Dans Chapitre 3, une combinaison de congélation directionnelle sous microscope confocal et d'analyse calorimétrique différentielle à balayage a été réalisée pour révéler l’environnement les levures *Saccharomyces cerevisiae* pendant la congélation et les interactions *in situ* entre les cellules et le front de congélation. Cette technique a ensuite été appliquée à la cryoprotection des globules rouges en présence de sérum d’albumine bovine (Chapitre 4). En conclusion, le freeze casting en présence de polymères biocompatibles a été appliqué avec succès pour l’élaboration de biomatériaux antimicrobiens et pour la cryopréservation de levures et des globules rouges.

Mots clés : [Freeze casting; Biopolymère; Antibactérien; Cryoconservation; Levure; Globules rouges]

Applications of freeze casting in biomaterials fabrication and cell cryopreservation

Abstract :

In order to achieve successful tissue engineering, biomaterials need to possess some essential properties such as porosity, mechanical strength, biocompatibility and immune acceptance. Freeze casting has been proved as a good approach for making porous scaffolds due to its high processing biocompatibility and the resultant high porosity (Chapter 1). In Chapter 2, we applied freeze casting to reverse engineer silk matrix with separated silk fibroin and silk sericin in order to obtain antibacterial dermal patches. Freeze casting also enables encapsulation (or cryopreservation) of cells and tissues. In Chapter 3, a combination of directional freezing under confocal microscope and differential scanning calorimetry analysis were performed to reveal surrounding environment of *Saccharomyces cerevisiae* during freezing and *in situ* interactions between cells and freezing front. This technique was also proved useful for red blood cell cryopreservation in presence of albumin (Chapter 4). In conclusion, freeze casting/directional freezing enabled antibacterial matrix fabrication and also cryopreservation of yeast and red blood cells.

Key words : [Freeze casting; Biopolymers; Antibacterial; Cryopreservation; Yeast; Red blood cells]